



Nonequilibrium Dynamics with Rydberg Facilitation: From Epidemic Spreading to Motional Squeezing

Dissertation

Daniel Steven Brady
Juni 2025

R **TU** **P** Rheinland-Pfälzische
Technische Universität
Kaiserslautern
Landau

Nonequilibrium Dynamics with Rydberg Facilitation: From Epidemic Spreading to Motional Squeezing

– DISSERTATION –

Daniel Steven Brady

Vom Fachbereich Physik der Rheinland-Pfälzischen Technischen Universität
Kaiserslautern-Landau zur Verleihung des akademischen Grades „Doktor der
Naturwissenschaften“ genehmigte Dissertation

Betreuer: PROF. DR. MICHAEL FLEISCHHAUER
Zweitgutachter: PROF. DR. HERWIG OTT

Datum der wissenschaftlichen Aussprache: 28. August 2025

DE-386

Abstract

Spreading processes play an integral role in our day to day lives. From the transmission of infectious diseases, to cascading power line failures which lead to black outs, to the fast spread of forest fires across dry landscapes, the underlying physics governing these outbreaks is quite similar. Therefore, understanding these processes, their scope, and their dynamics, is not without merit. In particular, these systems are described by a mix of network theory, basic epidemic models, and statistical physics. Within this thesis, we will apply these models to describe spreading processes on a microscopic level: interactions between individual atoms.

Our platform to investigate these spreading processes are Rydberg atoms. Specifically, by tailoring dipole interactions between these atoms, the so called *facilitation* regime can be reached, where the laser-driven excitation of an atom only becomes possible if an excited Rydberg atom is already present. This conditional excitation resembles the infection of a healthy individual only occurring in the presence of an already infected one.

Using facilitation as a platform, we first investigate spreading processes in the classical high-dephasing limit of Rydberg atoms in a gas, using large-scale Monte Carlo simulations. Here, a phase transition between an active phase (infinite spread) and an absorbing state (limited spread) exists. In the limit of low gas temperatures, we find the spreading of excitations to be constrained to an underlying network. For low network connectivity we find a heterogeneous Griffiths phase, which replaces the active-absorbing phase transition. For high network connectivity we find the universality class of the phase transition to depend on the gas temperature, displaying *directed percolation* universality — the most important class for nonequilibrium phase transitions — at low temperatures and mean field universality at high temperatures.

At intermediate temperatures we find activity spreading akin to Lévy flights, where a small number of very fast Rydberg atoms manage to excite (“infect”) atoms at very large distances. Consequently, the system falls into the *anomalous directed percolation* universality class, and we show possibly the first experimental evidence of a system displaying this universality class. Finally, we derive an analytical expression for the high dephasing rates between Rydberg atoms, which are a generic feature of these systems.

In addition to this, we investigate facilitation in the quantum regime using time-evolving block decimation simulations to model a one-dimensional chain of atoms trapped in a tweezer array. Here, we explicitly regard the motional degree of freedom of the atoms in the tweezer traps as quantized phonon excitations. Resulting from dipole-dipole interactions between Rydberg atoms, higher lying phonon states can be excited. Assuming a Lennard-Jones style dipole potential, resulting from an avoided crossing of different Rydberg states, we find a number of non-trivial effects. These include the generation of non-classical squeezed states, strong and long-range correlations between phonon excitations, the thermalization of local phonon degrees of freedom despite a purely unitary time-evolution, and a non-ergodic behavior of spin domains in the form of emergent Bloch oscillations. Under a Born-Oppenheimer approximation, we separate spin (internal ground and Rydberg states) and phonon degrees of freedom of the atoms, and manage to find a simple analytical description of the various processes in the system.

Zusammenfassung

Ausbreitungsprozesse spielen eine zentrale Rolle in unserem Alltag. Von der Übertragung von infektiösen Krankheiten über kaskadierende Stromausfälle bis hin zur schnellen Ausbreitung von Waldbränden in trockenen Landschaften – die zugrunde liegende Physik dieser Phänomene ist bemerkenswert ähnlich. Daher ist das Verständnis dieser Prozesse, ihres Umfangs und ihrer Dynamik von großer Bedeutung. Insbesondere lassen sich solche Systeme durch eine Kombination einfacher epidemischer Modelle, verschiedener Netzwerkgeometrien und statischer Physik beschreiben. Im Rahmen dieser Arbeit werden diese Modelle angewendet, um die Dynamik von Ausbreitungsprozessen in Systemen aus Spin- $\frac{1}{2}$ Teilchen zu beschreiben.

Unsere Plattform zur Untersuchung dieser Prozesse sind Rydbergatome. Insbesondere können Dipolwechselwirkungen zwischen diesen Atomen so gestaltet werden, dass das sogenannte *Facilitation*-Regime erreicht wird. In diesem ist die laserinduzierte Anregung eines Atoms nur möglich, wenn sich ein anderes, bereits angeregtes Rydbergatom in der Nähe befindet. Diese bedingte Anregung ähnelt der Infektion eines gesunden Menschen durch einen infizierten Menschen.

Im Rahmen des Rydberg-Facilitation-Regimes untersuchen wir zunächst Ausbreitungsprozesse im klassischen Limes eines Gases bei hohen Dephasierungsralten mithilfe von Monte-Carlo-Simulationen. Wir stellen fest, dass sich die Anregungen entlang eines zugrunde liegenden Netzwerks ausbreiten, was zu einer heterogenen Griffiths-Phase führt, im Falle geringer Konnektivität im Netzwerk. Zudem untersuchen wir den zugrunde liegenden Phasenübergang zwischen der aktiven Phase (unendliche Ausbreitung) und dem absorbierenden Zustand (begrenzte Ausbreitung). Wir finden, dass die Universalitätsklasse dieses Phasenübergangs von der Gasttemperatur abhängt: Bei niedrigen Temperaturen zeigt sich *Directed Percolation* (dt. gerichtete Perkolation) – die wichtigste Universalitätsklasse für Nichtgleichgewichts-Phasenübergänge – während bei hohen Temperaturen ein Mean-Field-Vehalten (dt. Molekularfeld) auftritt.

Bei mittleren Temperaturen beobachten wir, neben dem regulären Ausbreitungsmechanismus, eine weitere Ausbreitung der Aktivität, die Lévy-flights ähnelt, wobei wenige sehr schnelle Rydbergatome Atome über große Distanzen hinweg Grundzustandsatome anregen („infizieren“) können. Infolgedessen fällt das System in die Universalitätsklasse der *anomalous directed percolation* (dt. anomal gerichteten Perkolation), und wir zeigen möglicherweise den ersten experimentellen Befund eines Systems, welches diese Universalitätsklasse aufweist. Schließlich leiten wir einen analytischen Ausdruck für die hohen Raten der Dephasierung optisch getriebener Rydbergatome her, die ein generisches Merkmal solcher Systeme darstellen.

Des Weiteren untersuchen wir *Facilitation* im quantenmechanischen Regime mithilfe eines *time-evolving block decimation* (dt. zeitentwickelnde Block-Dezimierung) Algorithmus für eine eindimensionale Kette von Atomen, die in einer Reihe optischer Fallen, sog. *tweezer* (dt. Pinzetten), gefangen sind. Dabei berücksichtigen wir die Bewegung der Atome in den Fallen explizit als quantisierte Phononenanregungen. Aufgrund der Dipol-Dipol-Wechselwirkungen zwischen Rydberg-Atomen können dabei höher liegende Phononenzustände angeregt werden. Unter der Annahme eines Lennard-Jones-artigen Dipolpotentials finden wir eine Reihe nichttrivialer Effekte. Diese umfassen die Erzeu-

gung nichtklassischer gequetschter Zustände, starke und langreichweitige Korrelationen zwischen Phononenanregungen, die Thermalisierung lokaler Phononenfreiheitsgrade trotz einer rein unitären Zeitentwicklung sowie ein nicht-ergodisches Verhalten von Spin-domänen in Form emergenter Bloch-Oszillationen. Mithilfe der Born-Oppenheimer-Näherung gelingt es uns, Spin- (innere Grund- und Rydbergzustände) und Phononfreiheitsgrade der Atome zu trennen und eine überraschend einfache analytische Beschreibung der verschiedenen Prozesse im System herzuleiten.

Contents

List of Publications	ix
1. Introduction	1
1.1. Outline	3
1.2. Rydberg Atoms	5
1.2.1. Properties of Rydberg Atoms	5
1.2.2. Interacting Rydberg Atoms	6
1.2.3. Rydberg Blockade	9
1.2.4. Rydberg Facilitation	10
1.3. Phase Transitions, Universality, and Self-Organized Criticality	13
1.3.1. Equilibrium Phase Transitions and the Ising Model	14
1.3.2. Nonequilibrium Phase Transitions and Directed Percolation	17
1.3.3. Quantum Phase Transitions	19
1.3.4. Self-Organized Criticality	20
1.4. Epidemics on Complex Networks	23
1.4.1. Epidemic Models	23
1.4.2. Network Models	26
1.4.3. Epidemics on Networks	28
1.5. Squeezed States	31
1.5.1. The Quantized Electromagnetic Field	31
1.5.2. Quantum States of Light	32
1.5.3. Applications of Squeezing	37
2. Griffiths Phase in a Facilitated Rydberg Gas at Low Temperatures	39
3. Mean-Field Approach to Rydberg Facilitation in a Gas of Atoms at High and Low Temperatures	53
4. Anomalous Directed Percolation on a Dynamic Network Using Rydberg Facilitation	63
5. Nonequilibrium Universality of Rydberg-Excitation Spreading on a Dynamic Network	75
6. Non-Classical Spin-Phonon Correlations Induced by Rydberg Facilitation in a Lattice	91
7. Dephasing in Rydberg Facilitation Due to State-Dependent Dipole Forces	103
8. Summary and Outlook	111
Appendix	113
A. Simulating a Gas of Rydberg Atoms using the Monte Carlo Method	115
B. Derivation of the Facilitation Width	121

Bibliography	125
Curriculum Vitae	133
Acknowledgments	137

List of Publications

- [P1] D. Brady, J. Bender, P. Mischke, S. Ohler, T. Niederprüm, H. Ott, and M. Fleischhauer. "Griffiths Phase in a Facilitated Rydberg Gas at Low Temperatures". *Physical Review Research* **6**, 013052 (2024).
- [P2] D. Brady and M. Fleischhauer. "Mean-field approach to Rydberg facilitation in a gas of atoms at high and low temperatures". *Physical Review A* **108**, 052812 (2023).
- [P3] D. Brady, S. Ohler, J. Otterbach, and M. Fleischhauer. "Anomalous Directed Percolation on a Dynamic Network Using Rydberg Facilitation". *Physical Review Letters* **133**, 173401 (2024).
- [P4] S. Ohler, D. Brady, P. Mischke, J. Bender, H. Ott, T. Niederprüm, W. Ripken, J. S. Otterbach, and M. Fleischhauer. "Nonequilibrium Universality of Rydberg-Excitation Spreading on a Dynamic Network". *Physical Review Research* **7**, 033167 (2025).
- [P5] D. Brady and M. Fleischhauer. "Non-Classical Spin-Phonon Correlations Induced by Rydberg Facilitation in a Lattice". [arXiv:2504.19679](https://arxiv.org/abs/2504.19679) (2025).
- [P6] T. Schlegel*, E. Konstantinidou*, M. Fleischhauer, and D. Brady. "Dephasing in Rydberg Facilitation Due to State-Dependent Dipole Forces". [arXiv:2505.09314](https://arxiv.org/abs/2505.09314) (2025).

*These authors contributed equally.

Not included in this document.

- [P7] S. Ohler, D. Brady, W. Lötzsch, M. Fleischhauer, and J. S. Otterbach. "Towards Learning Self-Organized Criticality of Rydberg Atoms using Graph Neural Networks". *ICML 2nd AI4Science Workshop, Baltimore, MD* (2022).

List of Abbreviations

ADP	anomalous directed percolation
DP	directed percolation
ER	Erdős–Rényi
ftsMC	fixed time-step Monte Carlo
GGM	Generalized Growth Model
KMC	kinetic Monte Carlo
LZ	Landau-Zener
QCP	quantum critical point
RG	renormalization group
SIR	susceptible-infected-recovered
SIS	susceptible-infected-susceptible
SOC	self-organized criticality
TEBD	time-evolving block decimation

1. Introduction

Due to their stability and strong, long range interactions, Rydberg atoms allow for the study of various equilibrium and nonequilibrium processes in highly controlled experimental environments [1, 2]. By tuning laser parameters, these interactions can be tailored into the *facilitation* regime [3]. Facilitation is a process where an atom excited to a high-lying Rydberg state allows for the excitation of neighboring atoms into the Rydberg state on very fast time scales. Consequently, this process bears many similarities to epidemics, where Rydberg atoms act as hosts of an infection which they subsequently pass on to neighboring atoms [4].

In the scope of this thesis, we regard the dynamics of Rydberg facilitation in various settings. Under laser driving and dissipation, it has been shown that Rydberg facilitation hosts an absorbing-state phase transition [5], a hallmark type of nonequilibrium phase transitions. Moreover, both numerical [6] and experimental [7] indications were found which show this phase transition to fall into the *directed percolation* (DP) universality class. DP constitutes the most important universality class for nonequilibrium phase transitions as a result of its *postulated* ubiquity. In the early 1980s, Janssen [8] and Grassberger [9] formulated their celebrated DP-*conjecture*, which states that *any* system generically falls into the DP universality class if it meets four conditions (cf. Sec. 1.3.2). To date, no counter examples have been found and DP universality has even been found in systems where one or more of these conditions are violated [10]. It seems unexpected then that only very few systems exist where DP universality was unequivocally proven experimentally. This lies in the inherent difficulty in extracting the three DP critical exponents. The first experiment to measure the full set of DP critical exponents was in turbulent liquid crystals in 2007 [11] and since then, as mentioned above, one [7] and two [6] of the DP critical exponents were measured in Rydberg facilitation systems in low dimensional lattices.

In a laser-driven gas of atoms under dissipation, it has been shown that Rydberg facilitation displays signatures of *self-organized criticality* (SOC) [12, 13]. SOC is a process in which a system drives *itself* to the critical point of a phase transition [14]. Though not without controversy, SOC is postulated to be the process behind the abundance of power-laws throughout nature [15]. In an experiment on the Rydberg facilitation gas displaying SOC, one of the three critical exponents of the DP universality class was measured recently. Here, a significant deviation from the expected DP critical exponent was found, which was attributed to a loss of atoms in the system. This atomic loss is the driving force behind SOC, and it was postulated that SOC might generically modify the universal behavior of the system [12].

Finally, in an experiment observing the short time dynamics, i.e. the initial spreading of "infections", a sub-exponential growth in the excitation number, similar to real-world epidemics, was observed [16]. This slow, power-law growth hints at a heterogeneity in the gas. Furthermore, for the late-time dynamics, a power-law decay of the excitation number was also found, with continuously varying exponents depending on external parameters. A ubiquity of power-laws with non-universal exponents is a hallmark of a Griffiths phase [17]. The emergence of this phase was attributed to different velocity classes in the gas restricting which atoms can interact with each other, therefore

introducing heterogeneity into the spreading processes [16].

From here, we start by analyzing the gas of atoms in the facilitation regime. Due to high dephasing rates generically present in these systems [18–20], a description through classical rate equations becomes accurate [21–24]. Therefore, we simulate the dynamics using large-scale Monte Carlo simulations of classical rate equations (cf. Appendix A for an explicit description of the algorithm), which allow for simulations on the order of 10^4 atoms.

We investigate the Rydberg facilitation gas in [P1-P4]. In particular, in [P1] we prove existence of a heterogeneous Griffiths phase in the gas in the limits of low temperatures and low gas densities. We find this to emerge from an underlying network constraining the spread of excitations. Following this in [P2], we improve on the mean field Langevin equations presented in Ref. [12] leading to a much better agreement with our Monte Carlo simulations. Building on this in [P3], we investigate the universality class of the absorbing-state phase transition and find it to depend on the temperature of the gas. For low temperatures, DP critical behavior is present, but with increasing temperature, the *anomalous directed percolation* (ADP) universality class emerges, which is characterized by smoothly varying critical exponents. Notably, we are able to replicate the critical exponent measured in Ref. [12], showing that the deviation from DP universality likely stems from Lévy flights and not SOC. In [P4], we utilize a mapping of the DP critical exponents to *avalanche* exponents, allowing us access to extract the full set of DP critical exponents.

This concludes our work on the Rydberg facilitation gas and we turn to studying facilitation in a one-dimensional array of Rydberg atoms in optical tweezers. With laser driving under facilitation conditions, a Rydberg atom can only be excited or de-excited in the presence of exactly *one* other Rydberg atom. Spontaneous decay of Rydberg atoms can be neglected when regarding the dynamics on time-scales much shorter than the spontaneous decay rate. Consequently, when looking at the dynamics of *domains* of Rydberg atoms in 1D arrays, i.e. m neighboring Rydberg atoms with all others atoms being in the ground state, the dynamics simplify to the growing and shrinking of domains *at the domain edges*. Importantly, these domains cannot coalesce or split [25].

As a result of dipole interactions, Rydberg atoms repel each other, leading to the excitation of motional states within the tweezer traps. These motional excitations can have a measurable impact on the spin dynamics. In Ref. [26], the dipole potential between Rydberg atoms is Taylor expanded up to linear order. The authors find the coupling of internal electronic and external motional degrees of freedom to drastically slow the spreading of the domain, which would otherwise be ballistic. However, up to linear order all dipole interactions *within* a domain completely cancel out making it necessary to regard higher orders of the dipole potential expansion.

In [P5], we regard this system up to second order and with a harmonic or inverted harmonic dipole potential between Rydberg atoms. This is the leading-order expansion of a Lennard-Jones style dipole potential recently realized experimentally between Rydberg atoms [27]. With a harmonic potential, we now find highly correlated behavior with non-classical center of mass states (squeezed states) taken on by the Rydberg atoms. Furthermore, this also has an effect on the dynamics of the domain.

Finally, we turn to studying one of the causes for dephasing in Rydberg systems. As mentioned above, high dephasing rates are a generic feature of Rydberg systems, however despite this, a quantitative understanding is largely missing. In [P6] we derive

an analytical expression for the dephasing rate resulting from dipole interactions between Rydberg atoms. We find this expression to fit very well with our simulations in the regime where the laser detuning Δ is larger, but on the order of the Rabi frequency Ω .

1.1. Outline

This thesis is structured as follows. Chapter 1 contains an introduction, as well as a theoretical background into the fields research within this thesis. In particular, Sec. 1.2 discusses the physics of Rydberg atoms, Sec. 1.3 concerns phase transitions and universality, as well as discussing DP and SOC, Sec. 1.4 discusses epidemic and network models, and finally, Sec. 1.5 concerns non-classical squeezed states. Chapters 2-5 contain my contributions to the Rydberg facilitation gas with [P1-P4]. Chapter 6 contains my contribution to Rydberg facilitation in the one-dimensional tweezer array in [P5]. And finally, Chapter 7 concerns the derivation of an analytical expression for the dephasing rate of Rydberg atoms from [P6]. Publication [P7] is not discussed in this thesis. Finally, Chapter 8 contains a summary of our results, as well as an outlook for each of the fields researched within this thesis.

The artificial intelligence tool ChatGPT was used to correct Python and LaTeX code, as well as to facilitate literature search.

1.2. Rydberg Atoms

A Rydberg atom is any atom with one or more highly excited electrons. In the past two decades a resurgence of interest in Rydberg atoms has occurred. This has two main reasons, first the discovery of particular phenomena based on Rydberg-Rydberg interactions, such as Rydberg blockade [28–30] quickly made Rydberg atoms a promising candidate for neutral atom quantum computation and simulation. Second, a vast improvement in tweezer array protocols has allowed for the creation of defect-free arrays of neutral atoms with arbitrary shapes [31–33] (see Fig. 1.1a). For these reasons, Rydberg quantum simulators [34] have found a wide use of applications, such as in the study of coherent transport properties [35, 36] (Fig. 1.1b), the quantum Ising model [37–41], spin liquid phases [42, 43], or quantum phase transitions to \mathbb{Z}_N symmetric phases [39, 44, 45].

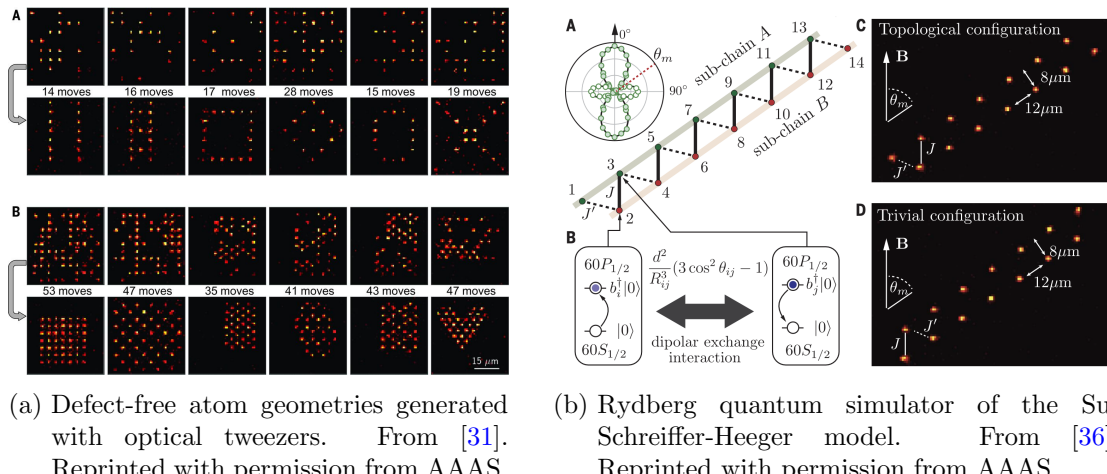


Figure 1.1.: Examples of current state-of-the-art tweezer arrays and Rydberg quantum simulators.

In this section, the physics of Rydberg atoms will be investigated. First, the core properties will be examined, after which the different two-atom dipole-dipole Rydberg interactions and resulting effects such as blockade and facilitation will be discussed.

1.2.1. Properties of Rydberg Atoms

Historically, the term *Rydberg atom* comes from the labeling of spectral lines in the late 1800s. In 1888 Swedish physicist Johannes Rydberg discovered that the energies of bound states of electrons of the Hydrogen atom are described by the empirical equation

$$E_n = -\frac{R_H}{n^2}, \quad (1.1)$$

where R_H is a constant, now known as the *Rydberg constant*, and n is an integer, later found to be the principle quantum number [46]. A quantitative derivation was achieved in the framework of quantum mechanics by Wolfgang Pauli in 1926 [47]. As n can be any integer value, eq. (1.1) implies the existence of an infinite number of energy levels,

becoming closer and closer to each other as n increases. It is these high lying states that became known as Rydberg states [1, 48].

When an atom becomes excited into a state with such a high principle quantum number n its properties become extreme, often scaling algebraically with n . For example, the radius of the atom, in terms of its electron wave function, scales as $\langle \Psi | \hat{r} | \Psi \rangle \sim n^2$ [49]. For hydrogen atoms with $n = 110$, observed for example in the Orion nebula in 1965 [50], this radius is on the order of 1 μm and is larger than a virus [48]. At such distances, the electron is only weakly bound to the nucleus making it extremely sensitive to external influences, such as electric fields or other Rydberg atoms [49].

As a result of the radius increasing with n , the radiative lifetime also becomes extreme, scaling as [49]

$$\tau_{sp} \sim n^3. \quad (1.2)$$

This results from the spatial extent of the wave function becoming very large for high n and, subsequently, the overlap between this highly excited state and the ground state wave function of the atom becomes very small, resulting in a small dipole matrix element [48]. However, in addition to a decay to the ground state, the atom could also radiatively decay into a neighboring state, which features a similarly spread out wave function. The dipole matrix element to neighboring states scales strongly with n as $\langle nS_{1/2} | \hat{d} | (n+1)P_{3/2} \rangle \sim n^2$ with the dipole operator \hat{d} . It is important to note that as n increases, the transition wavelength to neighboring states also increases. Fortunately for the stability of Rydberg atoms, the number of available vacuum modes into which the Rydberg state could spontaneously decay actually decreases faster than n^2 , making spontaneous decay into neighboring states unlikely [48].

Stimulated decay, however, is not affected by the constraint of available vacuum modes making it another relevant process governing the lifetimes of Rydberg states. The transitions between neighboring Rydberg states are typically in the microwave regime and therefore at frequencies populated by black-body radiation. One finds that, at finite temperature, the black-body induced lifetime is approximately given as [1]

$$\tau_{bb} \sim n^2. \quad (1.3)$$

The weaker scaling in n when compared to the radiative lifetime τ_{sp} shows that black-body induced decay poses a limitation on the lifetime of Rydberg atoms. See Ref. [51] for a review, especially concerning spontaneous versus stimulated decay of Rydberg states.

1.2.2. Interacting Rydberg Atoms

Rydberg atoms have two main properties which make them particularly useful in experimental applications. First, as a result of the large distance between nucleus and electron they become very sensitive to external fields making them ideal platforms for quantum sensing of microwave and terahertz radiation [49]. Second, Rydberg atoms feature strong interactions between *each other*. These interactions give rise to effects such as Rydberg blockade or Rydberg facilitation, which will be discussed later on.

In this section we will focus on the latter property, namely the strong interaction between Rydberg atoms. These interactions result from a virtual photon exchange between

Rydberg atoms and occur over large inter-atomic distances r of up to several μm . The two most relevant interactions are the resonant *dipolar* interaction, decaying as $1/r^3$ and the off-resonant *van-der-Waals* interaction, decaying as $1/r^6$.

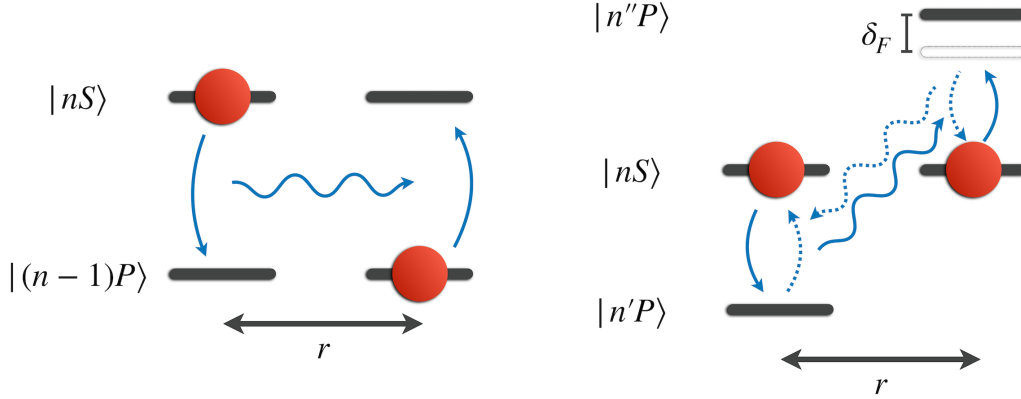


Figure 1.2.: (Left) Dipolar c_3 interaction. A resonant exchange of a virtual photon lets atom 1 decay to a neighboring Rydberg state while exciting atom 2. (Right) Van-der-Waals c_6 interaction. Since the energy spacing between $|n''P\rangle$, $|nS\rangle$, and $|n'P\rangle$, $|nS\rangle$ is shifted by δ_F , the second atom cannot be excited giving rise to an off-resonant interaction. Figure adapted from Ref. [48].

Dipolar c_3 Interaction

The dipolar interaction requires two Rydberg atoms to be in neighboring states with an allowed dipole transition, e.g. $|\alpha\rangle = |nS\rangle$ and $|\beta\rangle = |(n-1)P\rangle$. In the two atom basis, the states $|\alpha\beta\rangle$ and $|\beta\alpha\rangle$ are degenerate and can interact via a coherent exchange of a virtual photon (cf. Fig. 1.2 (left)). This is known as a *flip-flop* interaction, where atom 1 undergoes $|\alpha\rangle \rightarrow |\beta\rangle$ and atom 2 undergoes $|\beta\rangle \rightarrow |\alpha\rangle$.

In particular, under the multipole expansion, the leading order dipole-dipole interaction potential is given by

$$V_{dd}(\mathbf{r}) = \frac{1}{4\pi\epsilon_0} \frac{\mathbf{d}_1 \cdot \mathbf{d}_2 - 3(\mathbf{d}_1 \cdot \mathbf{n})(\mathbf{d}_2 \cdot \mathbf{n})}{r^3}, \quad (1.4)$$

with $\mathbf{n} = \mathbf{r}/r$ and the electric dipole operator of atom j labeled \mathbf{d}_j [52]. In the two atom basis, i.e. with states $\{|\alpha\beta\rangle, |\beta\alpha\rangle\}$, the interaction Hamiltonian can be written as

$$\hat{H} = \begin{pmatrix} 0 & V_{dd}(\mathbf{r}) \\ V_{dd}(\mathbf{r}) & 0 \end{pmatrix}. \quad (1.5)$$

As the states are degenerate, a coherent exchange between them is possible mediated by the interaction potential $V_{dd}(\mathbf{r})$. This potential is quadratic in the dipole operator and, as discussed in the previous section, therefore scales as $(n^2)^2 = n^4$. Furthermore, dipole-dipole interactions scale with the interatomic distance as $\sim 1/r^3$, and have a strong dependence on the angle between the atoms and the quantization axis. The total scaling of the interaction potential is therefore

$$V(r) = \frac{c_3}{r^3}(1 - 3 \cos^2 \theta), \quad (1.6)$$

with the angle between the quantization axis, set by e.g. the presence of an external magnetic field, and the interatomic axis θ , and the interaction constant $c_3 \sim n^4$, giving this interaction the colloquial name c_3 *interaction*.

Van-der-Waals c_6 Interaction

The van-der-Waals interaction on the other hand originates from an off-resonant exchange of a virtual photon. Here both Rydberg atoms are initially in the same state, e.g. $|nS\rangle$. Again, the first atom decays to a neighboring state $|n'P\rangle$ and emits a virtual photon, however, since most likely no state $|n''P\rangle$ exists with the same energy difference, the virtual photon is immediately re-emitted and the atoms return to their original states (cf. Fig. 1.2 (right)). The difference in energy between the states $|nS\rangle$, $|n'P\rangle$, and $|nS\rangle$, $|n''P\rangle$ is known as the *Förster defect* δ_F [53, 54]. The scaling of the interaction energy is more complicated in this regime and will be derived in detail in the following.

Consider the states (in the two atom basis) $|nS, nS\rangle$ and $|n'P, n''P\rangle$. In this basis, the interaction Hamiltonian can be written as

$$\hat{H} = \begin{pmatrix} \delta_F & V_{dd}(\mathbf{r}) \\ V_{dd}(\mathbf{r}) & 0 \end{pmatrix}. \quad (1.7)$$

Diagonalizing this Hamiltonian, one receives the eigenenergies given by

$$\lambda_{1,2} = \frac{1}{2} \left(\delta_F \pm \sqrt{\delta_F^2 + 4V_{dd}(\mathbf{r})^2} \right), \quad (1.8)$$

which can be Taylor expanded for large δ_F . Doing this, the eigenenergies are given as

$$\lambda_1 = \delta_F + \frac{V_{dd}(\mathbf{r})^2}{\delta_F}, \quad (1.9)$$

$$\lambda_2 = -\frac{V_{dd}(\mathbf{r})^2}{\delta_F}. \quad (1.10)$$

Due to the high density of energy levels for high n , this process occurs over many different pair states $|n'P, n''P\rangle$. Therefore, the interaction potential is received by summing over all pair states and reads

$$V(r) = \sum_{n', n''} \frac{|\langle n'P, n''P | V_{dd}(\mathbf{r}) | nS, nS \rangle|^2}{\delta_F(n', n'')}. \quad (1.11)$$

This interaction is often simply written as

$$V(r) = \frac{c_6}{r^6}, \quad (1.12)$$

with the van-der-Waals coefficient c_6 , which depends on the initial state of the Rydberg atoms. This coefficient scales as $c_6 \sim n^{11}$, since the potential scales with the fourth power of the dipole operator \mathbf{d}_j , and the Förster defect scales as $\delta_F \sim n^{-3}$. Furthermore, since the interaction potential is received by summing over different pair states, there is almost *no angular dependence* of the interaction and the c_6 interaction is (nearly) isotropic [53].

For $\delta_F \rightarrow 0$, the so-called *Förster resonance* occurs. In this case, a single term dominates in the sum and the c_3 interaction, in particular its angular dependence and $1/r^3$ scaling, is recovered. Note, that this will also occur for small interatomic distances, where $V_{dd}(\mathbf{r})^2 \gg \delta_F^2$, and the Taylor expansion in eq. (1.8) is no longer valid [2].

All Rydberg-Rydberg interactions discussed throughout this thesis are c_6 van-der-Waals interactions.

1.2.3. Rydberg Blockade

Perhaps the most important property that Rydberg atoms feature is *Rydberg blockade*. Theoretically predicted in 2001 [28] and subsequently experimentally realized for the first time in 2009 [29], Rydberg blockade is a process in which one Rydberg atom prevents the excitation of another within a certain radius r_b , called the *blockade radius* [30]. The blockade radius is typically on the order of μm and can even extend to tens of micrometers, see e.g. [55]. This process not only allows for the creation of qubit gates [2, 28, 56, 57], it also allows for the use of Rydberg atoms as quantum simulators [34].

The underlying physics is quite simple. Consider a two-atom system, with each atom laser coupled between a ground $|g\rangle$ and a Rydberg state $|r\rangle$. The effect is most prominent for low angular momentum Rydberg states, i.e. $|r\rangle = |nS\rangle$. Coupled by a (resonant) laser with Rabi-frequency Ω , the two-atom system can now be described in the basis

$$\{ |gg\rangle, |+\rangle, |-\rangle, |rr\rangle \}, \quad (1.13)$$

where $|\pm\rangle = \frac{1}{\sqrt{2}}(|gr\rangle \pm |rg\rangle)$. Starting in $|gg\rangle$, a resonant excitation to $|+\rangle$ occurs with the rate $\sqrt{2}\Omega$. Now, depending on the interatomic distance, the energy of the state $|rr\rangle$ is shifted by the Rydberg interaction potential $V(r)$. For large distances, such that $V(r) \ll \Omega$, the coupling between $|+\rangle$ and $|rr\rangle$ remains (nearly) resonant. However, for smaller distances, such that $V(r) \gg \Omega$, the shift becomes so large that the $|rr\rangle$ state becomes effectively decoupled from the dynamics. A simultaneous excitation of both atoms is no longer possible and the system performs Rabi oscillations between $|g\rangle$ and $|+\rangle$ at the rate $\sqrt{2}\Omega$ (cf. Fig. 1.3 (left)). The distance where the transition occurs is known as the blockade radius and is given by¹

$$r_b = \sqrt[6]{\frac{c_6}{\Omega}}. \quad (1.14)$$

This effect is not limited to two atoms. For N atoms closely packed within r_b , a single excitation is shared between all atoms and they perform Rabi oscillations with the rate $\sqrt{N}\Omega$. This collective behavior is called a *Rydberg superatom* and is particularly interesting in part due to its high level of entanglement [58].

¹Note in the literature, e.g. [48, 49], one also finds $r_b = \sqrt[6]{\frac{c_6}{\gamma_{\perp}}}$, where γ_{\perp} corresponds to the laser linewidth. In reality, r_b depends on the greatest of the two quantities.

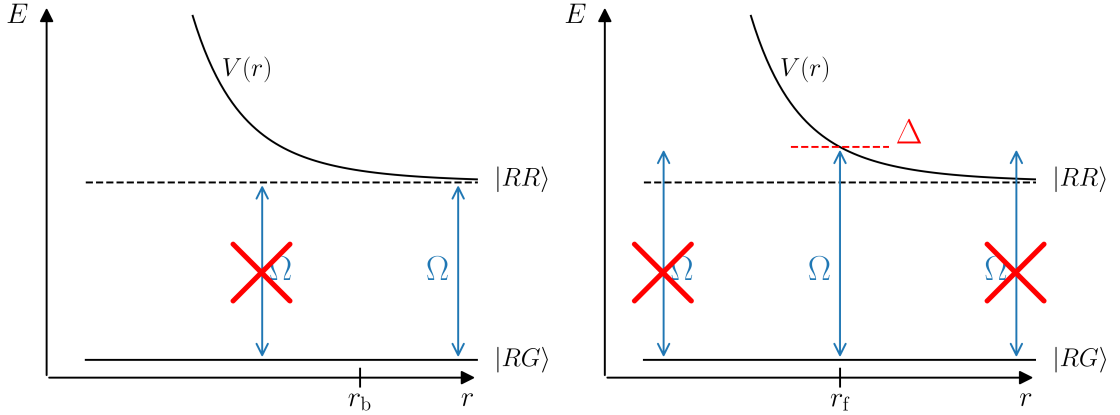


Figure 1.3.: *Blockade and Facilitation.* (Left) Rydberg blockade. For distances $r < r_b$ no excitation is possible, since the Rydberg-Rydberg interaction $V(r)$ pushes the doubly excited state $|RR\rangle$ out of resonance. (Right) Rydberg facilitation. The laser light is tuned away from resonance with detuning Δ . Consequently, a resonant excitation is *only* possible at the distance r_f , where the detuning cancels the Rydberg-Rydberg interaction, i.e. $\Delta + V(r_f) = 0$.

1.2.4. Rydberg Facilitation

Quite the opposite effect can be achieved if the driving laser light is strongly detuned, i.e. $\Delta \gg \Omega$, with the detuning from resonance Δ . Now excitations from $|gg\rangle$ to $|+\rangle$, as well as from $|+\rangle$ to $|rr\rangle$ are strongly suppressed. However, there exists a distance r_f , called the *facilitation radius*, where

$$V(r_f) + \Delta = 0, \quad (1.15)$$

i.e. the Rydberg-Rydberg interaction cancels out the detuning and a resonant coupling between $|+\rangle$ and $|rr\rangle$ occurs [3] (cf. Fig. 1.3 (right)). Eq. (1.15) is known as the *facilitation condition* and the facilitation distance r_f at which this occurs is given by²

$$r_f = \sqrt[6]{\frac{c_6}{\Delta}}. \quad (1.16)$$

As a result of the finite linewidth of the laser, coupling between $|+\rangle$ and $|rr\rangle$ not only occurs exactly at the facilitation radius r_f , but also within a spherical shell around a Rydberg atom with radius r_f . In the high dephasing limit, where Rydberg dynamics can be accurately modeled by classical rate equations [21–24], e.g. in a gas of Rydberg atoms, the facilitation rate is approximately a Lorentzian function of the interatomic distance. This allows us to define the approximate width of the facilitation shell as (see Appendix B for a derivation)

$$\delta r_f = \frac{\gamma_\perp}{2\Delta} r_f, \quad (1.17)$$

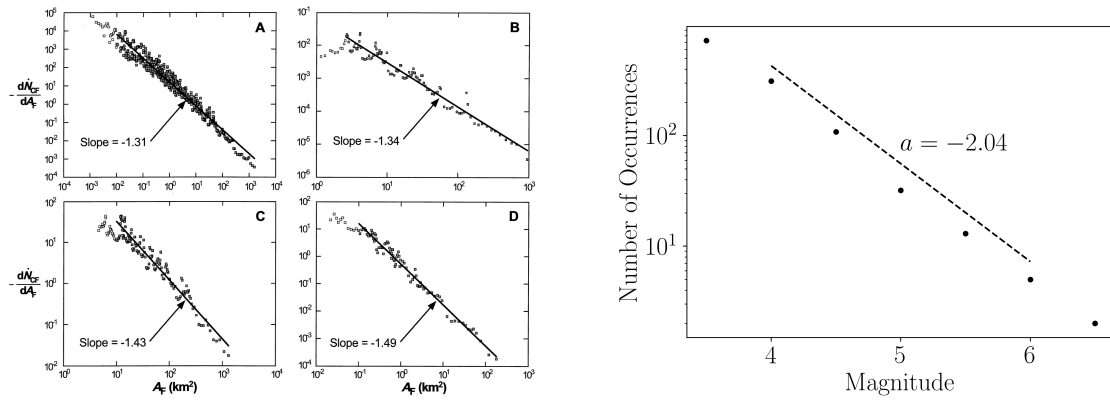
²Note that Rydberg blockade still occurs in this regime for all interatomic distances $r < r_f$. Therefore, the blockade radius is given by the facilitation radius in this regime.

with the dephasing rate of the Rydberg state γ_{\perp} .

Since facilitation corresponds to a conditional excitation, which only occurs if an excitation is already present, this can be mapped to an epidemic system (topic of [P2], see also [4, 16]). In this mapping, atoms in the Rydberg state correspond to infected individuals and atoms in the ground state correspond to healthy, susceptible individuals. The spontaneous decay of Rydberg atoms, which would normally be a nuisance for experiments, actually constitutes the recovery of infected individuals back into the ground (susceptible) state here and therefore becomes an integral part of the dynamics. As with epidemics, these systems exhibit an absorbing-state phase transition between an active phase, where activity (in the form of Rydberg excitations) is wide spread throughout the system, and an absorbing state without any Rydberg excitations [5]. Note, this mapping is only truly accurate in the limit $\Delta \rightarrow \infty$, as an absorbing state does not allow for spontaneous excitations.

1.3. Phase Transitions, Universality, and Self-Organized Criticality

No matter where you look in nature you will find power-laws. The size distribution of tsunamis [59], earthquakes [60, 61], forest fires [62], tornado groups [63], solar flares [64], neuron activations [65], epidemic outbreaks [66], among many other examples, all follow a power-law distribution [15] (cf. Fig. 1.4). However, from statistical mechanics, we understand that power-laws and scale-free behavior are a characteristic feature of systems at *criticality*, i.e. the critical point of a phase transition. For a system to be at criticality typically requires a fine-tuning of parameters, making it unclear how so many systems in nature could be critical.



(a) Forest fire size distributions in (A) U.S.A. 1986-1995, (B) western U.S.A. (1915-1960), (C) Alaskan boreal forests (1990-1991), and (D) Australian Capital Territory (1926-1991). From [62]. Reprinted with permission from AAAS.

(b) Number of occurrences of earthquakes of different (logarithmic) magnitudes from January, 1934 to May, 1943 in and around Southern California. Raw data taken from Ref. [60].

Figure 1.4.: Real-world distributions of forest-fire and earthquake sizes showing a power-law behavior. Note that the magnitude of earthquakes is already a logarithmic quantity.

Although it is the subject of some debate [15], *self-organized criticality (SOC)* offers an elegant and simple explanation for this [14]. In the presence of driving and dissipation, if a given system has a sufficiently large separation of these time-scales, it will drive itself to the critical point of an absorbing-state phase transition, and remain there for relevant time-scales.

In this section, we will first discuss the physics of phase transitions, including equilibrium, nonequilibrium, and quantum phase transitions. Following this, we will discuss criticality. In particular, systems at criticality tend to lose any form of length scales and consequently fractal-like structures emerge. Based on the behavior of a system at criticality, it can be grouped with other - typically microscopically very different systems - into universality classes. We will discuss the Ising and *directed percolation (DP)* universality classes, which are arguably the most important universality classes for equilibrium and nonequilibrium phase transitions respectively [10]. Finally, we will discuss **SOC**, utilizing the knowledge gained on phase transitions and universality.

1.3.1. Equilibrium Phase Transitions and the Ising Model

Phase transitions occur when a physical system changes state abruptly, and non-analytically, when varying a physical quantity like the temperature, pressure, or an external field. These quantities are known as the *control parameter* as they control which phase the system is in. The state of the system on either side of the phase transition is then either described as *ordered* or *disordered*. This is quantified by an *order parameter* which is zero in the disordered phase and non-zero in the ordered phase.³

Phase transitions are generally categorized into *first order* and *second order* phase transitions. First order phase transitions have a discontinuous change in the order parameter when crossing the critical point (cf. Fig. 1.5b), while second order phase transitions remain continuous in the order parameter, but are discontinuous in its derivatives (cf. Fig. 1.5c). For this reason, second order phase transitions are also called *continuous* phase transitions. See Fig. 1.5 for a visualization of this using the Ising model.

The quantitative framework for understanding continuous phase transitions was created in the context of *equilibrium* phase transitions, i.e. in systems at thermodynamic equilibrium. Emerging from this framework is the concept of *universality*, which can actually be applied to systems far from equilibrium [67] and to systems exhibiting a quantum phase transition [68].

Naturally a phase transition occurs in the wake of competing processes and it is considered an equilibrium phase transition if the system is in thermal equilibrium. In order to illustrate this, we will use the Ising model, which describes ferromagnetism [69]. Here the competing processes are the energy minimization which occurs when neighboring spins are co-aligned and thermal fluctuations, which causes spins to randomly flip. In the following, let us quantitatively look at the two dimensional Ising model. A phase diagram and the behavior of the order parameters around the critical temperature can be seen in Fig. 1.5.

Consider a two dimensional lattice, with spins σ_i at each vertex, which can either point up or down, i.e. $\sigma_i = \pm 1$. Neighboring spins interact with some interaction strength $J > 0$ and we can apply an external magnetic field with energy contribution h . Let (i, j) be the set of all neighboring indices, then the Hamiltonian of the system can be written as

$$H = -J \sum_{(i,j)} \sigma_i \sigma_j - h \sum_i \sigma_i. \quad (1.18)$$

From eq. (1.18) it is immediately clear that neighboring co-aligned spins, i.e. up-up or down-down, are energetically more favorable since this reduces the first term.

Now, if the thermal fluctuations are small, the co-alignment of spins wins and the system is in a phase with a global magnetization, i.e. an overwhelming majority of spins point in the same direction. Conversely, if thermal fluctuations are too strong, no globally ordered phase can exist and the system has a net zero magnetization. Therefore, the order parameter of the ferromagnetic phase is the magnetization $m = \sum_i \sigma_i$, where $\sigma_i = \pm 1$ is the alignment of spin i , and the control parameter is the temperature T , which dictates the strength of thermal fluctuations. The phase transition from a ferro- to a

³Note that phase transitions between different ordered states also exist, where the above discussion has to be generalized to different order parameters respectively.

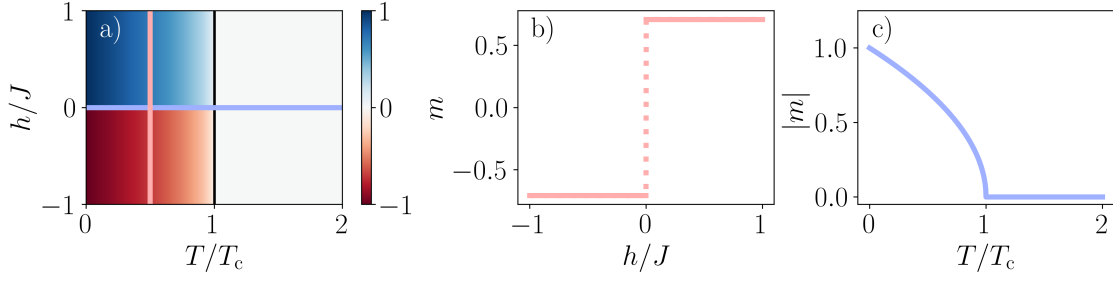


Figure 1.5.: *Ising Phases and Phase Transitions.* a) 2D Ising model phase diagram for temperature T in units of critical (Curie) temperature T_c and external magnetic field h in units of coupling strength J . Color represents the net magnetization $m \equiv \frac{1}{N} \sum_{i=1}^N \sigma_i$. b) Magnetization as a function of field strength for $T = \frac{1}{2} T_c$ (pink line in a)), displaying a *first order* phase transition at $h/J = 0$. c) Absolute value of magnetization as a function of temperature for $h/J = 0$ (light blue line in a)) displaying a *second order* phase transition at T_c . The trajectories of (b) and (c) can be seen in (a).

paramagnet occurs at the Curie temperature T_c [70]. These two competing processes are readily seen in the free energy $F = H - TS$ of the system, which it seeks to minimize in equilibrium. For example, co-alignment minimizes both the internal energy H , but also the entropy S .

For continuous phase transitions, systems close to the critical point are "habitually described by *power laws*" [10]. Power laws are functions of the form $f(x) = Cx^\alpha$, for some constant C and some real-valued exponent α . They intrinsically hold the property of *scale invariance*, i.e.

$$y_1 = Cx^\alpha \propto x^\alpha \quad (1.19a)$$

$$y_2 = C(kx)^\alpha \equiv Ck^\alpha x^\alpha \propto x^\alpha. \quad (1.19b)$$

When rescaling x with some constant k , both the function y_1 and the scaled function y_2 remain proportional to x^α , albeit with some other prefactor. This shows us that the behavior of the system does not depend on the scale at which we are looking at it. In Fig. 1.6 we can see what this means in the context of the 2D Ising model. Here, a 2D grid of spins is shown, with spins in the down state being black and spins in the up state being white. At criticality we can see spin up clusters (white regions) of any size emerging, reminiscent of fractal like structures.

A quantitative understanding of scale-invariant behavior in equilibrium systems was developed by Kenneth G. Wilson within the framework of the *renormalization group* (RG) formalism, earning him the Nobel Prize in Physics in 1982 [71, 72]. In the following, we will briefly discuss the scaling behavior of the 2D Ising model near criticality and the core concepts of Wilson's application of the RG formalism.

For the 2D Ising model, the scale-invariant properties near criticality include the magnetization m , the susceptibility χ , the specific heat C , the correlation length ξ , and the decay of the correlation function $G(r)$ with distance r . Defining the reduced temperature $\tau \equiv -\frac{T-T_c}{T_c}$, with $\tau = 0$ at criticality, these quantities obey

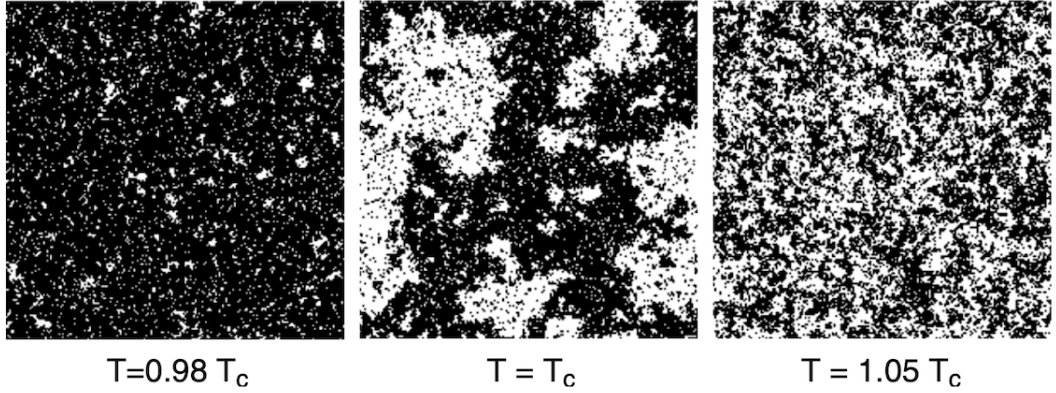


Figure 1.6.: Configurations of the two-dimensional Ising model below, at, and above the critical temperature T_c . White pixels correspond to spin-up and black pixels to spin-down sites. At the critical temperature the system shows a lack of size scale for spin-up clusters. Figure taken from Ref. [10], i.e. M. Henkel, H. Hinrichsen, and S. Lübeck, *Non-equilibrium phase transitions* (Springer 2008). Reproduced with permission from Springer Nature.

$$m(\tau) \propto \tau^\beta \quad (1.20a)$$

$$m(\tau = 0) \propto |h|^{1/\delta} \quad (1.20b)$$

$$\chi(\tau) \propto |\tau|^{-\gamma} \quad (1.20c)$$

$$C(\tau) \propto |\tau|^{-\alpha} \quad (1.20d)$$

$$\xi(\tau) \propto |\tau|^{-\nu} \quad (1.20e)$$

$$G(r, \tau = 0) \propto r^{-d+2-\eta}, \quad (1.20f)$$

near criticality, with the six *critical exponents* β , δ , γ , α , ν , and η , as well as the dimension d . Through a set of scaling relations from Rushbrooke [73], Widom [74], Fisher [75], and Josephson [76], relations between the critical exponents can be established (cf. [10]). Following these relations, the Ising model is described by two *independent* critical exponents.

These critical exponents describe all systems near universality which fall into the *Ising universality class*. This is given when a system shares the same global properties, such as dimensionality or symmetry, which is the case for e.g. the van-der-Waals gas. This means that despite having a completely different microscopic structure, both the Ising model and the van-der-Waals gas behave the same near criticality. This unexpected fact can be explained by the **RG** formalism, which will be briefly introduced in the following.

When looking at the parameter phase space of the Ising model, i.e. (T, h) , we can perform an **RG** approach. Here, we coarse-grain the Hamiltonian, averaging out short-range fluctuations. This process in turn modifies the parameters in the system, and an iterative application of this coarse-graining leads to a set of *flow equations* for the parameters of the system. If we regard these in phase space, we find a set of fixed points, corresponding to the critical points of the system. The fact that these are fixed points with respect to the flow equations shows us that here the system remains invariant under

coarse-graining, i.e. it is scale-invariant.

More so, in the RG approach, the iterative application of coarse-graining means that the microscopic details of the system become irrelevant. The fixed points only depend on general properties of the system, such as its dimension or its symmetries. Therefore, the behavior at these fixed points is universal and is shared with all systems that share the dimension or symmetries of the given system. This is the fundamental idea of defining universality classes, and the Ising model falls into – and is the namesake of – the *Ising universality class*. Other systems in this class, which follow the same scaling laws near criticality, are the van-der-Waals gas or critical opalescence in binary fluid mixtures.

1.3.2. Nonequilibrium Phase Transitions and Directed Percolation

In contrast to equilibrium phase transitions, continuous phase transitions in systems far from equilibrium are much less well understood [10]. Any system is considered *nonequilibrium* if it does not obey *detailed balance*. Detailed balance is given when all microscopic processes occur at the same rate as their respective reverse processes, i.e. the system obeys

$$w_{i \rightarrow j} S_i = w_{j \rightarrow i} S_j, \quad (1.21)$$

where S_ν is the equilibrium probability of being in state ν and $w_{\nu \rightarrow \mu}$ is the transition rate from state ν to state μ [77]. As long as detailed balance is given, the distribution of states in the system remains constant over time, i.e. the system is at equilibrium. For nonequilibrium systems, the absence of detailed balance means there is a breaking of time-reversal symmetry and as such, the time-evolution of the system becomes relevant in classifying the dynamics of the system. Consequently for the description of nonequilibrium systems, time enters the dimensionality in many cases, and the dimensionality for these systems is typically denoted as $d + 1$, where d is the number of spatial dimensions. Unlike spatial dimensions, the time dimension displays preferential directionality.

Arguably, the most important type of nonequilibrium phase transition is the *absorbing-state phase transition*. This phase transition separates a fluctuating *active phase*, where activity (e.g. fire in a forest, or infected patients in a population) is widespread in the system, and an absorbing state without activity. The key concept here is that if the system enters the absorbing state it cannot escape from it anymore. An example of this is if the last infected patient of a virus recovers without infecting anyone else. Following this the virus would be extinct and no further infections could take place. This fact alone signals a breaking of detailed balance, as the system can enter the absorbing state, but never leave it.

Absorbing-state phase transitions are key in the description of epidemics and disease spreading. The underlying framework of epidemic models is also used to describe the spread of information, traffic patterns, social behavior, and can even be mapped to the spreading of Rydberg excitations under the facilitation constraint (cf. [P1, P2], Sec. 1.4).

The concept of universality, discussed in the previous section, which was created in the context of continuous, equilibrium phase transitions, can be expanded to describe continuous, nonequilibrium phase transitions. Similar to how the Ising universality class is arguably the most important universality class for equilibrium systems, *directed percolation* (DP) emerges as the most important class for nonequilibrium systems [10]. Percolation pertains to connectivity and asks the question if a system is connected enough

for a given particle to move through the entire system. This displays a continuous phase transition between a disconnected and a connected phase (cf. Sec. 1.4.2). For directed percolation, the individual links in the system receive a preferential direction. Once again, it immediately becomes clear that detailed balance is broken - a particle can move through a given link, but cannot return the way it came.

One of the most simple DP systems is a one-dimensional lattice where neighboring sites are connected with probability p . At $p_c \approx 0.6447$ the system exhibits a percolation transition [10]. For $p > p_c$, activity can spread through the system and for $p < p_c$ activity quickly dies out. This can be seen in Fig. 1.7, where active sites are white and inactive sites are black.

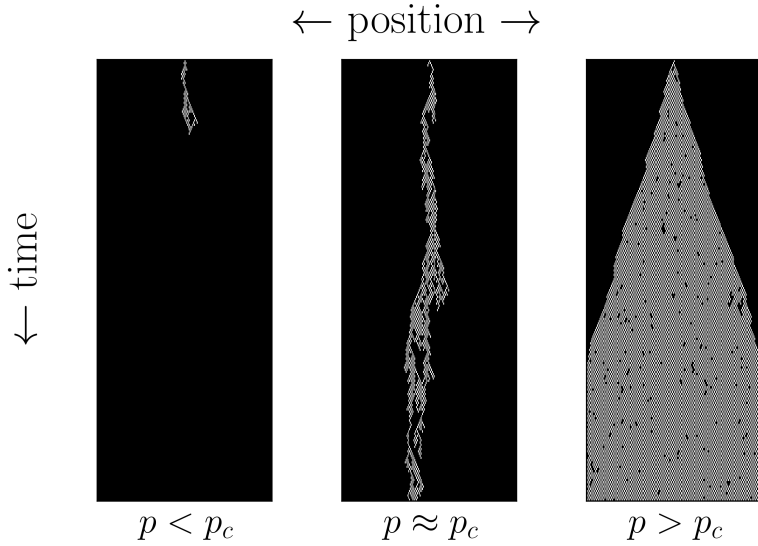


Figure 1.7.: *Directed percolation on a lattice.* 1D lattice with active nodes (white) and inactive nodes (black) starting with one initial active seed. In each time step activity can be passed on from a given active site to neighboring sites with probability p , whereupon the active site becomes inactive. At $p_c \approx 0.6447$ the system is critical as a balance between spreading and decay is present.

The reason DP is so important is due to its apparent ubiquity. In the early 1980s, Janssen [8] and Grassberger [9] conjectured that *any* nonequilibrium phase transition falls into DP universality if it meets the following four conditions [67]:

1. The system has a continuous phase transition between a fluctuating active phase and a *unique* absorbing state.
2. The phase transition has a positive, scalar order parameter.
3. The dynamic rules are short range.
4. There are no special attributes, such as additional symmetries, conservation laws, or quenched randomness.

To date, no counterexamples have been found [10] and DP universality has even been predicted in systems where one or several of these criteria are not fulfilled [78, 79].

However, despite the immense successes **DP** has enjoyed on the theoretical side, only a handful of experimental platforms are known where **DP** behavior has unambiguously been proven. This is due to the inherent difficulty that comes with measuring the **DP** critical exponents. The first such platforms was found in 2007 in turbulent liquid crystals and a full set of critical exponents in $d = 2 + 1$ dimensions was measured [11, 80]. Furthermore, in contrast to the Ising model, the critical exponents characterizing **DP** have so far only been estimated, as no general analytic framework exists yet. These numeric estimates, even for the simplest case of $d = 1 + 1$ dimensions, suggest that these exponents may be irrational numbers in contrast to simple rational numbers found in equilibrium 2D integrable systems [10].

Rydberg systems in the facilitation regime behave like epidemics and as such feature an absorbing-state phase transition. For 1D systems, **DP** universality was theoretically predicted [6] and subsequently experimentally observed [7]. These cases however, regarded the system in the absence of dissipation, specifically in the form of atomic losses. These atomic losses lead the system to drive itself to criticality, a process known as **SOC**. It was not understood if **SOC** modified the universal behavior of **DP**, or if it could compromise the universal behavior in its entirety [12, 78, 81]. In [P3] we showed that, in this system, **DP** universality actually persists in the presence of **SOC**, once again adding to the immense robustness **DP** universality seems to have.

1.3.3. Quantum Phase Transitions

Finally, let us touch on the subject of quantum phase transitions. In a classical system, a phase transition occurs at a finite temperature, e.g. the Curie temperature in the Ising model. Here, the temperature T corresponds to the control parameter as it dictates the strength of thermal fluctuations, which cause a breaking of order in the system. In a quantum phase transition however, order is broken by quantum fluctuations dictated by some control parameter g . Since quantum fluctuations would compete with thermal fluctuations at any finite temperature, a pure quantum phase transition is only given at absolute zero, i.e. $T = 0$. Here, the *quantum critical point* (**QCP**) emerges, i.e. at $T = 0$ and $g = g_c$ (cf. Fig. 1.8).

For continuous quantum phase transitions, as in the classical case, one finds a divergence of characteristic length scales near criticality. Once again, the behavior of the system near criticality does not depend on the microscopic details of the system and the concept of universality can be applied here. However, this singular behavior at criticality is only present in the *ground state* of the system, i.e. requiring $T = 0$. Since reaching this point is experimentally impossible, much of the theory of quantum phase transitions tries to describe the behavior of the system close to criticality [68].

For $T > 0$, and a control parameter sufficiently close to criticality, i.e. $g \approx g_c$, the *quantum critical phase* arises. Here, both types of fluctuations (thermal and quantum) play an important role. While the system looks critical with respect to the control parameter g , i.e. in the form of scale-invariance, it is driven away from criticality by thermal fluctuations [82]. In other words, this phase features thermal excitations of the quantum critical ground state. Finally, at high enough temperatures non-universality sets in when the thermal energy exceeds characteristic microscopic energy scales [82].

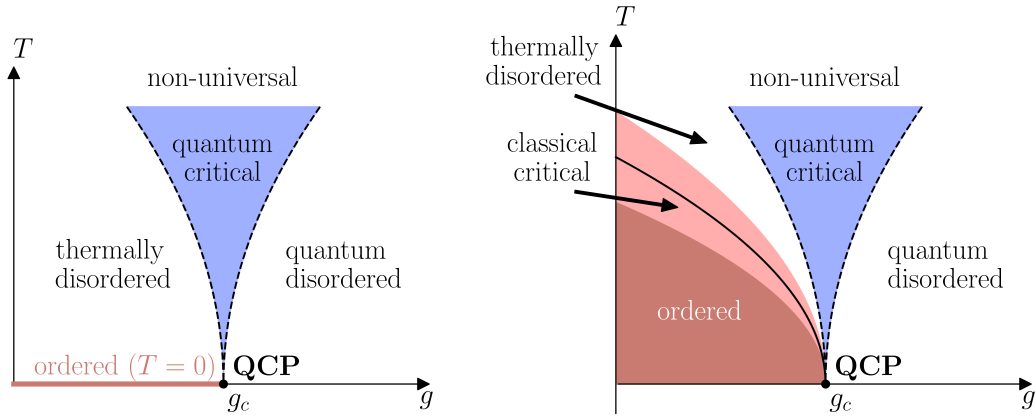


Figure 1.8.: *Phase Diagrams with Quantum Critical Point*. The figure shows two possibilities for quantum criticality, with (left) and without (right) a thermally ordered state, i.e. where order persists at $T > 0$. Figure adapted from Ref. [82].

1.3.4. Self-Organized Criticality

Having discussed the significance of scale-invariance and how this is a generic feature of continuous phase transitions at criticality, the question arises as to why power-laws are so ubiquitous in nature. In particular, we cannot assume that generic systems throughout nature are all fine-tuned to the critical point of a phase transition. An elegant explanation for this was offered through *self-organized criticality (SOC)* by Per Bak, Chao Tang, and Kurt Wiesenfeld in 1987 [14]. In their original paper, Bak, Tang, and Wiesenfeld introduced a sand pile model, which consists of a 2D lattice and where each point on the lattice contains either 0, 1, 2, or 3 sand grains. If any given point exceeds 3 sand grains, the site *topples* and the four sand grains are distributed evenly to all nearest neighbors. Starting with either a completely empty lattice, or a random distribution of sand grains throughout the lattice, the system dynamically evolves as follows:

1. Drop a sand grain onto a random site.
2. If the site now exceeds three sand grains it topples.
3. If the site topples redistribute four sand grains to the four nearest neighbors.
4. Then, if any of these sites exceeds four sand grains, they topple.
5. Wait until all toppling has finished and start with Step 1.

Typically this model uses open boundary conditions, meaning that when a site at the edge of the lattice topples one sand grain will be lost from the system. Importantly, this model assumes the limit of *infinitely slow* driving, i.e. the next grain of sand is only placed once all activity in the system has stopped. The system exhibits a phase transition between an unstable (active) phase, where, in the absence of dissipation, a single grain of sand would cause an infinite cascade of topplings and an absorbing state where the addition of a sand grain would not have any effect on the system at large.

In the active phase, the presence of dissipation at the boundaries and infinitely slow driving cause the system to naturally evolve toward criticality. Once there, the slow driving stabilizes the system and causes it to remain critical.

At criticality, the dynamics of the system are governed by *avalanches*, i.e. chained topplings of sand piles. Due to the critical nature of the system, these avalanches lose any scale and their size becomes power-law distributed. In three dimensions, the avalanche size distribution of the sand pile model follows [14]

$$P(s) \sim s^{-\tau}, \quad (1.22)$$

with the critical exponent $\tau \approx 1.35$. Therefore, Bak, Tang, and Wiesenfeld presented a model which drives itself to criticality under the requirement that the time-scales of driving and dissipation are sufficiently separated.

Following the work of Bak, Tang, and Wiesenfeld, exponents very similar to τ were identified in power-law behavior seen throughout nature. This led to considerable excitement and the emergence of ever bolder claims as to the role of **SOC** in nature. In Ref. [15], these interpretations are listed in order of increasing scope as

1. "Self-tuned phase transitions exist in nature."
2. "All fractals in nature are caused by **SOC**."
3. "All power-laws are caused by **SOC**."
4. "The contingency of nature is caused by **SOC**."

To this day, no concrete evidence exists supporting any of these claims beyond the first. More so, Claims 2 and 3 are long known to be wrong [15, 83, 84]. The true scope of **SOC** likely needs to be reduced to its core claim: that self-tuned phase transitions exist in nature. In systems with an absorbing-state phase transition, slow driving, paired with fast dissipation, allows the system to quickly decay to criticality and remain there on mesoscopic time-scales. This does explain why power-laws exist so abundantly in nature, but does not attempt to identify a universal power-law exponent among these systems.⁴

⁴There is also some controversy as to whether certain postulated **SOC** systems, i.e. systems without a conservation law, such as the Drossel-Schwabl forest fire model [85], are truly critical. These systems exhibit an exponential cutoff in their power-law distributions making them only "quasi-critical" or "apparently scale-invariant" [81].

1.4. Epidemics on Complex Networks

The study of infectious diseases has proven to be an incredibly powerful and versatile tool with applications reaching far beyond epidemics. Aside from infectious diseases, the underlying framework can be used to describe the spread of (mis-)information, social behavior, or power grid failures to name a few [86]. In this section, we will discuss the mathematical framework of compartmental epidemic models and network models.

Following the pioneering work of Kermack and McKendrick [87], modern epidemic models generally divide the population into compartments. The most important ones are: susceptible (S) individuals, who are healthy but can contract the disease; infected (I) individuals, who carry the disease and can transmit it to susceptible individuals; and recovered/removed (R) individuals who can no longer contract the disease because they are either immune or dead. In this section we will focus on models using only S , I , and R compartments, however, other compartments, such as exposed (E), can be incorporated depending on the nature of the disease (see [86] for a review article).

The most basic models assume a population-wide *homogeneous mixing* of infections. Under this assumption, all individuals interact equally with each other. While this does not describe a realistic setting, a lot can already be learned from these simple models. For example, these models feature an absorbing-state phase transition⁵ between an active (*endemic*) phase, where the infection persists perpetually in the population, and an absorbing phase, where the infection goes extinct.

In real-world epidemics an infected individual will not be able to infect all other individuals in the population equally. Instead, they are limited to individuals in their vicinity. In epidemic models this is quantified using network models. Within this framework, the spread of excitations is confined to an underlying network and, depending on the type of network, the properties of the epidemic are greatly altered. For example, on scale-free networks, such as the Internet, the absorbing state vanishes. As a result, even the smallest transmission rates of computer viruses cause an endemic state. Therefore, *scale-free networks are incredibly vulnerable to epidemics*.

To facilitate a systematic discussion of epidemic models on complex networks, this section is divided as follows:

- *Epidemic Models* - Here we discuss epidemic models under the homogeneous mixing assumption, i.e. in the complete absence of any network structure.
- *Network Models* - Here we discuss network models, the terminology, and different types of networks.
- *Epidemics on Networks* - Finally, we will put the findings of the previous two subsections together and discuss how spreading processes behave on different networks.

1.4.1. Epidemic Models

As stated above, the simplest epidemic models are based on population-wide random mixing [88]. This *homogeneous mixing* assumption states that all individuals interact at random with each other and neglects any form of underlying network structure [86].

⁵For models with only S and I compartments.

The most basic models, such as Kermack & McKendrick [87], Bailey [89], and Anderson & May [88] compartmentalize individuals based on their disease status.

For compartmental epidemic models the underlying rules are quite simple: consider a system of N *nodes* (these can be individuals, neurons, websites, etc.), which can either be infected/active (I) or susceptible/inactive (S). Each infected node can either recover to the susceptible state at rate γ , or pass on its infection to a susceptible node at rate λ . Typically, time is rescaled into units of the recovery rate γ . With this, the recovery rate is 1 and the infection rate is given as λ/γ , sometimes simply called λ .

The Susceptible-Infected-Susceptible Model

In the absence of any network structure and considering only infected (I) and susceptible (S) compartments, an epidemic is entirely characterized by the portion of the population which is infected, called $\rho \in [0, 1]$. The dynamics are governed by a master equation of the form

$$\frac{d}{dt}\rho = -\rho + \lambda\rho(1 - \rho). \quad (1.23)$$

Recovery is given at rate 1 and infection is a second order process, occurring at rate $\lambda\rho$. The rate $\lambda\rho$, at which susceptible individuals are infected is often called the *force of infection* [86]. Eq. (1.23) describes the so-called *susceptible-infected-susceptible* (**SIS**) model [88]. The **SIS** model describes an infection where individuals immediately become susceptible again after recovery. This model has for example been used to model sexually transmitted diseases where repeated infections are common [90].

This system exhibits an *absorbing-state phase transition* at $\lambda_c = 1$, between an active phase and an absorbing state. The critical infection rate λ_c is referred to as the *epidemic threshold*. In the active phase, i.e. for $\lambda > 1$, activity spreads indefinitely in the system and the density of infected individuals reaches a steady state $\rho(t \rightarrow \infty) > 0$. In the absorbing state, i.e. for $\lambda < 1$, activity dies out exponentially leading to $\rho(t \rightarrow \infty) = 0$. The critical point of the phase transition is characterized by a power-law decay of the infected density. Inserting $\lambda = \lambda_c = 1$ into eq. (1.23), the master equation reads

$$\frac{d}{dt}\rho = -\rho^2, \quad (1.24)$$

which has the solution $\rho(t) = \frac{1}{t + \frac{1}{\rho_0}}$, with $\rho_0 = \rho(t = 0)$. Therefore, for large t , the behavior of active density at the critical point is given by $\rho \sim t^{-1}$ (cf. Fig. 1.9).

The Susceptible-Infected-Recovered Model

For certain diseases reinfections are unlikely due to a subsequent immunization. Diseases such as whooping cough or measles bring forth a lifelong immunization in an individual [90]. These diseases are modeled with the *susceptible-infected-recovered* (**SIR**) model, which actually constitutes the first compartmental epidemic model (Kermack and McKendrick [87]).

As in the SIS model, in the SIR model infected individuals pass on their infection to a susceptible individual at rate λ . However, infected individuals recover at rate 1 into the

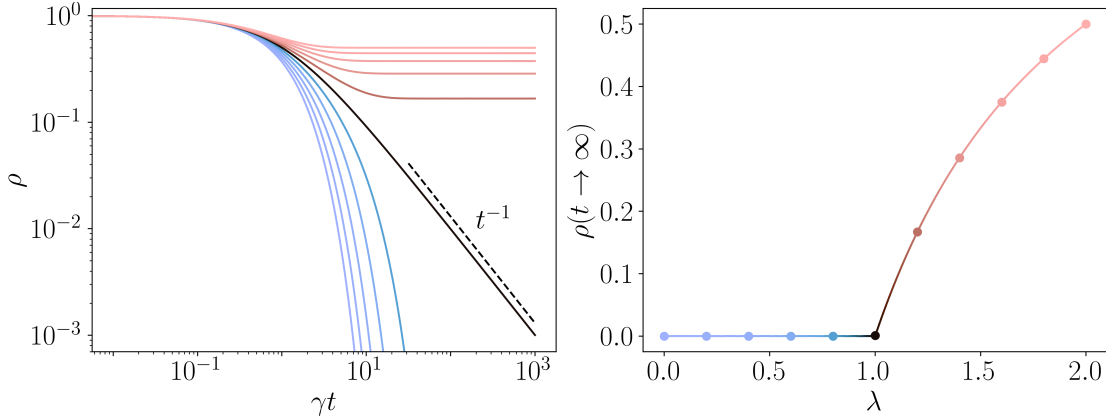


Figure 1.9.: *Dynamics and steady states of the SIS model.* (Left) Decay of infected density ρ over time t with an initially fully infected system, i.e. $\rho(t=0) = 1$. Blue signifies the absorbing state, characterized by an exponential decay of ρ to 0 (epidemic dies out) and red signifies the endemic (active) phase, where ρ reaches a steady state. At criticality (black) ρ decays as a power-law. (Right) phase diagram with the control parameter λ (infection rate) and the order parameter being the steady state infected density. A continuous phase transition is present.

recovered state, meaning the susceptible state never gets repopulated. The dynamics are now described by coupled differential equations as

$$\frac{d}{dt}\rho = -\rho + \lambda\rho(n - \rho) \quad (1.25a)$$

$$\frac{d}{dt}n = -\rho, \quad (1.25b)$$

where $n \leq 1$ is the percentage of the population in susceptible and infected states. In the SIS model $n = 1$ for all times. While in an SIS epidemic a steady state is reached, in the SIR model the disease will always die out at long times. Consequently, no endemic state can be reached in the SIR model. As opposed to the SIS model, where one typically regards steady-state properties, in the SIR model one is interested in the percentage of the population which will have been infected at $t \rightarrow \infty$, i.e. one asks the question, 'how far-reaching is the epidemic?'

We will later see that for SIR models on networks, this question directly maps to a percolation problem. A global spreading corresponds to a percolating phase, and a local, confined outbreak corresponds to the non-percolating phase.

The Generalized Growth Model

Looking at the decay of the active density, as done in Fig. 1.9, is an instructive theoretical tool to analyze phases present in the system. We used this in [P1] to prove the existence of a Griffiths phase (cf. Sec. 1.4.3) in the Rydberg facilitation gas. However, this requires a great portion of the population to be infected at time $t = 0$, making it, at best, cumbersome in real-world experiments.

A lot of information about an epidemic can be derived from its early time dynamics. The *Generalized Growth Model* (GGM) predicts the behavior of the growth of the cumulative number of incidences C . This follows

$$\frac{d}{dt}C = rC^p, \quad (1.26)$$

where r corresponds to the growth rate at early times and p is the deceleration of growth [91]. For $p = 1$ growth is exponential, whereas $p < 1$ corresponds to power-law growth with $C \sim t^{\frac{p}{1-p}}$. Power-law growth, being slower than exponential growth, is generally associated with factors impeding epidemic spreading. The most prominent factors are spatial constraints and heterogeneity in the network structure underlying the epidemic spread [16].

1.4.2. Network Models

Much information about complex systems can be derived by looking at connection patterns in the system. In this sense, the internet would be broken down into the connections between websites. When doing this, one finds that a handful of websites are connected to a huge number of other websites.

A *network* is a system composed of a certain number of *nodes*, which can be connected pairwise to each other by *links*. The terms *network* and *graph* are often used interchangeably, but have subtle differences. Networks describe how real-world systems, such as the Internet, a transportation network, or social networks behave. From a mathematical standpoint, these systems are described by *graphs* in which *vertices* are connected by *edges*. While networks apply to real-world systems and problems, graphs are purely abstract mathematical objects. The correspondence between these sets of terminology is listed in Tab. 1.1. However, a distinction between the two is rarely made [92].

Table 1.1.: Correspondence of terminology between *network science* and *graph theory* (from [92]).

Network Science	Graph Theory
Network	Graph
Node	Vertex
Link	Edge

Each node in a network has a *degree* k corresponding to the number of links to other nodes it has. The distribution of these degrees throughout the network is called the *degree distribution* $P(k)$ and allows for a typification of the network (see Tab. 1.2). For example, an *Erdős–Rényi* (ER) network (also known as a random network), has a Poissonian degree distribution [93], i.e.

$$P(k) = \frac{\langle k \rangle^k}{k!} e^{-\langle k \rangle}, \quad (1.27)$$

where $\langle k \rangle$ is the average degree of the network. For an ER network, a *percolation transition* occurs at $\langle k \rangle = 1$, separating a percolating and a non-percolating phase. In the percolating phase the system is composed of one giant connected component spanning the entire system. In the non-percolating phase, the system is composed of many small, disconnected clusters [93] (cf. Fig. 1.10). The percolation threshold depends on the nature of the graph, and some graphs may not have one at all.

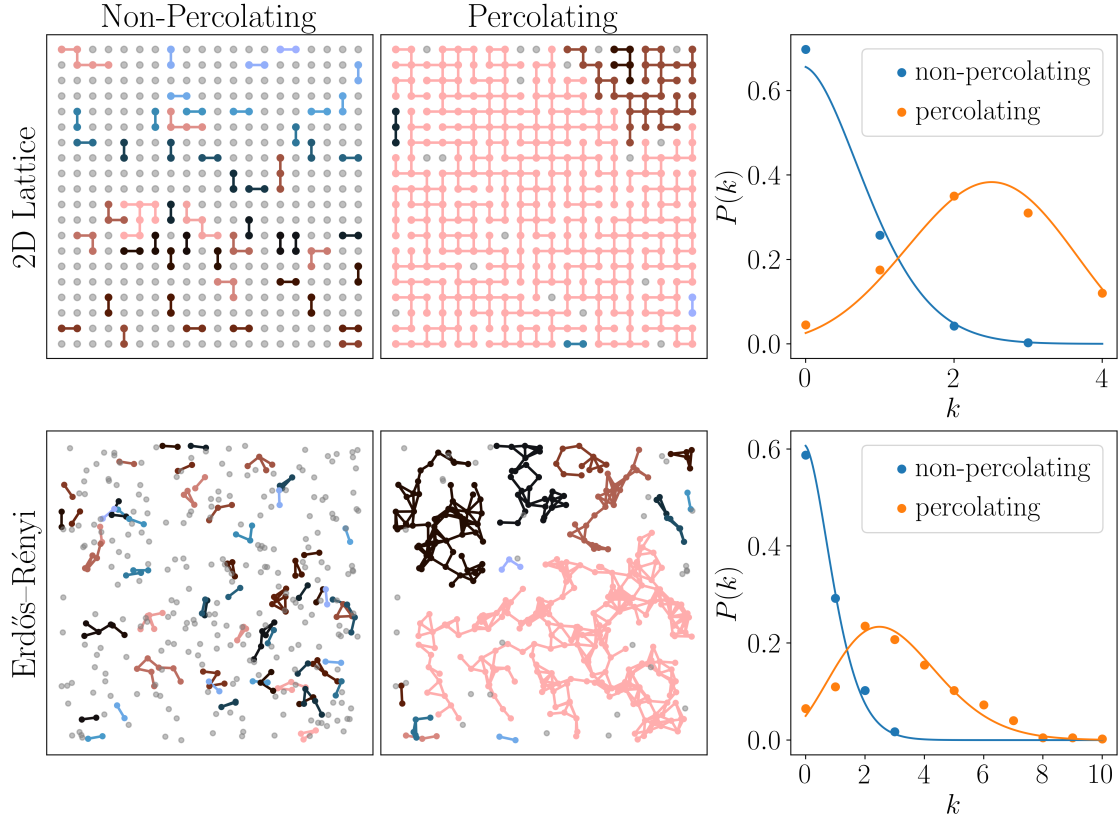


Figure 1.10.: (Top) 2D lattice with $p = 0.1$ (left) and $p = 0.6$ (center), as well as degree distribution (dots) and a binomial distribution (solid lines). (Bottom) Erdős-Rényi (ER) network with $\langle k \rangle = 0.5$ (left) and $\langle k \rangle = 3.0$ (center), as well as degree distribution (dots) and Poissonian distribution (solid lines). All data points use $N = 400$. The largest clusters are in pink and the smallest in baby blue with grey nodes being completely disconnect.

In addition to the degree distribution, the *adjacency matrix* A plays a central role in the typification of networks and can present information useful for understanding the nature of spreading on the network. The entries of the adjacency matrix are defined as follows

$$A_{ij} = \begin{cases} 1, & \text{if there is a link between } i \text{ and } j, \\ 0, & \text{else.} \end{cases} \quad (1.28)$$

For undirected networks A is symmetric. The adjacency matrix can reveal important structural features of the network, such as connected components.

Table 1.2.: Types of networks and their degree distributions. Note, this does not constitute a complete list.

Type	Degree Distribution
Erdős–Rényi	Poissonian
Scale-Free	$P(k) \sim k^{-\gamma}, \quad \gamma \leq 3$
Scale-Rich	$P(k) \sim k^{-\gamma}, \quad \gamma > 3$
Lattice	$\delta_{k,2d}$

1.4.3. Epidemics on Networks

Combining basic compartmental epidemic models with network structures allows for very complex and diverse dynamics to occur. In fact, the complexity becomes so great that few exact results for epidemic processes on networks have been found and many results rely on mean field theory [86].

For the **SIS** model on a network, one central result comes from the structure of the adjacency matrix. Namely, the epidemic threshold is shifted from $\lambda_c = 1$ depending on the properties of the network. Using a degree based mean field approach, the network dependent epidemic threshold can be calculated, yielding

$$\lambda_c = \frac{1}{\Lambda}, \quad (1.29)$$

where Λ is the largest eigenvalue of the adjacency matrix A [94]. Neglecting correlations between nodes of different degree k, k' , this can be further simplified to

$$\lambda_c = \frac{\langle k \rangle}{\langle k^2 \rangle}. \quad (1.30)$$

From eq. (1.30) it becomes apparent that in certain networks the epidemic threshold can *vanish*. In scale-free networks, where $P(k) \sim k^{-\gamma}$, and $2 < \gamma < 3$, the second moment diverges, i.e. $\langle k^2 \rangle \rightarrow \infty$, while $\langle k \rangle$ remains finite. Therefore, the epidemic threshold tends to $\lambda_c = 0$. Here, arbitrarily small infection rates will lead the system to be in an endemic state, making scale-free networks incredibly susceptible to epidemics [86]. This is a consequence of the structure of scale-free networks. These types of networks have a small number of nodes, called *hubs*, with many links, which can drastically increase the spread of infections. Therefore, in order to prevent the spread of diseases on these networks, it is crucial to prioritize immunizing hubs.

Finally, the dynamics of the **SIR** model on a network map directly to a bond percolation problem. As stated above, in the **SIR** model the question arises, 'what percentage of the population will have been infected?' Starting from a single infected node, the probability that it passes on its infection to another connected node *before recovering* is given by [95]

$$T = 1 - e^{-\lambda}, \quad (1.31)$$

with λ being the infection rate divided by the recovery rate. Since T is identical for all connections of infected nodes to susceptible nodes, we can map this problem to a bond percolation problem on a network (similar to the 2D lattice in Fig. 1.10). Here, bonds exist with the probability T and a percolation transition occurs at T_c , where T_c depends on the network geometry. For example, $T_c = \frac{1}{2}$ for a 2D lattice. From this, the epidemic threshold λ_c can be calculated, above which a global spreading of infections occurs, corresponding to a percolating network.

Griffiths Phase

For **SIS** epidemics on random, **ER** networks the epidemic threshold depends on the average degree $\langle k \rangle$ of the network. As one approaches the percolation threshold, the epidemic threshold begins to deviate significantly from its mean field prediction, $\lambda_c = 1$. A standard, but lengthy pair-approximation finds [17]

$$\lambda_c^{(1)} = \frac{\langle k \rangle}{\langle k \rangle - 1}, \quad (1.32)$$

with the mean-field value being recovered for infinite connectivity, i.e. $\lim_{\langle k \rangle \rightarrow \infty} \lambda_c^{(1)} = \lambda_c$. In particular, at the percolation threshold $\langle k \rangle = 1$, the epidemic threshold diverges, meaning that in the case of a non-percolating network, no active phase exists. Instead this phase is replaced with an extended *Griffiths phase* [17].

In the Griffiths phase activity spreading is constrained to local clusters, i.e. small groups of connected nodes. While the system is globally inactive, activity in local clusters can persist on very long timescales. To illustrate this, the decay of the global activity $\rho(t)$ in the Griffiths phase will be calculated in the following.

For a random network in the non-percolating phase, the size distribution of clusters is exponential, i.e.

$$P(s) \sim e^{-cs}, \quad (1.33)$$

where s is the size of a given cluster and $c \in \mathbb{R}_{>0}$ depends on the degree of the network. The average time for initially active cluster to become inactive also depends exponentially on the cluster size, but actually *increases* with the length of the cluster. This results from all nodes having to return to the susceptible state before another node can be infected. For *linear* clusters, i.e. all nodes forming a line, the characteristic lifetime τ of activity in a cluster of size s is given by

$$\tau(s) \sim e^{-bs}, \quad (1.34)$$

where $b = \ln \lambda - 1 + \frac{1}{\lambda}$ [96]. The global activity in the Griffiths phase can be calculated by averaging over different cluster sizes s with

$$\rho(t) = \int ds s P(s) e^{-t/\tau(s)}. \quad (1.35)$$

Using a saddle point approximation one finds $\rho(t) \sim t^{-c/b}$ [17]. Astonishingly, the two competing exponential processes result in a *generic* scale-invariant behavior of the activity in time, thus showing that activity can persist on very long timescales.

1.5. Squeezed States

A squeezed state is a quantum state in which the uncertainty of one of its observables is decreased below the *standard quantum limit* (see below), at the cost of increasing the uncertainty of the conjugate observable. For example, in a harmonic oscillator the uncertainties of position \hat{x} and momentum \hat{p} are bounded from below, following Heisenberg's uncertainty relation, with

$$\Delta\hat{x}\Delta\hat{p} \geq \frac{\hbar}{2}. \quad (1.36)$$

However, this only limits the product of the two observables. A minimal, *balanced* uncertainty (e.g. in a coherent state, cf. Sec. 1.5.2) occurs when uncertainties of the two observables are equal *and* saturate the uncertainty relation. Considering conjugate variables with a characteristic scale, e.g. ξ for \hat{X}_1 and $\frac{1}{\xi}$ for \hat{X}_2 , this takes the form

$$\Delta\hat{X}_1 = \Delta\hat{X}_2 = \frac{1}{\sqrt{2}}. \quad (1.37)$$

In the context of interferometry, eq. (1.37) is known as the *standard quantum limit* and it sets an upper boundary on the precision of measurements, where these become limited by quantum noise. Squeezed states offer a way of going beyond this limit by reducing the uncertainty of one variable below this limit, at the cost of increasing the uncertainty of the other, in a way that does not violate the uncertainty principle. Note that squeezed states do not need to saturate the uncertainty principle.

1.5.1. The Quantized Electromagnetic Field

Much of the work in understanding squeezed states has arisen in the context of squeezed states of light [97]. In the context of quantum field theory, the electromagnetic field is treated as an infinite set of uncoupled harmonic oscillators, one for each mode \mathbf{k} and polarization λ . The number of excitations in a given mode is quantized, i.e. as photons. The excitation and de-excitation of photons is modeled by creation \hat{a}^\dagger and annihilation \hat{a} operators on the respective mode oscillator⁶. The (complex) electric field in the mode \mathbf{k} and with polarization λ is given by

$$\hat{\mathbf{E}}(\mathbf{r}, t) = f(\omega)\epsilon_\lambda[\hat{a}e^{i(\mathbf{k}\cdot\mathbf{r}-\omega t)} + \hat{a}^\dagger e^{-i(\mathbf{k}\cdot\mathbf{r}-\omega t)}], \quad (1.38)$$

where $f(\omega)$ is a real-valued function of the frequency and the ϵ_λ is the vectorized polarization [98]. For the sake of representing the phase space distribution of the single-mode electric field, we can define two dimensionless operators as sums of creation and annihilation operators. These *field quadratures* can be written as

$$\hat{X}_1 = \frac{1}{\sqrt{2}}(\hat{a}^\dagger + \hat{a}), \quad (1.39a)$$

$$\hat{X}_2 = \frac{i}{\sqrt{2}}(\hat{a}^\dagger - \hat{a}), \quad (1.39b)$$

⁶For simplicity we drop the index \mathbf{k} of the oscillator mode energy and set $\hbar = 1$.

and from their definition, they resemble the position and momentum operators of a harmonic oscillator. Following a quick calculation, one can show that these obey $[\hat{X}_1, \hat{X}_2] = i$, meaning \hat{X}_1 and \hat{X}_2 behave like canonical conjugates and must obey the uncertainty principle, i.e. $\sqrt{\langle \Delta \hat{X}_1^2 \rangle} \sqrt{\langle \Delta \hat{X}_2^2 \rangle} \geq \frac{1}{2}$. We can rewrite the single mode electric field from eq. (1.38) in terms of these quadratures as

$$\hat{\mathbf{E}}(\mathbf{r}, t) = f(\omega) \epsilon_\lambda [\hat{X}_1 \cos(\mathbf{k} \cdot \mathbf{r} - \omega t) - \hat{X}_2 \sin(\mathbf{k} \cdot \mathbf{r} - \omega t)]. \quad (1.40)$$

Therefore, we can decompose the oscillating electric field into the quadratures \hat{X}_1 and \hat{X}_2 , corresponding to the amplitude and phase quadratures, respectively.

1.5.2. Quantum States of Light

Having briefly seen how the (single mode) electromagnetic field can be treated in the context of quantum field theory, we now turn to the quantum states which this field can take. Since the electromagnetic field is just an infinite collection of *uncoupled* harmonic oscillators, we can focus on a single mode, with its Hamiltonian given by

$$\hat{H}_\mathbf{k} = \omega_\mathbf{k} (\hat{a}^\dagger \hat{a} + \frac{1}{2}), \quad (1.41)$$

where $\omega_\mathbf{k}$ is the quantized, photon energy. There are different representations of a quantum state, described by a density matrix $\hat{\rho}$, of an electromagnetic mode in phase space. The most common representations are the Glauber-Sudarshan P representation [99, 100], the Husimi Q representation [101], and the Wigner distribution [102]. These can be defined by their characteristic functions, with $\xi \in \mathbb{C}$, as [103]

$$\chi_P(\xi, \xi^*) = \text{Tr}\{e^{i\xi\hat{a}^\dagger} e^{i\xi^*\hat{a}} \hat{\rho}\}, \quad (1.42a)$$

$$\chi_Q(\xi, \xi^*) = \text{Tr}\{e^{i\xi^*\hat{a}} e^{i\xi\hat{a}^\dagger} \hat{\rho}\}, \quad (1.42b)$$

$$\chi_W(\xi, \xi^*) = \text{Tr}\{e^{i\xi\hat{a}^\dagger + i\xi^*\hat{a}} \hat{\rho}\}. \quad (1.42c)$$

Thus the P function corresponds to normal ordering, the Q function corresponds to anti-normal ordering, and the Wigner function corresponds to symmetric ordering of operators. A given distribution can then be extracted via a two-dimensional Fourier transformation. For example, the Wigner function reads [103]

$$W(\alpha, \alpha^*) = \frac{1}{\pi^2} \iint d\xi d\xi^* \chi_W(\xi, \xi^*) e^{-i\xi\alpha^*} e^{-i\xi^*\alpha}. \quad (1.43)$$

The Wigner functions of various states of light discussed in throughout this section can be seen in Fig. 1.11.

Fock States

First and foremost, let us regard the eigenstates of Hamiltonian (1.41). These are the number states, or Fock states, and they correspond to n excitations (photons) being

present in the oscillator. Starting from the ground (vacuum) state $|0\rangle$, which we assume to be normalized, we can define higher-lying Fock states as

$$|n\rangle = \frac{1}{\sqrt{n!}} (\hat{a}^\dagger)^n |0\rangle. \quad (1.44)$$

These states obey $\langle m|n\rangle = \delta_{mn}$ and $\sum_{n=0}^{\infty} |n\rangle \langle n| = \hat{\mathbb{1}}$. A Fock state $|n\rangle$ describes an excitation of the electromagnetic field (in the mode \mathbf{k}) with exactly n photons of energy $\omega_{\mathbf{k}}$. Correspondingly, their average energy is

$$\langle n|\hat{H}|n\rangle = \omega_{\mathbf{k}} \left(n + \frac{1}{2} \right). \quad (1.45)$$

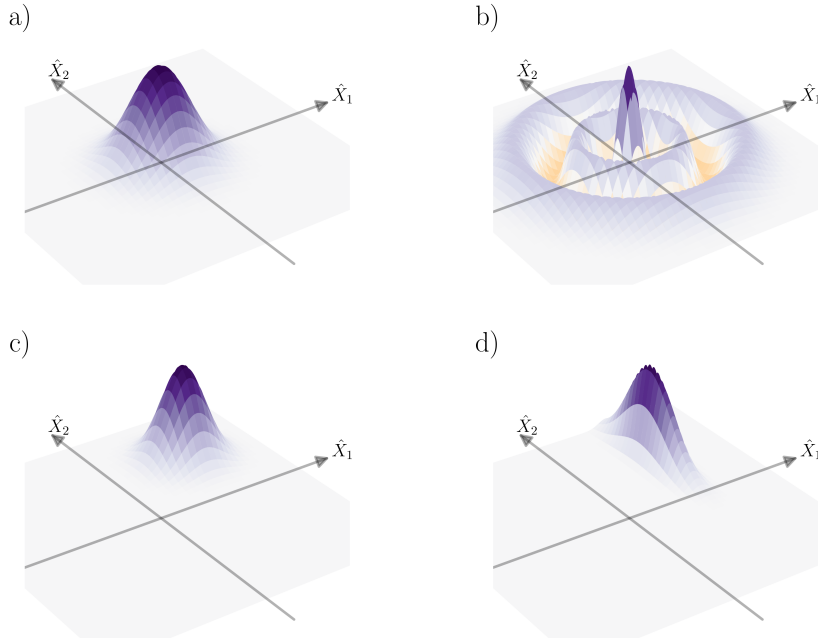


Figure 1.11.: *Phase space distribution of different states of light.* Wigner function $W(X_1, X_2)$ (cf. eq. (1.43)) of a (a) Fock $|0\rangle$ state, (b) Fock $|2\rangle$ state, (c) coherent state, and (d) squeezed state being squeezed in the \hat{X}_1 coordinate and stretched in the \hat{X}_2 coordinate. Purple corresponds to positive and yellow to negative values of the Wigner function.

In the vacuum state, i.e. Fock $|0\rangle$, we can calculate the expected value and the fluctuations of the electric field and receive

$$\langle \hat{\mathbf{E}}(\mathbf{r}, t) \rangle = \langle 0 | \hat{\mathbf{E}}(\mathbf{r}, t) | 0 \rangle = 0, \quad (1.46a)$$

$$\langle \Delta \hat{\mathbf{E}}(\mathbf{r}, t)^2 \rangle = \langle 0 | \hat{\mathbf{E}}(\mathbf{r}, t)^2 | 0 \rangle - \langle 0 | \hat{\mathbf{E}}(\mathbf{r}, t) | 0 \rangle^2 = \frac{f^2(\omega) \epsilon_{\lambda}^2}{2} > 0. \quad (1.46b)$$

As one would expect, the expected value of the electric field vanishes. However, the same is not true for its fluctuations. Despite the absence of photons, the fluctuations of the electric field are greater than zero. This means that in addition to the infinite energy background, which the electromagnetic field exhibits in a vacuum, the field also fluctuates. These *vacuum fluctuations* have measurable effects including allowing for atoms in excited electronic states to spontaneously decay [104, 105], causing the Lamb shift in the energy between two electron orbitals of the Hydrogen atom [106], and producing the Casimir effect, where two conducting metal plates in a vacuum become attracted to each other [107].

For a Fock state $|n\rangle$, with n photons present, the expectation value of the electric field can be calculated from eq. (1.38) and reads

$$\langle n|\hat{\mathbf{E}}(\mathbf{r}, t)|n\rangle = 0. \quad (1.47)$$

Interestingly, the expectation value of the electric field vanishes in this basis, despite n photons being present. Furthermore, the distribution of the Wigner function (cf. (1.43)) takes on negative values for Fock states with $n > 0$ and their photon statistics always show sub-Poissonian statistics, regardless of n . Both of these are indications of non-classical behavior, for example the photon statistics of classical light are *always* Poissonian or super-Poissonian. As a result of their highly non-classical nature, Fock states are extremely hard to produce experimentally [108].

Coherent States

Perhaps the most classical states of light in the context of quantum optics are the *coherent states* $|\alpha\rangle$. These are defined as right-handed eigenstates of the annihilation operator \hat{a} , i.e.

$$\hat{a}|\alpha\rangle = \alpha|\alpha\rangle, \quad (1.48)$$

with the eigenvalue $\alpha \in \mathbb{C}$. Now, if we regard the expectation value and fluctuations of the electric field in a coherent state, we find

$$\langle \alpha|\hat{\mathbf{E}}(\mathbf{r}, t)|\alpha\rangle = \sqrt{2}f(\omega)\epsilon_\lambda[\text{Re}\{\alpha\}\cos(\mathbf{k} \cdot \mathbf{r} - \omega t) + \text{Im}\{\alpha\}\sin(\mathbf{k} \cdot \mathbf{r} - \omega t)], \quad (1.49a)$$

$$\langle \alpha|\Delta\hat{\mathbf{E}}(\mathbf{r}, t)^2|\alpha\rangle = \frac{f^2(\omega)\epsilon_\lambda^2}{2}. \quad (1.49b)$$

From eq. (1.49a) we find the expectation value to effectively take its classical value, where $\text{Re}\{\alpha\}$ and $\text{Im}\{\alpha\}$ correspond to the field amplitudes. The fluctuations of the electric field take on the value of vacuum fluctuations (cf. (1.46b)) irrespective of the field amplitude. Furthermore, when regarding the uncertainties of the field quadratures of a coherent state, we find $\sqrt{\langle \Delta\hat{X}_1^2 \rangle} = \sqrt{\langle \Delta\hat{X}_2^2 \rangle} = \frac{1}{\sqrt{2}}$. From these we can discern that coherent states saturate the uncertainty relation, and in particular, the uncertainties in the quadratures are *balanced*. Therefore, when regarding coherent states in phase space (cf. Fig. 1.11), coherent states appear with circular shapes.

By projecting the coherent states into the Fock basis, we can investigate their photon statistics. In the Fock basis, these read

$$|\alpha\rangle = \sum_{n=0}^{\infty} \frac{\alpha^n}{\sqrt{n!}} e^{-|\alpha|^2/2} |n\rangle, \quad (1.50)$$

which yields the photon number distribution $P(n) = |\langle\alpha|n\rangle|^2 = e^{-|\alpha|^2/2} \frac{|\alpha|^{2n}}{n!}$. The number distribution of photons in a coherent state is Poissonian and therefore, once again, acts classically.

Lastly, let us turn to the relative noise of the electric field, calculated by using eqs. (1.49). In the context of interferometry and high precision measurements this is a key quantity. For coherent states, we can calculate the relative noise (RN) as

$$\text{RN} = \sqrt{\frac{\langle\alpha|\Delta\hat{\mathbf{E}}^2|\alpha\rangle}{[\langle\alpha|\hat{\mathbf{E}}|\alpha\rangle]^2}} \propto \frac{1}{|\alpha|}, \quad (1.51)$$

since $\langle\alpha|\Delta\hat{\mathbf{E}}^2|\alpha\rangle = \text{const.}$ and $\sqrt{[\langle\alpha|\hat{\mathbf{E}}|\alpha\rangle]^2} \propto |\alpha|$. Furthermore, $|\alpha|$ corresponds to the square root of the mean photon number, i.e. $|\alpha| = \sqrt{\langle\alpha|\hat{n}|\alpha\rangle}$, causing the relative noise to decrease with the square root of the mean photon number, i.e. $\text{RN} \sim \frac{1}{\sqrt{n}}$. Through their low and balanced relative noise – by saturating the Heisenberg uncertainty relation – coherent states resemble classical light most closely. In fact an idealized laser emits coherent states of light.

Coherent states can be generated from vacuum states by applying the unitary *displacement operator* $D(\alpha) = e^{\alpha\hat{a}^\dagger - \alpha^*\hat{a}}$ onto the vacuum state $|0\rangle$ [109, 110], i.e.

$$|\alpha\rangle = \hat{D}(\alpha) |0\rangle. \quad (1.52)$$

The displacement operator $\hat{D}(\alpha)$ can be thought of as moving a localized state in phase space by the complex magnitude α .

Squeezed States

The uncertainty relation only sets a minimum constraint on the *area* covered by quantum noise in phase space. For coherent states, which have minimal uncertainty, this area is circular. We can consider *squeezing* this area into an ellipse, where the uncertainty in one quadrature goes below the standard quantum limit, while the uncertainty in the other increases. These *squeezed states* offer a way to beat the $\frac{1}{\sqrt{n}}$ limit set by quantum noise on the accuracy of high precision measurements (cf. Fig. 1.12).

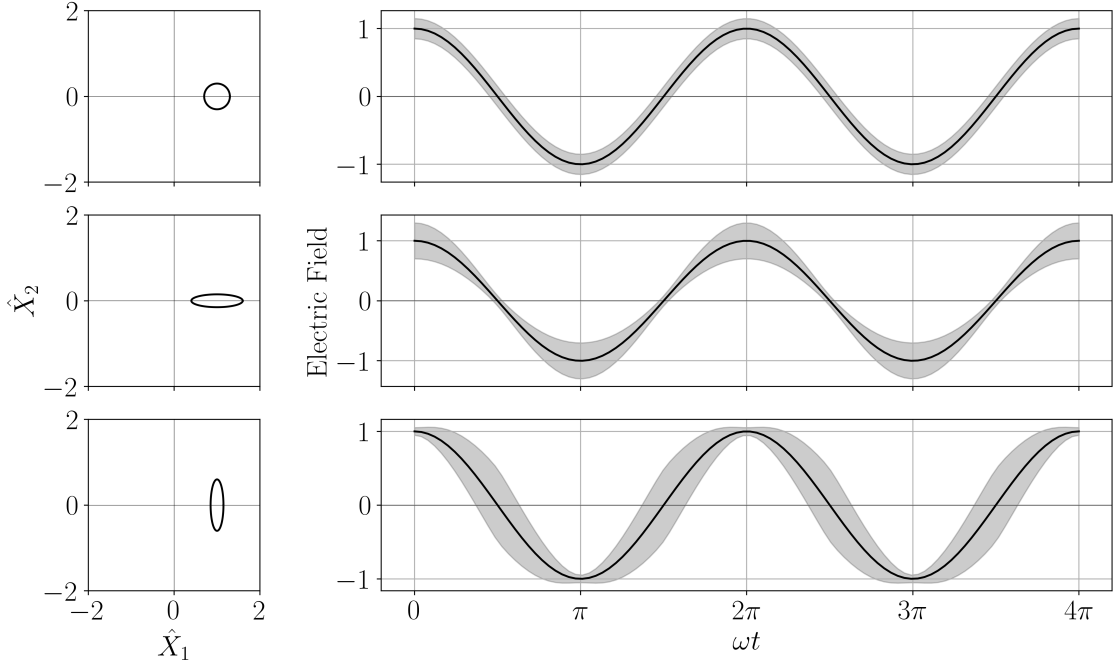


Figure 1.12.: *Time dynamics of squeezed states.* (Left column) Phase space distribution and (right column) expectation value (lines) and quantum fluctuations (shaded areas) of the electric field over time for (top row) a coherent state, (center row) a state squeezed with reduced noise in \hat{X}_2 (reduced *phase noise*), and (bottom row) a squeezed state with reduced noise in \hat{X}_1 (reduced *amplitude noise*).

Squeezed states can be generated from coherent states via the unitary *squeeze operator*, defined as [98]

$$\hat{S}(z) = e^{\frac{1}{2}(z^* \hat{a}^2 - z \hat{a}^{\dagger 2})} \quad (1.53)$$

with $z = re^{i\theta}$. In this case they are referred to as squeezed coherent states, and we will label them $|\alpha, z\rangle \equiv \hat{S}(z)\hat{D}(\alpha)|0\rangle$. As seen in Fig. 1.12, the area covered by a squeezed coherent state in phase space is squeezed into an ellipse of the same area as the coherent state. The eccentricity of the ellipse depends on the parameter r , as such this parameter is referred to as the *squeeze parameter*. The angle of the ellipse, i.e. the directions of the major/minor axes of the ellipse, are determined by the parameter θ , referred to as the *squeezing angle*. Note that the squeeze and displacement operators do not commute.

For a squeezed coherent state $|\alpha, z\rangle$, we can calculate the quadrature variances, corresponding to the length of the major and minor axes of the state in phase space. This is explicitly done for a squeezed coherent state $|\alpha, z\rangle$ in Ref. [103]⁷. The maximal and minimal quadrature variances do not depend on the squeezing angle θ , so for simplicity, we will regard $\theta = 0$. In this case, the maximal quadrature variance is in \hat{X}_2 and the minimal variance is in \hat{X}_1 , i.e.

⁷Note a factor $\frac{1}{\sqrt{2}}$ difference in the definition of \hat{X}_1 and \hat{X}_2 between Ref. [103] and the convention used here.

$$\langle \Delta \hat{X}_1^2 \rangle = \langle (\hat{X}_1)^2 \rangle - (\langle \hat{X}_1 \rangle)^2 \quad (1.54)$$

$$= \frac{1}{2} e^{-2r}, \quad (1.55)$$

$$\langle \Delta \hat{X}_2^2 \rangle = \langle (\hat{X}_2)^2 \rangle - (\langle \hat{X}_2 \rangle)^2 \quad (1.56)$$

$$= \frac{1}{2} e^{2r}. \quad (1.57)$$

For $r = 0$, we receive the variances of a coherent state, and for all $r > 0$ we find the variances to saturate the Heisenberg uncertainty relation, making a squeezed coherent state an ideal squeezed state [103]. Finally, the squeeze operator transforms the bosonic ladder operators to

$$\hat{b} = \hat{S}(z) \hat{a} \hat{S}^\dagger(z) = u \hat{a} + v \hat{a}^\dagger \quad (1.58a)$$

$$\hat{b}^\dagger = \hat{S}(z) \hat{a}^\dagger \hat{S}^\dagger(z) = v^* \hat{a} + u \hat{a}^\dagger, \quad (1.58b)$$

with $u = \cosh z$, $v = \sinh z$, and $|u|^2 - |v|^2 = 1$. The transformation (1.58) is of the form of a bosonic Bogoliubov transformation, useful for the diagonalization of quadratic Hamiltonians, which we use in [P5]. The generation of squeezed states has been experimentally realized with nonlinear optical media, e.g. via four wave mixing [111] or via parametric down conversion [112].

1.5.3. Applications of Squeezing

Finally, let us finish this section by discussing two manifestations of squeezing in and beyond quantum optics. For example, it was proposed quite some time ago to implement squeezing in the search for gravitational waves [113]. Following the groundbreaking measurement of gravitational waves in late 2015 [114], these interferometers have started using photon squeezing to enhance signal-to-noise ratios [115]. This has become more and more necessary as increasing the laser power to reduce the signal-to-noise ratio (cf. eq. (1.51)) has proven to be ultimately limited by the thermal deformation of optical components [116].

Another application comes in form of spin squeezing [117]. In atomic ensembles of ultra-cold atoms, collective spin states can be squeezed to enhance measurement precision (cf. Ref. [118] for a review). This can be used to detect quantum entanglement [119] or facilitate the construction of more precise atomic clocks [120].

2. Griffiths Phase in a Facilitated Rydberg Gas at Low Temperatures

D. Brady, J. Bender, P. Mischke, S. Ohler, T. Niederprüm, H. Ott, and M. Fleischhauer
Physical Review Research **6**, 013052 (2024)

This work is the first of our studies analyzing the epidemic-like behavior of Rydberg facilitation in a gas. It showcases an experimental observation of generic scale-invariance in the gas and investigates this using extensive theoretical modeling through Monte Carlo simulations and analytic considerations. Scale-invariance is a signature of a system at criticality, i.e. it should occur at a specific point in the parameter space and only with certain, characteristic power-law exponents (cf. Sec. 1.3). Therefore, a generic occurrence of scale-invariance with continuously varying power-law exponents hints at the existence of an exotic Griffiths phase [17] (cf. Sec. 1.4.3).

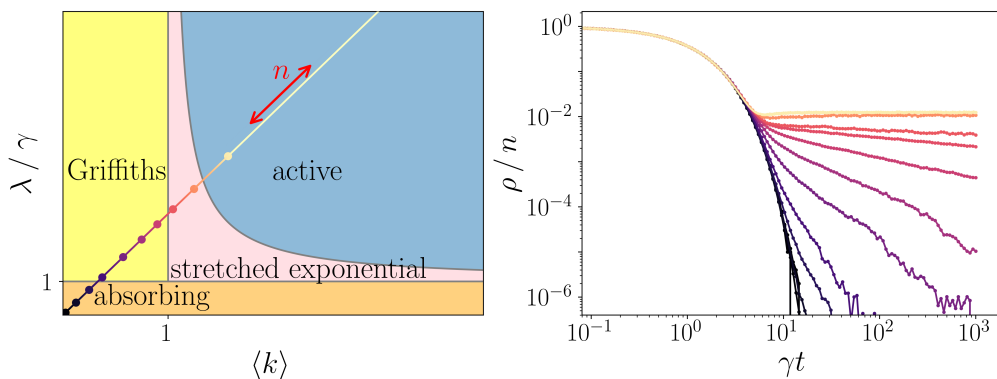


Figure 2.1.: (Left) Qualitative phase diagram of the low temperature Rydberg facilitation gas, with network connectivity $\langle k \rangle$ and normalized infection rate λ/γ . (Right) Decay of Rydberg density ρ with all atoms excited in the beginning, i.e. $\rho(t = 0) = n$ for different points in the phase diagram (colors). In the Griffiths phase a power-law decay of $\rho(t)$ with various different decay exponents is expected.

The central idea of this publication was to understand the origin of heterogeneous *Griffiths* effects in the gas. A recent experiment [16], as well as our own experiment, showed *generic* scale-invariance in the Rydberg gas. In Ref. [16] this was attributed to heterogeneity induced by different velocity classes in the gas. It was argued that Rydberg atoms with high velocities only very rarely interact with (infect) other atoms due to an exponentially decaying *Landau-Zener (LZ)* transition probability. In this publication, we prove the existence of a Griffiths phase within the Rydberg gas, but show that this phase does *not* originate from velocity classes. Instead, the Griffiths phase emerges at low temperatures as a result of excitation spreading being confined to a network.

Firstly, we show that the decaying *LZ* probability with increasing atom velocity is (mostly) correctly modeled in our Monte Carlo simulations. Our simulations, however,

do *not* show Griffiths effects at high temperatures, as would otherwise be expected following Ref. [16]. The reason for this being an increase in the number of atoms with which a fast atom can interact with in a given time, compensating the decreased excitation probability for each atom it passes. Consequently, the number of atoms a single Rydberg atom infects does not depend on its velocity and, therefore, for high gas temperatures we find a simple absorbing-state phase transition in the gas.

However, at low temperatures we discovered that the spreading of excitations is constrained to a random, *Erdős-Rényi (ER)* network [93]. An *ER* network exhibits a phase transition between a percolating phase for $\langle k \rangle > 1$ and a non-percolating phase for $\langle k \rangle < 1$, where $\langle k \rangle$ is the average number of connections a given node has (cf. Sec. 1.4.2). We discovered that we can quantitatively map the Rydberg facilitation gas to an *ER* network, where we find the average connectivity to be given by

$$\langle k \rangle = nV_s, \quad (2.1)$$

where n is the gas density and V_s is the volume of the facilitation shell.

Given an infection rate λ larger than the recovery rate γ , the spreading of infections through the system depends drastically on the network. For $\langle k \rangle > 1$, the infection can spread unhindered through the giant cluster in the system. Here, the infected density ρ will reach a non-zero steady state and infections persist indefinitely in the system (active phase). However, for $\langle k \rangle < 1$, the finite size of individual (disconnected) clusters hinders a global spread of infections. The system becomes *locally* active and a Griffiths phase emerges [17]. In this case, the infection cannot persist due to the finite size of infected clusters, and it decays (slower than exponentially) as a power-law over time. The exponent of this power-law decay depends explicitly on the infection and recovery rates and is therefore non-universal. Finally, if the recovery rate is stronger, i.e. $\lambda/\gamma < 1$, the infection dies out exponentially in time irrespective of the network structure (absorbing phase).

For the theoretical modeling we utilize large scale Monte Carlo simulations of classical rate equations. A detailed description of the algorithm can be found in Appendix A.

Author Contributions

Contribution	Primary Role	Supportive Role
Mapping to ER network	D.B.	-
Monte Carlo simulations	D.B.	S.O.
Rate equations w/ high velocities (LZ disussion)	D.B., M.F.	-
Experimental measurements	J.B., P.M., D.B.	-

The project was conceived by M.F and H.O. The theoretical work was supervised by M.F. and the experimental work was supervised by T.N. and H.O.

Copyright

Published by the American Physical Society under the terms of the [Creative Commons Attribution 4.0 International license \(CC BY 4.0\)](#).

Griffiths phase in a facilitated Rydberg gas at low temperatures

Daniel Brady ,^{1,*} Jana Bender ,¹ Patrick Mischke ,^{1,2} Simon Ohler ,¹ Thomas Niederprüm ,¹ Herwig Ott ,¹ and Michael Fleischhauer ,¹

¹Department of Physics and Research Center OPTIMAS, University of Kaiserslautern, D-67663 Kaiserslautern, Germany

²Max Planck Graduate Center with Johannes Gutenberg University Mainz (MPGC), D-55128 Mainz, Germany



(Received 29 March 2023; accepted 6 September 2023; published 16 January 2024)

The spread of excitations by Rydberg facilitation bears many similarities to epidemics. Such systems can be modeled with Monte Carlo simulations of classical rate equations to great accuracy as a result of high dephasing. Motivated by experiments, we theoretically analyze the dynamics of a Rydberg many-body system in the facilitation regime in the limits of high and low temperatures. In the high-temperature limit, a homogeneous mean-field behavior is recovered, while characteristic effects of heterogeneity can be seen in a frozen gas. At high temperatures, the system displays an absorbing-state phase transition and, in the presence of an additional loss channel, self-organized criticality. In a frozen or low-temperature gas, excitations are constrained to a network resembling an Erdős-Rényi graph. We show that the absorbing-state phase transition is replaced with an extended Griffiths phase, which we accurately describe by a susceptible-infected-susceptible model on the Erdős-Rényi network taking into account Rydberg blockade.

DOI: [10.1103/PhysRevResearch.6.013052](https://doi.org/10.1103/PhysRevResearch.6.013052)

I. INTRODUCTION

Rydberg atoms have gained a lot of attention in recent years due to their strong interactions over large distances [1]. This, paired with their long lifetimes in the order of milliseconds, creates a platform to explore quantum many-body physics of strongly interacting spin systems [2–9] and to implement key elements for quantum information processing [10–14]. Moreover, optically driven Rydberg atoms [see Fig. 1(a)] can be used to investigate many-body dynamics of spin systems in inherently dissipative environments [15–19], as the laser excitation into high-lying Rydberg states is often accompanied by strong dephasing. The latter includes important dynamical phenomena such as an absorbing-state phase transition [see Fig. 1(b)], one of the simplest classical nonequilibrium phase transitions displaying critical behavior and universality [20,21].

Absorbing-state phase transitions are of general interest as they occur in many phenomena outside of physics such as population dynamics, epidemics or the spreading of information in social media [22–25]. Systems with this phase transition are believed fall into the universality class of directed percolation (DP) [20]. The unambiguous experimental observation of DP universal behavior is, however, challenging and has only been achieved in a few systems in recent years [26–31]. More recently, experimental signatures of such

a transition have been reported in optically driven Rydberg gases [32].

In Rydberg systems, dissipation can give rise to another important dynamical phenomenon: self-organized criticality (SOC) [33,34], which is believed to be a cause for the abundance of scale invariance in nature [35–38]. An SOC system dynamically evolves to the critical point of a phase transition by itself due to dissipation and without the need for parameter fine tuning [see Fig. 1(c)]. Since the dissipation is strongly reduced once the critical point is reached, further evolution into the absorbing phase happens on much longer timescales. Recent experiments on Rydberg facilitation have shown some evidence of SOC through the use of ionization or a decay into an auxiliary inert (dead) state as a loss mechanism [see Fig. 1(a)] [39] (see Ref. [40] for related experiments).

However, the DP transition is known to be susceptible to disorder [41] and more recent experiments on Rydberg facilitation in a trapped ultracold gas of atoms gave indications for an emergent heterogeneity in the system [42]. In such a heterogeneous system, the critical point of the absorbing-state phase transition is replaced by an intermediate extended Griffiths phase. Griffiths phases are characterized by generic scale invariance and the lack of universal behavior. This is in contrast to an absorbing state phase transition where scale invariance is only expected at the critical point. As a result (e.g., in the Rydberg gas), one expects a power-law decay in active density over time with continuously varying exponents depending on the driving strength [43].

In Ref. [42], it was experimentally shown that a Rydberg system in the facilitation regime produces signatures of such a Griffiths phase for short times compared to the lifetime of the Rydberg state. A power-law decay in Rydberg density over time was observed with the decay exponents varying with driving strength and a phenomenological

*Corresponding author: brady@rptu.de

Published by the American Physical Society under the terms of the Creative Commons Attribution 4.0 International license. Further distribution of this work must maintain attribution to the author(s) and the published article's title, journal citation, and DOI.

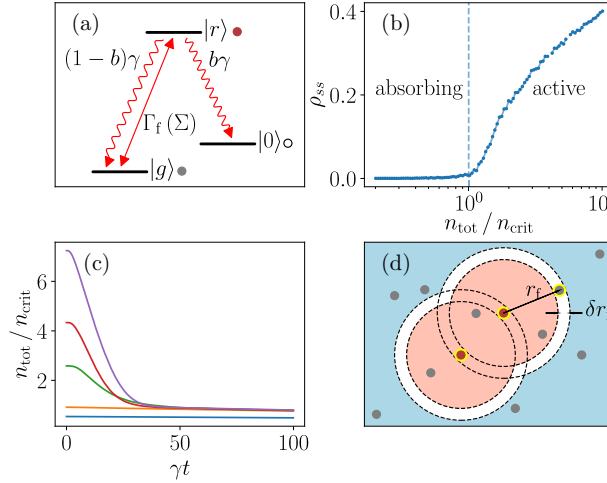


FIG. 1. (a) Laser field couples ground $|g\rangle$ and Rydberg $|r\rangle$ states, resulting in a transition rate $\Gamma_f(\Sigma)$ [see Eq. (3)]. The Rydberg state can spontaneously decay into $|g\rangle$ or an inert state $|0\rangle$. (b) Steady-state Rydberg density depending on total active density (i.e., in states $|g\rangle$ and $|r\rangle$) for $b = 0$ from Monte Carlo simulations. (c) Total active density n_{tot} over time from Monte Carlo simulations for $b > 0$, showing self-organization of the system to the critical density n_{crit} , if the initial density is larger. (d) Schematic of facilitation shell (white): Atoms (grey) in the red area are subject to Rydberg blockade and atoms in the blue area only weakly interact with the Rydberg atoms (red).

susceptible-infected-susceptible (SIS) network model was put forward to describe the observations. The model included a fitting function for the node weights of the network depending on the excitation rate κ . The interpretation being that in the network model, heterogeneity originates from a velocity selective excitation mechanism, where only atoms with relative velocities smaller than the Landau-Zener velocity $v_{\text{LZ}}(\kappa)$ could participate in facilitation dynamics. Above this velocity, all further excitations are exponentially suppressed.

In the present paper, we present experimental indications for generic scale invariance and strong theoretical indications for a Griffiths phase in a Rydberg facilitation gas by Monte Carlo simulations.

In the experiment, we continuously monitor the number of Rydberg excitations in a trapped ultracold gas of ^{87}Rb atoms. We show that the size distribution of the Rydberg excitation number follows a power-law distribution, i.e., shows a scale-free behavior, over an extended parameter regime, which is a key characteristic of a Griffiths phase.

To understand and quantitatively describe the emergence of the Griffiths phase, we theoretically analyze two limiting cases: (i) a frozen gas and (ii) a gas with high temperature. While we recover a direct absorbing-state phase transition in the high-temperature limit with no signs of a velocity induced heterogeneity, we can identify a Griffiths phase in the *frozen gas limit* as a result of the finite paths along which facilitated excitations can spread. We give a quantitative analysis of the factors contributing to the emergence of a Griffiths phase and provide an estimate for the characteristic exponents of the power-law decay of Rydberg activity in this phase.

The facilitation of Rydberg excitations in a gas of optically driven atoms can be microscopically described by a Lindblad master equation [44] for the density matrix $\hat{\rho}$, which takes the form

$$\frac{d}{dt} \hat{\rho} = i[\hat{\rho}, \hat{\mathcal{H}}] + \sum_l \hat{L}_l \hat{\rho} \hat{L}_l^\dagger - \frac{1}{2} [\hat{L}_l^\dagger \hat{L}_l, \hat{\rho}]. \quad (1)$$

Here, the atom-light interaction Hamiltonian $\hat{\mathcal{H}}$ is given by

$$\hat{\mathcal{H}} = \sum_i \left[\Omega (\hat{\sigma}_i^{gr} + \hat{\sigma}_i^{rg}) + \left(\sum_{j \neq i} \frac{c_6}{r_{ij}^6} \hat{\sigma}_j^{rr} - \Delta \right) \hat{\sigma}_i^{rr} \right], \quad (2)$$

where $\hat{\sigma}_j^{\mu\nu} = |\mu\rangle_{jj} \langle \nu|$ is the transition operator between states $|\nu\rangle$ and $|\mu\rangle$ of the j th atom. The strength of the laser driving shifted from the ground-Rydberg resonance frequency by the detuning Δ is described by the Rabi frequency Ω , and there is a van der Waals interaction proportional to c_6/r_{ij}^6 , with $r_{ij} = |\vec{r}_i - \vec{r}_j|$ being the distance between atoms i and j . Dissipative processes are taken into account by the Lindblad jump operators $\hat{L}_1^{(i)} = \sqrt{(1-b)\gamma} \hat{\sigma}_i^{gr}$, $\hat{L}_2^{(i)} = \sqrt{b\gamma} \hat{\sigma}_i^{r0}$ describing spontaneous decay of the Rydberg state into the ground state $|g\rangle$ and the inert state $|0\rangle$, with the branching parameter b . Finally, dephasing, attributed to laser phase noise and Doppler broadening [39] as well as the spread of the atomic wave packet over the van der Waals potential [45], is described by $\hat{L}_\perp^{(i)} = \sqrt{\gamma_\perp} \hat{\sigma}_i^{rr}$.

The strong van der Waals interaction of a Rydberg atom shifts energy levels of the surrounding atoms significantly up to distances of multiple μm . When the atoms are resonantly coupled to a laser field, this will block further excitations into Rydberg states from occurring for all atoms within a finite distance, a phenomenon known as Rydberg blockade [11]. On the other hand, if the laser excitation is strongly detuned, the excitation of isolated atoms is suppressed while atoms close to the facilitation distance $r_f \equiv \sqrt[6]{\frac{c_6}{\Delta}}$ are shifted into resonance [Fig. 1(d)] and are excited with a greatly increased rate. This process, termed Rydberg facilitation, leads to a cascade of excitations quickly spreading through the system following a single (off-resonant) excitation [46,47]. It is important to note that Rydberg blockade still occurs in this regime. The excitation of atoms with distances $r < r_f$ is greatly suppressed [red zone in Fig. 1(d)].

II. EXPERIMENTAL OBSERVATION OF SCALE-FREE BEHAVIOR IN A DRIVEN RYDBERG GAS

To experimentally test scale invariance, we investigate the excitation density in a trapped gas of ^{87}Rb atoms. To this end, we prepare a sample containing 150×10^3 atoms at a temperature of $1 \mu\text{K}$ in a crossed optical dipole trap. The sample has a density on the order of $10^{12}/\text{cm}^3$. From the $5S_{1/2}$ ground state, a UV laser at 297 nm continuously couples to the $40P_{3/2}$ Rydberg state with a detuning of $+40$ MHz and a resonant Rabi frequency of $2\pi \times 100$ kHz. The temperature of the gas corresponds to a most probable speed $\hat{v} = 0.7 r_f \gamma$ with the facilitation radius r_f and decay rate γ .

Atoms in the $40P_{3/2}$ state are ionized because of multiple intrinsic processes [48,49], which we use to continuously monitor the excitation number. To this end, we guide the resulting ions to a detector using a small electric field. This

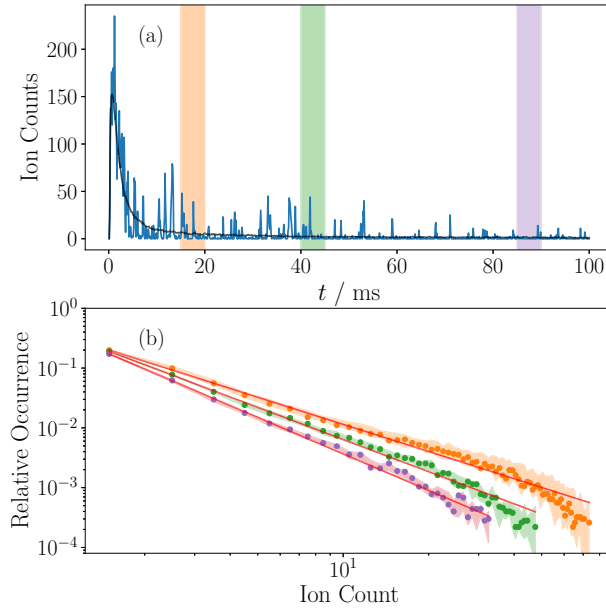


FIG. 2. (a) Ion signal per 10 μ s time interval for a single experiment run (blue line) and average over 1000 experimental runs (black line). The ground state is off-resonantly coupled to the Rydberg state for 100 ms. During the measurement, the density continuously decreases because of the intrinsic ionization of Rydberg atoms. In the first few milliseconds, the system is in the active phase, displaying continuously high activity. Afterward, the dynamics is dominated by isolated avalanches. The colored areas indicate the time segments evaluated in (b). (b) Experimentally found distribution of ion counts for different sample densities averaged over 1000 experimental runs. We choose exemplary 5 ms-long time segments at 15 ms (orange), 40 ms (green), and 85 ms (violet) corresponding to three densities. The distributions show power-law behavior (fitted in red), albeit with distinct exponents (-1.51, -1.79, and -2.03, respectively). The shaded region characterizes the uncertainty in the measurements. It represents the maximum (minimum) relative occurrence when shifting the evaluation windows by ± 5 ms.

yields a time-resolved signal proportional to the number of Rydberg excitations in the sample [Fig. 2(a)].

At the beginning of the continuous laser exposure, which lasts 100 ms, there are no excitations in the sample. As soon as the first off-resonant excitation is created, activity spreads through the system via facilitation, setting it up in the active phase. Due to the continuous atom loss caused by the ionization of excited atoms, the sample density decreases, reducing the effective driving strength. The sample thus approaches the phase transition.

We divide the ion signal in segments of 5 ms to account for the temporally varying effective driving. For each of these segments, we analyze the ion count distribution in 10 μ s bins and average over 1000 experimental runs. After about 10 ms, the average activity has dropped more than an order of magnitude compared to its maximum value, while in individual runs it is dominated by avalanches. Therefore, we assume that at this time the sample is leaving the active phase.

Our measurement data shows persistent power-law behavior in the distribution of avalanche sizes over a wide range of

densities [Fig. 2(b)]. Power laws are a clear signature of scale invariance, which is expected only at the critical point of an absorbing-state phase transition or in a Griffiths phase characterizing a heterogeneous system. The extracted exponent of the power-law distribution is not fixed but varies with density, strongly indicating nonuniversal behavior. While these observations are not an experimental proof of heterogeneity, we use them as motivation to theoretically investigate possible origins of heterogeneity and a related Griffiths phase in the system.

III. MICROSCOPIC MODEL OF RYDBERG FACILITATION

After having shown indications of scale-invariant behavior in the Rydberg facilitation gas, however, with varying exponents in the experiments, we now turn to a theoretical modeling of the microscopic dynamics.

In the limit of large dephasing, the dynamics of a many-body Rydberg gas are effectively governed by classical rate equations [50]. As such, we will simulate a gas of atoms governed by Eq. (1) using classical Monte Carlo simulations of a set of rate equations derived from Eq. (1) in the limit of large dephasing. After adiabatic elimination of coherences, Eq. (1) reduces to classical rate equations between ground, Rydberg, and inert states [see Fig. 1(a)], with the stimulated rate $\Gamma_f(\Sigma)$ given as

$$\Gamma_f(\Sigma) = \frac{2\Omega^2\gamma_\perp}{\gamma_\perp^2 + \Delta^2 \left(\sum_{j \neq i} \frac{r_f^6}{r_{ij}^6} - 1 \right)^2}, \quad (3)$$

where Σ is the set of indices of Rydberg-excited atoms. To ensure numerical stability in the simulation, the singularity of the potential in Eq. (3) is truncated at a cutoff value.

Using Eq. (3), we can formulate a set of classical rate equations for the probability of the i th atom being in the Rydberg state $P_r^{(i)}$ or the ground state $P_g^{(i)}$ as

$$\frac{d}{dt} P_r^{(i)} = \Gamma_f(\Sigma) P_g^{(i)} - (\Gamma_f(\Sigma) + \gamma) P_r^{(i)}, \quad (4a)$$

$$\frac{d}{dt} P_g^{(i)} = (\Gamma_f(\Sigma) + (1 - b)\gamma) P_r^{(i)} - \Gamma_f(\Sigma) P_g^{(i)}. \quad (4b)$$

If no other Rydberg atom exists in the gas or their distance is much larger than r_f , $\Gamma_f(\Sigma)$ reduces to the off-resonant excitation rate of an isolated atom:

$$\tau = \frac{2\Omega^2\gamma_\perp}{\gamma_\perp^2 + \Delta^2}. \quad (5)$$

As a result of the broadening of the ground-Rydberg transition, given by the dephasing rate γ_\perp , facilitation can occur in a smeared-out region around the facilitation distance r_f , given by

$$\delta r_f = \frac{\gamma_\perp}{2\Delta} r_f. \quad (6)$$

Therefore, each Rydberg atom spans a facilitation shell around it at the radius r_f and with the width δr_f [white disks in Fig. 1(d)]. Inside this shell, the stimulated rate takes its maximal value $\Gamma_f = \frac{2\Omega^2}{\gamma_\perp}$, referred to as the facilitation rate. Relevant for later mappings to epidemic models is this rate integrated over volume V_s of the facilitation shell given by

$$\kappa = \Gamma_f V_s. \quad (7)$$

The relevant quantities of interest here are the coarse-grained Rydberg density (in a small volume ΔV)

$$\rho(\vec{r}, t) = \frac{1}{\Delta V} \sum_{i: \vec{r}_i \in \Delta V} \langle \hat{\sigma}_i^{rr} \rangle, \quad (8)$$

and the total active density of ground-state and Rydberg atoms:

$$n(\vec{r}, t) = \frac{1}{\Delta V} \sum_{i: \vec{r}_i \in \Delta V} (\langle \hat{\sigma}_i^{rr} \rangle + \langle \hat{\sigma}_i^{gg} \rangle). \quad (9)$$

In the following, n will be referred to as the total density of the gas, for simplicity. As atoms in state $|0\rangle$ do not participate in the dynamics of the system [see Fig. 1(a)], a decay into this state corresponds to a reduction of the total density, i.e., atom loss.

With this, $n\kappa$ corresponds to the rate with which excitations spread through the cloud.

The gas is simulated in a cube with size L^3 and periodic boundary conditions, typically $L = 7 r_f$. Atom positions are chosen randomly and velocities are sampled from the Maxwell-Boltzmann distribution with the temperature parameter \hat{v} , corresponding to the most probable atom velocity in the gas. After choosing a fixed time step ($dt = 1/400 \gamma$), the time evolution of the system is given by a fixed time step Monte Carlo (ftSMC) algorithm [51]. We choose a ftSMC algorithm as opposed to a kinetic Monte Carlo algorithm [52] as atomic movement, paired with long-range interactions leads to quickly changing transitional rates in the system.

In Ref. [39], Langevin equations have been derived to macroscopically describe the density of Rydberg atoms ρ and the total density n in the system. As shown in Ref. [39], the homogeneous mean-field solution, in which diffusion terms are neglected, is sufficient to model the system. These equations then take the form

$$\frac{d}{dt} \rho = -\kappa(2\rho^2 - \rho n) - \gamma\rho - \tau(2\rho - n) + \xi, \quad (10a)$$

$$n = n_0 - b\gamma \int_0^t dt' \rho(t'), \quad (10b)$$

with the off-resonant excitation rate τ and a noise term ξ . The parameter b characterizes the percentage of Rydberg atoms which spontaneously decay into the dead state $|0\rangle$ [see Fig. 1(a)]. As mentioned above, atoms that decay into this state are effectively removed from the system.

Assuming a gas with a heterogeneous density, diffusion results in a stabilization of the critical point over long times. For details pertaining to this, see Ref. [53].

In the absence of decay into $|0\rangle$, i.e., for $b = 0$, and in the absence of an off-resonant excitation, i.e., $\tau = 0$, the dynamics described by Eqs. (10) feature an absorbing-state phase transition at the critical atom density

$$n_{\text{crit}} = \frac{\gamma}{\kappa}, \quad (11)$$

when the facilitation rate is fixed or, alternatively, at the critical facilitation rate $\kappa_{\text{crit}} = \gamma/n_0$ for fixed density. Below the critical point, any initially existing excitations in the system will eventually decay and the steady state of the system is one where all atoms are in the ground state (absorbing

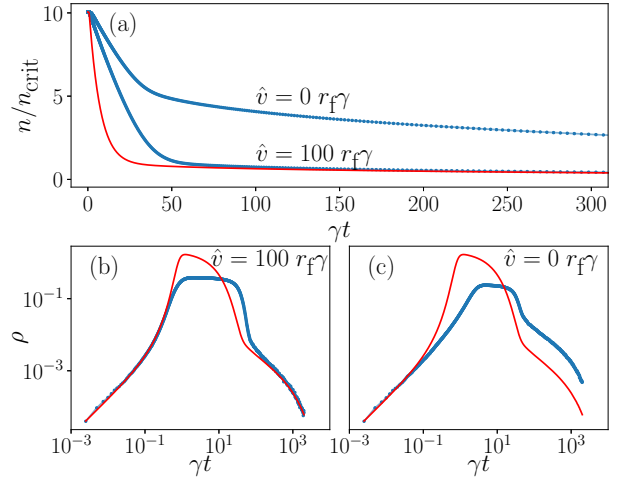


FIG. 3. (a) Sum of Rydberg and ground state atom densities over time from Monte Carlo simulations (blue dots) for $\hat{v} = 0 r_f\gamma$ compared with the prediction from the Langevin Eqs. (10) from Ref. [39] (red line). (b) Rydberg density for $\hat{v} = 100 r_f\gamma$. (c) Rydberg density for $\hat{v} = 0 r_f\gamma$. For all plots, we use the parameters: $n_0 = 4 r_f^{-3}$, $\Omega/\gamma = 20$, $\Delta/\gamma = 2000$, $\gamma_{\perp}/\gamma = 20$, $b = 0.3$, $L/r_f = 7$.

phase). Above the critical point, any arbitrarily small number of excitations initially present in the system will facilitate further excitations cascading through the system until a steady state with finite excitation density $\rho(t \rightarrow \infty) > 0$ is reached (active phase).

Off-resonant excitations, with the rate τ , will seed an excitation cascade in the active phase; whereas, in the absorbing phase, they cause fluctuations in the excitation number. As a result, the true absorbing state $\rho = 0$ can only be approximately reached experimentally through a large separation of the off-resonant and facilitation timescales, suppressing off-resonant excitations on the experimentally relevant facilitation timescales.

Finally, the (slow) decay into a dead state $|0\rangle$ with rate $b\gamma$ is responsible for the self-organized approach to the critical point when starting in the active phase, as indicated in Fig. 1(c). Starting at an initial density n_0 above the critical value n_{crit} , i.e., in the active phase, the large number of atoms in the Rydberg state causes a fast loss of atoms into the dead state. As a consequence, the total density of atoms n effectively participating in the facilitation process, i.e., atoms in states $|g\rangle$ and $|r\rangle$ decrease quickly and approach the critical value. This loss continues at the critical density and drives the system further into the absorbing state. However, this happens on a much slower timescale, as fewer Rydberg excitations are present at the critical point.

In Fig. 3, we have plotted the time evolution of the total density n , initially ten times higher than the critical density n_{crit} , and the Rydberg density ρ for a frozen gas as well as a high-temperature gas with otherwise identical conditions, obtained from Monte Carlo simulations. Here, all atoms in the system are initially in the ground state until one atom is off-resonantly excited to the Rydberg state. For comparison, we also show the solution of the mean-field Langevin

Eqs. (10), which capture the long-time SOC dynamics of the high-temperature gas, but fail to describe the frozen gas outside of very short times [see Figs. 3(b) and 3(c)]. The discrepancy in the peak values of ρ can be attributed to Rydberg blockade, which truncates the maximum number of Rydberg excitations simultaneously present in the gas.

Qualitatively, the Rydberg density in the frozen gas displays a similar time dynamic to that of the high temperature gas, albeit with substantial quantitative differences in the long-time limit. We will show that in the low-temperature regime of the Rydberg gas, the absorbing state phase transition is replaced with an extended Griffiths phase, whose characteristic features become visible when off-resonant excitations and decay into state $|0\rangle$ are negligible.

It is important to note that for $b > 0$ the decay into $|0\rangle$ dominates the dynamics at times $t > 1/b\gamma$. Thus, to experimentally observe a Griffiths phase by monitoring the long-time dynamics with this system, ionization and loss of Rydberg atoms (manifested in the parameter b) must be reduced as much as possible.

In Ref. [42], it was argued that a Rydberg atom moving at an average velocity larger than the Landau-Zener velocity $v_{LZ} = 2\pi^2\Omega^2r_f/(3\Delta)$ effectively decouples from the excitation cascade. As a result, it was argued that this system features an emerging heterogeneity at high temperatures. Considering the two limiting cases of a frozen gas and a high-temperature gas, we argue that the Griffiths phase, which originates from spatial inhomogeneity, disappears when the atom's average velocity is increased above a certain limit, resulting in a direct absorbing-state phase transition.

A quantitative discussion of the crossover between a frozen system with an extended Griffiths phase and a high-temperature gas with a direct absorbing-state phase transition is beyond the scope of the present paper and is subject to future work. Instead we will focus on the quantitative description of the facilitation dynamics in a low-temperature or frozen gas.

IV. NETWORK STRUCTURE OF FACILITATION PATHS IN A FROZEN GAS

The emergence of a Griffiths phase results from facilitation events being constrained to a network structure. In the limit of a frozen gas, atoms have random but fixed positions. If we regard the system at the timescale of facilitated excitations, off-resonant excitations can be neglected. Therefore, the dynamics are described by the facilitated spreading of Rydberg excitations, which is only possible if atomic distances are approximately r_f . As a result, we can regard the structure of atom positions and the paths along which excitations can spread as a random graph with edges where atoms have the distance $r \in [r_f - \frac{\delta r_f}{2}, r_f + \frac{\delta r_f}{2}]$.

Assuming a uniform distribution of atom positions in the gas, the probability that a randomly selected atom has k atoms in its facilitation shell [see Fig. 1(d)], meaning the atom is of degree k , is given by the Poissonian distribution:

$$P(k) = \frac{(nV_s)^k}{k!} \exp(-nV_s). \quad (12)$$

As the degree distribution is Poissonian, we can map this problem to a random Erdős-Rényi (ER) network [54]. In contrast, the network structure of atoms trapped by an optical lattice or tweezer array would be given by a regular lattice network.

Of particular interest in random graph theory is the question if a system percolates. In a percolating system, the probability p that a bond between two randomly selected atoms exists is high enough, such that a path exists which runs through the entire system, i.e. there almost surely exists a single cluster (i.e., a single connected set of vertices) with its size in the order of the system size. If, however, the connectivity is below a critical threshold for bond connectivity $p < p_c$, the system is composed of many small, disconnected clusters [54,55]. For $p = p_c$, the percolation transition occurs. A 2D network with $p = p_c$ from Monte Carlo sampling is illustrated in Fig. 4.

If N is the number of atoms and $s_1(N)$ is the size of the largest connected cluster (LCC), then the system percolates if $\lim_{N \rightarrow \infty} s_1(N)/N > 0$. For an ER network, the percolation transition occurs when the average network degree is $\langle k \rangle = 1$ [55,56]. Using Eq. (12), the density at which the percolation transition occurs is therefore

$$n_{\text{perc}} = \frac{1}{V_s}. \quad (13)$$

This density is a factor Γ_f/γ larger than the critical density n_{crit} of the absorbing state phase transition, given by Eq. (11). We can verify that Eq. (13) corresponds to the correct percolation density by calculating the size of the LCC s_1 depending on the density of the gas (Fig. 4). In the thermodynamic limit, $s_1/N = 0$ for all densities $n < n_{\text{perc}}$. As numeric simulations are restricted to a finite system size, however, we instead consider the percolation transition to occur when s_1 grows faster than linear with the density n (the black dashed line in Fig. 4 corresponds to linear growth).

Of relevance for the Griffiths phase is the size distribution of clusters in the network. Using Monte Carlo simulations, we can verify that the lengths of clusters follow a geometric distribution $P(s) \sim e^{-cs}$ under the assumption that clusters are made of linear chains of s atoms. This assumption holds true for small cluster sizes and an average network degree $\langle k \rangle \ll 1$.

We can then approximate the decay constant c , with p_0 being the probability of an atom having the degree $k = 0$, as

$$P(s) = p_0(1 - p_0)^{s-1} \quad (14a)$$

$$= e^{-nV_s}(1 - e^{-nV_s})^{s-1} \quad (14b)$$

$$\propto e^{-cs}, \quad (14c)$$

with $c = -\ln(1 - e^{-nV_s})$. In Fig. 5, a comparison between cluster sizes in Monte-Carlo simulations and Eqs. (14) is shown. The agreement is very good for small densities as almost all clusters in the gas are composed of linear chains. As the density of the gas increases, the probability that at least one atom in the cluster has more than two connections, i.e., $k \geq 3$, increases. While the distribution remains exponential, the probability for larger clusters to exist in the system greatly increases compared to the prediction by Eqs. (14).

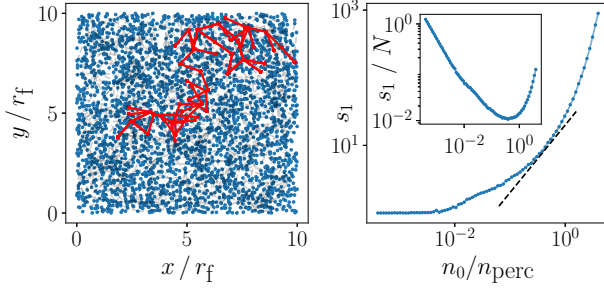


FIG. 4. Schematic frozen gas atom positions (blue dots) for a 2D system with $L = 10 r_f$. Network clusters connecting atoms which have distances $r_{ij} \in [r_f - \frac{\delta r_f}{2}, r_f + \frac{\delta r_f}{2}]$ (grey dashed lines) and the largest connected cluster of these (red lines) for $n_0 = n_{\text{perc}}$ are shown (left). Size of largest connected cluster (LCC) s_1 depending on the density from Monte Carlo samples in a 3D cube with $L = 7 r_f$ (right). The black dashed line corresponds to a power law with exponent $v = 1$. And LCC divided by number of atoms N depending on density (inset).

V. EPIDEMIC DYNAMICS ON THE NETWORK

It is known that Rydberg systems in the facilitation regime bear close similarities to epidemics [42,57]. In the following, we will systematically analyze the Rydberg facilitation dynamics on the random network formed by atoms within their respective facilitation shells. For this, we will map the dynamics to the SIS epidemic model [58–60]. We will (i) disregard the decay of Rydberg atoms into the dead state $|0\rangle$ [parameter $b = 0$, see Fig. 1(a)], reducing the dynamics of each atom to a two-level system. Additionally, we will (ii) neglect off-resonant excitations by setting $\tau = 0$, meaning excitations can only be created by means of facilitation. We will refer to simulations carried out with these two constraints as the SIS approximation.

One major difference between our Rydberg system in the SIS approximation and a classical SIS system remains with Rydberg blockade. Atoms excited to the Rydberg state do not

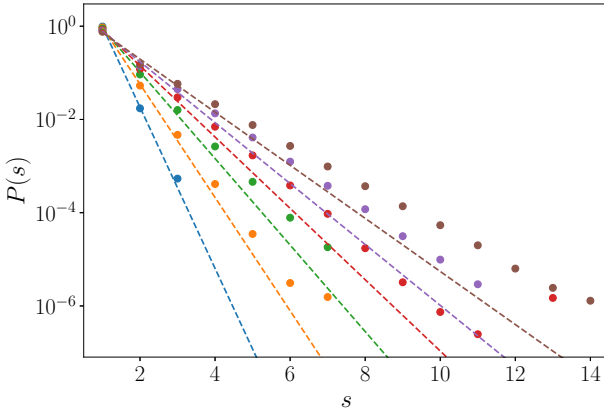


FIG. 5. Network cluster size probability distribution from 3D Monte-Carlo samples (dots) and Eqs. (14) (dashed lines). From left to right for the densities $n_0/n_{\text{perc}} = [0.019, 0.063, 0.125, 0.188, 0.250, 0.313]$.

only facilitate the spread of excitations, they can also block the spreading in adjacent clusters. This will be analyzed more systematically later.

The network structure of a cluster of atoms in facilitation distance of each other strongly depends on the temperature of the gas. If the RMS average relative velocity \bar{v} is large, such that each excited Rydberg atom meets many ground-state atoms during its lifetime γ^{-1} , i.e., if in a 3D gas

$$\bar{v} \gg \gamma n^{-1/3}, \quad (15)$$

any network structure is effectively washed out and the system is homogeneous. Close to the critical point of the absorbing-state phase transition, the above condition is equivalent to $\bar{v} \gg \gamma r_f$. If, on the other hand, the average velocity of atoms is very small, such that during a facilitation time Γ_f^{-1} they do not move out of the facilitation shell, i.e., if

$$\bar{v} \ll \Gamma_f \delta r_f, \quad (16)$$

the atoms form a finitely connected network. We will now discuss these two limits.

A. High-temperature limit

In a high-temperature gas with RMS average relative velocity $\bar{v} \gg \gamma n^{-1/3}$, we can map the system to the SIS epidemic model [58–60]. The SIS model is characterized by the infection and recovery rates, λ and μ , respectively, which for the Rydberg gas read

$$\lambda = n\kappa, \quad (17a)$$

$$\mu = \gamma. \quad (17b)$$

The SIS model predicts an active (absorbing) phase transition when

$$\lambda_c^{(1)} = \mu, \quad (18)$$

where excitation spread equals spontaneous decay. This corresponds to the critical density Eq. (11) of the absorbing state phase transition discussed before.

In Fig. 6(a), Monte Carlo simulations of the Rydberg system with the SIS approximation and $\rho(t=0) = n$ are shown for the high-temperature gas for different values of n and a fixed facilitation rate Γ_f . We note that as shown in the Appendix, the excitation probabilities following from Monte Carlo simulations of rate equations and those from full coherent density matrix simulations agree, showing that the rate equation approach remains valid also in the high-temperature limit. One recognizes that an active (absorbing)-state phase transition occurs for $\lambda = \lambda_c^{(1)}$, with the Rydberg density either exponentially decaying at the timescale μ (for $\lambda < \lambda_c^{(1)}$) or decaying to a steady-state active density (for $\lambda > \lambda_c^{(1)}$). At the critical density [green curve in Fig. 6(a)], the system should decay with $\rho \sim t^{-1}$ [61], however, this decay is truncated by an exponential decay due to finite system size.

B. Frozen gas limit

In the limit of an effectively frozen gas, the atoms that can participate at the facilitation process form a network. The dynamics of an SIS epidemic strongly depend on the structure of this underlying network. For example, in the case of a

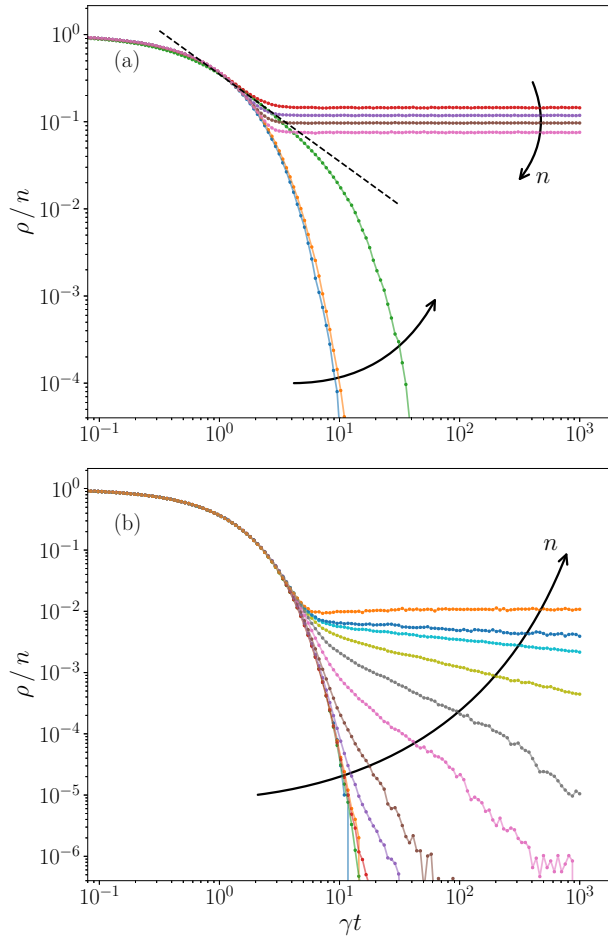


FIG. 6. Decay of Rydberg density over time from Monte Carlo simulations in the SIS approximation ($b = 0$, $\tau = 0$) with an initial density $\rho(t = 0) = n$ for the gas at high temperature (a) with $\hat{v} = 100 r_f \gamma$ and for the frozen gas (b) with $\hat{v} = 0 r_f \gamma$. The black dashed line in (a) is a power-law decay with $\rho \sim t^{-1}$, expected at the critical density. The colors show total system densities (increasing from left to right) with $n = 0.003, 0.03, 0.39, 1.98, 3.97, 5.95, 9.12, 11.90, 14.28, 15.91, 16.66$, and 19.94 . (a) only shows the lowest seven densities. The critical density is $n_{\text{crit}} = 0.39$. Between the percolation density $n_{\text{perc}} = 15.91$ and $n_{\text{crit}}^{(2)} = 16.6$, the curves feature a decay (see Fig. 7).

heterogeneous but *scale-free* network, i.e., $P(k) \sim k^{-\nu}$, the absorbing phase can disappear altogether, leaving the system in an endemic phase regardless of the infection rate [62–64].

For the case of a heterogeneous ER network, which describes the frozen gas of atoms, an active phase can only occur if the network is above the percolation threshold (i.e., $\langle k \rangle > 1$). However, for a finitely connected (but percolating) ER network, the threshold for the active phase is modified since activity occurs in localized regions and thus the effective infection rate is reduced. One finds [61]

$$\lambda_c^{(2)} = \mu \frac{\langle k \rangle}{\langle k \rangle - 1}, \quad (19)$$

with $\langle k \rangle$ being the average degree of the network. For $\langle k \rangle \rightarrow \infty$, the threshold given by Eq. (18) is recovered. For a fixed facilitation rate and facilitation volume, this threshold can be expressed in terms of a critical density of atoms using $\langle k \rangle = nV_s$:

$$n_{\text{crit}}^{(2)} = \frac{1}{V_s} + \frac{\gamma}{\kappa} \equiv n_{\text{perc}} + n_{\text{crit}}^{(1)}. \quad (20)$$

If the network is below the percolation threshold, the finite size of clusters truncates the spread of activity through the system. Therefore, the network cannot support an active phase and, instead, a Griffiths phase emerges above the critical infection rate $\lambda_c^{(1)}$ [61]. One of the most distinguishing characteristics of a Griffiths phase is the presence of rare regions with above average activity which lead to a slow, algebraic decay of excitations [43].

In the nonpercolating network (i.e., $\langle k \rangle < 1$), for $\lambda \leq \mu$ decay dominates, leading to very short times until all activity disappears in clusters as excitations cannot sustain themselves. If, however, $\lambda > \lambda_c^{(1)} = \mu$, the time until activity disappears in clusters increases exponentially with cluster size s and is given by [65]

$$\tau(s) \propto \sqrt{\frac{2\pi}{s}} \frac{\lambda}{(\lambda - 1)^2} \exp\left\{s\left(\ln(\lambda) - 1 + \frac{1}{\lambda}\right)\right\}. \quad (21)$$

In the following, we will refer to $\tau(s)$ as the extinction time of activity in a cluster. As a result of the convolution of exponentially rare cluster sizes $P(s) \sim e^{-cs}$ and a cluster lifetime increasing exponentially with cluster size $\tau(s) = e^{as}$, the activity in the Griffiths phase decays with a power law:

$$\rho(t) = \int ds s P(s) e^{-t/\tau(s)}. \quad (22)$$

Using Eqs. (14) and (21), the integral in Eq. (22) can be approximated with Laplace's method and results in an algebraic decay

$$\rho \sim t^{-c/a}, \quad (23)$$

with the coefficient a given by Eq. (21) as $a = \ln(\lambda) - 1 + \frac{1}{\lambda}$. If the network is above the percolation threshold, i.e., if $\langle k \rangle \geq 1$, but the driving strength is below the critical value for the active phase $\lambda_c^{(2)}$, the decay of activity is expected to follow a stretched exponential. A qualitative phase diagram of the facilitation dynamics in the frozen Rydberg gas is shown in Fig. 7.

Figure 6(b) shows the results of Monte Carlo simulations for a frozen gas in the SIS approximation for the same parameters and color code as in the high-temperature case of Fig. 6(a). For $n < n_{\text{crit}}$, all initial excitations decay exponentially (curves 1 and 2 from left to right), corresponding to the absorbing phase. The behavior changes at and above the critical point but below the percolation threshold $n_{\text{crit}} \leq n < n_{\text{perc}}$ (curves 3–7). Here, the system is in an extended Griffiths phase with a power-law decay with varying exponents. Above the percolation threshold but below the threshold of the active phase $n_{\text{perc}} \leq n < n_{\text{crit}}^{(2)}$, the decay is expected to become a stretched exponential [61], which we cannot resolve, however, in our simulations due to the very long timescale of this decay.

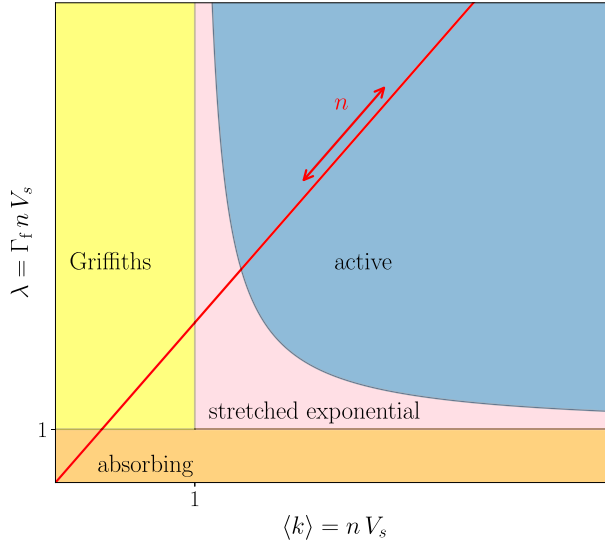


FIG. 7. Schematic phase diagram of Rydberg facilitation of a frozen gas with the percolation threshold given at $\langle k \rangle = 1$. Increasing the density n of the gas, one moves along the red line crossing from an absorbing into a Griffiths phase at n_{crit} , and subsequently into a phase with stretched exponential decay at the percolation threshold n_{perc} and eventually into the active phase at $n_{\text{crit}}^{(2)}$. Time has been rescaled such that $\mu = 1$.

Finally, for $n \geq n_{\text{crit}}^{(2)}$ the system enters the active phase where excitations simply decay to a steady state.

In the following, we want to give a quantitative estimate for the power-law decay coefficient in the Griffiths phase based on the SIS model and compare them with those from the Monte Carlo simulations. In contrast to the standard SIS model, a Rydberg system features Rydberg blockade and facilitated de-excitation, making it unclear if analytic predictions from an SIS model would be accurate. To check this, we compare the extinction time of activity in clusters in a linear excitation chain, given by Eq. (21), using the spreading rate $\lambda = \Gamma_f V_s \times 1r_f^{-3}$, with Monte Carlo simulations of the SIS approximation in Fig. 8. For this, we simulate a 1D cluster of length s , where each atom is initially in the Rydberg state and measure the average time until all atoms are decayed. Here, we assume the above-mentioned SIS approximation (no decay to $|0\rangle$ and no off-resonant excitations). One recognizes that Eq. (21) gives a good approximation of the extinction time.

Using Eqs. (14) and (21), we can approximate the power-law exponent ν in the Griffiths phase dependent on the density and internal rates. We receive

$$\nu \equiv -\frac{c}{a} = -\frac{\ln(1 - e^{-nV_s})}{\ln(\lambda) - 1 + \lambda^{-1}}, \quad (24)$$

with $\lambda = 4\pi \Gamma_f \frac{\delta r_f}{r_f}$. The comparison with exponents fitted from the power-law decay of Rydberg density in Monte Carlo simulations of the frozen gas under the SIS approximation (seen in Fig. 6) can be seen in Fig. 9(b). Our very rough approximation of the Griffith-phase decay exponents qualitatively fits with Monte Carlo data.

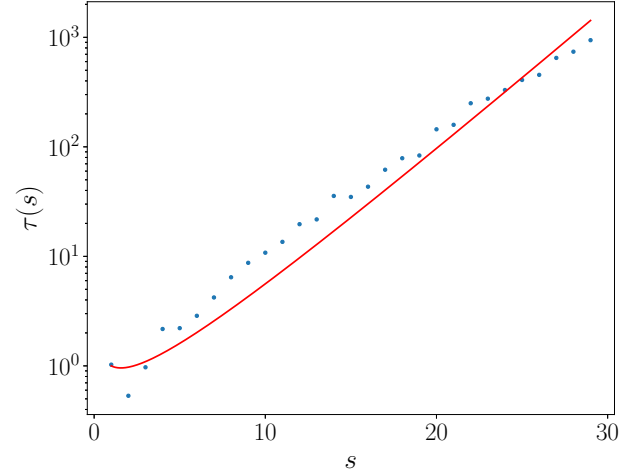


FIG. 8. Extinction times for activity in clusters in Monte Carlo simulations of 1D lattice chains of length s (blue dots) and prediction by Ref. [65] (red line).

A fundamental difference between Rydberg facilitation and classical SIS activity spreading is Rydberg blockade. Considering the frozen gas limit, two effects arise from Rydberg blockade: First, if an atom is surrounded by two Rydberg atoms in the facilitation distance, i.e., the atom is in the middle of a cluster, then it cannot be facilitated, as it receives twice the dipole shift and is pushed out of resonance again. If this atom decays or is in the ground state at the beginning, it cannot be excited, resulting in a hole splitting the cluster [19]. Additionally, Rydberg atoms can block excitations from spreading through adjacent clusters. However, neither of these effects change the actual structure of the network, instead they effectively retard the timescale at which excitations spread. For a quantitative comparison, we simulate the Rydberg gas and compare the decay of excitations in the SIS approximation with and without Rydberg blockade (Fig. 9).

As blockade allows fewer Rydberg atoms to be present in the system, the steady-state Rydberg density of the active phase, and therefore the density at which the power-law decay of the Griffiths phase begins is much lower. However, as seen in Fig. 9, the exponents of the power-law decay in the Griffiths phase show no qualitative change depending on the presence of Rydberg blockade in the system.

VI. CONCLUSION

We studied the facilitation dynamics of Rydberg excitations in an ultracold gas of atoms. In the homogeneous limit, the system is expected to show a phase transition between an absorbing phase and an active phase, and—in the presence of an additional loss channel from the Rydberg state—SOC. However, experiments with a gas of trapped ^{87}Rb atoms at low temperatures show signs of scale-invariant dynamics in an extended parameter regime, which is a signature of a Griffiths phase replacing the critical point of the absorbing-state phase transition.

To understand the emergence of scale invariance in the experiment in an extended parameter regime, we numerically

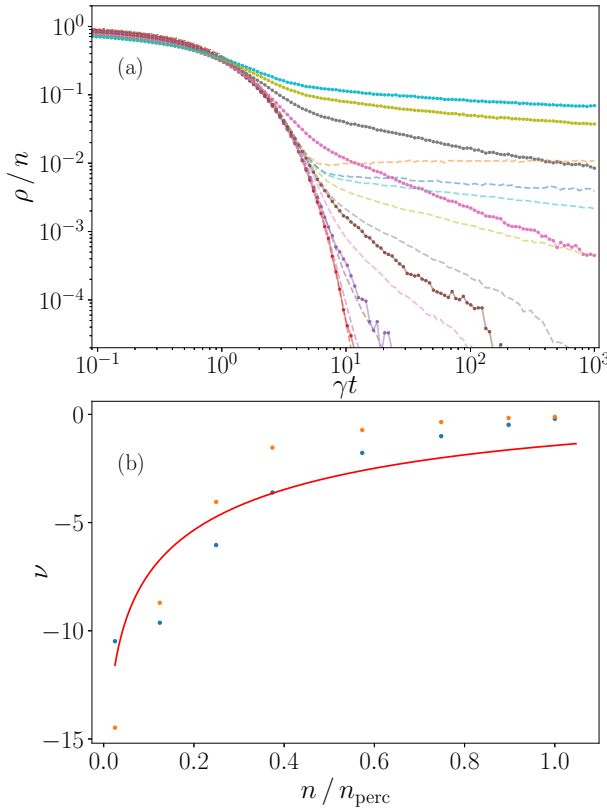


FIG. 9. (a) Decay of Rydberg density over time from Monte Carlo simulations in the SIS approximation for the frozen gas without Rydberg blockade (full lines) compared to the results from Fig. 6(b) (dashed lines). The colors show total system densities (increasing from left to right) with $n = 0.003, 0.03, 0.39, 1.98, 3.97, 5.95, 9.12, 11.90, 14.28, 15.91, 16.66$, and 19.94 . (b) Power-law decay exponent $v = -c/a$ of Rydberg density over time fitted from frozen-gas Monte Carlo simulations in the SIS approximation from Fig. 9(a) with Rydberg blockade (blue dots), without Rydberg blockade (orange dots), and from the analytical approximation given by Eq. (24) (red line).

simulated the many-body Rydberg gas in the facilitation regime through the use of Monte Carlo simulations in the classical rate-equation approximation. We showed that the latter is well justified for the large dephasing characteristic for the experiment even for a high-temperature gas. Since a Griffiths phase originates from heterogeneity in the system, we numerically and theoretically analyzed two limiting cases: (i) a high-temperature gas and (ii) a frozen gas. While in the high-temperature limit, a homogeneous mean-field behavior is recovered, with a clear absorbing-state phase transition and SOC, the facilitation dynamics in a low-temperature or frozen gas is governed by the presence of a network structure of atoms that can participate in the excitation spread. Numerical simulations show characteristic power-law decay of Rydberg excitations in time if off-resonant excitations and atom losses are neglected.

We have shown that in the frozen gas the spread of excitations is constrained to a network resembling a random ER

graph. Increasing the density of atoms, the ER network has a percolation transition from a fragmented phase, in which the maximum cluster size of connected atoms remains finite, to a phase where the size of the largest cluster scales with the size of the system. A theoretical explanation of the Rydberg facilitation dynamics observed in Monte Carlo simulations can then be given by mapping to a SIS epidemic model on such an ER graph taking into account the effects of Rydberg blockade, which truncates the maximum Rydberg excitation density. An active phase of self-sustained Rydberg excitations is only possible above the percolation threshold. Below this threshold, an extended Griffiths phase emerges in the place of the (for homogeneous systems) expected absorbing-state phase transition. We showed that the modified SIS model quantitatively explains the observed power-law decay exponents as well as the overall dynamics of the Rydberg density.

While the limits of a high-temperature and a frozen gas are well captured with our model, it does not yet allow the study of the crossover between the two regimes. To this end, the Rydberg facilitation process needs to be mapped to a dynamical network, which is beyond the scope of the present paper and will be the subject of future work. Furthermore, to quantitatively understand the power-law exponents in the number distribution of Rydberg atoms in a given time interval observed in the experiment, it is necessary to extend the microscopic simulations to much larger system sizes matching those used in the experiments. To this end, different approaches, e.g., using machine-learning algorithms might be useful [66]. Finally, the interplay between coherent quantum dynamics and dynamical network structures in Rydberg facilitation under conditions where dephasing is much less dominant could give rise to very different dynamics [67,68]. The latter requires, however, the development of microscopic simulation techniques capable of incorporating quantum coherences in 3D Rydberg gases, at least in an approximate way [69].

ACKNOWLEDGMENTS

The authors thank J. Otterbach for fruitful discussions. Financial support from the DFG through SFB TR 185, Project No. 277625399, is gratefully acknowledged.

D.B. and M.F. developed the theoretical models, D.B. performed all numerical simulations and developed the mapping to the ER network with support by S.O. M.F., T.N., and H.O. conceived the project. J.B., P.M., and D.B. performed the experiments guided by T.N. and H.O. D.B. and M.F. wrote the initial version of the paper with support by J.B. All authors discussed the results and contributed to the writing of the paper.

APPENDIX: EFFECTS OF RELATIVE MOTION BETWEEN ATOMS

The rate equation approximation used for the Monte Carlo simulations [e.g., Eq. (3)] is valid as long as the population dynamics are slow compared to the dephasing rate. In a frozen gas, the relevant timescales are solely determined by the internal dynamics of an individual atom for a given (fixed) configuration of Rydberg atoms in its vicinity. If, however,

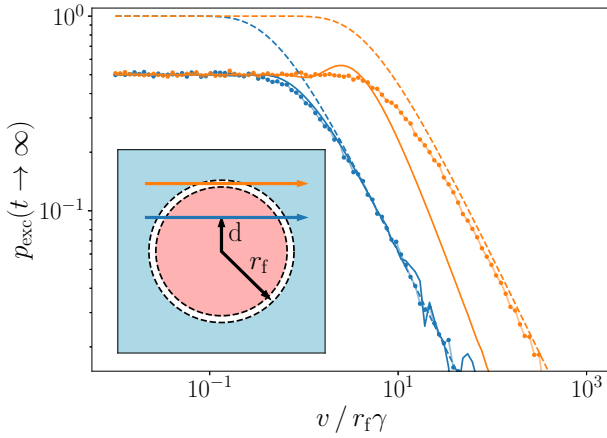


FIG. 10. Velocity-dependent excitation probability of a ground-state atom flying past a Rydberg atom for the impact parameter $d = 0.5r_f$ (blue) and $d = r_f$ (orange) (see inset) calculated from Monte Carlo simulations with fixed time step $dt = 1/400\gamma$ (dots), full numeric density matrix simulation (solid lines), and analytical Landau-Zener formula Eq. (A2) (dashed lines). Full solution and rate equation approximation only differ for the case of grazing incidence ($d = r_f$).

the gas of atoms has a finite temperature, a ground state atom can fly in and out of the facilitation volume V_s of a Rydberg atom, which can amount to a fast sweep of the detuning of the ground state atom. Thus, there is an additional timescale given by the crossing time $\sim \delta r_f/v$.

To analyze the effects of atomic motion onto the facilitation process, we consider the two-body problem of a ground state atom moving with velocity v and with the impact parameter d relative to a Rydberg atom (see inset of Fig. 10). For $d > r_f$, the ground state atom is not shifted into resonance and no facilitation occurs. For $d \leq r_f$, one has to distinguish two cases depending on the impact parameter: (i) $d < r_f$ the ground-state atom flies through the facilitation shell twice (blue case in Fig. 10) and (ii) $d \approx r_f$ the ground-state atom grazes the facilitation shell and is only briefly shifted into resonance (orange case in Fig. 10).

In case (i), using the excitation rate from Eq. (3) as $\Gamma_{\uparrow}(t)$, we find the excitation probability after a single pass of the ground state atom through the facilitation shell as

$$p_{\text{exc}} = 1 - \exp \left\{ - \int_{t_i}^{t_f} dt \Gamma_{\uparrow}(t) \right\} = 1 - \exp \left\{ -2\Omega^2 \int_{t_i}^{t_f} dt \frac{\gamma_{\perp}}{\Delta(t)^2 + \gamma_{\perp}^2} \right\}. \quad (\text{A1})$$

Note that this expression assumes a short passage time through the facilitation shell, so the facilitated de-excitation process can be ignored. For longer passage times, the excitation probability approaches the steady-state value of $1/2$, as can be seen Fig. 10.

Linearizing the time-dependent detuning $\Delta(t)$ for times $t_i < t < t_f$, while passing through the facilitation shell, we receive $\Delta(t) \approx \dot{\Delta} \times (t - t_0)$, yielding

$$p_{\text{exc}} = 1 - \exp \left\{ - \frac{2\Omega^2}{\dot{\Delta}} \int_{\Delta_i}^{\Delta_f} d\Delta \frac{\gamma_{\perp}}{\Delta^2 + \gamma_{\perp}^2} \right\} \approx 1 - \exp \left\{ -2\pi \frac{\Omega^2}{\dot{\Delta}} \right\}, \quad (\text{A2})$$

where we have assumed that $|\Delta_{i,f}| = |\Delta(t_{i,f})| \gg \gamma_{\perp}$, which is exactly the same expression as given by the Landau-Zener formula.

If p_{exc} is small, the asymptotic excitation probability after two passages is just $p_{\text{exc}} \approx 1 - \exp\{-4\pi\Omega^2/\dot{\Delta}\}$. From this discussion, we expect the rate equations to accurately describe the facilitation process even for large atom velocities as long as the impact parameter d is different from $r_f \pm \delta r_f$.

In case (ii), however, i.e., for grazing incidence, the Landau-Zener formula is no longer valid and there could be a difference between the rate-equation approximation and the solution of the full two-particle density matrix equations. This is indeed the case, as can be seen from Fig. 10, where we have plotted the asymptotic excitation probability of the ground-state atom as a function of relative velocity and impact parameter both from a simulation of the full density-matrix equations (dashed lines), the analytic Landau Zener formula (solid line), and by a Monte Carlo simulation of the rate equation in the large-dephasing limit with time step $dt = 1/400\gamma$ (dots). One recognizes perfect agreement except for large relative velocities and impact parameters close to the facilitation radius $d \approx r_f$, where the rate equations predict up to an order of magnitude higher excitation probabilities than the full simulation. Since $\delta r_f \ll r_f$, the contribution of these grazing-incidence cases is negligibly small, allowing us to accurately describe high gas temperatures with a fixed time-step Monte Carlo algorithm.

Furthermore, at high temperatures (as can be seen from Fig. 10), the excitation probability above the Landau-Zener velocity $v_{\text{LZ}} = 2\pi^2\Omega^2 r_f / (3\Delta)$ indeed quickly drops and scales as $1/v$, the number of ground-state atoms seen by a moving Rydberg atom in a given time increases linearly with its velocity v , too. This compensates the former effect, and thus does not lead to an emerging heterogeneity in phase space as argued in Ref. [42], as long as the Rydberg atom does not move out of the gas sample.

- [1] T. Gallagher, *Rydberg Atoms* (Cambridge University Press, Cambridge, 2006).
- [2] H. Weimer, M. Müller, I. Lesanovsky, P. Zoller, and H. P. Büchler, A Rydberg quantum simulator, *Nat. Phys.* **6**, 382 (2010).
- [3] P. Schauß, M. Cheneau, M. Endres, T. Fukuhara, S. Hild, A. Omran, T. Pohl, C. Gross, S. Kuhr, and I. Bloch, Observation of spatially ordered structures in a two-dimensional Rydberg gas, *Nature (London)* **491**, 87 (2012).
- [4] H. Bernien, S. Schwartz, A. Keesling, H. Levine, A. Omran, H. Pichler, S. Choi, A. S. Zibrov, M. Endres, M. Greiner, V. Vuletić, and M. D. Lukin, Probing many-body dynamics on a 51-atom quantum simulator, *Nature (London)* **551**, 579 (2017).

[5] A. Browaeys and T. Lahaye, Many-body physics with individually controlled Rydberg atoms, *Nat. Phys.* **16**, 132 (2020).

[6] F. M. Surace, P. P. Mazza, G. Giudici, A. Lerose, A. Gambassi, and M. Dalmonte, Lattice Gauge Theories and String Dynamics in Rydberg Atom Quantum Simulators, *Phys. Rev. X* **10**, 021041 (2020).

[7] P. Scholl, M. Schuler, H. J. Williams, A. A. Eberharter, D. Barredo, K.-N. Schymik, V. Lienhard, L.-P. Henry, T. C. Lang, T. Lahaye, A. M. Läuchli, and A. Browaeys, Quantum simulation of 2D antiferromagnets with hundreds of Rydberg atoms, *Nature (London)* **595**, 233 (2021).

[8] S. de Léséleuc, V. Lienhard, P. Scholl, D. Barredo, S. Weber, N. Lang, H. P. Büchler, T. Lahaye, and A. Browaeys, Observation of a symmetry-protected topological phase of interacting bosons with Rydberg atoms, *Science* **365**, 775 (2019).

[9] G. Semeghini, H. Levine, A. Keesling, S. Ebadi, T. T. Wang, D. Bluvstein, R. Verresen, H. Pichler, M. Kalinowski, R. Samajdar, A. Omran, S. Sachdev, A. Vishwanath, M. Greiner, V. Vuletić, and M. D. Lukin, Probing topological spin liquids on a programmable quantum simulator, *Science* **374**, 1242 (2021).

[10] D. Jaksch, J. I. Cirac, P. Zoller, S. L. Rolston, R. Côté, and M. D. Lukin, Fast Quantum Gates for Neutral Atoms, *Phys. Rev. Lett.* **85**, 2208 (2000).

[11] M. D. Lukin, M. Fleischhauer, R. Cote, L. M. Duan, D. Jaksch, J. I. Cirac, and P. Zoller, Dipole Blockade and Quantum Information Processing in Mesoscopic Atomic Ensembles, *Phys. Rev. Lett.* **87**, 037901 (2001).

[12] A. Gaëtan, Y. Miroshnychenko, T. Wilk, A. Chotia, M. Viteau, D. Comparat, P. Pillet, A. Browaeys, and P. Grangier, Observation of collective excitation of two individual atoms in the Rydberg blockade regime, *Nat. Phys.* **5**, 115 (2009).

[13] E. Urban, T. A. Johnson, T. Henage, L. Isenhower, D. Yavuz, T. Walker, and M. Saffman, Observation of Rydberg blockade between two atoms, *Nat. Phys.* **5**, 110 (2009).

[14] M. Saffman, T. G. Walker, and K. Mølmer, Quantum information with Rydberg atoms, *Rev. Mod. Phys.* **82**, 2313 (2010).

[15] S. Helmrich, A. Arias, and S. Whitlock, Uncovering the nonequilibrium phase structure of an open quantum spin system, *Phys. Rev. A* **98**, 022109 (2018).

[16] H. Schempp, G. Günter, M. Robert-de Saint-Vincent, C. S. Hofmann, D. Breyel, A. Komnik, D. W. Schönleber, M. Gärttner, J. Evers, S. Whitlock, and M. Weidemüller, Full Counting Statistics of Laser Excited Rydberg Aggregates in a One-Dimensional Geometry, *Phys. Rev. Lett.* **112**, 013002 (2014).

[17] N. Malossi, M. M. Valado, S. Scotto, P. Huillery, P. Pillet, D. Ciampini, E. Arimondo, and O. Morsch, Full Counting Statistics and Phase Diagram of a Dissipative Rydberg Gas, *Phys. Rev. Lett.* **113**, 023006 (2014).

[18] A. Urvoy, F. Ripka, I. Lesanovsky, D. Booth, J. P. Shaffer, T. Pfau, and R. Löw, Strongly Correlated Growth of Rydberg Aggregates in a Vapor Cell, *Phys. Rev. Lett.* **114**, 203002 (2015).

[19] F. Letscher, O. Thomas, T. Niederprüm, M. Fleischhauer, and H. Ott, Bistability Versus Metastability in Driven Dissipative Rydberg Gases, *Phys. Rev. X* **7**, 021020 (2017).

[20] H. Hinrichsen, Non-equilibrium critical phenomena and phase transitions into absorbing states, *Adv. Phys.* **49**, 815 (2000).

[21] M. Henkel, H. Hinrichsen, S. Lübeck, and M. Pleimling, *Non-equilibrium Phase Transitions* (Springer, Dordrecht, The Netherlands, 2008), Vol. 1.

[22] P. Grassberger, On the critical behavior of the general epidemic process and dynamical percolation, *Math. Biosci.* **63**, 157 (1983).

[23] J.-T. Kühr, M. Leisner, and E. Frey, Range expansion with mutation and selection: Dynamical phase transition in a two-species eden model, *New J. Phys.* **13**, 113013 (2011).

[24] J. A. Bonachela, M. A. Muñoz, and S. A. Levin, Patchiness and demographic noise in three ecological examples, *J. Stat. Phys.* **148**, 724 (2012).

[25] J. Xie, F. Meng, J. Sun, X. Ma, G. Yan, and Y. Hu, Detecting and modelling real percolation and phase transitions of information on social media, *Nat. Hum. Behav.* **5**, 1161 (2021).

[26] H. Hinrichsen, On possible experimental realizations of directed percolation, *Braz. J. Phys.* **30**, 69 (2000).

[27] P. Rupp, R. Richter, and I. Rehberg, Critical exponents of directed percolation measured in spatiotemporal intermittency, *Phys. Rev. E* **67**, 036209 (2003).

[28] K. A. Takeuchi, M. Kuroda, H. Chaté, and M. Sano, Directed Percolation Criticality in Turbulent Liquid Crystals, *Phys. Rev. Lett.* **99**, 234503 (2007).

[29] K. A. Takeuchi, M. Kuroda, H. Chaté, and M. Sano, Experimental realization of directed percolation criticality in turbulent liquid crystals, *Phys. Rev. E* **80**, 051116 (2009).

[30] G. Lemoult, L. Shi, K. Avila, S. V. Jalikop, M. Avila, and B. Hof, Directed percolation phase transition to sustained turbulence in Couette flow, *Nat. Phys.* **12**, 254 (2016).

[31] M. Kohl, R. Capellmann, M. Laurati, S. Egelhaaf, and M. Schmiedeberg, Directed percolation identified as equilibrium pre-transition towards non-equilibrium arrested gel states, *Nat. Commun.* **7**, 11817 (2016).

[32] R. Gutiérrez, C. Simonelli, M. Archimi, F. Castellucci, E. Arimondo, D. Ciampini, M. Marcuzzi, I. Lesanovsky, and O. Morsch, Experimental signatures of an absorbing-state phase transition in an open driven many-body quantum system, *Phys. Rev. A* **96**, 041602(R) (2017).

[33] P. Bak, C. Tang, and K. Wiesenfeld, Self-organized criticality, *Phys. Rev. A* **38**, 364 (1988).

[34] P. Bak, *How Nature Works: The Science of Self-Organized Criticality* (Springer Science & Business Media, New York City, USA, 2013).

[35] A. Sornette and D. Sornette, Self-organized criticality and earthquakes, *Europhys. Lett.* **9**, 197 (1989).

[36] C. J. Rhodes and R. M. Anderson, Power laws governing epidemics in isolated populations, *Nature (London)* **381**, 600 (1996).

[37] B. D. Malamud, G. Morein, and D. L. Turcotte, Forest fires: An example of self-organized critical behavior, *Science* **281**, 1840 (1998).

[38] J. Hesse and T. Gross, Self-organized criticality as a fundamental property of neural systems, *Front. Syst. Neurosci.* **8**, 166 (2014).

[39] S. Helmrich, A. Arias, G. Lohead, T. M. Wintermantel, M. Buchhold, S. Diehl, and S. Whitlock, Signatures of self-organized criticality in an ultracold atomic gas, *Nature (London)* **577**, 481 (2020).

[40] D.-S. Ding, H. Busche, B.-S. Shi, G.-C. Guo, and C. S. Adams, Phase Diagram and Self-Organizing Dynamics in a Thermal

Ensemble of Strongly Interacting Rydberg Atoms, *Phys. Rev. X* **10**, 021023 (2020).

[41] T. Vojta and M. Dickison, Critical behavior and Griffiths effects in the disordered contact process, *Phys. Rev. E* **72**, 036126 (2005).

[42] T. M. Wintermantel, M. Buchhold, S. Shevate, M. Morgado, Y. Wang, G. Lochead, S. Diehl, and S. Whitlock, Epidemic growth and Griffiths effects on an emergent network of excited atoms, *Nat. Commun.* **12**, 103 (2021).

[43] R. B. Griffiths, Nonanalytic Behavior Above the Critical Point in a Random Ising Ferromagnet, *Phys. Rev. Lett.* **23**, 17 (1969).

[44] G. Lindblad, On the generators of quantum dynamical semigroups, *Commun. Math. Phys.* **48**, 119 (1976).

[45] W. Li, C. Ates, and I. Lesanovsky, Nonadiabatic Motional Effects and Dissipative Blockade for Rydberg Atoms Excited from Optical Lattices or Microtraps, *Phys. Rev. Lett.* **110**, 213005 (2013).

[46] C. Ates, T. Pohl, T. Pattard, and J. M. Rost, Antiblockade in Rydberg Excitation of an Ultracold Lattice Gas, *Phys. Rev. Lett.* **98**, 023002 (2007).

[47] T. Amthor, C. Giese, C. S. Hofmann, and M. Weidemüller, Evidence of Antiblockade in an Ultracold Rydberg Gas, *Phys. Rev. Lett.* **104**, 013001 (2010).

[48] M. Schlagmüller, T. C. Liebisch, F. Engel, K. S. Kleinbach, F. Böttcher, U. Hermann, K. M. Westphal, A. Gaj, R. Löw, S. Hofferberth, T. Pfau, J. Pérez-Ríos, and C. H. Greene, Ultracold Chemical Reactions of a Single Rydberg Atom in a Dense Gas, *Phys. Rev. X* **6**, 031020 (2016).

[49] T. Niederprüm, O. Thomas, T. Manthey, T. M. Weber, and H. Ott, Giant Cross Section for Molecular ion Formation in Ultracold Rydberg Gases, *Phys. Rev. Lett.* **115**, 013003 (2015).

[50] E. Levi, R. Gutiérrez, and I. Lesanovsky, Quantum non-equilibrium dynamics of Rydberg gases in the presence of dephasing noise of different strengths, *J. Phys. B: At., Mol. Opt. Phys.* **49**, 184003 (2016).

[51] V. Ruiz Barlett, J. Bigeón, M. Hoyuelos, and H. Martín, Differences between fixed time step and kinetic Monte Carlo methods for biased diffusion, *J. Comput. Phys.* **228**, 5740 (2009).

[52] A. Chotia, M. Viteau, T. Vogt, D. Comparat, and P. Pillet, Kinetic Monte Carlo modeling of dipole blockade in Rydberg excitation experiment, *New J. Phys.* **10**, 045031 (2008).

[53] K. Klocke, T. M. Wintermantel, G. Lochead, S. Whitlock, and M. Buchhold, Hydrodynamic Stabilization of Self-Organized Criticality in a Driven Rydberg Gas, *Phys. Rev. Lett.* **126**, 123401 (2021).

[54] P. Erdős and A. Rényi, On the evolution of random graphs, *Publ. Math. Inst. Hung. Acad. Sci.* **5**, 17 (1960).

[55] M. Li, R.-R. Liu, L. Lü, M.-B. Hu, S. Xu, and Y.-C. Zhang, Percolation on complex networks: Theory and application, *Phys. Rep.* **907**, 1 (2021).

[56] H. Sayama, *Introduction to the Modeling and Analysis of Complex Systems* (Open SUNY Textbooks, Geneseo, NY, USA, 2015).

[57] C. Pérez-Espigares, M. Marcuzzi, R. Gutiérrez, and I. Lesanovsky, Epidemic Dynamics in Open Quantum Spin Systems, *Phys. Rev. Lett.* **119**, 140401 (2017).

[58] G. H. Weiss and M. Dishon, On the asymptotic behavior of the stochastic and deterministic models of an epidemic, *Math. Biosci.* **11**, 261 (1971).

[59] J. D. Murray, *Mathematical Biology* (Springer, New York City, USA, 2002).

[60] N. T. Bailey, *The Mathematical Theory of Infectious Diseases and its Applications* (Charles Griffin & Company Ltd., High Wycombe, 1975).

[61] M. A. Muñoz, R. Juhász, C. Castellano, and G. Ódor, Griffiths Phases on Complex Networks, *Phys. Rev. Lett.* **105**, 128701 (2010).

[62] S. Chatterjee and R. Durrett, Contact processes on random graphs with power law degree distributions have critical value 0, *Ann. Probab.* **37**, 2332 (2009).

[63] S. Morita, Six susceptible-infected-susceptible models on scale-free networks, *Sci. Rep.* **6**, 22506 (2016).

[64] R. Pastor-Satorras, C. Castellano, P. Van Mieghem, and A. Vespignani, Epidemic processes in complex networks, *Rev. Mod. Phys.* **87**, 925 (2015).

[65] H. Andersson and B. Djehiche, A threshold limit theorem for the stochastic logistic epidemic, *J. Appl. Probab.* **35**, 662 (1998).

[66] S. Ohler, D. Brady, W. Lötzsch, M. Fleischhauer, and J. S. Otterbach, Towards learning self-organized criticality of Rydberg atoms using graph neural networks, *ICML 2022 2nd AI for Science Workshop* (PMLR, Baltimore, Maryland, 2022).

[67] M. Mattioli, A. W. Glätzle, and W. Lechner, From classical to quantum non-equilibrium dynamics of Rydberg excitations in optical lattices, *New J. Phys.* **17**, 113039 (2015).

[68] M. Marcuzzi, M. Buchhold, S. Diehl, and I. Lesanovsky, Absorbing State Phase Transition with Competing Quantum and Classical Fluctuations, *Phys. Rev. Lett.* **116**, 245701 (2016).

[69] C. D. Mink, D. Petrosyan, and M. Fleischhauer, Hybrid discrete-continuous truncated Wigner approximation for driven, dissipative spin systems, *Phys. Rev. Res.* **4**, 043136 (2022).

3. Mean-Field Approach to Rydberg Facilitation in a Gas of Atoms at High and Low Temperatures

D. Brady and M. Fleischhauer
Physical Review A **108**, 052812 (2023)

Having understood the nuances of the Rydberg facilitation gas in the high and low temperature regimes respectively, we now tackle improving the mean field description in terms of macroscopic Langevin equations presented in Ref. [12]. In particular, these equations show a large discrepancy when compared to our Monte Carlo simulations in (i) the maximum number of excitations and (ii) the late-time dynamics in the low temperature gas.

For this, we regard the evolution of the number of Rydberg atoms ρ over time, which corresponds to the number of infected in an epidemic picture. This can be roughly separated into three regimes [86]: (i) *epidemic growth* where ρ rises rapidly as initial excitations quickly infect and spread throughout the gas, (ii) *saturation* where ρ is roughly constant as an intermediate steady-state between infection and recovery is reached, and finally (iii) *relaxation* where ρ decays back to zero. This decay results from infected individuals being immunized after recovery, or dying.

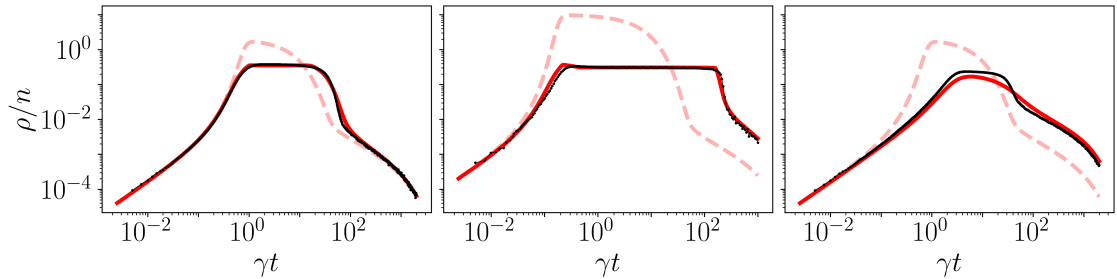


Figure 3.1.: Rydberg density over time for the cases of (left) high temperature, (center) low temperature and percolating network, and (right) low temperature and non-percolating network. The black dots are taken from Monte Carlo simulations of the Rydberg facilitation gas, the dashed red line corresponds to the mean field equations from Ref. [12] and the solid red line corresponds to our mean field equations, which take into account Rydberg blockade and the network structure.

The first discrepancy is in the maximum number of Rydberg excitations in the system. We show that Rydberg blockade sets an upper limit to the number of excitations possible in the system. In the epidemic picture this corresponds to lockdowns being in place. By simply modifying the infection rate λ to include blockade effects, we receive a fantastic agreement on the mean field level between the new Langevin equations and our Monte Carlo simulations in the high temperature regime.

For the low temperature regime, we have learned that network effects play a crucial role in the dynamics. In this regime we find the second discrepancy, namely in the late-time dynamics of ρ . We show that the infection rate λ needs to be reduced to account for the finite connectivity of the network, even in the percolating regime. We derive a new infection rate which accounts for the network structure and gives a fantastic agreement for the low temperature percolating case and a good agreement for the low temperature non-percolating case. As the latter case represents a strongly heterogeneous phase (Griffiths phase), we do not expect to find a perfect mean field description there.

Author Contributions

Contribution	Primary Role	Supportive Role
Derivation of MF equations	D.B.	M.F.
Monte Carlo simulations	D.B.	-

The project was conceived and supervised by M.F.

Copyright

Reprinted full article with permission from Daniel Brady and Michael Fleischhauer, *Physical Review A* **108**, 052812 (2023). Copyright (2023) by the American Physical Society.

Mean-field approach to Rydberg facilitation in a gas of atoms at high and low temperatures

Daniel Brady  and Michael Fleischhauer 

Department of Physics and Research Center OPTIMAS, University of Kaiserslautern-Landau, D-67663 Kaiserslautern, Germany



(Received 11 September 2023; accepted 1 November 2023; published 15 November 2023)

The excitation spread caused by Rydberg facilitation in a gas of laser-driven atoms is an interesting model system for studying epidemic dynamics. We derive a mean-field approach to describe this facilitation process in the limits of high and low temperatures, which takes into account Rydberg blockade and the network character of excitation spreading in a low-temperature gas. As opposed to previous mean-field models, our approach accurately predicts all stages of the facilitation dynamics from the initial fast epidemic growth, an extended saturation period, to the final relaxation phase.

DOI: [10.1103/PhysRevA.108.052812](https://doi.org/10.1103/PhysRevA.108.052812)

I. INTRODUCTION

Rydberg atoms have gained a lot of interest in the last few decades due to their strongly exaggerated properties. In particular, they have very long life times and strong interactions over distances covering several m [1]. These features allow Rydberg systems to be especially useful in a multitude of applications such as quantum information processing [2–6] or the study of many-body spin physics [7–14].

One interesting process in many-body Rydberg systems is Rydberg facilitation, which has been used to study dissipative or kinetically constrained spin systems [15,16], transport and localization phenomena in disordered systems [17], or self-organized criticality [18,19].

In this type of many-body system, atoms are coupled off-resonantly to a Rydberg state. As a result of the Rydberg dipole interaction, however, atoms near an already excited Rydberg atom can be excited resonantly. Thus an initial seed excitation can lead to a cascade of excitations. It has been shown experimentally that this type of system bears close similarities to epidemic dynamics [20].

The most simple description of epidemic-type systems is given by susceptible-infected-susceptible (SIS) models. Here, each individual has two internal states, susceptible (S) or infected (I). Susceptible individuals are infected with the rate κ and infected individuals return to the susceptible state with the rate γ [21–23].

Under the assumption of homogeneous mixing, where all individuals interact with each other completely at random, all information about the epidemic dynamics is contained in the total fractions ρ^v in the susceptible ($v = S$) and infected state ($v = I$), which obey the simple homogeneous mean-field equations given by [24]

$$\frac{d}{dt}\rho^I = \kappa\rho^I\rho^S - \gamma\rho^I, \quad (1a)$$

$$\frac{d}{dt}\rho^S = -\kappa\rho^I\rho^S + \gamma\rho^I. \quad (1b)$$

This system features an absorbing-state phase transition between two dynamical phases, namely, an absorbing phase in which all infections die out, and an active phase where, in the

thermodynamic limit, infections last forever. A suitable order parameter to distinguish these phases is the steady-state active (infected) density ρ_{ss}^I . From Eq. (1a) one recognizes that this phase transition occurs when

$$\rho^S\kappa = \gamma. \quad (2)$$

In addition to the SIS model, which describes diseases where repeat infections are common (predominantly sexually transmitted diseases) the susceptible-infected-recovered (SIR) model can be used to describe diseases which feature life-long immunity in individuals following an infection, such as measles or whooping cough [25]. The SIR model features a recovered state R , with the respective population as ρ^R . The dynamics are given by [26–28]

$$\frac{d}{dt}\rho^S = -\kappa\rho^I\rho^S, \quad (3a)$$

$$\frac{d}{dt}\rho^I = \kappa\rho^I\rho^S - \gamma\rho^I, \quad (3b)$$

$$\frac{d}{dt}\rho^R = \gamma\rho^I. \quad (3c)$$

The dynamics of both SIS and SIR models are well understood in the homogeneous mean-field regime. While the homogeneous mixing assumption is well justified in systems where the infection spreading occurs on a regular lattice in high spatial dimensions, it fails in many relevant cases, for example, if the the SIS-SIR dynamics take place on real-life networks. For such network systems, including, e.g., random Erdős-Rényi (ER) [29] and scale-free (SF) networks [30], a large body of more sophisticated approximation methods have been developed [31–33], but many questions remain unsolved. Here, Rydberg atoms provide a platform to experimentally investigate the epidemic dynamics on a variety of complex networks, which can, e.g., be engineered by the use of tweezer arrays [10]. Moreover, in a gas of atoms contained in some macroscopic trapping potential one can investigate the transition between a random ER network at very low temperatures, where the motion of atoms on the relevant timescales of the facilitation process can be ignored, to the homogeneous

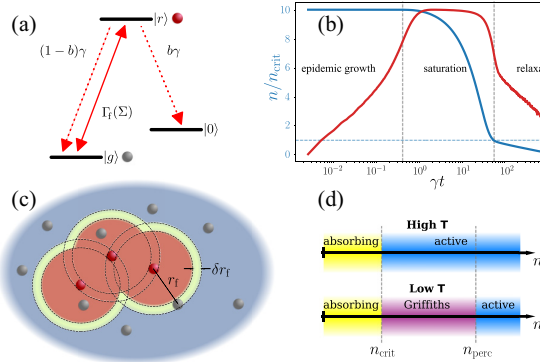


FIG. 1. (a) Level scheme of internal atomic states with ground $|g\rangle$ (susceptible) state, Rydberg $|r\rangle$ (infected) state, and inert $|0\rangle$ (recovered) state. An external laser drives the transition between $|g\rangle$ and $|r\rangle$ and spontaneous decay occurs from $|r\rangle$ to either $|g\rangle$ or $|0\rangle$, modulated by branching parameter $b \in [0, 1]$. (b) Monte Carlo data of the Rydberg density ρ (red) and total active density n (in states $|g\rangle$ and $|r\rangle$) (blue) over time, with $b = 0.3$ and initial condition $\rho(t = 0) = 0$, showing the typical epidemic stages. The blue dashed line corresponds to $n/n_{\text{crit}} = 1$. (c) Schematic of Rydberg atoms (red dots) spanning facilitation shells (yellow region) and blockade spheres (red region). Ground-state atoms (gray dots) in the blue region are subject to off-resonant laser coupling. (d) Schematic phase diagram for the high (top) and low (bottom) temperature regimes depending on the total gas density n .

mixing limit for a gas of high temperatures [34]. The latter corresponding to an annealed random network.

For Rydberg facilitation systems, each atom can be considered as a three-level system with the ground (susceptible), Rydberg (infected), and inert or ionized (recovered) states [see Fig. 1(a)]. A concrete mapping of the Rydberg facilitation system to SIS and SIR models will be discussed later. The decay from the Rydberg to the inert state, given by the rate $b\gamma$, results in a loss of susceptible and infected individuals in the population, moving the system into an absorbing state. This gives rise to three typical epidemic stages, which were experimentally observed in Rydberg facilitation systems [20]. Following an initial infection, there is a rapid epidemic growth in infected individuals, or Rydberg atoms, in the system. This is followed by a saturation and an eventual relaxation at long times as a result of the system reaching an absorbing-state on these timescales [see Fig. 1(b)].

To describe the macroscopic dynamics of the Rydberg facilitation process in a gas, a simple mean-field model was put forward in [18], which, however, fails to provide a quantitative prediction of the microscopic dynamics, accurately calculated by Monte Carlo simulations [34] (see Fig. 2). This discrepancy results from the mean-field model not regarding (i) Rydberg blockade, which prevents the excitation of any atom closer than some radius r_{blockade} to a Rydberg atom and (ii) the emergent ER network at low temperatures.

In the following, we will develop a mean-field description of the dynamics of Rydberg excitations in a many-body-facilitated gas that accounts for both of these effects and provides accurate predictions of the full facilitation dynamics, which we demonstrate by comparing our predictions with

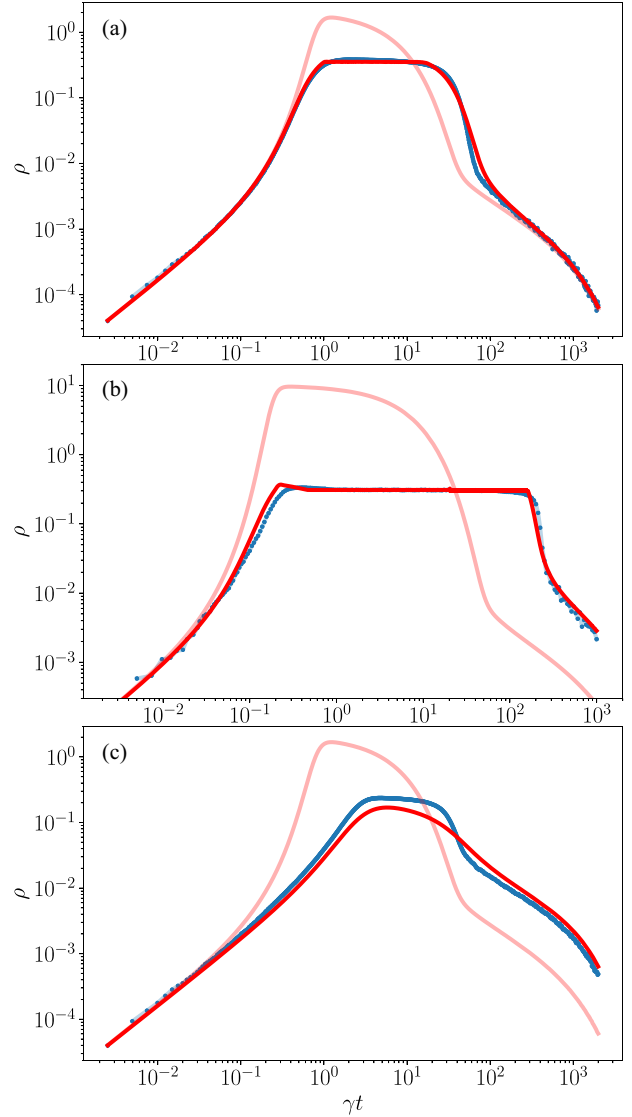


FIG. 2. Rydberg density ρ over time for $\rho(t = 0) = 0$ and $b = 0.3$ modeled with Monte Carlo simulations (blue dots), Eq. (12) (red, faint), and Eq. (33) (red, solid), for (a) high-temperature gas with starting density $n_0 = 4.0 r_f^{-3} > n_{\text{crit}}$, (b) low-temperature percolating gas with $n_0 = 20 r_f^{-3} > n_{\text{perc}}$, and (c) low-temperature nonpercolating gas with $n_0 = 4 r_f^{-3} < n_{\text{perc}}$.

Monte Carlo simulations. The network structure of the cold gas leads to a higher total gas density at very long times and subsequently a higher Rydberg density in the saturation phase in comparison to mean-field predictions. Rydberg blockade causes a significant modification of the facilitation (infection) rate if the density of Rydberg excited atoms (infected individuals) reaches some threshold value. Similarly to the effect of regulatory measures on the dynamics of epidemics (“lockdown”), it limits the maximum density of Rydberg-excited atoms (infected individuals), but at the same time leads to a substantial prolongation of the slow transition into the absorbing (recovery) phase.

II. MICROSCOPIC MODEL OF RYDBERG FACILITATION

A microscopic description of Rydberg facilitation in a gas can be achieved from a Lindblad master equation of the density matrix $\hat{\rho}$ which takes the form

$$\frac{d}{dt}\hat{\rho} = i[\hat{\rho}, \hat{\mathcal{H}}] + \sum_l \hat{L}_l \hat{\rho} \hat{L}_l^\dagger - \frac{1}{2} \{ \hat{L}_l^\dagger \hat{L}_l, \hat{\rho} \}, \quad (4)$$

with the atom-light interaction Hamiltonian $\hat{\mathcal{H}}$ given by

$$\hat{\mathcal{H}} = \sum_i \left[\Omega(\hat{\sigma}_i^{gr} + \hat{\sigma}_i^{rg}) + \left(\sum_{j \neq i} \frac{c_6}{r_{ij}^6} \hat{\sigma}_j^{rr} - \Delta \right) \hat{\sigma}_i^{rr} \right]. \quad (5)$$

Here $\hat{\sigma}_i^{\mu\nu} = |\mu\rangle_{ii}\langle\nu|$ is the projection operator of the i th atom from the internal state ν to μ . The external driving field is described by the Rabi frequency Ω and the detuning Δ , and the van der Waals interaction energy between Rydberg atoms i and j is given by c_6/r_{ij}^6 , with r_{ij} being the distance between the atoms. Finally, in Eq. (4) dissipation is described by the jump operators \hat{L}_l . These take the form $\hat{L}_1^{(i)} = \sqrt{(1-b)\gamma} \hat{\sigma}_i^{gr}$, $\hat{L}_2^{(i)} = \sqrt{b\gamma} \hat{\sigma}_i^{0r}$ for spontaneous decay from $|r\rangle$ to $|g\rangle$ and $|0\rangle$, as well as $\hat{L}_3^{(i)} = \sqrt{\gamma_\perp} \hat{\sigma}_i^{rr}$ for the dephasing of the Rydberg state. The parameter $b \in [0, 1]$ corresponds to the percentage of Rydberg atoms, which spontaneously decay to $|0\rangle$ and are thereby removed from the system. Therefore, if $b = 0$ the system corresponds to a two-level system and resembles an SIS epidemic [see Fig. 1(a)].

Dephasing results from, e.g., Doppler broadening or the spread of the atomic wave packet over the van der Waals potential [18,35]. In the large dephasing limit, the dynamics of a many-body Rydberg gas are effectively governed by classical rate equations [36]. As a result, this system can be simulated to great accuracy using Monte Carlo simulations. Starting from Eq. (4), after adiabatic elimination of coherences, one can formulate a set of rate equations for the probabilities of atom i being in the Rydberg state with $P_r^{(i)}$ or ground state with $P_g^{(i)}$ as

$$\frac{d}{dt} P_r^{(i)} = \Gamma_f(\Sigma) P_g^{(i)} - (\Gamma_f(\Sigma) + \gamma) P_r^{(i)}, \quad (6a)$$

$$\frac{d}{dt} P_g^{(i)} = (\Gamma_f(\Sigma) + (1-b)\gamma) P_r^{(i)} - \Gamma_f(\Sigma) P_g^{(i)}, \quad (6b)$$

with the stimulated excitation rate given by

$$\Gamma_f(\Sigma) = \frac{2\Omega^2 \gamma_\perp}{\gamma_\perp^2 + \Delta^2 \left(\sum_{j \neq i} \frac{r_f^6}{r_{ij}^6} - 1 \right)^2}. \quad (7)$$

Here Σ is the set of indices of Rydberg-excited atoms. If no other Rydberg atom exists in the gas or their distance is much larger than r_f , $\Gamma_f(\Sigma)$ reduces to the off-resonant excitation rate of an isolated atom

$$\tau = \frac{2\Omega^2 \gamma_\perp}{\gamma_\perp^2 + \Delta^2}. \quad (8)$$

If a Rydberg atom is present in the system, the atoms located around a certain distance to it, called facilitation distance r_f , are shifted into resonance and can be excited on a much faster timescale, given by the facilitation rate $\Gamma_f = 2\Omega^2/\gamma_\perp$. The

facilitation distance is given by

$$r_f = \sqrt{\frac{c_6}{\Delta}}. \quad (9)$$

Rydberg facilitation can be observed when $\Delta \gg \Omega$, as this naturally gives rise to a hierarchy in timescales such that

$$\Gamma_f \gg \gamma \gg \tau. \quad (10)$$

In this case, off-resonant excitations and the decay of Rydberg atoms are effectively static on the timescale of facilitated excitations. Each Rydberg atom spans a spherical shell, with distance r_f and approximate width δr_f , in which atoms are resonantly coupled to the driving laser field. The width of the facilitation shell is thereby determined by the effective linewidth of the excitation transition and reads

$$\delta r_f = \frac{\gamma_\perp}{2\Delta} r_f. \quad (11)$$

Atoms closer than $r_f - \delta r_f/2$ to a Rydberg atom are subject to Rydberg blockade [3] and cannot be excited since they are shifted out of resonance again. These three regions around a Rydberg atom (off-resonant coupling, facilitation, and blockade) can be schematically seen in Fig. 1(c).

In [18], a mean-field equation for a macroscopic description of the many-body Rydberg facilitation dynamics has been derived. For a homogeneous gas this reads

$$\frac{d}{dt} \rho = -\kappa(2\rho^2 - \rho n) - \gamma \rho - \tau(2\rho - n), \quad (12a)$$

$$\frac{d}{dt} n = -b\gamma \rho. \quad (12b)$$

Here ρ corresponds to the coarse-grained Rydberg density (in a small volume ΔV)

$$\rho(\vec{r}, t) = \frac{1}{\Delta V} \sum_{i: \vec{r}_i \in \Delta V} \langle \hat{\sigma}_i^{rr} \rangle, \quad (13)$$

and n is the density of ground and Rydberg state atoms

$$n(\vec{r}, t) = \frac{1}{\Delta V} \sum_{i: \vec{r}_i \in \Delta V} (\langle \hat{\sigma}_i^{rr} \rangle + \langle \hat{\sigma}_i^{gg} \rangle). \quad (14)$$

Note that n does not count $|0\rangle$ state atoms and therefore decreases over time if $b > 0$. The spreading rate of Rydberg excitations in the many-body gas is given by the two-body facilitation rate integrated over the facilitation shell

$$\kappa = \Gamma_f V_s, \quad (15)$$

with the volume of the facilitation shell $V_s \approx 4\pi \delta r_f r_f^2$. The above equations predict an absorbing-state phase transition between an active and absorbing phase for the critical gas density

$$n_{\text{crit}} = \frac{\gamma}{\Gamma_f V_s}. \quad (16)$$

Equation (12a) for the (mean-field) Rydberg density in the many-body gas strongly resembles the SIS equation of motion of infected individuals given by Eq. (1a). However, in contrast to SIS-SIR epidemics, Rydberg systems additionally feature (i) off-resonant excitations with rate τ , (ii) resonant (facilitated) deexcitations of Rydberg atoms [described by the

term $-2\kappa\rho^2$ in Eq. (12a)], and (iii) Rydberg blockade which is not regarded in Eq. (12a).

For the atom number conserving limit ($b = \tau = 0$) [18], Eq. (12a) directly maps to those of the SIS dynamics [Eq. (1)] by identifying $\rho^I = 2\rho$ and $\rho^S = n - 2\rho \geq 0$ with conserved total density $\rho^I + \rho^S = n - 2\rho + 2\rho = n$. Moreover in the high-temperature limit, the deexcitation can effectively be neglected as it is a second-order process in terms of Rydberg density.

For the low-temperature gas, the excitation dynamics are constrained to an ER network in which the individual nodes are comprised of atoms (either in $|g\rangle$ or $|r\rangle$), and connections between nodes, say i and j , exist if $r_{ij} \approx r_f$. The number of connections a node has (i.e., the number of atoms with distance r_f to an atom) is called the degree k of the atom. In an ER network the node degrees follow a Poissonian distribution with average degree

$$\langle k \rangle = nV_s. \quad (17)$$

An ER network features a percolation transition at $\langle k \rangle = 1$ between an (almost fully) connected network and a fragmented network, comprised of many small disconnected clusters. Here, clusters refers to a group of connected nodes. From Eq. (17), we can identify the gas density at which the percolation transition occurs as

$$n_{\text{perc}} = \frac{1}{V_s}. \quad (18)$$

This density is a factor Γ_f/γ larger than the critical density of the phase transition to the absorbing phase for a homogeneous gas [34]. A schematic phase diagram for the high- and low-temperature gas can be seen in Fig. 1(d). For further details on the mapping of the Rydberg facilitation gas to an ER network see [34].

In this paper, we model the actual many-body dynamics using Monte Carlo simulations of the rate equations (6). We assume a cubic box with length $L = 7r_f$ and periodic boundary conditions. Atom positions are chosen randomly and velocities are sampled from a Maxwell-Boltzmann distribution with temperature parameter \hat{v} , corresponding to the most probable atom velocity in the gas. For the time evolution we utilize a fixed time step Monte Carlo algorithm [37], with the time step $dt = 1/400\gamma^{-1}$, as long-range interactions paired with the fast movement of atoms in the high-temperature case results in quickly changing transitional rates in the system. To ensure numeric stability the c_6 potential in Eq. (7) is truncated at a cutoff value around the singularity $r_{ij} \rightarrow 0$.

III. MODIFIED LANGEVIN DESCRIPTION OF EPIDEMIC EVOLUTION

In the following section, we develop an effective macroscopic theory of the Rydberg facilitation process, expanding the Langevin equation (12), starting from the microscopic model. This new equation takes into account Rydberg blockade, as well as the network structure in the case of the low-temperature gas.

In Fig. 2, the dynamics of Rydberg excitations predicted by the improved Langevin equation and by Monte Carlo simulations are compared for the cases: (i) high-temperature gas with

$n_0 > n_{\text{crit}}$, (ii) low-temperature gas initially above the percolation threshold with $n_0 > n_{\text{perc}}$, and (iii) low-temperature gas initially below the percolation threshold $n_0 < n_{\text{perc}}$. Here n_0 refers to the gas density at $t = 0$. Additionally, we use a branching parameter $b = 0.3$, allowing some loss into the recovered state $|0\rangle$. Therefore, for all cases (i) to (iii), the system drives itself to the absorbing-state and follows the typical epidemic stages as seen in Fig. 1(b).

We start from the microscopic Heisenberg-Langevin equations describing the quantum many-body dynamics of Rydberg excitations for atoms at given spatial positions given by

$$\frac{d}{dt}\hat{\sigma}_i^{rr} = -i\Omega(\hat{\sigma}_i^{rg} - \hat{\sigma}_i^{gr}) - \gamma\hat{\sigma}_i^{rr} + \hat{\xi}_1, \quad (19)$$

$$\frac{d}{dt}\hat{\sigma}_i^{rg} = -i(\Omega(\hat{\sigma}_i^{rr} - \hat{\sigma}_i^{gg}) - \hat{V}_i\hat{\sigma}_i^{rg}) - \gamma_{\perp}\hat{\sigma}_i^{rg} + \hat{\xi}_2. \quad (20)$$

These equations can be obtained from the Lindblad master equation [Eq. (4)] using $\frac{d}{dt}\langle\hat{\sigma}_i^{rr}\rangle = \text{Tr}\{\hat{\sigma}_i^{rr}\frac{d}{dt}\hat{\rho}\}$ noting that for the operator dynamics a Langevin noise term $\hat{\xi}$ has to be added to conserve commutation relations [38]. These noise terms disappear in the quantum mechanical average and their properties can be obtained from the fluctuation-dissipation relation [39].

The operator \hat{V}_i describes the detuning of the i th atom and depends on the states of all other atoms. It is given by

$$\hat{V}_i = \Delta \left(-1 + \sum_{j \neq i} \frac{r_f^6}{r_{ij}^6} \hat{\sigma}_j^{rr} \right). \quad (21)$$

We note that the operator-valued quantities are objects in Hilbert space describing the quantum mechanical evolution and are subject to the classical statistics of the (time-dependent) random positions of the atoms. The dynamics of the atom positions are treated classically, which is well justified in the high-dephasing limit, assumed throughout the present paper.

Furthermore, the effect of c_6 forces acting on the center-of-mass motion of the atoms due to the distance dependence of \hat{V}_i are disregarded in the present paper. They will be discussed elsewhere in more detail [40], where we will show that, under typical experimental conditions, they can be accounted for by a change of the atoms velocity distribution and, in the case of a trapped gas, by an additional loss channel.

Assuming high dephasing $\gamma_{\perp} \geq \Omega$, the coherences $\hat{\sigma}_i^{rg}$ quickly decay to quasistationary values relative to the relevant many-body timescales. Therefore, we adiabatically eliminate coherences ($\frac{d}{dt}\hat{\sigma}_i^{rg} = 0$) and arrive at

$$\frac{d}{dt}\hat{\sigma}_i^{rr} = -\frac{2\Omega^2\gamma_{\perp}}{\gamma_{\perp}^2 + \hat{V}_i^2}(\hat{\sigma}_i^{rr} - \hat{\sigma}_i^{gg}) - \gamma\hat{\sigma}_i^{rr} + \hat{\xi}. \quad (22)$$

As a result of the quickly decaying potential \hat{V}_i with interatomic distance, only Rydberg atoms with distances $r_{ij} \leq r_f$ are relevant for the internal dynamics of atom i . Therefore, we can perform a spatially local approximation by introducing the projection operator $\hat{\Pi}_i(m)$, projecting onto m Rydberg atoms with distances $r_{ij} \leq r_f$. Using the completeness relation

$$\sum_m \hat{\Pi}_i(m) = \hat{1}, \quad (23)$$

we are able to expand the fraction in Eq. (22) giving

$$\begin{aligned} \frac{d}{dt} \hat{\sigma}_i^{rr} = & -\hat{\Pi}_i(0) \frac{2\Omega^2 \gamma_\perp}{\gamma_\perp^2 + \Delta^2} (\hat{\sigma}_i^{rr} - \hat{\sigma}_i^{gg}) \\ & - \hat{\Pi}_i(1) \underbrace{\frac{2\Omega^2 \gamma_\perp}{\gamma_\perp^2 + \Delta^2 \left(\left(\frac{r_f}{r_{li}} \right)^6 - 1 \right)^2} (\hat{\sigma}_i^{rr} - \hat{\sigma}_i^{gg})}_{(*)} \\ & + \dots \\ & - \gamma \hat{\sigma}_i^{rr} + \hat{\xi}. \end{aligned} \quad (24)$$

All rates for more than one Rydberg atom in the facilitation *sphere* ($m > 1$) are strongly suppressed due to blockade. As a result, we truncate the expansion at $m = 1$.

Finally, we calculate the expectation value of the operator $\hat{\sigma}_i^{rr}$ with a double averaging over the quantum mechanical state and the ensemble of the many different atom positions in the gas. We will denote these double averages as $\langle\langle \hat{\sigma}_i^{rr} \rangle\rangle$ and write

$$\begin{aligned} \frac{d}{dt} \langle\langle \hat{\sigma}_i^{rr} \rangle\rangle = & -\tau \langle\langle \hat{\Pi}_i(0) (\hat{\sigma}_i^{rr} - \hat{\sigma}_i^{gg}) \rangle\rangle \\ & - \Gamma_f \langle\langle \hat{\Pi}_i(1) (\hat{\sigma}_i^{rr} - \hat{\sigma}_i^{gg}) \rangle\rangle \\ & - \gamma \langle\langle \hat{\sigma}_i^{rr} \rangle\rangle \end{aligned} \quad (25)$$

$$\begin{aligned} \approx & -\tau \langle\langle \hat{\Pi}_i(0) \rangle\rangle (\langle\langle \hat{\sigma}_i^{rr} \rangle\rangle - \langle\langle \hat{\sigma}_i^{gg} \rangle\rangle) \\ & - \Gamma_f p_{\text{shell}} \langle\langle \hat{\Pi}_i(1) \rangle\rangle (\langle\langle \hat{\sigma}_i^{rr} \rangle\rangle - \langle\langle \hat{\sigma}_i^{gg} \rangle\rangle) \\ & - \gamma \langle\langle \hat{\sigma}_i^{rr} \rangle\rangle. \end{aligned} \quad (26)$$

Here we introduce the off-resonant excitation rate $\tau = \frac{2\Omega^2 \gamma_\perp}{\gamma_\perp^2 + \Delta^2}$, the facilitated excitation rate $\Gamma_f = \frac{2\Omega^2}{\gamma_\perp}$, and (assuming a randomly distributed gas) the classical probability $p_{\text{shell}} = V_s/V_f$ that the Rydberg atom is in the facilitation *shell* if it is already in the facilitation *sphere*.

With the random gas assumption, we can approximate the probabilities $\langle\langle \hat{\Pi}_i(m) \rangle\rangle$ as Poissonian with the rate ρV_f (i.e., $\langle\langle \hat{\Pi}_i(m) \rangle\rangle = (\rho V_f)^m e^{-\rho V_f} / m!$) resulting in

$$\langle\langle \hat{\Pi}_i(0) \rangle\rangle = e^{-\rho V_f}, \quad (27)$$

$$p_{\text{shell}} \langle\langle \hat{\Pi}_i(1) \rangle\rangle \equiv \frac{V_s}{V_f} \langle\langle \hat{\Pi}_i(0) \rangle\rangle = \rho V_s e^{-\rho V_f}. \quad (28)$$

We then perform the coarse-graining given by Eqs. (13) and (14) and arrive at

$$\begin{aligned} \frac{d}{dt} \rho = & -\kappa e^{-\rho V_f} \rho (2\rho - n) \\ & - \gamma \rho - \tau (2\rho - n). \end{aligned} \quad (29)$$

Furthermore, we assume here $e^{-\rho V_f} \tau \approx \tau$ as the off-resonant rate is only relevant when $\rho V_f \ll 1$.

The spreading rate of excitations κ is now exponentially damped by the density of Rydberg atoms. This gives a better description of the spreading of Rydberg excitations in the epidemic growth stage. However, as all atoms with distances closer than r_{blockade} to a Rydberg atom cannot be excited due to Rydberg blockade [red region in Fig. 1(c)], there exists a maximum density of Rydberg atoms ρ_{max} , given by the

packing density of nonoverlapping spheres, above which no more excitations are possible.

To quantify the blockade induced saturation density in the gas, we introduce the parameter η corresponding to the packing density of spheres in a given volume.

For the high-temperature gas, this corresponds to the densest packing of spheres, given by $\eta = \frac{\pi}{3\sqrt{2}} \approx 74.0\%$. In this regime we can assume this packing density to be achieved, as the high motion of the atoms allow the system to organize itself to this state.

For the frozen gas, the packing density is slightly lower, and is given by the closest density of *randomly* packed spheres, which is given by $\eta \approx 63.5\%$ [41].

As $\delta r_f \ll r_f$ we can approximate the blockade radius as $r_{\text{blockade}} \approx r_f$ and write

$$\rho_{\text{max}} = 2 \frac{\eta}{V_{\text{fac}}}, \quad (30)$$

with the approximate volume of the blockade sphere $V_{\text{fac}} = \frac{4}{3}\pi r_f^3$. The factor of 2 emerges as when a facilitation event occurs, the facilitated atom is centered on the blockade sphere of the facilitating Rydberg atom. As a result, the blockade spheres of these atoms overlap. If, however, a third Rydberg atom is facilitated (by the second Rydberg atom), its blockade sphere borders the blockade sphere of the first Rydberg atom with, on average, very little overlap [see Fig. 1(c)].

As the laser coupling smoothly changes from resonant, for an atom with distance $r = r_f$ to a Rydberg atom, to strongly suppressed for $r < r_f$, this can be regarded as a packing of soft spheres with an uncertainty in volume of $\delta V_{\text{fac}} = 4\pi \delta r_f r_f^2$. The result is a smearing out of ρ_{max} given by $\delta \rho_{\text{max}} = \delta V_{\text{fac}} \frac{2\eta}{V_{\text{fac}}^2}$. We can now add a heuristic function which sets the facilitation rate to 0 if $\rho > \rho_{\text{max}}$ as

$$h(\rho) = \frac{1}{2} \left[1 + \tanh \left(\frac{\rho_{\text{max}} - \rho}{\delta \rho_{\text{max}}} \right) \right]. \quad (31)$$

The added factors $e^{-\rho V_f}$ and $h(\rho)$ to the facilitation rate κ suffice to accurately describe the dynamics of the Rydberg density in the high-temperature gas [see Fig. 2(a)].

Moreover, the truncation of the maximum number of infected individuals as a result of blockade gives qualitative agreement with the effect of control measures such as lockdowns seen in the COVID-19 pandemic [42].

For the low-temperature gas the finite connectivity greatly reduces the facilitation rate. Taking into account that facilitation can only occur if the degree of the atom k is not 0, we alter the facilitation rate to

$$\kappa \rightarrow \kappa P(k > 0). \quad (32)$$

For an ER network with average degree $\langle k \rangle \ll 1$, we can approximate $P(k > 0) \approx \langle k \rangle$. In this case the new infection rate κ corresponds to the Kephart-White model [43,44].

The full Langevin equation for the Rydberg density reads

$$\begin{aligned} \frac{d}{dt} \rho = & -\kappa e^{-\rho V_f} h(\rho) P(k > 0) \rho (2\rho - n) \\ & - \gamma \rho - \tau (2\rho - n), \end{aligned} \quad (33)$$

with $P(k > 0) = 1 - e^{-nV_s}$ for the low-temperature gas and $P(k > 0) = 1$ at high temperatures, as the thermal velocity of atoms allows for random-mixing of all atoms. As a result, the high-temperature regime is described excellently by the classical SIS-SIR models [Eqs. (1) and (3)] with the addition of blockade.

In Fig. 2 we compare the predictions from the modified Langevin equation (33) with Monte Carlo simulations in the high-temperature gas, the frozen percolating gas, and the frozen nonpercolating gas. For the high temperature and the frozen percolating case, Eq. (33) has a very good agreement for all epidemic stages with Monte Carlo data. In particular, it predicts the correct density in the saturation stage in the high-temperature and the low-temperature percolating gas in contrast to Eq. (12).

Furthermore, for the case of the low temperature gas, Eq. (33) gives a much better approximation of the relaxation epidemic stage (i.e., for times $\gamma t \gtrsim 10^2$). In this stage, the Rydberg density is much higher than the expected MF density (predicted by the faint red line), which holds for high temperatures. In contrast to the high-temperature regime, the system leaves the active phase at much higher gas density due to the finite connectivity of excitation paths in the gas. The factor $P(k > 0)$ in the facilitation rate gives a much better approximation of this increased Rydberg density.

IV. CONCLUSION

In conclusion, we developed a modified mean-field approach to model the Rydberg density over time in a many-body gas under facilitation conditions for the limits of high and low temperature. In the low temperature regime, we additionally differentiated between a system with initial density $n_0 > n_{\text{perc}}$ and $n_0 < n_{\text{perc}}$, where n_{perc} is the percolation density below which heterogeneous effects play a large role.

Our modeling is similar to that developed in [18], but with three key improvements to the facilitation (or infection) rate κ . We consider (i) random atom positions leading to a Poissonian distribution in the number of Rydberg atoms closer than r_{blockade} to a given atom. In this case, the atom cannot be excited or deexcited due to Rydberg blockade. As a result,

with increasing Rydberg density, the global facilitation rate κ exponentially decreases.

Additionally, (ii) excited Rydberg atoms can be seen as soft spheres inside of which no atoms can be excited due to blockade. Therefore, there exists a tightest packing of excited atoms beyond which the facilitation rate κ vanishes. In the high-temperature regime, this packing density corresponds to the tightest packing of spheres in a given volume, as the high thermal velocities allow the system to continuously organize itself to this state. In the low-temperature regime the packing density is given by that of randomly placed spheres in a given volume, which, in comparison, is slightly lower.

Finally, (iii) for the low-temperature regime, one has to additionally consider the finite connectivity of the underlying network along which facilitated excitations can spread. On a mean-field level, we described this by reducing the facilitation rate in correspondence with the portion of atoms with network degree (i.e., the number of atoms in their facilitation shell) $k = 0$. The percentage of these isolated atoms increases as the network connectivity decreases, and is therefore dependent on the total density of the gas.

For both the high temperature, as well as the low temperature, high density case Eq. (33) gives excellent correspondence to Monte Carlo data for all epidemic stages.

For the low temperature, low density gas the system is characterized by strong heterogeneity making an accurate mean-field description challenging. However, for this case we still see a large improvement in the Langevin description of the dynamics.

ACKNOWLEDGMENTS

The authors thank Simon Ohler and Johannes Otterbach for fruitful discussions. Financial support from the DFG 436 through SFB TR 185, Project No. 277625399, and through the Research Group Linkage Programme of the DFG SPP 1929 GiRyd is gratefully acknowledged. The simulations were executed on the high performance cluster “Elwetritsch” at the University of Kaiserslautern, which is part of the “Alliance of High Performance Computing Rheinland-Pfalz” (AHRP). We kindly acknowledge the support of the RHRZ.

- [1] T. Gallagher, *Rydberg Atoms* (Springer, New York, 2006).
- [2] D. Jaksch, J. I. Cirac, P. Zoller, S. L. Rolston, R. Côté, and M. D. Lukin, Fast quantum gates for neutral atoms, *Phys. Rev. Lett.* **85**, 2208 (2000).
- [3] M. D. Lukin, M. Fleischhauer, R. Cote, L. M. Duan, D. Jaksch, J. I. Cirac, and P. Zoller, Dipole blockade and quantum information processing in mesoscopic atomic ensembles, *Phys. Rev. Lett.* **87**, 037901 (2001).
- [4] A. Gaetan, Y. Miroshnychenko, T. Wilk, A. Chotia, M. Viteau, D. Comparat, P. Pillet, A. Browaeys, and P. Grangier, Observation of collective excitation of two individual atoms in the Rydberg blockade regime, *Nat. Phys.* **5**, 115 (2009).
- [5] E. Urban, T. A. Johnson, T. Henage, L. Isenhower, D. Yavuz, T. Walker, and M. Saffman, Observation of Rydberg blockade between two atoms, *Nat. Phys.* **5**, 110 (2009).
- [6] M. Saffman, T. G. Walker, and K. Mølmer, Quantum information with Rydberg atoms, *Rev. Mod. Phys.* **82**, 2313 (2010).
- [7] H. Weimer, M. Müller, I. Lesanovsky, P. Zoller, and H. P. Büchler, A Rydberg quantum simulator, *Nat. Phys.* **6**, 382 (2010).
- [8] P. Schauß, M. Cheneau, M. Endres, T. Fukuhara, S. Hild, A. Omran, T. Pohl, C. Gross, S. Kuhr, and I. Bloch, Observation of spatially ordered structures in a two-dimensional Rydberg gas, *Nature (London)* **491**, 87 (2012).
- [9] H. Bernien, S. Schwartz, A. Keesling, H. Levine, A. Omran, H. Pichler, S. Choi, A. S. Zibrov, M. Endres, M. Greiner, V. Vuletić, and M. D. Lukin, Probing many-body dynamics on a 51-atom quantum simulator, *Nature (London)* **551**, 579 (2017).
- [10] A. Browaeys and T. Lahaye, Many-body physics with individually controlled Rydberg atoms, *Nat. Phys.* **16**, 132 (2020).

[11] F. M. Surace, P. P. Mazza, G. Giudici, A. Lerose, A. Gambassi, and M. Dalmonte, Lattice gauge theories and string dynamics in Rydberg atom quantum simulators, *Phys. Rev. X* **10**, 021041 (2020).

[12] P. Scholl, M. Schuler, H. J. Williams, A. A. Eberharter, D. Barredo, K.-N. Schymik, V. Lienhard, L.-P. Henry, T. C. Lang, T. Lahaye, A. M. Läuchli, and A. Browaeys, Quantum simulation of 2D antiferromagnets with hundreds of Rydberg atoms, *Nature (London)* **595**, 233 (2021).

[13] S. de Léséleuc, V. Lienhard, P. Scholl, D. Barredo, S. Weber, N. Lang, H. P. Büchler, T. Lahaye, and A. Browaeys, Observation of a symmetry-protected topological phase of interacting bosons with Rydberg atoms, *Science* **365**, 775 (2019).

[14] G. Semeghini, H. Levine, A. Keesling, S. Ebadi, T. T. Wang, D. Bluvstein, R. Verresen, H. Pichler, M. Kalinowski, R. Samajdar, A. Omran, S. Sachdev, A. Vishwanath, M. Greiner, V. Vuletić, and M. D. Lukin, Probing topological spin liquids on a programmable quantum simulator, *Science* **374**, 1242 (2021).

[15] S. Helmrich, A. Arias, and S. Whitlock, Uncovering the nonequilibrium phase structure of an open quantum spin system, *Phys. Rev. A* **98**, 022109 (2018).

[16] M. Magoni, P. Mazza, and I. Lesanovsky, Phonon dressing of a facilitated one-dimensional Rydberg lattice gas, *SciPost Physics Core* **5**, 041 (2022).

[17] M. Marcuzzi, J. Minář, D. Barredo, S. de Léséleuc, H. Labuhn, T. Lahaye, A. Browaeys, E. Levi, and I. Lesanovsky, Facilitation dynamics and localization phenomena in Rydberg lattice gases with position disorder, *Phys. Rev. Lett.* **118**, 063606 (2017).

[18] S. Helmrich, A. Arias, G. Lochead, T. M. Wintermantel, M. Buchhold, S. Diehl, and S. Whitlock, Signatures of self-organized criticality in an ultracold atomic gas, *Nature (London)* **577**, 481 (2020).

[19] D.-S. Ding, H. Busche, B.-S. Shi, G.-C. Guo, and C. S. Adams, Phase diagram and self-organizing dynamics in a thermal ensemble of strongly interacting Rydberg atoms, *Phys. Rev. X* **10**, 021023 (2020).

[20] T. M. Wintermantel, M. Buchhold, S. Shevate, M. Morgado, Y. Wang, G. Lochead, S. Diehl, and S. Whitlock, Epidemic growth and griffiths effects on an emergent network of excited atoms, *Nat. Commun.* **12**, 103 (2021).

[21] R. M. Anderson and R. M. May, *Infectious Diseases of Humans: Dynamics and Control* (Oxford University Press, New York, 1991).

[22] N. T. Bailey *et al.*, *The Mathematical Theory of Infectious Diseases and its Applications* (Charles Griffin & Company, High Wycombe, England, 1975).

[23] J. D. Murray, Epidemic models and the dynamics of infectious diseases, *Math. Biol.* **19**, 610 (1993).

[24] R. Pastor-Satorras, C. Castellano, P. Van Mieghem, and A. Vespignani, Epidemic processes in complex networks, *Rev. Mod. Phys.* **87**, 925 (2015).

[25] M. J. Keeling and K. T. Eames, Networks and epidemic models, *J. R. Soc., Interface* **2**, 295 (2005).

[26] T. Harko, F. S. Lobo, and M. Mak, Exact analytical solutions of the susceptible-infected-recovered (sir) epidemic model and of the sir model with equal death and birth rates, *Appl. Math. Comput.* **236**, 184 (2014).

[27] O. N. Bjørnstad, K. Shea, M. Krzywinski, and N. Altman, Modeling infectious epidemics, *Nature Methods* **17**, 455 (2020).

[28] R. Beckley, C. Weatherspoon, M. Alexander, M. Chandler, A. Johnson, and G. S. Bhatt, Modeling epidemics with differential equations, Tennessee State University Internal Report, 2013.

[29] P. Erdős and A. Rényi, On the evolution of random graphs, *Publ. Math. Inst. Hung. Acad. Sci.* **5**, 17 (1960).

[30] A.-L. Barabási, Scale-free networks: a decade and beyond, *Science* **325**, 412 (2009).

[31] R. Pastor-Satorras and A. Vespignani, Epidemic spreading in scale-free networks, *Phys. Rev. Lett.* **86**, 3200 (2001).

[32] R. Pastor-Satorras and A. Vespignani, Epidemic dynamics in finite size scale-free networks, *Phys. Rev. E* **65**, 035108(R) (2002).

[33] C. Durón and A. Farrell, A mean-field approximation of sir epidemics on an erdos-rényi network model, *Bull. Math. Biol.* **84**, 70 (2022).

[34] D. Brady, J. Bender, P. Mischke, T. Niederprüm, H. Ott, and M. Fleischhauer, Griffiths phase in a facilitated Rydberg gas at low temperature, [arXiv:2302.14145](https://arxiv.org/abs/2302.14145).

[35] W. Li, C. Ates, and I. Lesanovsky, Nonadiabatic motional effects and dissipative blockade for Rydberg atoms excited from optical lattices or microtraps, *Phys. Rev. Lett.* **110**, 213005 (2013).

[36] E. Levi, R. Gutiérrez, and I. Lesanovsky, Quantum non-equilibrium dynamics of Rydberg gases in the presence of dephasing noise of different strengths, *J. Phys. B: At., Mol. Opt. Phys.* **49**, 184003 (2016).

[37] V. Ruiz Barlett, J. Bigeón, M. Hoyuelos, and H. Martín, Differences between fixed time step and kinetic monte carlo methods for biased diffusion, *J. Comput. Phys.* **228**, 5740 (2009).

[38] C. Gardiner and P. Zoller, *Quantum Noise: A Handbook of Markovian and Non-Markovian Quantum Stochastic Methods with Applications to Quantum Optics* (Springer Science & Business Media, New York, 2004).

[39] R. Kubo, The fluctuation-dissipation theorem, *Rep. Prog. Phys.* **29**, 255 (1966).

[40] D. Brady and M. Fleischhauer, (unpublished).

[41] Y. Wu, Z. Fan, and Y. Lu, Bulk and interior packing densities of random close packing of hard spheres, *J. Mater. Sci.* **38**, 2019 (2003).

[42] T. Oraby, M. G. Tyshenko, J. C. Maldonado, K. Vatcheva, S. Elsaadany, W. Q. Alali, J. C. Longenecker, and M. Al-Zoughool, Modeling the effect of lockdown timing as a covid-19 control measure in countries with differing social contacts, *Sci. Rep.* **11**, 3354 (2021).

[43] J. O. Kephart and S. R. White, Directed-graph epidemiological models of computer viruses, in *Computation: The Micro and the Macro View* (World Scientific, Singapore, 1992), pp. 71–102.

[44] D. Chakrabarti, Y. Wang, C. Wang, J. Leskovec, and C. Faloutsos, Epidemic thresholds in real networks, *ACM Transactions on Information and System Security (TISSEC)* **10**, 1 (2008).

4. Anomalous Directed Percolation on a Dynamic Network Using Rydberg Facilitation

D. Brady, S. Ohler, J. Otterbach, and M. Fleischhauer

Physical Review Letters **133**, 173401 (2024)

In this study, we further build on what we learned in [P1], especially concerning the phases of the system. Here, we study the phase transitions in the system, and how they are altered by the thermal movement of atoms. We have seen the low temperature gas to behave strikingly different to the high temperature gas, as a result of the underlying network constraining excitation spread. From [P1], we know that at low temperatures and in the non-percolating regime, the absorbing-state phase transition of the system is replaced by an extended Griffiths phase. However, in the percolating regime, the absorbing-state phase transition persists. Our goal is to quantify if and how the universality class of this phase transition is affected by the gas temperature.

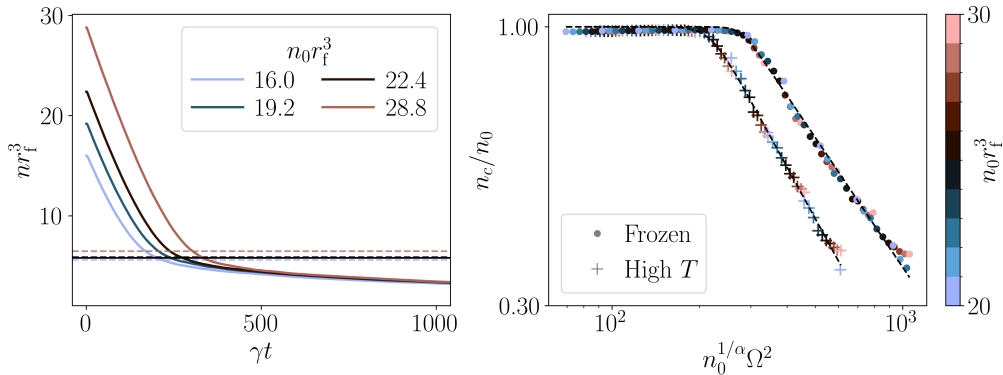


Figure 4.1.: (Left) Gas density over time self-organizing to critical point (horizontal lines) as a result of atomic losses. At the critical density, the density decay slows dramatically. (Right) Critical over initial density as a function of driving in the percolating gas. The curves collapse for different initial densities (colors) onto a single universal line, which decays as a power-law for high driving and yields the critical exponents $\beta_{\text{frozen}} \approx 0.809(13)$ for the frozen gas (dots), $\beta_{\text{high } T} = 0.996(18)$ for the high temperature gas (crosses). Within the error, these values fall in line with DP and mean field predictions respectively.

It has been shown that Rydberg facilitation systems in low-dimensional lattices, in the absence of atomic losses, belong to the *directed percolation* (DP) universality class [6, 7]. With atomic losses, Rydberg facilitation displays signatures of *self-organized criticality* (SOC) [12, 13] and it is not clear if and how these atomic losses modify the universality class of the system [12]. Universality refers to the emergence of shared behavior near criticality across different systems, irrespective of microscopic parameters. Different

classes of behavior can be distinguished by scaling relations near criticality, namely

$$\rho \sim |p - p_c|^\beta, \quad \xi_{\parallel} \sim |p - p_c|^{-\nu_{\parallel}}, \quad \xi_{\perp} \sim |p - p_c|^{-\nu_{\perp}}, \quad (4.1)$$

where ρ is the active density, ξ_{\parallel} and ξ_{\perp} are the temporal and spatial correlation lengths respectively, $|p - p_c|$ corresponds to the distance from the critical point, and β , ν_{\parallel} , and ν_{\perp} are the three critical exponents. In the experiment of Ref. [12], the authors find the exponent $\beta_{\text{exp}} = 0.910(4)$, which is in between DP universality ($\beta_{\text{DP}} \approx 0.81$) and mean field universality ($\beta_{\text{MF}} = 1.00$) predictions. They speculate that the deviation between β_{exp} and β_{DP} might arise from atomic losses and underlying SOC effects.

Using the scaling relation developed in Ref. [12], we find a universal collapse of our Monte Carlo data both at high temperatures and in the low temperature, percolating gas. Here, we find a value of the exponent β very close to the expected mean field exponent in the high temperature gas, and a value of β very close to the expected DP critical exponent in the low temperature, percolating gas. We further support this by determining the critical exponent ν_{\parallel} for the low and high temperature cases and find these to fall in line with the DP and mean field critical values of ν_{\parallel} respectively. For the low temperature, non-percolating gas, we do not find a universal collapse of data reflecting the extended Griffiths phase replacing the absorbing-state phase transition.

Our results suggest the Rydberg facilitation gas at low temperatures to fall into DP universality and at high temperatures to fall into mean field universality. However, in order to understand the exponent measured in Ref. [12], we need to look at the behavior at intermediate temperatures. Here, we find universal behavior at every temperature in between the above limits, albeit with a *continuously varying* critical exponent β . We find this to result from rare, long-range Lévy flights [121] mediated by a few, very fast atoms. Here the *anomalous directed percolation* (ADP) universality class emerges, where the critical exponents depend on the characteristic length scale of the Lévy flights [10]. We find an analytical expression for the distribution of Lévy flights dependent on the gas temperature and map a field theoretical model to approximate the critical exponent β near the mean field phase.

Following this study, we can conclude that SOC does *not* modify the universal behavior of this system. For the experimental parameters from Ref. [12], we find their temperature to be in between the DP and mean field limits, and at that temperature our simulations approximately replicate their measured exponent β_{exp} .

Author Contributions

Contribution	Primary Role	Supportive Role
Monte Carlo simulations	D.B.	S.O.
Development of machine learning algorithm	D.B.	S.O., J.O.
Mapping to Lévy flights	D.B., M.F.	S.O.

The project was conceived and supervised by M.F.

Copyright

Reprinted full article with permission from Daniel Brady, Simon Ohler, Johannes Otterbach, and Michael Fleischhauer, *Physical Review Letters* **133**, 173401 (2024). Copyright (2024) by the American Physical Society.

Anomalous Directed Percolation on a Dynamic Network Using Rydberg Facilitation

Daniel Brady¹, Simon Ohler¹, Johannes Otterbach¹, and Michael Fleischhauer¹¹Department of Physics and Research Center OPTIMAS, RPTU Kaiserslautern, D-67663 Kaiserslautern, Germany²Orthogonal Otter UG, Berlin, Germany

(Received 29 May 2024; revised 15 July 2024; accepted 16 September 2024; published 22 October 2024)

The facilitation of Rydberg excitations in a gas of atoms provides an ideal model system to study epidemic evolution on (dynamic) networks and self-organization of complex systems to the critical point of a nonequilibrium phase transition. Using Monte Carlo simulations and a machine learning algorithm we show that the universality class of this phase transition can be tuned but is robust against decay inherent to the self-organization process. The classes include directed percolation (DP), the most common class in short-range spreading models, and mean-field (MF) behavior, but also different types of anomalous directed percolation (ADP), characterized by rare long-range excitation processes. In a frozen gas, ground state atoms that can facilitate each other form a static network, for which we predict DP universality. With atomic motion the network becomes dynamic by long-range (Lévy-flight type) excitations. This leads to continuously varying critical exponents, varying smoothly between DP and MF values, corresponding to the ADP universality class. These findings also explain the recently observed critical exponent of Rydberg facilitation in an ultracold gas experiment [Helmrich *et al.*, *Nature (London)* **577**, 481 (2020)], which was in between DP and MF values.

DOI: 10.1103/PhysRevLett.133.173401

Introduction—Nonequilibrium phase transitions [1] and the dynamical self-organization of complex systems to the corresponding critical point [2,3] are key phenomena believed to be the underlying reason for the abundance of scale invariance in nature. They are characteristic for a broad spectrum of spreading processes ranging from epidemic dynamics of diseases [4,5], earthquakes [6], and forest fires [7], to neural networks [8], electric circuits, and information spreading in the internet [9]. The most relevant nonequilibrium phase transitions are those between an active and an inactive phase (absorbing state) of dynamical activity. In contrast to their equilibrium counterpart, they are much less understood. However, the behavior near the critical point shows universal features characterized by different non-equilibrium universality classes [1].

One of the most prominent such universality class is directed percolation (DP) [1], originally describing the flow of fluids through porous materials. Janssen and Grassberger conjectured that nonequilibrium transitions in *any* classical system should belong to the DP universality class if they (i) exhibit a continuous phase transition between an active and a unique absorbing state, (ii) the transition is characterized by a positive one-component order parameter, (iii) the dynamical rules involve only short-range interactions, and (iv) the system has no special attributes such as additional symmetries or quenched randomness [10,11]. To date no counterexamples to these criteria have been found [12], and DP universality has even been predicted in more general systems, e.g., with multiple absorbing states [13,14].

In spite of its the apparent generality only few experimental platforms are known for which DP behavior has unambiguously been proven.

In 2007 the first such platform was found in turbulent liquid crystals and a full set of critical exponents in $d = 2 + 1$ dimensions was measured [15,16]. Since then, interacting systems of Rydberg atoms in the facilitation regime have been suggested to study absorbing state phase transitions, for which DP universal behavior was predicted on a lattice with nearest neighbor interactions [17], and subsequently experimentally observed in a 1D gas [18]. One important aspect, relevant for the emergence of scale invariance, which these model systems lack is the effect of losses from the system. In a *number nonconserving regime* the gas density in the active phase decreases over time which drives the system to its critical point [19,20], a phenomenon called self-organized criticality (SOC) [2,3].

It is not conclusively understood if, and to which extend SOC modifies DP universality [13,19,21]. An experiment investigating Rydberg facilitation in a 3D gas, performed in this number nonconserving regime [19], showed signatures of SOC, but a deviation from DP universality. This deviation was attributed to the self-organization process, as it has been shown that losses can modify the universal properties of the phase transition and may compromise criticality altogether [21]. Specifically in sandpile models dissipation is a relevant perturbation in the renormalization group sense and any degree of bulk dissipation (in the absence of loading) breaks criticality [21,22].

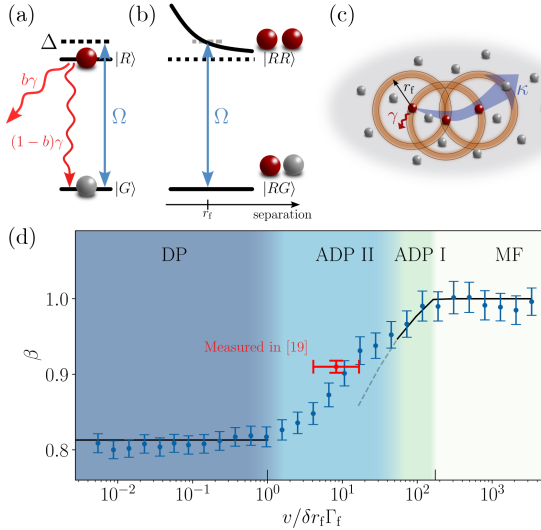


FIG. 1. (a) Single atom dynamics: ground $|G\rangle$ and Rydberg states $|R\rangle$ are laser-coupled with Rabi-frequency Ω and detuning $\Delta \gg \Omega$. $|R\rangle$ decays with rate γ and with branching $b \in [0, 1]$ out of the system. (b) Two atom scheme. Dipole interaction shifts $|RR\rangle$ into resonance at the facilitation distance r_f . (c) Schematic of spreading dynamics: Facilitation is constrained to orange shells with radius r_f and width δr_f . Spreading then occurs at effective rate κ (see main text). (d) Critical exponent β (blue dots, see main text) as a function of mean gas velocity v . Also shown is the theoretical prediction (black line, see main text), for the mean field, directed percolation, and anomalous directed percolation I regimes. Errors in β are given by the covariance matrix when fitting (see text). All points use the parameters $b = 0.3$, $\Delta/\gamma = 2000$, with varied $\Omega/\gamma \in [1, 10]$ and gas density $n_0 r_f^3 \in [20, 30]$.

Through numerical experiments and analytic considerations we show that the deviation in the Rydberg experiment is neither due to SOC [19] nor due to heterogeneity [23], but results from a violation of the Jansen-Grassberger conditions leading to a dependency of the universality class on the relative velocity of the atoms in the gas. Tuning the parameters which set the reference scale of the atomic velocity, the system can either display DP, mean-field (MF), or anomalous directed percolation (ADP) universality. In Fig. 1 numerical results for the critical exponent of the active density around the critical point can be seen as a function of the root mean square (rms) velocity of the atoms. Also shown is the critical exponent measured in [19] along with the estimated region of velocities in the experiment ranging between the average thermal velocity of the atoms and that resulting from the acceleration in the repulsive Van der Waals potential.

Several real-life spreading processes go beyond the Janssen-Grassberger conjecture. For example, the spread of diseases by flying insects in addition to direct contact violates the condition of short-range excitations [24,25]. Likewise, spreading processes often take place on

dynamical rather than static networks [26]. These often change on a timescale comparable with that of the spreading process [27].

Microscopic system—We consider a three-dimensional gas of N atoms coupled between a ground $|G\rangle$ and a Rydberg $|R\rangle$ state with a laser with Rabi frequency Ω and detuning Δ [see Fig. 1(a)]. The unitary dynamics are described by the Hamiltonian $\hat{H} = \sum_i \Omega \hat{\sigma}_i^x - \Delta \hat{\sigma}_i^{rr} + \sum_{j < i} (c_6/r_{ij}^6) \hat{\sigma}_i^{rr} \hat{\sigma}_j^{rr}$, where $\hat{\sigma}_i^{rr}$ is the projection operator of the i th atom onto its Rydberg state, c_6 is the Van der Waals coefficient for the Rydberg-Rydberg interaction potential, and $r_{ij} = |\vec{r}_i - \vec{r}_j|$ is the distance between atoms i and j .

In addition to the unitary dynamics, we account for spontaneous decay of the Rydberg state into the ground or an additional dark state $|0\rangle$ described by the jump operators $\hat{L}_{1,i} = \sqrt{(1-b)\gamma} |G\rangle_{ii} \langle R|$ and $\hat{L}_{2,i} = \sqrt{b\gamma} |0\rangle_{ii} \langle R|$, respectively. Here the parameter $b \in [0, 1]$ describes the portion of atoms lost from the system, e.g., following decay into inert states, or state-changing collisions. Finally, dephasing is accounted for by $\hat{L}_{3,i} = \sqrt{\gamma} |R\rangle_{ii} \langle R|$. Typically in Rydberg gases $\gamma \geq \Omega$, allowing classical rate equations to describe these systems to high accuracy [28].

The evolution of the N -body density matrix is given by the Lindblad master equation $(d/dt)\hat{\rho} = -i[\hat{H}, \hat{\rho}] + \hat{\mathcal{L}}(\hat{\rho})$, with the superoperator $\hat{\mathcal{L}}(\hat{\rho})$ [29]. After adiabatic elimination of coherences a set of rate equations for the occupation probabilities in Rydberg (p_r^j) and ground states (p_g^j) of the j th atom can be derived. These read

$$\frac{d}{dt} p_r^j = -(\Gamma_j + \gamma) p_r^j + \Gamma_j p_g^j, \quad \frac{d}{dt} (p_r^j + p_g^j) = -b\gamma p_r^j, \quad (1)$$

where the rate $\Gamma_j = 2\Omega^2 \gamma_{\perp} / (\gamma_{\perp}^2 + V_j^2)$ with $V_j = \Delta[-1 + \sum_{l \in \Sigma} (r_f^6 / r_{jl}^6)]$ depends on the dipole-dipole shift induced by all other Rydberg atoms denoted by Σ .

For all simulations we initiate random positions in a 3D box with length $L = 7r_f$ and periodic boundary conditions. Atom velocities are sampled from a Maxwell-Boltzmann distribution, i.e., a Gaussian in each direction, with rms velocity v . Furthermore, we use $\gamma_{\perp}/\gamma = 20$ and a Monte Carlo algorithm [30] with fixed time step $\gamma dt = 0.0025$.

For Rydberg facilitation systems, atoms are continuously driven far from resonance, i.e., $\Delta \gg \Omega$. As a result of the strong detuning, off-resonant (seed) excitations are strongly suppressed. However, in the presence of a Rydberg atom, other atoms with distance $r \approx r_f \equiv \sqrt[6]{(c_6/\Delta)}$ are shifted into resonance as a result of the vdW interaction [see Fig. 1(b)].

Consequently, atoms within a spherical shell with volume $V_s \approx 4\pi \delta r_f r_f^2$ around a Rydberg atom can be *facilitated* (i.e., excited on much faster timescales). Here $\delta r_f \approx (\gamma_{\perp}/2\Delta)r_f$ is the width of the facilitation shell. The rate of excitation for atoms within the facilitation shell is

$\Gamma_f = 2\Omega^2/\gamma_\perp$. Facilitation can also be interpreted as infection processes, with a global spreading rate $\kappa = \Gamma_f n V_s$, where n is the gas density. Spontaneous decay of Rydberg atoms back to the ground state then corresponds to recovery with rate γ .

Critical scaling—These systems feature a nonequilibrium phase transition between an absorbing phase, for $\kappa < \gamma$, with no excited atoms in the thermodynamic limit, and an active phase, for $\kappa > \gamma$, featuring widespread and infinitely long-lived activity. Near the critical driving strength $\kappa \approx \gamma$, there is universal behavior characterized by scaling relations for the Rydberg density ρ , as well as the temporal and spatial correlation lengths, ξ_{\parallel} and ξ_{\perp} , respectively,

$$\rho \sim (p - p_c)^\beta, \quad \xi_{\parallel, \perp} \sim |p - p_c|^{-\nu_{\parallel, \perp}}. \quad (2)$$

Here $p - p_c$ corresponds to the distance of the control parameter from the critical point, and β , ν_{\parallel} , ν_{\perp} are critical exponents. Finally, while seed excitations are strongly suppressed, they still occur with rate $\tau \sim 1/\Delta^2$.

In the following, we consider the system in the SOC regime, allowing Rydberg atoms to additionally decay to an inert state, effectively removing them from the system, with the rate $b\gamma$ [see Fig. 1(a)]. As a consequence, the system drives itself to the critical density given in MF approximation by $n_c = (\Delta\gamma/4\pi\Omega^2)r_f^{-3}$.

The SOC dynamics for different initial gas densities can be seen in Fig. 2(a). In the initial active phase there is a fast loss of atoms to inert states until the critical point is reached where this loss slows down substantially. To observe universal critical behavior these two timescales must be well separated [31].

Since an infinite separation of timescales is not numerically feasible, a slow decay of the density at the critical point is expected [this can be seen in Fig. 2(a)]. This, however, poses a challenge for the determination of the critical density. To this end, we trained a machine learning (ML) algorithm to predict n_c based on the time-dependent density $n(t)$ [32]. Predictions of n_c can be seen in Fig. 2(a) as horizontal dashed lines for each trajectory.

For the critical scaling we first consider the limit where the thermal movement of atoms occurs on a much slower timescale than the internal dynamics, rendering them effectively static (i.e., the thermal gas velocity is $v < \delta r_f \Gamma_f$.) In this *frozen-gas* limit, the spreading of excitations is constrained to a random Erdős-Rényi network with the average network degree $\langle k \rangle$ given by $\langle k \rangle = n V_s$ [34].

At $\langle k \rangle = 1$ a transition occurs between a nonpercolating network of ground state atoms with distance r_f , composed of many small disconnected clusters, and a percolating network with one large cluster on the order of the size of the system [35]. For $\langle k \rangle < 1$ this gives rise to a heterogeneous, nonuniversal Griffiths phase replacing the critical point. Above the percolation transition, however, i.e., $\langle k \rangle > 1$, the

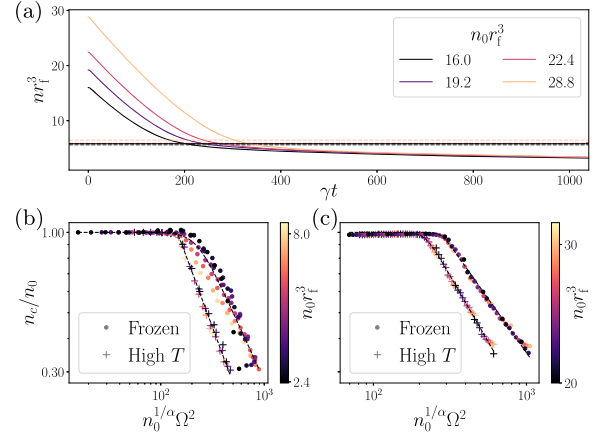


FIG. 2. (a) SOC dynamics of density of ground and Rydberg atoms in high temperature limit ($v/\delta r_f \Gamma_f = 5443$) for $b = 0.3$, $\Omega/\gamma = 3.7$, and $\Delta/\gamma = 1000$, with varied n_0 showing self-organized criticality to a single density n_c . Machine learning predictions of the critical density for each trajectory (horizontal dashed lines) and n_c (horizontal solid black line). (b) ML predictions of critical density n_c normalized by initial density n_0 depending on the rescaled driving (see main text) for (b) the nonpercolating gas, $\langle k \rangle < 1$ (left) and (c) for the percolating gas, $\langle k \rangle > 1$ (right) for both frozen ($v/\delta r_f \Gamma_f = 0$) and high temperature ($v/\delta r_f \Gamma_f = 5443$) limits. The exponent α is tuned until all data points collapse. For the frozen, nonpercolating gas no collapse can be found.

absorbing-state phase transition is recovered [34,36]. (The SOC dynamics do not change the Erdős-Rényi character of the network, but only lead to a reduction of $\langle k \rangle$).

At high gas temperatures the continuous mixing of atomic positions and subsequent fast decay of spatial correlations leads to mean field behavior regardless of $\langle k \rangle$ [37].

An unambiguous signature of universal behavior and a precise method for the classification into a certain universality class is the collapse of data obtained over a large parameter range onto specific scaling functions. Following Ref. [19], we consider the density of atoms in active states (i.e., in the ground and Rydberg state, but not in the inert state) at the critical point n_c , normalized to the initial density n_0 as a function of the generalized driving strength $\Omega^2 n_0^{1/\alpha}$, with α being tuned until all data points collapse onto a single curve. Scale invariance requires

$$\frac{n_c}{n_0} = f\left(\Omega^2 n_0^{1/\alpha}\right) \quad (3)$$

to hold over the entire parameter range, with a scaling function $f(x)$, which can be chosen as $f(x) = x_c^\beta (x^{\mu\beta} + x_c^{\mu\beta})^{-1/\mu}$ [19], where x_c and μ are free parameters defining the position and sharpness of the critical point. Finally, β corresponds to the critical exponent from Eq. (2).

For both high temperature and frozen limits, the results are plotted in Figs. 2(b) and 2(c) for $\langle k \rangle < 1$ and $\langle k \rangle > 1$, respectively. For the high temperature limit we receive a collapse of all data points onto a single power-law using $\alpha = 1.08(1)$ ($\langle k \rangle < 1$) and $\alpha = 1.26(1)$ ($\langle k \rangle > 1$). We then extract the critical exponents $\beta_{\text{low}} \langle k \rangle = 1.049(19)$ and $\beta_{\text{high}} \langle k \rangle = 0.996(18)$, respectively, which both fall in line with the expected mean field exponent $\beta_{\text{MF}} = 1.00$. Errors are calculated from the covariance matrix of the fit parameters.

For the low temperature regime, on the other hand, [dots in Figs. 2(b) and 2(c)] we find no collapse of data below the percolation threshold, i.e., $\langle k \rangle < 1$, for values of $\alpha \in [0.5, 2.0]$, indicating nonuniversal behavior which is consistent with a heterogeneous Griffiths phase [34]. For $\langle k \rangle > 1$, however, the data collapse onto a single power-law for $\alpha = 0.88(1)$, with the slope clearly differing from the high temperature one. Furthermore, when using the above mentioned fit function we obtain the power-law exponent $\beta_{\text{frozen}} = 0.809(13)$, very close to the expected 3D DP critical exponent $\beta_{\text{DP}} \approx 0.813$ [12].

To unambiguously confirm DP and MF universality in the low and high temperature limits, we also determine the critical exponent ν_{\parallel} governing temporal correlations around the critical point. We find a good agreement with literature values. A detailed analysis including numerical results can be found in Supplemental Material [32].

Anomalous directed percolation—From the above discussion one would naively expect that there is a critical value of the mean gas velocity where a phase transition between DP and MF behavior takes place. Astonishingly however, we find for gas temperatures between the two limits (and $\langle k \rangle > 1$) a universal collapse of data points with a *monotonously changing critical exponent* β over multiple orders of magnitude in the rms gas velocity [Fig. 1(d)].

Increasing the temperature the system leaves the DP regime at rather low velocities corresponding to the (very small) width of the facilitation shell per facilitation time, i.e., $v_- = \delta r_f \Gamma_f$ (left mark in Fig. 1). This is due to the number of ground-state atoms that can be facilitated by a single Rydberg atom increasing once this velocity is exceeded. On the other hand, for velocities greater than $v_+ = r_f \Gamma_f$, i.e., when an atom flies distances larger than the facilitation distance in the facilitation time, the network character of (ground) state atoms becomes completely washed out (right mark in Fig. 1).

In the following we show that the critical behavior with continuously varying β in the velocity range between these two limiting values is a signature of ADP universality, resulting from effective long-range spreading processes and heavy-tailed waiting time distributions [38].

Absorbing-state phase transitions in complex systems where excitation distances follow a Lévy flight distribution for large r as

$$P(r) \sim \frac{1}{r^{d+\sigma}}, \quad (4)$$

where d is the dimension and σ is a free parameter, no longer fulfill the Janssen-Grassberger conjecture if σ becomes too small. Such systems, however, still show universal behavior, albeit with continuously varying critical exponents depending on the value of σ [12,38]. The same is true if the distribution of time intervals between successive excitations [i.e., waiting time distribution $P(\delta t)$] is heavy tailed. In general, the algebraic spatial and temporal distributions effectively reduce the upper critical dimension, and the critical exponents approach the MF values.

In the frozen gas limit each atom is confined to a cluster and has k atoms in its facilitation shell, with k given by a Poissonian distribution as $P(k) = [(nV_s)^k / k!] e^{-nV_s}$. With increasing thermal velocity, the probability that an atom finds another connection outside of its original cluster increases. Since the underlying network is a random network, even small distances in real space can correspond to completely new connections, i.e., very distant jumps in the network.

For an initially excited Rydberg atom with velocity v , the distribution of distances to the next facilitated atom can be seen in Fig. 3(a), where the dots are from MC simulations. Outside of the facilitation shell (vertical black dashed line), we find that this probability decays as a power-law with an exponent σ decreasing with increasing atom velocity. For large distances around v/Γ_f the excitation probability is exponentially truncated.

This distribution can be described analytically outside of the facilitation shell by

$$P(r) = 2\pi\xi r \int_0^\pi d\theta \frac{e^{-\xi(\sqrt{\cos^2\theta+r^2-1}-\cos\theta)}}{\sqrt{\cos^2\theta+r^2-1}}, \quad (5)$$

with $\xi = (\langle k \rangle / \delta r_f)(1 - e^{-\delta r_f \Gamma_f / v})$ [black solid line in Fig. 3(a)]. The derivation of Eq. (5) can be found in the Supplemental Material [32].

In 3D systems, (long-range) MF behavior occurs for $\sigma < 1.5$ [lower black dashed line in Fig. 3(b)], while for $\sigma > 2.118(17)$ regular DP behavior is expected [upper black dashed line in Fig. 3(b)] [12]. In between these limits, the long range interactions are prevalent enough to disrupt DP universality, but not strong enough to suppress all correlations. Here, the system is governed by a family of continuously varying universality classes (ADP), labeled by the long-range parameter σ [12].

Fitting the spatial distribution of excitation distances with an exponentially truncated power-law $f(x) = c_1 x^{-c_2} e^{-c_3 x}$, with $c_2 = \sigma - 1$ [as $P(\vec{r}) d^3 r = P(r) 4\pi r^2 dr$], we receive very good agreement between the data and the fit function [dashed lines in Fig. 3(a)]. From this we can extract the power-law slope $\sigma(v)$ governing the flight

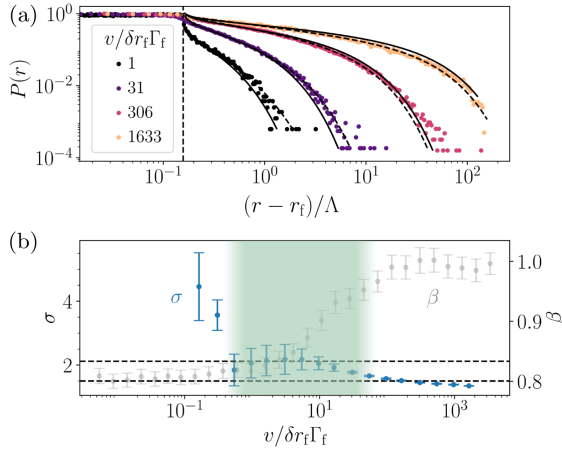


FIG. 3. (a) Distribution of distances between excitations in units of mean free path Λ for different rms gas velocities v . Half width of facilitation shell is given by vertical gray dashed line. The black dashed lines are combined power-law and exponential fits and the black solid lines are analytical predictions given by Eq. (5). (b) Power-law exponent σ (blue) of excitation distance distribution [from fit in (a)] and field theoretical limits of ADP (horizontal dashed lines), as well as critical scaling exponent β (gray) continuously changing between MF and DP plateaus for gas velocities where σ is within ADP bounds. In the green shaded region the distribution of times between excitations deviates from exponential. Both plots use $\Omega/\gamma = 20$, $\Delta/\gamma = 2000$, $n_0 r_f^3 = 20$.

distance distribution depending on the thermal gas velocity seen in Fig. 3(b).

For the distribution of times between excitations (see Supplemental Material [32]), we find a deviation from a pure exponential distribution for gas velocities in the interval $v/\delta r_f \Gamma_f \in [0.5, 50.0]$. In this regime [reflected by the green shaded region in Fig. 3(b)], spatial and temporal long-range processes are relevant.

For gas velocities in the interval $v/\delta r_f \Gamma_f \in [50, 160]$, we find an exponential waiting time distribution, but a spatial power-law distribution with $\sigma > 1.5$, giving rise to the ADP I regime [1]. Here the critical exponents β and ν_{\parallel} can be field theoretically approximated in perturbation theory to one-loop order, which yields [12] for $\sigma > 1.5$

$$\beta = 1 - 2 \frac{2\sigma - 3}{7\sigma}, \quad \nu_{\parallel} = 1 + \frac{2\sigma - 3}{7\sigma^2}, \quad (6)$$

and $\beta = \nu_{\parallel} = 1$ for $\sigma \leq 1.5$. For gas velocities $v/\delta r_f \Gamma_f \gtrsim 50$ we see a very good agreement between the field theoretical approximation of $\beta[\sigma(v)]$ and our simulation results (black line in Fig. 1). With decreasing velocity, i.e., entering the ADP II regime, the field theoretical predictions begin to diverge (gray dashed line in Fig. 1) resulting from the nonexponential distribution in waiting times and the failure of the perturbation expansion.

Conclusion—Systems of facilitated Rydberg excitations form an accessible experimental platform to investigate nonequilibrium dynamics. Using Monte Carlo simulations we discover the existence of rare Lévy-flight type excitations which, if prevalent enough, can alter the universality class of the nonequilibrium phase transition in the system. This deviation from directed percolation universality was previously assumed to be a result of self-organized criticality. However, for low temperatures we find critical exponents which coincide with DP universality while the system also displays SOC.

One important aspect is whether all universality classes can be experimentally realized. For typical ultracold Rydberg gases temperatures below $1 \mu\text{K}$ [39] are reachable. The critical temperature to reach the DP regime is given by $v_- = \delta r_f \Gamma_f \equiv (\kappa/4\pi r_f^2)$ (explicitly $T_- = (mk/3k_B)4\pi r_f^2$, with the atom mass m). For the parameters used in [19] this becomes $T_- \approx 7 \mu\text{K}$.

Acknowledgments—Financial support from the DFG through SFB TR 185, Project No. 277625399, is gratefully acknowledged. The authors also thank the Allianz für Hochleistungsrechnen (AHRP) for giving us access to the “Elwetritsch” HPC Cluster.

- [1] H. Hinrichsen, Non-equilibrium critical phenomena and phase transitions into absorbing states, *Adv. Phys.* **49**, 815 (2000).
- [2] P. Bak, C. Tang, and K. Wiesenfeld, Self-organized criticality, *Phys. Rev. A* **38**, 364 (1988).
- [3] P. Bak, *How Nature Works: The Science of Self-Organized Criticality* (Springer Science & Business Media, New York, 2013).
- [4] N. T. Bailey *et al.*, *The Mathematical Theory of Infectious Diseases and its Applications* (Charles Griffin & Company Ltd., Bucks, 1975).
- [5] R. Pastor-Satorras, C. Castellano, P. Van Mieghem, and A. Vespignani, Epidemic processes in complex networks, *Rev. Mod. Phys.* **87**, 925 (2015).
- [6] A. Sornette and D. Sornette, Self-organized criticality and earthquakes, *Europhys. Lett.* **9**, 197 (1989).
- [7] B. Drossel and F. Schwabl, Self-organized critical forest-fire model, *Phys. Rev. Lett.* **69**, 1629 (1992).
- [8] N. Friedman, S. Ito, B. A. W. Brinkman, M. Shimono, R. E. Lee DeVille, K. A. Dahmen, J. M. Beggs, and T. C. Butler, Universal critical dynamics in high resolution neuronal avalanche data, *Phys. Rev. Lett.* **108**, 208102 (2012).
- [9] L. A. Adamic and B. A. Huberman, Power-law distribution of the world wide web, *Science* **287**, 2115 (2000).
- [10] H.-K. Janssen, On the nonequilibrium phase transition in reaction-diffusion systems with an absorbing stationary state, *Z. Phys. B Condens. Matter* **42**, 151 (1981).
- [11] P. Grassberger, On phase transitions in Schrödiger's second model, *Z. Phys. B Condens. Matter* **47**, 365 (1982).
- [12] H. Hinrichsen, Non-equilibrium phase transitions, *Physica (Amsterdam)* **369A**, 1 (2006).

[13] M. A. Muñoz, G. Grinstein, R. Dickman, and R. Livi, Critical behavior of systems with many absorbing states, *Phys. Rev. Lett.* **76**, 451 (1996).

[14] M. Muñoz, G. Grinstein, and R. Dickman, Phase structure of systems with infinite numbers of absorbing states, *J. Stat. Phys.* **91**, 541 (1998).

[15] K. A. Takeuchi, M. Kuroda, H. Chaté, and M. Sano, Directed percolation criticality in turbulent liquid crystals, *Phys. Rev. Lett.* **99**, 234503 (2007).

[16] K. A. Takeuchi, M. Kuroda, H. Chaté, and M. Sano, Experimental realization of directed percolation criticality in turbulent liquid crystals, *Phys. Rev. E* **80**, 051116 (2009).

[17] M. Marcuzzi, E. Levi, W. Li, J. P. Garrahan, B. Olmos, and I. Lesanovsky, Non-equilibrium universality in the dynamics of dissipative cold atomic gases, *New J. Phys.* **17**, 072003 (2015).

[18] R. Gutiérrez, C. Simonelli, M. Archimi, F. Castellucci, E. Arimondo, D. Ciampini, M. Marcuzzi, I. Lesanovsky, and O. Morsch, Experimental signatures of an absorbing-state phase transition in an open driven many-body quantum system, *Phys. Rev. A* **96**, 041602(R) (2017).

[19] S. Helmrich, A. Arias, G. Lochead, T. Wintermantel, M. Buchhold, S. Diehl, and S. Whitlock, Signatures of self-organized criticality in an ultracold atomic gas, *Nature (London)* **577**, 481 (2020).

[20] D.-S. Ding, H. Busche, B.-S. Shi, G.-C. Guo, and C. S. Adams, Phase diagram and self-organizing dynamics in a thermal ensemble of strongly interacting Rydberg atoms, *Phys. Rev. X* **10**, 021023 (2020).

[21] J. A. Bonachela and M. A. Muñoz, Self-organization without conservation: True or just apparent scale-invariance?, *J. Stat. Mech.* (2009) P09009.

[22] K. B. Lauritsen, S. Zapperi, and H. E. Stanley, Self-organized branching processes: Avalanche models with dissipation, *Phys. Rev. E* **54**, 2483 (1996).

[23] T. M. Wintermantel, M. Buchhold, S. Shevate, M. Morgado, Y. Wang, G. Lochead, S. Diehl, and S. Whitlock, Epidemic growth and Griffiths effects on an emergent network of excited atoms, *Nat. Commun.* **12**, 103 (2021).

[24] D. Mollison, Spatial contact models for ecological and epidemic spread, *J. R. Stat. Soc. Ser. B* **39**, 283 (1977).

[25] P. Grassberger, *Fractals in Physics*, edited by L. Pietronero and E. Tosatti (Elsevier, New York, 2012).

[26] P. Holme and J. Saramäki, Temporal networks, *Phys. Rep.* **519**, 97 (2012).

[27] K. Zhao, M. Karsai, and G. Bianconi, Entropy of dynamical social networks, *PLoS One* **6**, e28116 (2011).

[28] E. Levi, R. Gutiérrez, and I. Lesanovsky, Quantum non-equilibrium dynamics of Rydberg gases in the presence of dephasing noise of different strengths, *J. Phys. B* **49**, 184003 (2016).

[29] G. Lindblad, On the generators of quantum dynamical semigroups, *Commun. Math. Phys.* **48**, 119 (1976).

[30] V. R. Barlett, J. Bigéon, M. Hoyuelos, and H. Martín, Differences between fixed time step and kinetic Monte Carlo methods for biased diffusion, *J. Comput. Phys.* **228**, 5740 (2009).

[31] D. Marković and C. Gros, Power laws and self-organized criticality in theory and nature, *Phys. Rep.* **536**, 41 (2014).

[32] See Supplemental Material at <http://link.aps.org/supplemental/10.1103/PhysRevLett.133.173401>, which includes Ref. [33] for a description of the machine learning algorithm, a derivation of Eq. (5), as well as a discussion on further distributions and critical exponents.

[33] P. J. Huber, Robust estimation of a location parameter, *Ann. Math. Stat.* **35**, 73 (1964).

[34] D. Brady, J. Bender, P. Mischke, S. Ohler, T. Niederprüm, H. Ott, and M. Fleischhauer, Griffiths phase in a facilitated Rydberg gas at low temperatures, *Phys. Rev. Res.* **6**, 013052 (2024).

[35] P. Erdős and A. Rényi, On the evolution of random graphs, *Publ. Math. Inst. Hung. Acad. Sci.* **5**, 17 (1960).

[36] M. A. Muñoz, R. Juhász, C. Castellano, and G. Ódor, Griffiths phases on complex networks, *Phys. Rev. Lett.* **105**, 128701 (2010).

[37] D. Brady and M. Fleischhauer, Mean-field approach to Rydberg facilitation in a gas of atoms at high and low temperatures, *Phys. Rev. A* **108**, 052812 (2023).

[38] H. Hinrichsen, Non-equilibrium phase transitions with long-range interactions, *J. Stat. Mech.* (2007) P07006.

[39] A. D. Bounds, N. C. Jackson, R. K. Hanley, R. Faoro, E. M. Bridge, P. Huillery, and M. P. A. Jones, Rydberg-dressed magneto-optical trap, *Phys. Rev. Lett.* **120**, 183401 (2018).

Supplementary Material

Anomalous Directed Percolation on a Dynamic Network using Rydberg Facilitation

Machine Learning the Critical Density

In the following we detail the machine learning (ML) algorithm used to determine the critical density n_c from the time-dependent total density $n(t)$ (ground and Rydberg state atoms) as the system drives towards (and beyond) the critical point.

Upon the system reaching its critical density, the total density continues to decay as a result of a finite separation of time-scales in the system (see Fig. 2a in the main text), which makes the unambiguous determination of the true critical point difficult. For the case of high gas temperatures, specifically an average thermal velocity $v/\delta r_f \Gamma_f = 5443$, the dynamics of the system are accurately described by mean field equations [36]. For the mean field limit the critical density n_c is given by $n_c = \frac{\Delta \gamma}{4\pi\Omega^2} r_f^{-3}$ (see main text).

We train the ML algorithm on data in the mean field regime by passing it a sub-sampled vector X , consisting of 100 density values from $n(t)$, which are equally spaced in time. The times are spaced in the interval $\gamma t \in [0, 2000]$ and have a spacing of $\gamma \delta t = 20$. All training trajectories use $v/\delta r_f \Gamma_f = 5443$ and are the average of 50 Monte-Carlo runs. As all training data is in the percolating limit, the system consists of roughly 10^4 atoms, resulting in a fast convergence of Monte-Carlo simulations.

In total, the algorithm is trained using 5866 trajectories, each with a unique combination of Ω and n_0 . The algorithm outputs $Y \in [0, 1]$ and predicts $\bar{Y} \equiv n_c(\Omega)/n_0$ for $n_c < n_0$ and $\bar{Y} \equiv 1$ for $n_c \geq n_0$, where we found a modified Huber-Loss function [39] to give the most accurate predictions. This is defined as

$$L_\Delta(Y - \bar{Y}) = \begin{cases} 100 \times \frac{1}{2} \frac{|Y - \bar{Y}|^2}{\bar{Y}}, & |Y - \bar{Y}| \leq \Delta \\ 100 \times \frac{\Delta}{2} \frac{|Y - \bar{Y}|}{\bar{Y}}, & |Y - \bar{Y}| > \Delta \end{cases}. \quad (1)$$

Using $\Delta = 1$ yields an average percentage error of 4 % between the predicted critical density and the mean field value. After successfully training the algorithm in the MF regime, we apply the algorithm to determine n_c/n_0 for arbitrary v .

Analytical Description of Lévy Flights

The heavy-tailed distribution of excitation distances $P(r)$ is caused by atomic motion as we will show in the following. To this end we describe the distribution considering the distance z a Rydberg atom would cover before facilitating another atom. By discretizing space into infinitesimal steps δz we can write the probability that the excitation happens *after* at least J steps as $P(X > J) = (1 - p_{\text{exc}})^J$. Here p_{exc} is the excitation probability in a given time interval $\delta t = \delta z/v$. As the number of atoms in the facilitation shell of a Rydberg atom in $t + \delta t$ are given by the Poissonian distribution, the excitation probability reads $p_{\text{exc}} = \sum_{k=0}^{\infty} P(k)(1 - (1 - p_{\uparrow})^k)$, i.e.

$$p_{\text{exc}} = 1 - \exp\left\{-\langle k \rangle \frac{\delta z}{\delta r_f} (1 - e^{-\delta r_f \Gamma_f / v})\right\}, \quad (2)$$

with the excitation probability in a single time step $p_{\uparrow} = 1 - e^{-\Gamma_f \delta t}$. Inserting (2) into $P(X \geq J)$ and taking the limit $\delta z \rightarrow 0$ for fixed $z = J\delta z$, we receive an exponential distribution $f_Z(z) = \xi e^{-\xi z}$, with $\xi = \langle k \rangle / \delta r_f (1 - e^{-\delta r_f \Gamma_f / v})$. After the Rydberg atom flies the distance z , an atom is facilitated in a random position around it with distance r_f , i.e. in spherical coordinates with uniformly distributed random variables $\theta \in [0, \pi]$ and $\varphi \in [0, 2\pi]$, as well as a fixed $r \equiv r_f$. The probability distribution of the distance from the initial position of the Rydberg to the position where the first atom is facilitated is given by

$$P(r) = 2\pi\xi r \int_0^\pi d\theta \frac{e^{-\xi(\sqrt{\cos^2 \theta + r^2 - 1} - \cos \theta)}}{\sqrt{\cos^2 \theta + r^2 - 1}}, \quad (3)$$

where $\vec{r} = r_f \hat{e}_r(\theta, \varphi) + (0, 0, z)^T$. In eq. (3) the distribution is given up to a numerically solvable integral and the solution can be seen as the black solid lines in Fig. 4a in the main text. We see an excellent agreement between the distribution given by eq. (3) and the numerical data.

Critical Exponent δ in the Number Conserving Regime

In the following we determine the critical exponent $\delta = \beta/\nu_{\parallel}$ for low and high temperature limits. To this end, we consider the decay of excitations from the fully excited state $\rho(t=0) = n(t=0)$, in the number conserving case, i.e. $b = \tau = 0$.

For the case of weak driving, i.e. in the absorbing phase $\kappa < \gamma$, a pure exponential decay to $\rho(t \rightarrow \infty) = 0$ is expected, while for strong driving, i.e. in the active phase $\kappa > \gamma$, a non-zero steady state density emerges [12] $\rho(t \rightarrow \infty) > 0$. At the critical driving strength, i.e. $\kappa = \kappa_c = \gamma$, there is a power-law decay in the active density of the form $\rho \sim t^{-\delta}$ with the exponent $\delta = \beta/\nu_{\parallel}$. For contact processes on networks, the critical driving strength is expected to be slightly larger however, i.e. $\kappa_c \gtrsim \gamma$ [35]. For MF $\delta = \beta = \nu_{\parallel} = 1$, whereas for 3D DP universality one expects a less steep slope with exponent $\delta \approx 0.732$, since $\nu_{\parallel}^{\text{DP}} = 1.11(1)$, see e.g. Ref. [1].

In Fig. S1 we see this expected behavior with an intermediate power-law for the driving strength $\kappa(\Omega, n_0) = \kappa_c$, which is exponentially truncated as a result of finite size effects. For the high temperature limit we receive $\delta = 1.0(1)$ with the literature value being $\delta_{\text{MF}} = 1.00$; and for the frozen gas we receive $\delta = 0.65(10)$ with the literature value being $\delta_{\text{DP}} \approx 0.73$. The behavior around the critical driving strength is very sensitive to the Rabi frequency Ω , which is reflected in the rather large error margins in δ . Still, we find a good agreement with the DP and MF predictions of δ and a clear difference between the values δ takes in the two limits.

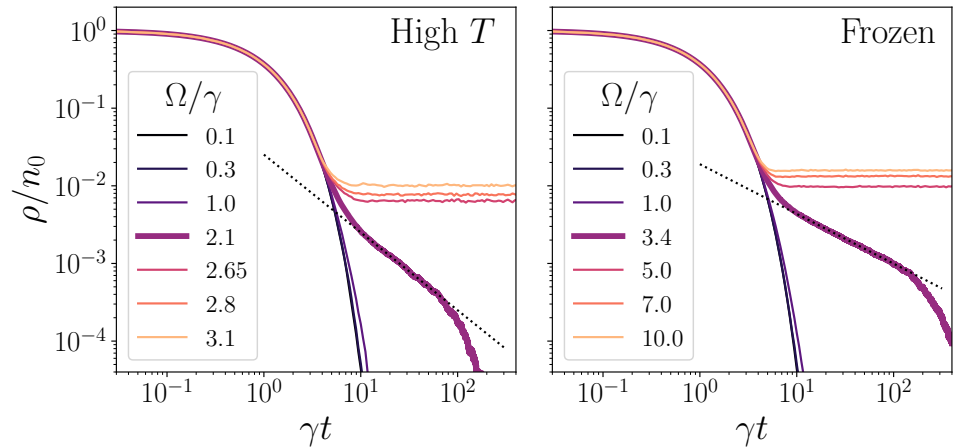


FIG. S1: Decay of the density of excited atoms over time taken from Monte-Carlo simulations with all atoms initially excited $\rho(t=0) = n_0$ with varying driving Ω with $n_0 \tau_f^3 = 20$ for high temperature ($v/\delta r_f \Gamma_f = 5443$, left) and the frozen gas ($v/\delta r_f \Gamma_f = 0$, right). Both plots display an absorbing state phase transition with exponential decay for $\kappa < \kappa_c \approx \gamma$, decay to a steady state for $\kappa > \kappa_c$ and power-law decay for $\kappa = \kappa_c$. The dashed lines represent a power-law decay with exponent $\delta = 1.0(1)$ (left) and $\delta = 0.65(10)$ (right). Furthermore we use $\Delta/\gamma = 1000$ and $b = 0$.

Waiting Time Distribution

In addition to the spatial distribution of excitations discussed in the main text, the temporal distribution plays an important role in determining the universality class of the underlying phase transition. For mean gas velocities in the interval $v/\delta r_f \Gamma_f \in [0.5, 50]$ we find a deviation from an exponential distribution in the waiting times (central plot in Fig. S2). In particular, we find an exponentially truncated power-law distribution making long waiting times much more likely when compared to the pure exponential distribution (see Fig. S2). Consequently, systems with spatial and temporal long-range interactions generically fall into a mixed anomalous directed percolation (called ADP II in the main text) universality class differing from anomalous directed percolation (called ADP I in the main text) [12]. In particular the field-theoretical approximations for the critical exponents (given by eq. (6) in the main text) no longer hold in this regime.

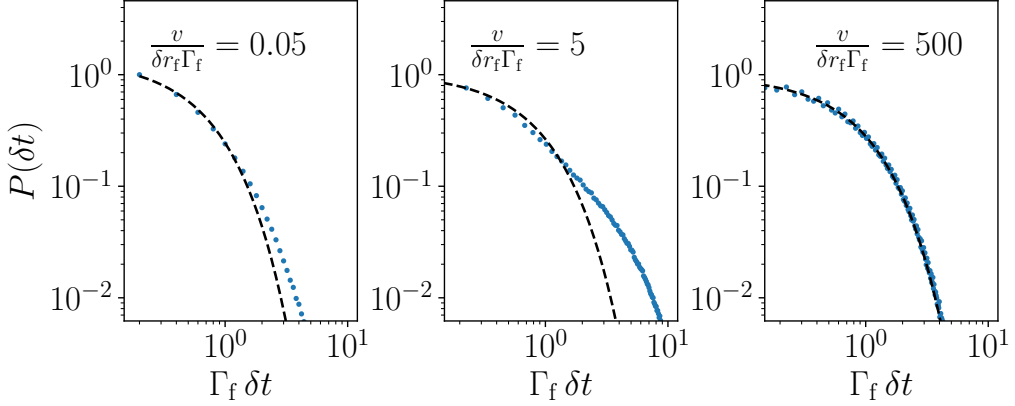


FIG. S2: Distribution of times δt taken from Monte-Carlo simulations (blue dots) until the first facilitation event occurs from an initial seed for different gas velocities v and exponential fit (black dashed lines). All plots are in the percolating regime, i.e. $\langle k \rangle > 1$ and use $\Omega/\gamma = 20$, $\Delta/\gamma = 2000$, $n_0 r_f^3 = 20$.

[1] H. Hinrichsen, Non-equilibrium critical phenomena and phase transitions into absorbing states, *Advances in physics* **49**, 815 (2000)

[12] H. Hinrichsen, Non-equilibrium phase transitions, *Physica A: Statistical Mechanics and its Applications* **369**, 1 (2006)

[35] M. A. Muñoz, R. Juhász, C. Castellano, and G. Ódor, Griffiths phases on complex networks, *Physical Review Letters* **105**, 128701 (2010)

[36] D. Brady and M. Fleischhauer, Mean-field approach to rydberg facilitation in a gas of atoms at high and low temperatures, *Physical Review A* **108**, 052812 (2023).

[39] P. J. Huber, Robust Estimation of a Location Parameter, *The Annals of Mathematical Statistics* **35**, 73 (1964)

5. Nonequilibrium Universality of Rydberg-Excitation Spreading on a Dynamic Network

S. Ohler, D. Brady, P. Mischke, J. Bender, H. Ott, T. Niederprüm, W. Ripken, J. S. Otterbach, and M. Fleischhauer

Physical Review Research **7**, 033167 (2025)

This constitutes our final study of the Rydberg facilitation gas. Here, we once again investigate the temperature dependent universality class transition from *directed percolation (DP)* via *anomalous directed percolation (ADP)* to mean field universality, discovered in [P3]. The phase transition is characterized by three critical exponents β , ν_{\parallel} , and ν_{\perp} , each corresponding to a different type of scaling behavior in the vicinity of the critical point. In Ref. [10], these exponents were mapped to the distribution of areas, sizes, and durations of *avalanches* - short bursts of activity - at the critical point. Avalanches represent one of the prime experimentally accessible quantities of absorbing-state phase transitions. These quantities are power-law distributed near the critical point, i.e. they follow $P(\nu) \sim \nu^{-\tau_{\nu}}$, with $\nu \in \{a, s, t\}$ (area, size, and time). The *avalanche exponents* for area a , size s , and time t , mapped from the critical exponents, for the dimension d , are given by [10]

$$\tau_a = 1 + \frac{\beta}{d\nu_{\perp}}, \quad \tau_s = 1 + \frac{\beta}{\nu_{\parallel} + d\nu_{\perp} - \beta}, \quad \tau_t = 1 + \frac{\beta}{\nu_{\parallel}}. \quad (5.1)$$

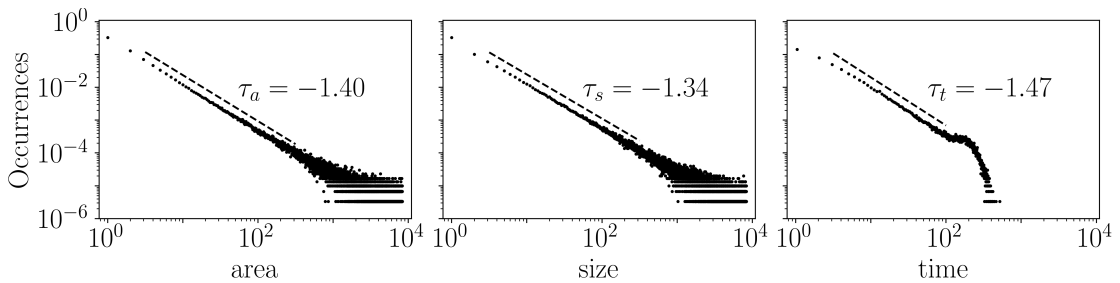


Figure 5.1.: Distributions of avalanche areas, sizes, and times from Monte Carlo simulations. All distributions clearly follow a power-law over multiple decades. In order to quantitatively measure the exponents, a finite-size extrapolation needs to be undertaken.

These avalanche exponents allow us to access the critical exponents ν_{\perp} and ν_{\parallel} , corresponding to the spatial and temporal correlation length scaling exponents respectively. While we were able to numerically determine ν_{\parallel} in [P3], the method used there came with tremendous numerical effort and is experimentally unfeasible. We therefore were only able to find ν_{\parallel} for two values of the gas temperature T , i.e. in the low and high

temperature limits. But especially ν_\perp has eluded our study in [P3] due to the inherent difficulty of extracting it directly from scaling relations around the critical point. Following the above mapping, we have access to the full set of critical exponents and are able to extract these for various temperatures numerically and in the **ADP** phase experimentally.

From our simulations we can strongly underline the behavior found in [P3]. Namely, that the universality class of the system changes *smoothly* from **DP** at low temperatures, to various stages of **ADP**, and finally to mean field universal behavior at high temperatures. We also investigate the effects of dissipation on the avalanche (and critical) exponents. Here, we find the exponents to be quite robust against dissipative effects.

Finally, we also measure the avalanche exponents experimentally for one temperature within the **ADP** phase. Here, we find an agreement between the expected and the measured time exponents, as well as the experimental *magnitude* exponent. The magnitude exponent is a combination of area and size exponents, as these cannot be distinguished in the experiment. However, in the **ADP** phase, the values of the area and size exponents are roughly the same.

Author Contributions

Contribution	Primary Role	Supportive Role
Theoretical understanding (esp. exponent mapping)	S.O.	D.B., J.S.O., M.F.
Monte Carlo simulations	S.O.	D.B., W.R., J.S.O.
Experimental measurements	J.B., P.M., D.B.	-

The project was conceived by M.F and H.O. The theoretical work was supervised by M.F. and the experimental work was supervised by T.N. and H.O.

Copyright

This work is licensed under the [Creative Commons Attribution 4.0 International license \(CC BY 4.0\)](#).

Nonequilibrium universality of Rydberg-excitation spreading on a dynamic network

Simon Ohler¹, Daniel Brady¹, Patrick Mischke^{1,2}, Jana Bender¹, Herwig Ott¹, Thomas Niederprüm¹,
Winfried Ripken¹,^{3,4} Johannes S. Otterbach⁵, and Michael Fleischhauer¹

¹Department of Physics and Research Center OPTIMAS, Rheinland-Pfälzische Technische Universität Kaiserslautern-Landau,
67663 Kaiserslautern, Germany

²Max Planck Graduate Center with Johannes Gutenberg University Mainz (MPGC), 55128 Mainz, Germany

³Machine Learning Group, Technische Universität Berlin, 10587 Berlin, Germany

⁴Berlin Institute for the Foundations of Learning and Data, 10587 Berlin, Germany

⁵Orthogonal Otter UG, 10961 Berlin, Germany



(Received 27 February 2025; accepted 13 July 2025; published 19 August 2025)

Understanding the universal properties of nonequilibrium phase transitions of spreading processes is a challenging problem. This applies in particular to irregular and dynamically varying networks. We here investigate an experimentally accessible model system for such processes, namely, the absorbing-state phase transition (ASPT) of Rydberg-excitation spreading, known as Rydberg facilitation, in a laser-driven gas of mobile atoms. It occurs on an irregular graph, set by the random atom positions in the gas, and, depending on temperature, changes its character from static to dynamic. By studying the behavior of the order parameter in the work of Brady *et al.* [Phys. Rev. Lett. **133**, 173401 (2024)], we showed numerical evidence for a crossover from directed percolation (DP) universality through various phases of anomalous directed percolation (ADP) to mean-field (MF) behavior when the temperature of the gas is increased. As the behavior of the order parameter is not sufficient to uniquely determine the universality class, we here analyze the distribution of avalanches—characteristic of nonequilibrium critical behavior—to fully characterize the ASPT. Performing extended numerical calculations and experiments on a cold ^{87}Rb atom gas, we confirm our earlier numerical findings and our phenomenological model that maps the dynamic network to a static one with power-law tails of the distribution of excitation distances. Furthermore, we discuss the influence of dissipation, present in the experiment and a necessary ingredient for the self-organization of the system to the critical point. In particular, we study the potential modification of the universality class by losses as a function of dissipation strength.

DOI: 10.1103/8rlg-169g

I. INTRODUCTION

The critical behavior at nonequilibrium phase transitions and the phenomenon of self-organized criticality (SOC) [1–3] are closely related to avalanche events—sudden, fast outbursts of energy after longer periods of inactivity. Although the topic is not without its controversies [4], the SOC mechanism is believed to be key to the abundance of real world examples of power-law distributed avalanche events like earthquakes [5], solar flares [6,7], and neuron activation in the brain [8,9], since it describes how a system can evolve in time to the critical point of a phase transition without an external drive or fine tuning. One of the most important categories of nonequilibrium phase transitions in spreading processes concerns absorbing-state phase transitions (ASPT). Here the behavior of the system changes from an active (spreading) phase with perpetual excitation cascades to an inactive (absorbing) phase, where a single excitation does not change the system at large.

Power-law distributed avalanche events are then observed at the critical point between these two phases, reflecting the scale invariance of the critical state. In this situation, a minimal perturbation can cause a scale-free reaction of the system.

Avalanche events of self-organized critical systems have first been studied in the context of sandpile models, most notably the Bak-Tang-Wiesenfeld (BTW) model [1,2]. Shortly after, additional systems were proposed that display SOC behavior, such as the Manna [10], Drossel-Schwabl [11], or Olami-Feder-Christensen model (OFC) [12] for a different type of sandpile, forest fires, and earthquakes, respectively. Most of the avalanche research so far has focused on lattice models, where a toppling or relaxation event is defined as the transfer of, e.g., energy or particles to adjacent sites on the lattice. Some works have adapted these models to *networks*, where adjacency is not defined by nearest neighbors on the lattice but instead by links of the graph structure. Here, it was found that the type of graph structure itself can significantly affect the critical behavior [13].

Additionally, most work so far has been done on *static* systems, where the adjacency relations between individual sites do not change over time. This simplification is justified in many cases, since avalanches typically happen on very short timescales compared to other processes in the system.

Published by the American Physical Society under the terms of the Creative Commons Attribution 4.0 International license. Further distribution of this work must maintain attribution to the author(s) and the published article's title, journal citation, and DOI.

However, in other systems, for example, epidemic spreading, the dynamical properties of the network are very important and happen on relevant timescales [14]. The extent to which graph dynamicity can impact the critical properties of the system is not well understood. In the context of the OFC model, for instance, it was found that the dissipative random-neighbor version results in noncritical behavior compared to critical scaling for fixed connectivity [15]; however, other authors claim that also in the latter case the model turns noncritical [16].

Generally, nonequilibrium phase transitions can be associated with a set of critical exponents that describe the scaling of physical observables close to the critical point. For ASPTs, these critical exponents can be related to the exponents of the power-law distributions of avalanche events [17]. Obtaining these critical exponents through experiments or simulations is essential to identify the universality class of the ASPT and can help in understanding the relevant physical processes.

For certain ASPTs, however, finding experimental representations can be very difficult. One example is the well-known universality class *directed percolation* (DP), where to this day well-controllable experimental systems are rare, the first one only being discovered in 2007 [18].

Gases of Rydberg atoms offer a versatile experimental platform for the investigation of many-body phenomena, where high-precision measurements on gases as well as on tailored geometries can be performed [19–21]. Interactions of Rydberg atoms can also be tuned to simulate the dynamics of the SIS (susceptible-infected-susceptible) model [22,23], which is an important example of a spreading model displaying an absorbing-state phase transition, and Rydberg atoms have been used experimentally to measure avalanche distributions and other critical exponents [24]. In this context, the excitation of an atom into a highly excited (Rydberg) state that can spread to other atoms is considered the “active” or infected state, whereas the ground state of the atom is the “passive” or susceptible state.

Absorbing-state phase transitions and DP universality of ensembles of Rydberg atoms have been previously studied on fixed lattices, yielding numerical [25] and experimental [26] signatures of DP in a one-dimensional chain of atoms. Additionally, cluster growth processes have been studied in a similar fashion [27]. In general, however, the spreading of an excitation occurs on a *network* of atoms with fixed spatial separation, given by the so-called facilitation distance. This network can be a regular lattice, if the atoms are trapped, e.g., in optical lattice potentials or tweezer arrays, or can be static but random, e.g., in a cold gas. An important further aspect of atomic gases is their thermal *motion*. In a recent publication we provided numerical evidence that the ASPT of a driven Rydberg gas under facilitation conditions changes its universality class as a function of the (root mean square) gas velocity [28]. For low temperatures we obtained DP scaling, changing to anomalous DP (ADP) and eventually mean-field (MF) for higher temperatures. These simulation results explained the unusual experimental measurement value of the critical exponent β obtained in a previous publication [24]. However, the change in universality was only shown for the critical exponent β as well as for one of the correlation length exponents ν_{\parallel} [28], lacking the third critical exponent

ν_{\perp} . Determining the exponents of the avalanche distribution functions at the critical point provides an alternative way to unambiguously determine the universality class, and we will pursue this approach in the present paper, by both numerical simulations and experimental studies. In addition, the scaling of avalanche critical exponents on dynamical networks such as in Rydberg facilitation remains a mostly open question, with only one exponent having been measured in Ref. [24].

In this paper, we numerically study the avalanche events in a three-dimensional gas of atoms that are driven by an external laser field and compare the results with experimental data as well as field-theoretical predictions for an effective static model with temperature-dependent power-law tails in the excitation distance. The atomic cloud is characterized by a tunable velocity distribution that, combined with the distance-dependent interaction, yields a dynamical graph on which excitations can spread. As a function of velocity we obtain the avalanche-exponents for area, size, and time of the avalanches (for a definition see Sec. III B) and confirm the universality class crossover from DP to anomalous directed percolation that we found in a previous publication [28] analyzing the β exponent of the order parameter, i.e., the Rydberg density. This is a nontrivial result since predicting the avalanche exponents requires knowledge of all three ASPT critical exponents ($\beta, \nu_{\parallel}, \nu_{\perp}$). The numerical results are supported by experimental observations of avalanche distributions of Rydberg facilitation in a cold, trapped gas of ^{87}Rb atoms. With this, our work also provides the first experimental indication consistent with ADP universality.

Secondly, the loss mechanisms inherent to self-organization of a system to the critical point of an absorbing-state phase transition can affect the universal behavior at criticality or even destroy criticality altogether. For this reason we consider additionally the effect of losses from the excited state and quantify its influence on criticality and exponent values for a frozen gas as well as a finite-temperature gas by numerical simulations. This is especially relevant in the context of our experimental results that invariably include loss.

II. RYDBERG FACILITATION, MODEL, AND EXPERIMENTAL SETUP

A. Microscopic system

We study a driven-dissipative system of atoms in three dimensions, where any atom can at any time belong to one of three states, namely, the ground state $|G\rangle$, the Rydberg state $|R\rangle$, and the “removed” state $|0\rangle$, which describes a state in which the atom does not take part in the dynamics at all (often called “immune” in the context of epidemic spreading). We apply an external driving (laser field) with Rabi frequency Ω that couples $|G\rangle$ to $|R\rangle$ with detuning Δ (see Fig. 1). The Rydberg state can spontaneously decay to the ground state with rate $(1-b)\gamma$ with $0 \leq b \leq 1$. The quantum mechanical evolution of the system can then be described by a Lindblad master equation [29] for the density operator $\hat{\rho}$, which reads (we set $\hbar = 1$)

$$\frac{d}{dt}\hat{\rho} = i[\hat{\rho}, \hat{H}] + \sum_l \left(\hat{L}_l \hat{\rho} \hat{L}_l^\dagger - \frac{1}{2} \{\hat{L}_l^\dagger \hat{L}_l, \hat{\rho}\} \right), \quad (1)$$

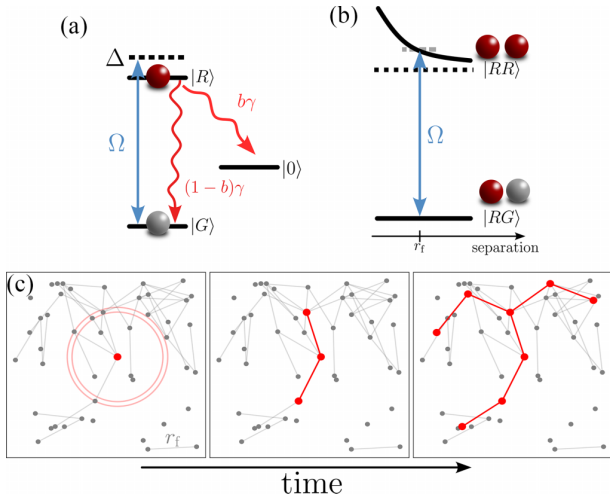


FIG. 1. Overview over the microscopic physics in our model. (a) Single atom under external drive Ω with decay channels into ground and inactive states. The parameter b controls the ratio between the decay processes. (b) Two atoms with interatomic van der Waals force that shifts the two-Rydberg state as a function of distance. At $r = r_f$, the shift cancels the external detuning and the transition becomes resonant. (c) Spreading of an avalanche on a network.

where the unitary evolution of the system is given by

$$\hat{H} = \sum_i \Omega \hat{\sigma}_i^x - \Delta \hat{n}_i + \sum_{j < i} \frac{c_6}{r_{ij}^6} \hat{n}_i \hat{n}_j. \quad (2)$$

Here, $\hat{n}_i = (|R\rangle \langle R|)_i$ is the number operator of the Rydberg $|R\rangle$ state, $r_{ij} = |\vec{r}_i - \vec{r}_j|$ is the interatomic distance, and $\hat{\sigma}^x$ is the Pauli x matrix. The last term in (2) corresponds to the van der Waals interaction between two Rydberg atoms with c_6 being the van der Waals coefficient. Using the Lindblad master equation, the dissipation in the system is taken into account by the Lindblad jump operators $\hat{L}_1^{(i)} = \sqrt{(1-b)\gamma} (|G\rangle \langle R|)_i$, $\hat{L}_2^{(i)} = \sqrt{b\gamma} (|0\rangle \langle R|)_i$, which describe spontaneous decay of the i 'th atom from the Rydberg state into the ground state $|G\rangle$ and the inert state $|0\rangle$, respectively, with the branching parameter b . Additionally, we include the effect of dephasing, which stems mainly from laser phase noise and Doppler broadening [24], but also from the nonzero width of the wave function of the atom over the van der Waals potential [30], and differential van der Waals forces [31]. The dephasing Lindblad operator reads $\hat{L}_\perp^{(i)} = \sqrt{\gamma_\perp} \hat{n}_i$, where γ_\perp is the dephasing rate.

In this publication, we always consider the high-dephasing limit of the Rydberg gas, which has been proven to be a good approximation for gaseous Rydberg systems [32]. In this limit, the dynamics of the system is governed by effective rate equations, which can be modeled using a classical Monte Carlo approach [33] (for more details see Appendix A).

B. Facilitation mechanism

The level scheme of a single Rydberg atom and the two-Rydberg dynamics is illustrated in Fig. 1. In the *facilitation* regime, the detuning Δ is chosen sufficiently large to

suppress spontaneous (seed) excitations from the ground state. However, if one atom in the system is initially in the Rydberg state, then the van der Waals interaction shifts the Rydberg energy levels of the nearby ground-state atoms. Since the van der Waals interaction is distance dependent, there exists a distance called the *facilitation radius* $r_f = (c_6/\Delta)^{1/6}$, at which the van der Waals interaction exactly cancels the detuning. In this way, a Rydberg atom can resonantly “pass on” the excitation to other atoms in a spherical shell with radius r_f around it. The width of this shell δr_f is given by $\delta r_f = \frac{\gamma_\perp}{2\Delta} r_f$ with $\delta r_f/r_f \ll 1$ [34]. The rate of the resonant facilitation is denoted by $\Gamma_f = 2\Omega^2/\gamma_\perp$, which is an important timescale in the system. Combining these two effects, we see that while an initial (seed) excitation is very unlikely, as soon as Rydberg atoms exist in the system it is possible to observe avalanche-like cascades of excitations. For this a sufficiently high density and strong enough external driving is needed such that the global facilitation rate is stronger than the decay from the Rydberg state to the ground state. At high atom velocities, the Rydberg atoms see a homogeneous ground-state background and the number of facilitated excitations is determined by the density and driving strength only. For a frozen gas with velocity $v = 0$, however, the atoms form a network where two atoms are connected if and only if their distance falls into the very narrow interval $r_f \pm \delta r_f$. Since the atomic positions are distributed uniformly, the resulting network of atoms that in principle can participate in the Rydberg facilitation is of the Erdős-Rényi type [35].

C. Rydberg gas as a dynamical graph

The Erdős-Rényi network for the frozen gas is characterized by a Poissonian distribution P_{ER} of the number k of atoms in the facilitation shell of a single Rydberg atom,

$$P_{ER}(k) = \frac{(nV_s)^k}{k!} \exp(-nV_s). \quad (3)$$

Here, $V_s \approx 4\pi \delta r_f r_f^2$ is the volume of the facilitation shell and $n = n_G + n_R$ the total density of remaining atoms in the ground and Rydberg states. It is well known that such a network features a percolation transition at the average network degree $\langle k \rangle = 1$. To be able to observe universal behavior, the network needs to be above this threshold, since otherwise the system is comprised of disconnected, finite clusters [34] and a universal data collapse cannot be achieved [28]. Therefore, the average degree $\langle k \rangle = nV_s$ needs to be sufficiently larger than unity. To increase $\langle k \rangle$ in our simulations we increase n ; however, that comes with significantly increased computational cost, leading us to choose $\langle k \rangle \sim 2.5$ as a reasonable compromise. For this value, approximately 90% of atoms are contained in the largest connected cluster (LCC) of atoms that in principle could undergo Rydberg facilitation. For finite temperature, the system has to be represented as a dynamical graph, since the distances between the atoms change over time. This implies that the pairs of atoms between which an excitation can spread (pairs of atoms with a mutual distance close to r_f) change over time, which, in the language of graph theory, corresponds to the creation and destruction of links between nodes. Changing the gas velocity then allows to change the rate of link creation and destruction and therefore

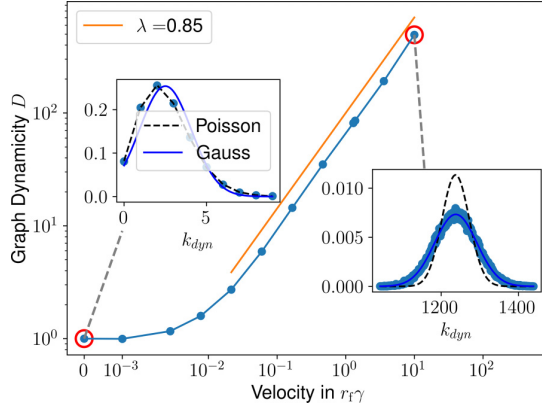


FIG. 2. Average number of unique links an atom encounters over the time $1/\gamma$ as a function of rms velocity normalized to the $v = 0$ case. The insets show the full distribution for velocities $v = 0$ (left) and $v = 10r_f\gamma$ (right) as well as Poissonian and Gaussian fits.

the degree to which dynamical effects become relevant. We quantify the degree to which the graph is dynamical by introducing the graph dynamicity D , which reads

$$D = \frac{\langle k \rangle_{\text{dyn}}}{\langle k \rangle_{\text{stat}}}, \quad (4)$$

where k_{dyn} counts all unique atoms (nodes) that an atom has ever been connected to during the inverse decay time $1/\gamma$ and k_{stat} is the average number of instantaneous connections (determined fully by the density and width of the facilitation shell). The result can be seen in Fig. 2. We observe that after a period of slow growth, starting from $v \sim 0.02r_f\gamma$ we see a continuous power-law increase in the number of unique connections. Additionally, at this point the distribution of unique partners changes from Poissonian (low-velocity) to Gaussian (high-velocity). Coincidentally, this velocity scale agrees well with the upper limit of DP universality found in Ref. [28]. In addition to the data, we also show the power-law fit to the velocity interval from $v > 0.06r_f\gamma$, which yields the exponent $\lambda = 0.85$. The relevance of this power-law increase in dynamicity is, however, unclear. We note that this consideration takes into account solely the dynamical graph structure of atoms on which Rydberg facilitation is in principle possible, not the actual excitation dynamics that depends on other factors like the external drive intensity.

D. Experimental setup

To experimentally study the collective Rydberg facilitation dynamics, we prepare a cloud of ^{87}Rb atoms in a crossed optical dipole trap with trapping frequencies of $\omega_{x,y,z} = 2\pi \times (332, 332, 73)$ Hz. The experimental setup is sketched in Fig. 3. Forced evaporation in the dipole trap is stopped at a final temperature of $T = 1 \mu\text{K}$, leading to a thermal cloud with a density of $\rho = 2.2 \times 10^{13} \text{ cm}^{-3}$. This temperature corresponds to an rms velocity of $v = 0.39 \pm 0.26r_f\gamma$. The facilitation dynamics is induced by off-resonant, blue-detuned ($\Delta = 40$ MHz), continuous excitation from the $|G\rangle \equiv |5S_{1/2} F=2 m_F=2\rangle$ ground state to the $|R\rangle \equiv |40P_{3/2}\rangle$ Rydberg state for a total duration of 100 ms. Due to

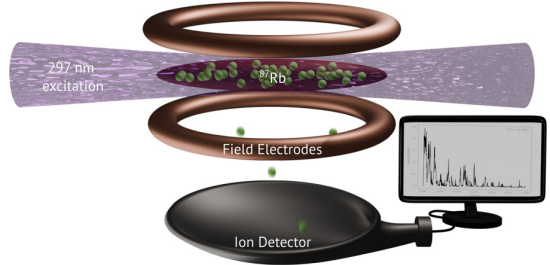


FIG. 3. Sketch of the experimental setup. The Rydberg laser off-resonantly drives facilitation dynamics and cascades of Rydberg excitations (green circles) appear in the cold cloud. Rydberg atoms can decay into ions via photo- or associative ionization, which are guided to an ion detector where their arrival time is recorded. This allows to observe the facilitation dynamics continuous in time.

photoionization from the dipole trap lasers and associative ionization, a fraction of the Rydberg population gets ionized. This decay channel contributes to the dissipation process that brings atoms into the inactive state $|0\rangle$. This state accounts for ions, atoms lost from the system since the Rydberg state is not trapped, and also atoms that decayed to the $|5S_{1/2} F=1\rangle$ ground state, which does not participate in the excitation dynamics. We estimate that approximately 2/3 of the Rydberg excitations decay back to the $|G\rangle$ state, i.e., the branching ratio is $b \approx 0.3 \pm 0.15$. The created ions are accelerated through a small electric field toward an ion detector, where their arrival time is detected. In this way, we obtain a time-continuous measurement signal proportional to the Rydberg density, which allows the observation of the facilitation dynamics *in situ*. Due to the discrete nature of the ion arrival information, binning the data is required to obtain an ion rate.

III. UNIVERSALITY CLASS AND AVALANCHE DISTRIBUTION

A. Crossover of universality classes in Rydberg facilitation

In Ref. [28], it was shown by extensive numerical simulations that the absorbing-state phase transition in a Rydberg gas changes its universality class from DP through ADP to MF by varying the velocity of the atoms. This crossover was explained by mapping the Rydberg facilitation dynamics on the dynamic network to a spreading process on a fixed network, however with long-distance power-law tails in the distribution of excitation distances. The power-law tails in the probability distribution of distances between excitations emerge since, due to the finite temperature of the gas, excited Rydberg atoms can move larger distances before actually exciting another ground-state atom. In order to determine the probability distribution of distances r a Rydberg atom needs to move before facilitating another atom, the space covered by the Rydberg atom is discretized, i.e., $r = J\delta z$ with $J \in \mathbb{N}$ [28]. This probability reads $Q(X > J) = (1 - p_{\text{exc}})^J$, where p_{exc} is the excitation probability in a given discretized interval δz . In particular, if the Rydberg atom moves at velocity v , the time spent in δz is given by $\delta t = \delta z/v$. For a single atom the excitation probability in this interval δt is Poissonian and reads $p_{\uparrow} = 1 - e^{-\Gamma_i \delta t}$. Furthermore, the number of atoms in

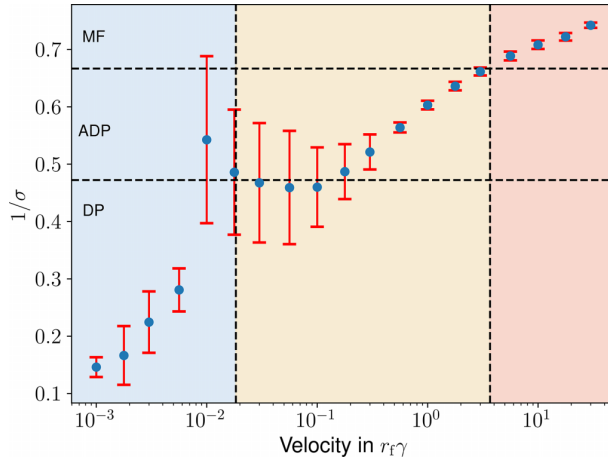


FIG. 4. Reciprocal Lévy-flight parameter as a function of gas velocity. The horizontal lines denoting the transition from one universality class to another are given by Ref. [17]. The vertical lines correspond to the velocities $v_- = \delta r_f \Gamma_f$ and $v_+ = r_f \Gamma_f$. Shown data has also been presented in Ref. [28].

the facilitation shell of a Rydberg atom also follows a Poissonian distribution and therefore the excitation probability reads $p_{\text{exc}} = \sum_{k=0}^{\infty} P(k)(1 - (1 - p_{\uparrow})^k)$, i.e.,

$$p_{\text{exc}} = 1 - \exp\{-\xi \delta z\}, \quad (5)$$

with $\xi = \frac{\langle k \rangle}{\delta r_f}(1 - e^{-\delta r_f \Gamma_f / v})$. This then yields the probability distribution of distances r from the initial position of the Rydberg atom for the first successive excitation

$$Q(r) = 2\pi \xi r \int_0^\pi d\theta \frac{e^{-\xi(\sqrt{\cos^2 \theta + r^2 - 1} - \cos \theta)}}{\sqrt{\cos^2 \theta + r^2 - 1}}, \quad (6)$$

where $\vec{r} = r_f \hat{e}_r(\theta, \varphi) + (0, 0, z)^T$. We have shown in Ref. [28] that this distribution agrees very well with the numerically obtained distribution of first excitations in the finite-temperature gas. It also agrees very well with a power-law fit of the form

$$P_{\text{hop}}(r) \sim \frac{1}{r^{d+\sigma}}, \quad (7)$$

which resembles a Lévy-flight statistic for d being the dimension of space and σ the Lévy-flight parameter.

In Fig. 4 we show the inverse Lévy-flight parameter over the gas velocity $1/\sigma$, obtained from power-law fits to the distances between excitations in the simulated gas [28]. We see that the Lévy-flight parameter $\sigma = \sigma(\bar{v})$ depends on the average velocity $\bar{v} = (\langle v^2 \rangle)^{1/2}$ of the atoms, causing a transition between universality classes. The critical exponents $(\beta, \nu_{\parallel}, \nu_{\perp})$ characterizing the behavior of the order parameter (Rydberg density), temporal, and spatial correlations, respectively, can be approximated as a function of σ close to the MF regime via a renormalization-group approach. In this case, for $d = 2\sigma - \epsilon$, ϵ being a small parameter representing the distance to the upper critical dimension, the exponents can be

written as [36]

$$\begin{aligned} \beta &= 1 - \frac{2\epsilon}{7\sigma} + O(\epsilon^2), \\ \nu_{\perp} &= \frac{1}{\sigma} + \frac{2\epsilon}{7\sigma^2} + O(\epsilon^2), \\ \nu_{\parallel} &= 1 + \frac{\epsilon}{7\sigma} + O(\epsilon^2). \end{aligned} \quad (8)$$

In Ref. [28] we determined two of the three critical exponents β and ν_{\parallel} , characterizing the order parameter and temporal correlations, while the third one, ν_{\perp} , which determines spatial correlations, was not accessible. In the following we discuss an alternative approach to fully determine the universality class, which we pursue in this work, both numerically and experimentally.

B. Avalanches

A characteristic phenomenon in dynamical systems close to the critical point of an ASPT is the appearance of avalanches, i.e., cascades of excitation events spreading through the system. Their time t (duration), area a , and size s are random but show a power-law probability distribution, which reflects the scale invariance at the critical point. For the definitions of area and size we follow Ref. [17], where the area is the number of unique sites (in our case atoms) that were involved in the avalanche, while size is the total number of relaxation (in our case decay) events that took place in the avalanche, counting possibly multiple relaxations for a single atom. Time is measured from the first excitation to the last decay of the avalanche. The distributions then scale as

$$P(t) \sim t^{-\tau_t}, \quad P(s) \sim s^{-\tau_s}, \quad P(a) \sim a^{-\tau_a}. \quad (9)$$

Generally, the critical exponents of the ASPT $(\beta, \nu_{\parallel}, \nu_{\perp})$ are connected to these avalanche exponents in the following way [17]:

$$\tau_a = 1 + \frac{\beta}{d\nu_{\perp}}, \quad \tau_s = 1 + \frac{\beta}{\nu_{\parallel} + d\nu_{\perp} - \beta}, \quad \tau_t = 1 + \frac{\beta}{\nu_{\parallel}}. \quad (10)$$

For the MF case, the critical exponents $\beta, \nu_{\perp}, \nu_{\parallel}$ are known exactly, while for DP there exist numerical estimates in the literature [37]. For the case of ADP, the critical scaling of the system depends on the Lévy-flight parameter $\sigma = \sigma(\bar{v})$.

1. Simulation results

To numerically investigate the critical properties at the boundary between absorbing and active phase in the Rydberg gas, we first need to pinpoint the parameters to obtain the critical state, namely, the critical driving-strength parameter Ω_c and the corresponding critical density n_c . To see universal scaling in our system, the underlying Erdős-Rényi network needs to be well above the percolation threshold [34], so we fix $n_c = 20.0 r_f^{-3}$, which corresponds to an average network degree of $\langle k \rangle = 2.5$. This holds for all gas velocities that we consider, while Ω_c changes as a function of velocity. We then determine the critical driving strength Ω_c via active-density decay, where we start with all atoms in the excited state and observe the decay process to the ground state ($b = 0$) (see

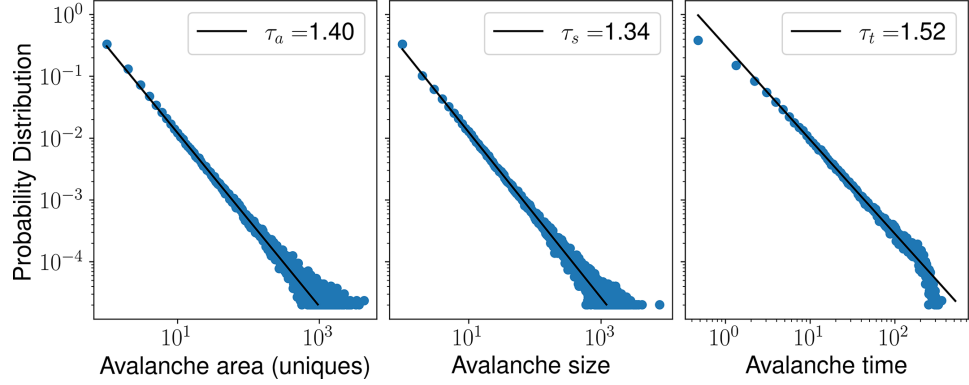


FIG. 5. Simulation avalanche area, size, and time distributions for $v = 0$ and a system size of $L = 20r_f$. The power-law fit function is shown in black. Note that statistically insignificant counts have been omitted. The broadening and drop in the distributions for large values are results of low statistics and finite-size effects.

also Appendix C). In the absorbing state, the active density ρ will decrease exponentially with time, for an active state ρ approaches a constant value, and for the critical state we expect power-law decay [34,38]. Note that we could simply use the SOC mechanism ($b \neq 0$) to obtain the critical state by starting in the active phase and time-evolving to the phase transition. However, to achieve sufficient accuracy this would necessitate an extreme separation of time scales, which is computationally more expensive.

Having obtained the critical parameters, we perform repeated calculations where we generate a gas of ground-state atoms at density $n = n_c$ and driving $\Omega = \Omega_c$. Furthermore, we use $\Delta/\gamma = 1000$, $\gamma_\perp/\gamma = 20$, and a cubic simulation volume with edge length L and periodic boundary conditions. During a simulation, we place a single excitation in the gas and let the system evolve until no excited atoms remain, extracting the area, size, and time of the avalanche. In this manner, we obtain approximately 10^5 avalanches for each configuration of parameters, allowing us to analyze the occurrence statistics. See Fig. 5 for example distributions for a fixed system size at $v = 0$. We do not extract the avalanche exponents from such distributions directly, but perform a finite-size expansion on the fitted exponents for system sizes up to $L = 20r_f$. For more details see Appendix B.

Using the two sets of equations, Eqs. (8) and (10), and the mapping $\sigma(v)$ from Ref. [28] (see Fig. 4), we can make predictions about the expected avalanche exponents τ_t, τ_a, τ_s over the Rydberg gas' velocity in the DP, ADP, and MF regimes. In Ref. [28] we additionally found that the Rydberg gas enters the ADP II phase in between DP and ADP, which is additionally characterized by Lévy-flight distributed waiting times between facilitation (infection) events [39]. For this regime, however, we cannot obtain theoretical predictions for the critical exponents.

In Fig. 6 we show the predictions in the DP, ADP, and MF phases combined with both the results of the simulations as well as the experimental data for the time and magnitude exponents. The experimental magnitude exponent corresponds to the area and size exponents; see the next section for details. For the DP values, the thickness of the bars indicate the uncertainty of the avalanche exponents derived from the uncertainty of the critical exponents ($\beta, \nu_\perp, \nu_\parallel$) in the literature. For the

ADP values, the uncertainty interval is computed from the σ uncertainty as shown in Fig. 4. The ADP predictions for smaller velocities are shown with dashed lines and a shaded uncertainty area, since the position at which a crossover to the ADP II phase occurs is not known precisely. We observe that for the expected DP and ADP universality classes the simulation results agree very well with the literature values and the ADP values found in Ref. [28]. For the case of $v = 10r_f\gamma$ in the MF regime we see that while the time exponent remains close to theoretical predictions, the area and size exponents are larger than the expected long-range (LR) MF case.

There are two distinct MF cases that result in different area and size exponents, depending on the dimension and the range of interactions [17]. Short-range (SR) MF is expected for $d \geq 4$ and $\sigma \geq 2$ and is characterized by the critical exponent $\nu_\perp^{\text{SR}} = 1/2$. In contrast, the LR MF case appears for arbitrary dimension as long as $\sigma < \min(2, d/2)$ and is associated with the value $\nu_\perp^{\text{LR}} = 1/\sigma$. Our simulations give values of the area/size exponents that are in between the SR and LR mean-field predictions. We do not have an understanding for this behavior. However, it is important to note that both the SR-MF as well as the LR-MF literature values were obtained from static models on regular lattices, whereas we consider a dynamical graph. Obviously, the mapping of moving atoms with close-range interactions to a static network with long-range connections (Lévy flights) breaks down when the atom velocity becomes too large.

2. Experimental results

In order to observe the system at the critical point in the experiment, the gas is initialized with parameters for the density and driving strength such that the dynamics always starts in the active phase. Due to atom loss, as described above, the density and thus the effective driving strength are reduced and the system evolves toward the critical point (self-organization of criticality). In the vicinity of the critical point the detected ion signal distribution becomes clearly non-Poissonian and avalanches of various sizes can be observed. The atom loss rate is reduced as it scales with the Rydberg density. After reaching the critical point, the system evolves slowly away

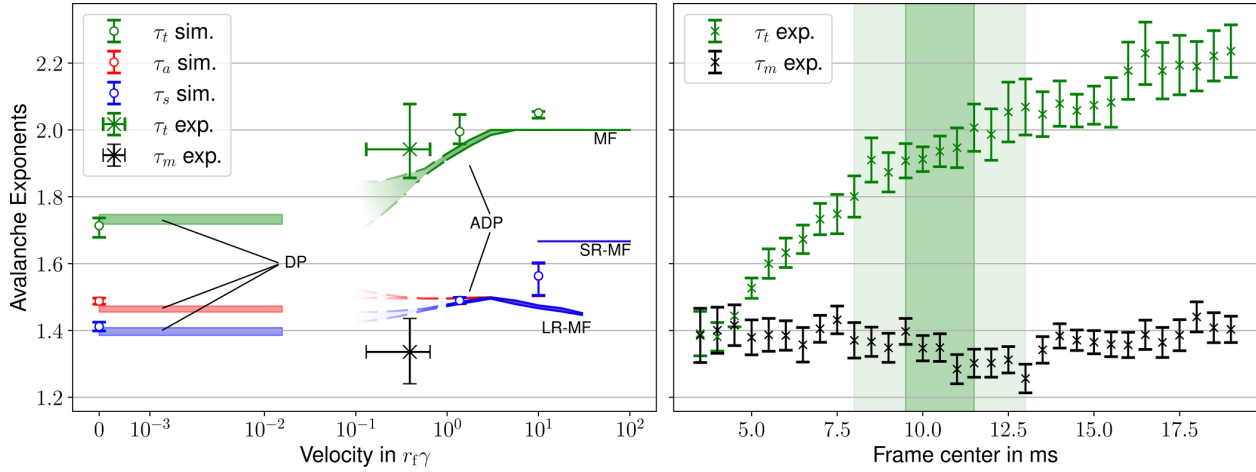


FIG. 6. Left plot: Simulation avalanche exponents over velocity (in units of $r_f \gamma$) for $b = 0$. Each velocity uses a different value of $\Omega = \Omega_c$. Note that for both mean-field cases, the theoretical predictions for area and size become identical. The perturbative ADP predictions fade out away from mean field. Also shown are the experimentally extracted values for time and magnitude (in the experiment area and size cannot be distinguished). For an explanation of the latter, see text. Experimental values are derived from the highlighted area in the right plot. Right plot: Experimental avalanche exponents as a function of time. Error bars represent the fit uncertainty; additional systematic errors may arise from, e.g., binning. The dark green area corresponds to our estimate for t_{crit} , at which the critical point of the ASPT is reached. For more details on the t_{crit} estimation see Appendix C.

from the critical point for two reasons. Firstly, the off-resonant driving laser continues to create excitations at a low rate even in the absorbing phase. Secondly, as long as there are Rydberg excitations present, atoms will continue to become ionized or decay into inert states. In the absorbing phase, the system, even though it is noncritical, still shows power-law scaling over finite scales. This dynamic in the measurement poses two challenges when extracting the critical avalanche exponents: (1) We need to find a reliable method to extract avalanches in a system where the starting and ending time of avalanches are masked by a random seed process, and (2) we have to estimate rather accurately where the critical point is reached during the time evolution of the sample. To distinguish different avalanches, we bin our data in $t_{\text{bin}} = 50 \mu\text{s}$ intervals corresponding to the theoretical lifetime of the $40P_{3/2}$ Rydberg state and consider an avalanche to end and the next avalanche to start if one of those bins does not contain any counts. The duration of an avalanche is then given by the number of consecutive nonempty bins, and the magnitude of the avalanche is quantified by the number of events in those bins. It is not possible to count the number of times an atom gets excited to the Rydberg state and decays back to the ground state, and at the same time, not all atoms that have been excited end up ionized. Therefore, the experimental magnitude of an avalanche cannot be exactly mapped to either the area or size exponent, and we are unable to define an exact relation between the empirical τ_m and τ_a as well as τ_s . However, the difference in theoretical prediction between both exponents in the ADP regime is negligible compared to the experimental uncertainty.

When the system evolves from the active to the absorbing state, it eventually becomes critical. It is, however, not trivial to precisely determine at what time t_{crit} the critical point is

reached, as can be seen by looking at the average ion count rate during the measurement shown in the left plot of Fig. 7. Starting in the active phase, we observe a steep drop in the signal 2 ms after the pulse started, corresponding to a rapid reduction in the number of facilitation partners due to loss into the inert state.

In contrast, after 15 ms the strongly reduced decay rate signals the absorbing phase where the decay is driven by the off-resonantly created seeds and the exponentially dying avalanches. The distribution of avalanche durations and magnitudes continues to follow a power law around the critical point as shown in Fig. 7. To account for the uncertainty in the precise time t_{crit} at which the critical point is reached, we analyze the avalanche exponents in three overlapping time windows of length $\Delta t_{\text{window}} = 3 \text{ ms}$ in the time range 3.5–14.5 ms. By fitting a power law to the avalanche occurrence statistics in the respective time window, we can extract the time and magnitude exponents for the avalanches. Since the power-law behavior prevails even away from the critical point, its presence alone cannot serve as an indicator for the time at which the system is critical. Instead, to estimate t_{crit} , we analyze the activity distribution in the corresponding time windows as detailed in Appendix C and obtain an estimate of $t_{\text{crit}} \approx 8 \dots 13 \text{ ms}$ (light green in Fig. 6), i.e., centers of the overlapping evaluation windows ranging from 9.5 to 11.5 ms (dark green in Fig. 6).

In Fig. 6 we plot the results for the simulation along with the data extracted from the experiment. The horizontal error bars in the left plot denote the uncertainty regarding the lifetime of the Rydberg states. In the right plot, the continuously changing avalanche exponents are shown. Additional contributions to the uncertainty in the exponent values emerge from systematic sources such as the choice of t_{bin} and are not shown.

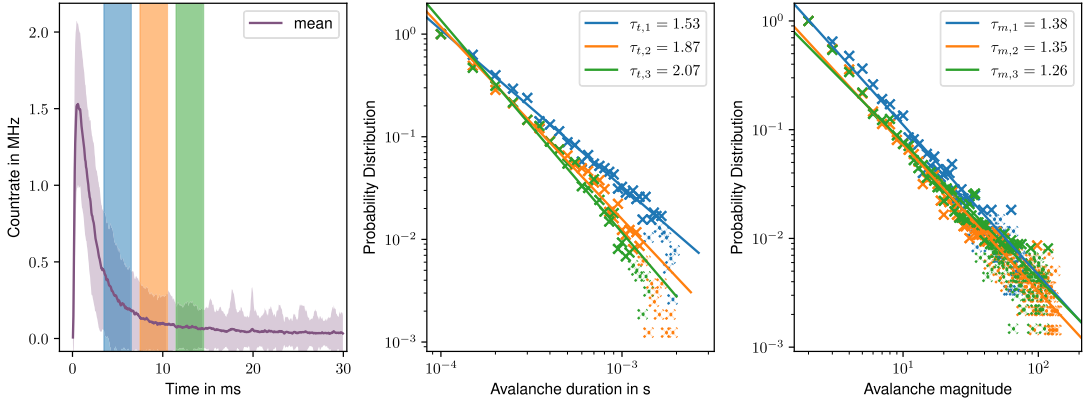


FIG. 7. (Left) Average ion countrate during the excitation pulse, averaged over 1000 realizations (purple). The dynamics starts in the active phase. The shaded purple area illustrates the standard deviation between runs. The colored vertical boxes show the $\Delta t_{\text{window}} = 3$ ms long time windows used to extract the avalanche exponents (centered at blue: 5 ms, orange: 9 ms, green: 13 ms). (Middle) Normalized distribution of (middle) avalanche durations and (right) avalanche magnitudes in the three different time windows (blue, orange, and green). Dashed data points have been ignored for fitting the power-law distribution.

We can see that the experimental time exponent for the critical interval falls into the ADP range and is clearly incompatible with the DP universality class. The magnitude exponent is smaller than expected for ADP universality, however it is unclear if this deviation might be caused by our measurement imperfections.

Additionally, the experimental data allows to exclude other, similar universality classes like the Manna class [10], where in three dimensions a time exponent of $\tau_t^{\text{Manna}} \approx 1.78$ is expected. We can also rule out that the Rydberg gas belongs in the BTW-class universality, as for that model a three-dimensional (3D) time exponent of $\tau_t \sim 0.92$ was predicted [2]. However, one should note that the two-dimensional (2D) predictions of said Ref. [2] are the subject of intense debate since no simple finite-size scaling seems to exist [17,40,41].

IV. INFLUENCE OF DISSIPATION

A. Effect of self-organization on Erdős-Rényi character of excitation graph

One important question is how the decay channel $b\gamma$ into the inert state $|0\rangle$, responsible for the self-organization of the facilitated Rydberg gas to the critical point, affects the properties of the network of possible excitations. As atoms in the inert state no longer interact with other atoms, we do not consider them as part of the graph. Furthermore since the decay into the inert state affects only atoms in the Rydberg state, it may lead preferentially to a loss of large clusters of atoms that are pairwise in facilitation distance. This could affect the structure of the network in particular for a frozen gas, where this network is a static Erdős-Rényi network. To analyze this effect, we calculate the degree distribution $P(k)$ for an initially percolating graph with loss parameter $b = 0.3 > 0$ (see Fig. 8).

By fitting with a Poissonian function, with fit parameter $\langle k \rangle$, we find that the degree distribution $P(k)$ remains Poissonian, albeit with a continuously changing average degree $\langle k \rangle$, plotted in the inset.

B. Effect of dissipation on the universality class

Dissipation is an essential ingredient of the SOC mechanism. It typically introduces characteristic length and time scales and thus strict scale invariance is lost. In the context of branching processes, for example, nonconservation of the particle number leads to a self-organization into an attractor state that is not critical but *subcritical*, leading to an exponentially truncated distribution of avalanches [42]. As a result, the distribution functions of avalanches no longer decay as a pure power law, but rather as

$$\begin{aligned} P(t) &\sim t^{-\tau_t} h_t(t/t_c), \\ P(s) &\sim s^{-\tau_s} h_s(s/s_c), \\ P(a) &\sim a^{-\tau_a} h_a(a/a_c), \end{aligned} \quad (11)$$

where the $h_\mu(x)$ are cutoff functions with cutoff scales x_c that grow with decreasing dissipation strength. Some authors have referred to this as *quasicriticality* [16]. It is also argued [16]

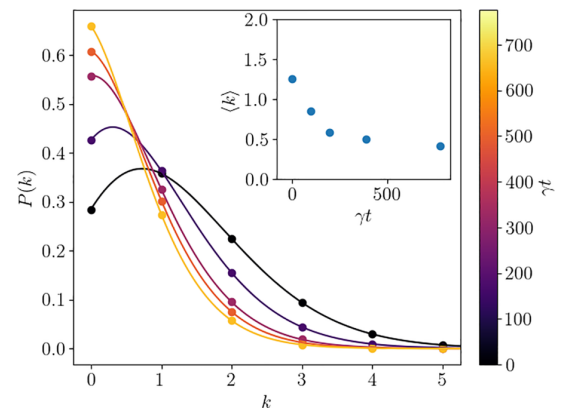


FIG. 8. Node degree distribution (dots) for different times in the frozen gas with loss parameter $b = 0.3$ and Poissonian fit with fit parameter $\langle k \rangle$ (solid lines). Fit parameter (average degree) $\langle k \rangle$ over time (inset).

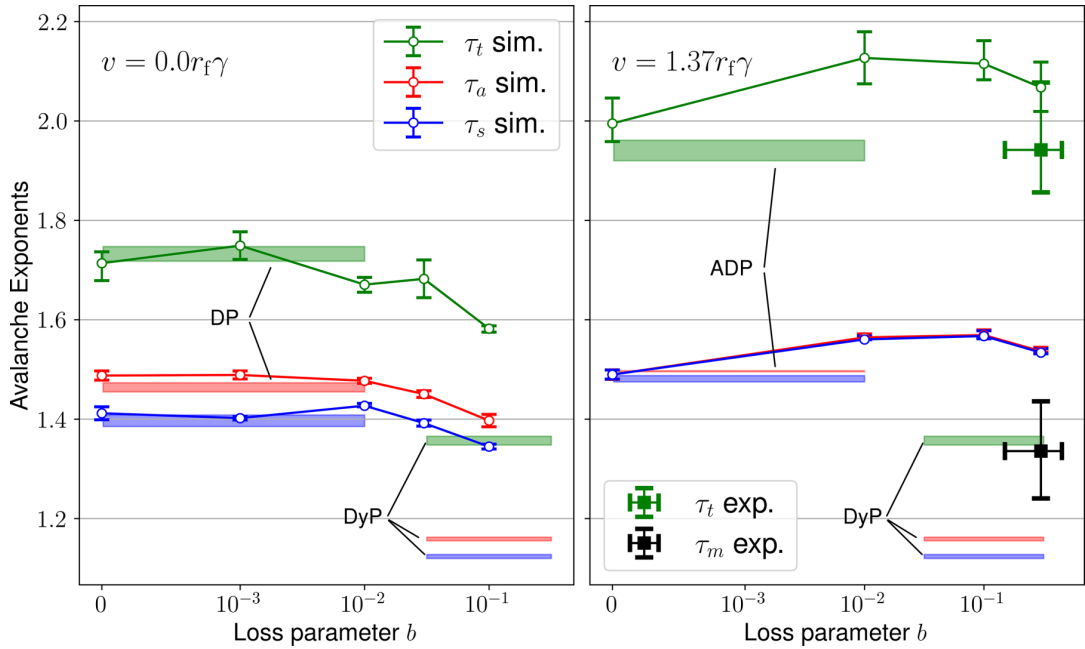


FIG. 9. Finite-size extrapolated avalanche exponents over loss parameter b , for the cases of $v = 0$ in the DP regime (left) and $v = 1.37r_f\gamma$ for the ADP case (right). The red, blue, and green bars show the expected exponents of area, size, and time, respectively, for the universality class as stated. Note that in the case of the frozen gas for $b > 0.1$ the distributions of area, size, and time become increasingly characterized by an early exponential cutoff, resulting in a poor power-law fit, which is why we focus on $b < 0.1$. Importantly, for both velocity cases the exponents do not approach the values expected from the dynamical percolation (DyP) universality class.

that a “loading mechanism” can counteract the dissipation by replenishing the lost particles after each avalanche, as is done in, e.g., the OFC model of SOC [43].

As long as there are no observable differences for experimentally relevant system sizes, we will here not distinguish between *quasi-critical* and *critical*, i.e., truly scale-free behavior. Instead, we focus on the question of whether or not dissipation modifies the universality class in the spreading process of Rydberg facilitation, i.e., if the critical exponents τ_μ in Eq. (11) are modified. In particular, we will explore by numerical simulations if dissipation acts as a relevant perturbation in the renormalization sense. Since our atom loss mechanism is conceptually very similar to that of the generalized epidemic process (GEP) or, more generally, of dynamical percolation (DyP), the presence of dissipation may change the critical behavior to that of the DyP universality class, and we will compare our results with the corresponding predictions. In the GEP and DyP models, an individual’s probability to be infected for the first time and that of all subsequent infections differ, the latter being set to zero in the extreme (GEP) case, which is referred to as perfect immunization. For the more general case of reduced repeated infection probability, the phase transition is part of the DyP universality class [17,44]. The three-dimensional case of DyP is characterized by the critical exponents [17]

$$\beta = 0.417, \quad \nu_{\parallel} = 1.169, \quad \nu_{\perp} = 0.875, \quad (12)$$

which via (10) then result in

$$\tau_a \approx 1.159, \quad \tau_s \approx 1.123, \quad \tau_t \approx 1.357. \quad (13)$$

In our model of Rydberg facilitation, dissipation is controlled by the b parameter. The value $b = 0$ corresponds to a dynamics where all Rydberg atoms return to the ground state after an exponentially distributed time. The value $b = 1$, however, leads to the guaranteed irreversible loss of this atom from a Rydberg state.

To address the effect of dissipation, we simulate the avalanches in the system with varying values of $b > 0$. Generically, we find a power law scaling over 1–2 orders of magnitude truncated by an exponential cutoff function, Eq. (11). We extract the power-law exponents and perform finite-size extrapolations. The result can be seen in Fig. 9. We observe that at $v = 0$ for loss parameters $b < 0.01$, we do not find a difference in the values of the exponents larger than our uncertainty. For larger b , the found exponents diminish in magnitude, especially the time exponent. For the case of $v = 1.37r_f\gamma$, which is approximately the gas velocity in the experiment, we find that the avalanche exponents follow a nonmonotonous behavior of increase for smaller b and decreasing in magnitude again for larger b . Importantly, this implies that the avalanche exponents found in the experiment, which we also show in Fig. 9, do not incur a significant additional systematic error based on nonvanishing b values. In Fig. 9 we also show the predicted values for DyP. We observe that neither the simulated nor the experimentally measured values agree with those of DyP, showing that despite the conceptual similarity, Rydberg facilitation cannot be simply pictured as an epidemic spreading with immunization. We have checked that this deviation does not result from the network structure set by the random atom positions in a gas by

repeating our avalanche simulations on a regular 2D lattice of atoms with nearest-neighbor facilitation. Here, we also find no agreement with DyP exponents for $b \rightarrow 1$. We speculate that the difference might be found in the infection mechanism: In lattice models of DyP, an infected site passes on the infection to adjacent sites with a given probability, but decays after a single step of discrete time [44,45], whereas in our model, both infection and decay occur probabilistically according to certain rates.

V. CONCLUSION

We studied the critical properties of excitation growth in a gas of atoms under conditions of Rydberg facilitation, which represents an experimentally accessible model system for a spreading process on a random and dynamical network. In particular we determined the power-law exponents of the distribution of avalanches at the critical point of the absorbing-state phase transition (ASPT) from both numerical simulations and experimental measurements. These exponents can be related to the full set of critical exponents of the nonequilibrium phase transition and thus uniquely determine the universality class Eq. (10). In a previous theoretical work we have provided numerical evidence that with increasing rms velocity of the atoms in the gas, the character of the ASPT smoothly changes from directed percolation (DP) universality through different classes of anomalous directed percolation (ADP) to eventually mean-field (MF) behavior, which also explained previous experimental observations [24]. The velocity-dependent crossover was interpreted using a phenomenological model that mapped the Rydberg facilitation in the gas of moving atoms, resembling a dynamic network to an excitation spreading process on a random static network with Lévy-flight tails in the distribution of excitation distances [28]. Our simulations together with experimental results confirm that the avalanche distribution exponents follow the predictions obtained from the phenomenological model in Ref. [28] using the mapping relations (10) combined with previous results on the velocity dependence of the Lévy-flight parameter at the ASPT. Furthermore, our work has given experimental evidence of ADP universality.

We also investigated the network structure and its effects on the SOC mechanism. Since SOC on dynamical networks has been little researched and is as of yet poorly understood, we first characterize the dynamical properties of the underlying network structure of atoms in mutual facilitation distance as a function of gas velocity and quantify the number of dynamical connections. Secondly, we investigated the influence of dissipation, important for the SOC, on the critical behavior. For the frozen gas, we first verified that the Erdős-Rényi character of the network is unaffected by decay. We then analyzed the influence of decay on the critical scaling in the DP and ADP regimes. While we cannot make any claims about the presence or absence of true critical behavior over arbitrary time and length scales, the observed power laws in the avalanche distributions over extended parameter ranges even in the presence of losses are consistent with at least quasi-critical behavior. The question we addressed instead was whether losses modify the universality class of the ASPT in Rydberg facilitation, which could be the case if dissipation

was a relevant perturbation in the renormalization sense. For a frozen gas we find that below a minimal dissipation probability we cannot detect a measurable influence on the scaling exponents. At stronger dissipation we see that the avalanche exponents are slightly reduced in magnitude. However, despite the conceptual similarities, we do not obtain exponents belonging to the dynamical percolation (DyP) universality class.

ACKNOWLEDGMENTS

The authors thank Fabian Isler for fruitful discussions. Financial support from the DFG through SFB TR 185, Project No. 277625399, is gratefully acknowledged. The authors also thank the Allianz für Hochleistungsrechnen (AHRP) for giving us access to the Elwetritsch HPC Cluster. This work was also supported by the Max Planck Graduate Center with the Johannes Gutenberg-Universität Mainz (MPGC) and the Quantum Initiative Rhineland-Palatinate (QUIP) and the Research Initiative Quantum Computing for Artificial Intelligence QC-AI. W.R. acknowledges support by the German Ministry of Education and Research (BMBF) for BIFOLD (01IS18037A).

S.O. performed the numerical calculations and the analysis of critical exponents with support from D.B. The experiment was performed by J.B., P.M., and D.B., guided by T.N., and H.O.; W.R. and J.S.O. helped in numerical implementation and optimization. J.S.O. additionally helped in supervising the theoretical work. M.F. and T.N. conceived the project and supervised the theoretical (M.F.) and experimental parts (T.N.) of the project, respectively. S.O., D.B., and M.F. wrote the initial version of the paper. All authors discussed the results and contributed to the writing of the final manuscript.

DATA AVAILABILITY

The data that support the findings of this article are openly available [46].

APPENDIX A: RATE EQUATION MODELING

All numerical data is obtained using fixed-time-step Monte Carlo simulations [47] of classical rate equations in the high dephasing limit. It has been shown that in this limit dynamics become effectively classical and can therefore be described by classical Monte Carlo simulations to a high degree of accuracy [33].

For atom i , the excitation probability is given by the projection operator onto the Rydberg state $|R\rangle_i$, i.e., $\hat{n}_i = |R\rangle_i \langle R|_i$. Using the Lindblad master equation, given by Eq. (1), we can formulate a set of differential equations for the ground state $|G\rangle_i$, Rydberg state $|R\rangle_i$, and inert state $|0\rangle_i$ of the i th atom. After adiabatic elimination of coherences, e.g., $\frac{d}{dt}\sigma_i^{gr} = 0$, (where $\sigma^{gr} = |G\rangle\langle R|$), we receive the rate equations [22,34]

$$\frac{d}{dt}p_r^{(i)} = -(\gamma_{\text{stim}} + \gamma_{\text{spont}})p_r^{(i)} + \gamma_{\text{stim}}p_g^{(i)}, \quad (\text{A1})$$

$$\frac{d}{dt}p_g^{(i)} = -\gamma_{\text{stim}}p_g^{(i)} + (\gamma_{\text{stim}} + (1-b)\gamma_{\text{spont}})p_r^{(i)}, \quad (\text{A2})$$

$$\frac{d}{dt}p_0^{(i)} = b\gamma_{\text{spont}}p_r^{(i)}. \quad (\text{A3})$$

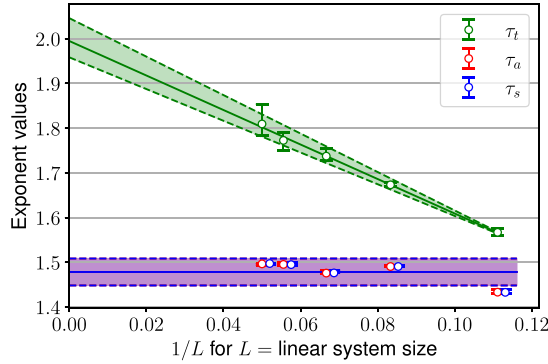


FIG. 10. Finite-size expansion of the avalanche exponents. The shaded area corresponds to the uncertainty interval. Size values are shifted slightly along the x axis for better visibility.

Here, γ_{spont} corresponds to the spontaneous decay rate and γ_{stim} corresponds to the stimulated (de)excitation rate. Explicitly, the stimulated rate reads

$$\gamma_{\text{stim}} = \frac{2\Omega^2\gamma_{\perp}}{\gamma_{\perp}^2 + \Delta^2 \left(\sum_{\substack{j \neq i \\ j \in \Sigma}} \frac{r_{ij}^{\delta}}{r_{ij}^{\delta} - 1} \right)^2}, \quad (\text{A4})$$

where Σ corresponds to the subset of atoms in the Rydberg state.

We initiate N atoms with random positions in a cubic simulation box with length L and periodic boundary conditions. Velocities are sampled from the Maxwell-Boltzmann distribution, i.e., a Gaussian in each direction, with the most probable velocity v . Furthermore, we dynamically adjust the (fixed) time-step length depending on the facilitation rate with $\Gamma_f dt = \frac{1}{10}$. In order to receive good avalanche fits, we use approximately 200 000 trajectories per parameter set.

APPENDIX B: FINITE-SIZE EXPANSION OF AVALANCHE DATA

All of the simulation exponent values reported in this paper were obtained using a system size extrapolation. We fit a linear function $f(1/L)$, where L is the linear system size, to the exponent values for different system sizes and then extrapolate to $f(0)$. In Fig. 10 we show the extrapolation for the case of $v = 1.37r_f\gamma$ in the ADP phase. For the time exponent we see a clear finite-size scaling with an increasing value for larger systems, whereas the area and size exponents do not show a clear trend over system size as well as a much smaller variation. The shaded areas correspond to the uncertainty region.

APPENDIX C: DETERMINING THE CRITICAL POINT

1. Numerical simulations

Finding the correct critical point Ω_c is essential in obtaining power-law distributed avalanches. We determine Ω_c in our numerical simulations by starting from the fully inverted state (all atoms in the Rydberg state) and considering the decay process as a function of the system size. In the

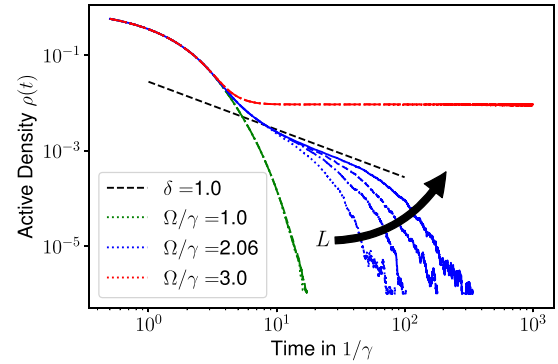


FIG. 11. Finite-size expansion of the active density decay method of finding Ω_c for $v = 10r_f\gamma$. For all values of Ω , we show the averaged decay data for $L \in \{5, 7, 9\}r_f$; for $\Omega/\gamma = 2.06$ we also show $L = 12r_f$. The linestyles with increasing system size are: dotted, dash-dotted, dashed, and solid.

absorbing phase, the decay is exponential and shows no strong dependence on system size. In the active phase, the Rydberg density approaches a constant. For values of Ω close to the critical point, a regime with power-law decay emerges for intermediate time scales, where the precise value of Ω_c is then obtained by fitting a power-law function with the exponent $\delta = \frac{\beta}{\nu_{\parallel}}$ to increasing system sizes L as shown in Fig. 11. Note that for the absorbing as well as the active case the curves for all system sizes lie on top of each other. Also see Ref. [38] for more details. We find $\Omega_c/\gamma \approx 3.40$ for the frozen gas, $\Omega_c/\gamma \approx 2.325$ for the ADP regime ($v = 1.37r_f\gamma$), and $\Omega_c/\gamma \approx 2.06$ for the mean-field regime ($v = 10r_f\gamma$).

2. Experimental data

The extracted exponents of the power-law distributed avalanches strongly depend on the time windows in which they are evaluated. It is a challenging task to determine the correct point in time at which the critical point is reached. In the active phase, the system typically forms a single large cluster of Rydberg excitations where the total number of excited atoms is effectively limited by the size of the system. In Fig. 12 we show histograms of the count numbers in a single evaluation bin for different time windows. As the number of ions in a fixed time t_{bin} is proportional to the number of Rydberg atoms times the decay rate, this can be understood as a measure for the activity of the system. In the active phase, which is our starting point, the histograms show a characteristic activity bump for large counts. We estimate that the active phase ends when the distribution shows no residuals of such an activity bump clearly visible in the first evaluation frame. In our experiment, we estimate that this is the case between 8 and 13 ms, i.e., time window centers of 9.5 and 11.5 ms.

We note that other, more indirect ways to estimate the critical point are possible, e.g., by exploiting scaling relations of avalanche shapes [48]. Moreover, the critical point may be reached after slightly different times in each individual experimental realization, given that the loss process is stochastic.

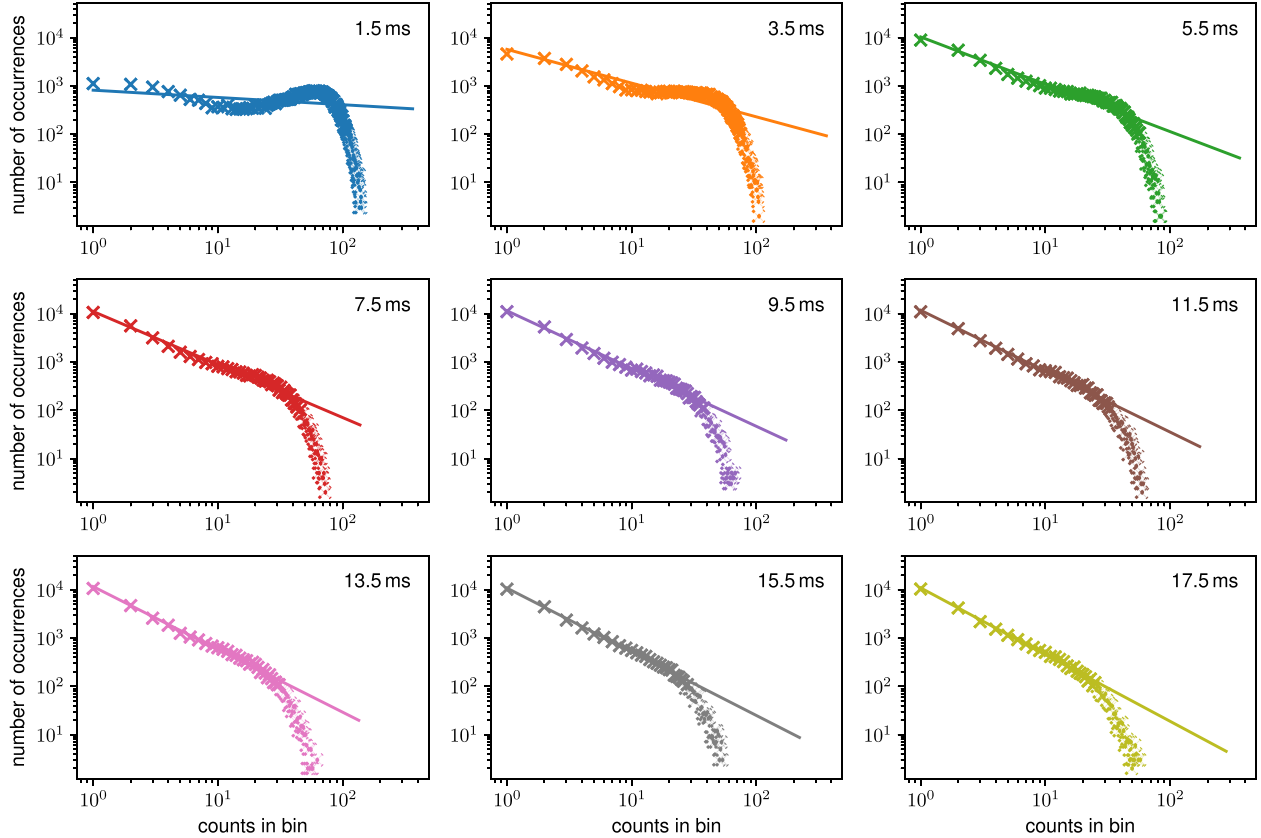


FIG. 12. The activity distribution of the experimental system at different time intervals. In each subplot, the activity distribution for a different time interval of $\Delta t = 3$ ms is shown, centered as indicated in the corner of the plot. The distribution of count numbers in 50- μ s bins is shown. The fitted lines serve as a guide to the eye to evaluate whether the distribution is active. For early times up until the interval of 6–9 ms we find a “bump” at large activity sizes, which is indicative of the active phase. We estimate that in the subsequent time windows of 8–13 ms the critical point is reached.

- [1] P. Bak, C. Tang, and K. Wiesenfeld, Self-organized criticality: An explanation of the 1/f noise, *Phys. Rev. Lett.* **59**, 381 (1987).
- [2] P. Bak, C. Tang, and K. Wiesenfeld, Self-organized criticality, *Phys. Rev. A* **38**, 364 (1988).
- [3] C. Tang and P. Bak, Critical exponents and scaling relations for self-organized critical phenomena, *Phys. Rev. Lett.* **60**, 2347 (1988).
- [4] N. W. Watkins, G. Pruessner, S. C. Chapman, N. B. Crosby, and H. J. Jensen, 25 years of self-organized criticality: Concepts and controversies, *Space Sci. Rev.* **198**, 3 (2016).
- [5] A. Sornette and D. Sornette, Self-organized criticality and earthquakes, *Europhys. Lett.* **9**, 197 (1989).
- [6] E. T. Lu and R. J. Hamilton, Avalanches and the distribution of solar flares, *Astrophysical Journal, Part 2-Letters* **380**, L89 (1991).
- [7] M. J. Aschwanden, N. B. Crosby, M. Dimitropoulou, M. K. Georgoulis, S. Hergarten, J. McAteer, A. V. Milovanov, S. Mineshige, L. Morales, N. Nishizuka *et al.*, 25 years of self-organized criticality: solar and astrophysics, *Space Sci. Rev.* **198**, 47 (2016).
- [8] D. Plenz, T. L. Ribeiro, S. R. Miller, P. A. Kells, A. Vakili, and E. L. Capek, Self-organized criticality in the brain, *Front. Phys.* **9**, 639389 (2021).
- [9] J. Hesse and T. Gross, Self-organized criticality as a fundamental property of neural systems, *Front. Syst. Neurosci.* **8**, 166 (2014).
- [10] S. S. Manna, Two-state model of self-organized criticality, *J. Phys. A: Math. Gen.* **24**, L363 (1991).
- [11] B. Drossel and F. Schwabl, Self-organized critical forest-fire model, *Phys. Rev. Lett.* **69**, 1629 (1992).
- [12] Z. Olami, H. J. S. Feder, and K. Christensen, Self-organized criticality in a continuous, nonconservative cellular automaton modeling earthquakes, *Phys. Rev. Lett.* **68**, 1244 (1992).
- [13] F. Caruso, V. Latora, A. Pluchino, A. Rapisarda, and B. Tadić, Olami-Feder-Christensen model on different networks, *Eur. Phys. J. B* **50**, 243 (2006).
- [14] M. Dottori and G. Fabricius, Sir model on a dynamical network and the endemic state of an infectious disease, *Physica A* **434**, 25 (2015).

[15] S. Lise and M. Paczuski, Nonconservative earthquake model of self-organized criticality on a random graph, *Phys. Rev. Lett.* **88**, 228301 (2002).

[16] J. A. Bonachela and M. A. Munoz, Self-organization without conservation: true or just apparent scale-invariance? *J. Stat. Mech.* (2009) P09009.

[17] M. Henkel, H. Hinrichsen, and S. Lübeck, *Non-Equilibrium Phase Transitions*, 1st ed., Theoretical and Mathematical Physics (Springer Science+Business Media, Dordrecht, 2008), Vol. 1.

[18] K. A. Takeuchi, M. Kuroda, H. Chaté, and M. Sano, Directed percolation criticality in turbulent liquid crystals, *Phys. Rev. Lett.* **99**, 234503 (2007).

[19] A. Browaeys and T. Lahaye, Many-body physics with individually controlled Rydberg atoms, *Nat. Phys.* **16**, 132 (2020).

[20] M. Saffman, T. G. Walker, and K. Mølmer, Quantum information with Rydberg atoms, *Rev. Mod. Phys.* **82**, 2313 (2010).

[21] C. S. Adams, J. D. Pritchard, and J. P. Shaffer, Rydberg atom quantum technologies, *J. Phys. B: At. Mol. Opt. Phys.* **53**, 012002 (2019).

[22] D. Brady and M. Fleischhauer, Mean-field approach to Rydberg facilitation in a gas of atoms at high and low temperatures, *Phys. Rev. A* **108**, 052812 (2023).

[23] T. Wintermantel, M. Buchhold, S. Shevate, M. Morgado, Y. Wang, G. Lochead, S. Diehl, and S. Whitlock, Epidemic growth and Griffiths effects on an emergent network of excited atoms, *Nat. Commun.* **12**, 103 (2021).

[24] S. Helmrich, A. Arias, G. Lochead, T. Wintermantel, M. Buchhold, S. Diehl, and S. Whitlock, Signatures of self-organized criticality in an ultracold atomic gas, *Nature (London)* **577**, 481 (2020).

[25] M. Marcuzzi, E. Levi, W. Li, J. P. Garrahan, B. Olmos, and I. Lesanovsky, Non-equilibrium universality in the dynamics of dissipative cold atomic gases, *New J. Phys.* **17**, 072003 (2015).

[26] R. Gutiérrez, C. Simonelli, M. Archimi, F. Castellucci, E. Arimondo, D. Ciampini, M. Marcuzzi, I. Lesanovsky, and O. Morsch, Experimental signatures of an absorbing-state phase transition in an open driven many-body quantum system, *Phys. Rev. A* **96**, 041602 (2017).

[27] I. Lesanovsky and J. P. Garrahan, Out-of-equilibrium structures in strongly interacting Rydberg gases with dissipation, *Phys. Rev. A* **90**, 011603 (2014).

[28] D. Brady, S. Ohler, J. Otterbach, and M. Fleischhauer, Anomalous directed percolation on a dynamic network using Rydberg facilitation, *Phys. Rev. Lett.* **133**, 173401 (2024).

[29] G. Lindblad, On the generators of quantum dynamical semigroups, *Commun. Math. Phys.* **48**, 119 (1976).

[30] W. Li, C. Ates, and I. Lesanovsky, Nonadiabatic motional effects and dissipative blockade for Rydberg atoms excited from optical lattices or microtraps, *Phys. Rev. Lett.* **110**, 213005 (2013).

[31] T. Schlegel, E. Konstantinidou, M. Fleischhauer, and D. Brady [arXiv:2505.09314](https://arxiv.org/abs/2505.09314).

[32] C. Ates, T. Pohl, T. Pattard, and J. Rost, Strong interaction effects on the atom counting statistics of ultracold Rydberg gases, *J. Phys. B: At. Mol. Opt. Phys.* **39**, L233 (2006).

[33] E. Levi, R. Gutiérrez, and I. Lesanovsky, Quantum non-equilibrium dynamics of Rydberg gases in the presence of dephasing noise of different strengths, *J. Phys. B: At. Mol. Opt. Phys.* **49**, 184003 (2016).

[34] D. Brady, J. Bender, P. Mischke, S. Ohler, T. Niederprüm, H. Ott, and M. Fleischhauer, Griffiths phase in a facilitated Rydberg gas at low temperatures, *Phys. Rev. Res.* **6**, 013052 (2024).

[35] P. Erdős and A. Rényi, On the evolution of random graphs, *Publ. math. inst. hung. acad. sci.* **5**, 17 (1960).

[36] H. Hinrichsen and M. Howard, A model for anomalous directed percolation, *Eur. Phys. J. B* **7**, 635 (1999).

[37] M. A. Munoz, R. Dickman, A. Vespignani, and S. Zapperi, Avalanche and spreading exponents in systems with absorbing states, *Phys. Rev. E* **59**, 6175 (1999).

[38] M. A. Munoz, R. Juhász, C. Castellano, and G. Ódor, Griffiths phases on complex networks, *Phys. Rev. Lett.* **105**, 128701 (2010).

[39] H. Hinrichsen, Non-equilibrium phase transitions with long-range interactions, *J. Stat. Mech.* (2007) P07006.

[40] S. Manna, Large-scale simulation of avalanche cluster distribution in sand pile model, *J. Stat. Phys.* **59**, 509 (1990).

[41] S. Lübeck and K. Usadel, Numerical determination of the avalanche exponents of the Bak-Tang-Wiesenfeld model, *Phys. Rev. E* **55**, 4095 (1997).

[42] K. B. Lauritsen, S. Zapperi, and H. E. Stanley, Self-organized branching processes: Avalanche models with dissipation, *Phys. Rev. E* **54**, 2483 (1996).

[43] S. Lise and H. J. Jensen, Transitions in nonconserving models of self-organized criticality, *Phys. Rev. Lett.* **76**, 2326 (1996).

[44] P. Grassberger, H. Chaté, and G. Rousseau, Spreading in media with long-time memory, *Phys. Rev. E* **55**, 2488 (1997).

[45] A. Jiménez-Dalmaroni and H. Hinrichsen, Epidemic processes with immunization, *Phys. Rev. E* **68**, 036103 (2003).

[46] S. Ohler, D. Brady, P. Mischke, J. Bender, H. Ott, T. Niederprüm, W. Ripken, J. S. Otterbach, and M. Fleischhauer, Nonequilibrium universality of Rydberg-excitation spreading on a dynamic network [dataset] RPTU Kaiserslautern-Landau (2025), [10.26204/data/9](https://doi.org/10.26204/data/9).

[47] V. R. Barlett, J. Bigeón, M. Hoyuelos, and H. Martín, Differences between fixed time step and kinetic Monte Carlo methods for biased diffusion, *J. Comput. Phys.* **228**, 5740 (2009).

[48] J. P. Sethna, K. A. Dahmen, and C. R. Myers, Crackling noise, *Nature (London)* **410**, 242 (2001).

6. Non-Classical Spin-Phonon Correlations Induced by Rydberg Facilitation in a Lattice

D. Brady and M. Fleischhauer
[arXiv:2504.19679 \(2025\)](https://arxiv.org/abs/2504.19679)

Here we shift gears from studying facilitation in a gas of Rydberg atoms to a one-dimensional lattice of Rydberg atoms in tweezer arrays, explicitly taking into account motional degrees of freedom of the atoms. While gases of Rydberg atoms generically feature high dephasing rates, damping quantum effects and leading to largely classical dynamics [21–24], the same is not true in a lattice. This makes tweezer arrays of Rydberg atoms especially interesting for the field of quantum simulation [35–41] (see also Sec. 1.2). For 1D tweezer arrays, facilitation dynamics effectively reduce to the growing and shrinking of spin domains, where the Rydberg state corresponds to spin-up $|R\rangle \equiv |\uparrow\rangle$ and the ground state corresponds to spin-down $|G\rangle \equiv |\downarrow\rangle$ [25].

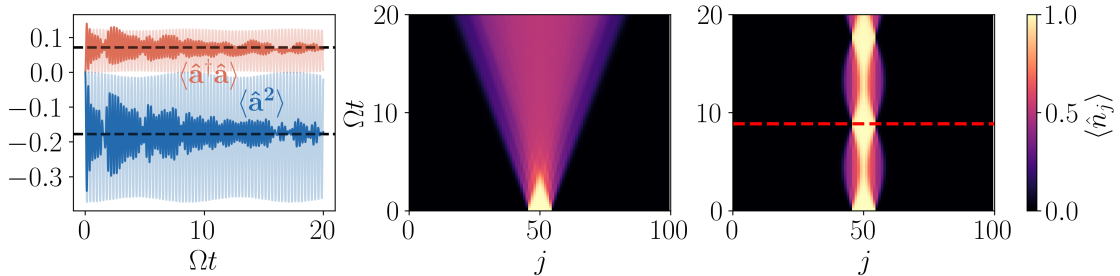


Figure 6.1.: Spin and phonon dynamics in the Rydberg facilitation chain under a quadratic spin-spin interaction potential. (Left) Local phonon observables within a spin domain. Phonons are quickly excited from the vacuum $|0\rangle$ state and, despite a purely unitary time evolution, thermalize over long time-scales. (Center and right) Spin up population over time and lattice site j , starting with an initial spin domain of size 9. Without spin-phonon interactions (center) the spin domain expands ballistically, whereas in the presence of spin-phonon interactions (right) the domain size oscillates in time (Bloch oscillations) and remains spatially localized. The red dashed line corresponds to our analytically derived Bloch period.

One open question is how the dipolar forces between Rydberg atoms, which become especially strong in the facilitation regime, affect the stability of the array. Ref. [26] investigates this by explicitly accounting for the motional degree of freedom of the atoms in their respective tweezer traps. Specifically, they linearize the dipolar interaction potential between Rydberg atoms and treat atomic motion (phonons) with bosonic ladder operators. It is important to note that this interaction completely cancels out in linear order within the spin domain, making higher orders relevant. The authors of Ref. [26] find the dipolar interaction to act as a source of motional excitations (phonons) at the

border of the spin domain, which in turn slows what would otherwise be a ballistic expansion of the spin domain.

Furthermore, in a recent experiment the dipolar Rydberg-Rydberg interaction potential was tailored to a Lennard-Jones style potential by laser-coupling to an avoided crossing of high-lying Rydberg levels [27]. Consequently, the dipolar interaction potential becomes quadratic (harmonic) in leading order. Motivated by this, we investigate the spin-phonon dynamics in the presence of a quadratic (harmonic) Rydberg-Rydberg interaction potential. In particular this quadratic potential would stabilize the chain, as opposed to pushing the atoms apart.

Starting with an initial spin-up domain of neighboring Rydberg atoms (spin-ups), we investigate the time dynamics modified by the coupling to motional degrees of freedom. We simulate the full dynamics using a *time-evolving block decimation* (TEBD) algorithm [122] and analytically decouple spin and phonon degrees of freedom using a Born-Oppenheimer approximation. Despite the apparent simplicity of the model, we find a number of nontrivial effects at play. In particular, we find the Rydberg-Rydberg interaction to bring phonons into non-classical position states (squeezed states) and to mediate strong correlations between individual phonons. Furthermore, we find the displacement of phonons from their respective trap centers to be correlated and to be in-phase for a harmonic coupling potential and out-of-phase for an inverted harmonic coupling potential.

Finally, as a result of a shift in ground state energy which phonons experience depending on if they are inside or outside of the spin domain, the energy of the spin domain depends on its size. In particular, the energy grows linearly with the spin domain size. This is reminiscent of a Wannier-Stark ladder [123, 124] and results in Bloch oscillations in the spin-domain size in the presence of spin-phonon coupling. Through the diagonalization of the phonon Hamiltonian within a given spin domain and a mapping to a tight-binding model [125], we are able to analytically describe the Bloch period.

Author Contributions

Contribution	Primary Role	Supportive Role
Diagonalization of phonon Hamiltonian	D.B.	M.F.
Mapping to Tight-Binding model	D.B.	M.F.
TEBD simulations	D.B.	-

The project was conceived and supervised by M.F.

Copyright

This work is licensed under the [Creative Commons Attribution 4.0 International license \(CC BY 4.0\)](#).

Non-Classical Spin-Phonon Correlations Induced by Rydberg Facilitation in a Lattice

Daniel Brady¹ and Michael Fleischhauer¹

¹Department of Physics and Research Center OPTIMAS,
RPTU Kaiserslautern, D-67663 Kaiserslautern, Germany

(Dated: April 29, 2025)

We investigate the interplay between mechanical forces and the internal-state dynamics of a chain of Rydberg atoms trapped in tweezer arrays under the facilitation constraint. Dipole interactions between Rydberg atoms couple electronic (spin) degrees of freedom with excited motional (phonon) states. We show that this interaction leads to highly correlated and non-classical phonon states in the form of squeezed center of mass position states of the Rydberg atoms. Coupling with either a normal or an inverted Lennard-Jones-type potential, resulting from an avoided crossing of Rydberg potential curves, leads to in-phase or out-of-phase correlated oscillations in the atom positions respectively. Furthermore, the growth dynamics of a finite cluster of excited Rydberg atoms can be mapped to the dynamics of a single particle in a semi-infinite lattice subject to a linear potential gradient caused by spin-phonon interactions. This results in Bloch oscillations in the spin cluster size, which in turn localize spin excitations in the system.

Introduction – Rydberg atoms have become a powerful tool for constructing neutral-atom quantum simulators and quantum information systems [1] due to their strong, long-range dipole interactions. These interactions are typically on the order of GHz and on μm length scales [2] and can be tailored simply by adjusting laser parameters. With advances in ultra-cold atom trapping using tweezer arrays, arbitrary geometries of neutral atoms can be programmed [3–5]. Through this high level of experimental control, Rydberg simulators of many-body quantum spin systems [6] have found a wide use of applications, for example to study the quantum Ising model [7–11], coherent transport properties [12], modeling topological systems [13], or quantum phase transitions to \mathbb{Z}_N symmetric phases [14–16], and spin liquid phases [17, 18]. When coupling with an off-resonant laser, the dipole interaction between Rydberg atoms can compensate the laser detuning, allowing for the resonant excitation of Rydberg atoms only if they are in the presence of another. These so-called *facilitation* systems [19] behave similar to epidemics [20, 21] and feature an absorbing-state phase transition [22, 23], can adhere to multiple different non-equilibrium universality classes [24], and can feature kinetic constraints, leading to non-ergodic behavior [25, 26].

A key problem of Rydberg quantum simulators are the mechanical forces accompanying the dipole-dipole interactions, which can lead to a dephasing of optical transitions [27] and mechanical instabilities. Consequently quantum simulations involving Rydberg blockade or facilitation are typically performed on short time scales, where motional effects can be neglected. Here we show that the mechanical forces in fact give rise to very rich physics. They can induce non-classical spin-phonon correlations and lead to an oscillatory dynamics in the Rydberg facilitation akin of Bloch oscillations in a lattice.

Specifically, we investigate the dynamics of interacting Rydberg atoms in a 1D tweezer array in the facili-

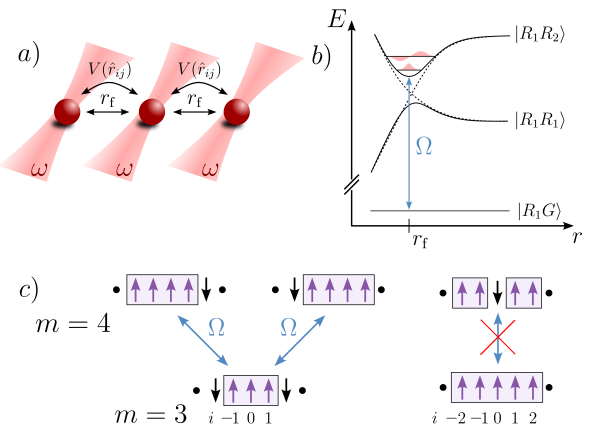


FIG. 1. *System schematics.* (a) Sketch of 1D tweezer array with lattice spacing r_f (facilitation distance) and trapping frequency ω . (b) Two atom energy spectrum depending on distance r . Laser coupling with Rabi frequency Ω to an avoided crossing of attractive and repulsive Rydberg-Rydberg interaction potentials creates a nearly harmonic potential. (c) Spin domain dynamics. Due to strong detuning (see text) spin domains can only grow or shrink symmetrically at the edges, but they cannot coalesce or split. Here m is the domain size and i is the spin position within the domain.

tation regime. Dipole interactions couple the electronic (spin) degrees of freedom with excited motional states (phonons) in the tweezer traps. This coupling produces strong non-local correlations throughout the spin domain and non-classical center of mass movements of the Rydberg atoms in the form of squeezing. Finally, a shift in phonon ground state energy slightly detunes Rydberg atoms from resonance, causing emergent Bloch oscillations [25] in the growth dynamics of spin domains.

Physical System – We consider a 1D chain of N atoms in tweezer traps with lattice spacing r_f , each having an

internal electronic (spin) and a vibrational (phonon) degree of freedom with trapping frequency ω , see Fig. 1a. The atoms are laser coupled with a Rabi frequency Ω between a ground $|\downarrow\rangle$ and a high lying Rydberg $|\uparrow\rangle$ state. Furthermore, the laser has a large detuning from resonance Δ , such that $\Delta \gg \Omega$. Strong dipolar interactions between Rydberg atoms give rise to a Rydberg-Rydberg interaction potential $V(\hat{r}_{ij})$, where \hat{r}_{ij} corresponds to the interatomic distance. The full Hamiltonian is given by

$$\hat{H} = \sum_{j=1}^N \Omega \hat{\sigma}_j^x + \Delta \hat{n}_j + \omega \left(\hat{a}_j^\dagger \hat{a}_j + \frac{1}{2} \right) + \sum_{i < j} V(\hat{r}_{ij}) \hat{n}_i \hat{n}_j, \quad (1)$$

with $\hat{\sigma}^x = |\uparrow\rangle\langle\downarrow| + |\downarrow\rangle\langle\uparrow|$, and projection operator onto Rydberg states $\hat{n} = |\uparrow\rangle\langle\uparrow|$, and $\hbar = 1$.

Typically the dipole potential takes the form of a van-der-Waals (vdW) potential, i.e. $V(\hat{r}_{ij}) \sim \hat{r}_{ij}^{-6}$ [2], which is nearly linear at the lattice spacing r_f , and gives rise to strong repulsive (or attractive) forces between atoms in the Rydberg state. While mechanical forces resulting from these interactions completely cancel out inside a defect free domain of excited Rydberg atoms (spin domain), they are highly relevant at the edges. This phonon source at the borders can make the spin domain unstable and thus severely affect the facilitation dynamics [26]. This strong effect can be partially avoided by laser coupling from a ground state to an avoided crossing of two high-lying Rydberg states (see Fig. 1b), which is the situation we consider here (cf. [28] for an experimental realization). In this case the interaction potential is approximately harmonic, and can even be inverted when laser coupling to the lower avoided crossing level. As opposed to the vdW potential, the resulting Lennard-Jones-type potential actually stabilizes neighboring Rydberg atoms, instead of pushing them apart. Finally, we consider the system under the *facilitation constraint*, i.e. $V(r_f) + \Delta = 0$, where the detuning cancels out the dipole potential at the lattice spacing r_f . As a result, atoms neighbored by exactly *one* Rydberg atom are resonantly coupled to the light field.

Assuming the Lennard-Jones-type potential and only nearest neighbor interactions, we can write the Rydberg-Rydberg interaction to second-order as $V(\hat{r}_{j,j+1}) \approx V(r_f) + \frac{1}{2}V''(r_f)(\hat{r}_{j,j+1} - r_f)^2$. The relative distance can be expressed as $\hat{r}_{j,j+1} = r_f + \hat{x}_{j+1} - \hat{x}_j$, where \hat{x}_j is the position operator of the j th atom relative to the center of tweezer trap j . Expressing the position operator in terms of bosonic creation and annihilation operators, i.e. $\hat{x}_j = \sqrt{\frac{1}{2m\omega}}(\hat{a}_j^\dagger + \hat{a}_j)$, we receive the spin-phonon Hamiltonian as

$$\hat{H} = \sum_{j=1}^N \left\{ \Omega \hat{\sigma}_j^x + \Delta \hat{n}_j + \omega \left(\hat{a}_j^\dagger \hat{a}_j + \frac{1}{2} \right) + V_{NN}^{(0)} \hat{n}_j \hat{n}_{j+1} + \kappa \left(\hat{S}_j + \hat{S}_{j+1} - 2\hat{T}_{j,j+1} \right) \hat{n}_j \hat{n}_{j+1} \right\}, \quad (2)$$

with $V_{NN}^{(0)} \equiv V(r_f)$ and spin-phonon coupling $\kappa = V''(r_f)/4m\omega$. Here we introduced the operators $\hat{S}_j = \hat{a}_j^{\dagger 2} + \hat{a}_j^2 + 2\hat{a}_j^\dagger \hat{a}_j + 1$ describing *local* squeezing terms and $\hat{T}_{j,j+1} = \hat{a}_{j+1}^\dagger \hat{a}_j^\dagger + \hat{a}_{j+1}^\dagger \hat{a}_j + \text{h.c.}$ describing *non-local* pair-creation/annihilation, as well as phonon transport terms. κ is positive (negative) when coupling to the upper (lower) avoided crossing level, see Fig. 1b. As we will show in the following, the quadratic and transport terms, not present in the linear approximation of strictly local phonons assumed in [26], are crucial as they lead to non-classical correlations in the atomic positions and to a fast thermalization of local degrees of freedom in the dynamics from a general initial state.

We perform numerical simulations using a time evolving block decimation (TEBD) algorithm [29] on the Hamiltonian (2). For all simulations we use $\omega = 8\Omega$, $N = 100$, $V_{NN}^{(0)} = 500\Omega$, and we truncate the local phonon Hilbert space at $n_{\max} = 7$. As a result of the strong detuning Δ , only atoms with a single Rydberg neighbor are resonantly laser coupled. Consequently, the many-body spin dynamics reduce to the dynamics of spin domains which can either grow or shrink at the edges with rate Ω . However, due to Rydberg blockade two domains cannot coalesce or split [25] (see Fig. 1c).

Squeezed phonon states inside a Rydberg cluster – Let us first discuss the behaviour of the system well inside a large connected cluster of m excited Rydberg atoms. Inside the domain the Rabi coupling is far off-resonant as any given atom experiences the shift from *two* Rydberg atoms, where we assume $\Omega \ll \Delta = V_{NN}^{(0)}$. As a consequence we can disregard the spin dynamics and consider only the motional degrees of freedom.

The phonon Hamiltonian inside the fixed spin domain reads

$$\hat{h}_p = \sum_{j=1}^m \left\{ \omega \left(\hat{a}_j^\dagger \hat{a}_j + \frac{1}{2} \right) + \kappa \left(\hat{S}_j + \hat{S}_{j+1} - 2\hat{T}_{j,j+1} \right) \right\} \quad (3)$$

In the Supplemental Material we diagonalize this phonon Hamiltonian by introducing the Fourier and Bogoliubov transformed phonon operator with normalized lattice momentum $k = \frac{2\pi}{m-1}q$, and $q = 1, 2, \dots, m-1$:

$$\hat{d}_k = \frac{1}{\sqrt{m-1}} \sum_{j=1}^{m-1} e^{-ijk} \hat{d}_j, \quad (4)$$

where $\hat{d}_j = (u \hat{a}_j - v \hat{a}_j^\dagger)$, and $u = \cosh \theta$ and $v = \sinh \theta$. Squeezing terms are eliminated at the angle $\theta_c = \frac{1}{2} \text{artanh} \left(-\frac{4\kappa(1-\cos aq)}{\omega+4\kappa(1-\cos aq)} \right)$, with $a = \frac{2\pi}{m-1}$. Assuming a sufficiently large spin domain, we can introduce continuous fields $\hat{d}(k) = \lim_{m \rightarrow \infty} \hat{d}_k \sqrt{\frac{m-1}{2\pi}}$ (see Supplementary) and find

$$\hat{h}_p(m) \approx \int_0^{2\pi} dk \tilde{\omega}(k) \left(\hat{d}^\dagger(k) \hat{d}(k) + \frac{m-1}{4\pi} \right). \quad (5)$$

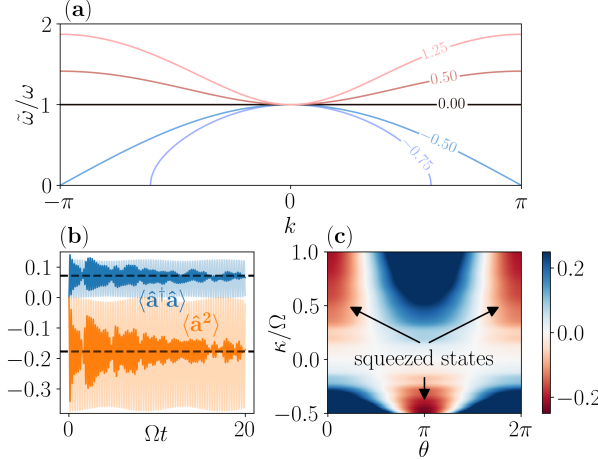


FIG. 2. *Phonon Dynamics.* (a) Dispersion relation from eq. (6) for different values of κ/Ω (inline numbers). Here, $\kappa/\Omega = -0.5$ corresponds to the critical coupling strength κ_c and $\kappa/\Omega = -0.75$ is in the unstable phase as $\tilde{\omega}$ becomes imaginary for $|k| \gtrsim 0.6\pi$. (b) Dynamics of expectation values of local oscillators \hat{a}_j in center of spin domain of size $m = 9$ and for $\kappa = \Omega$. The faint blue and orange lines are the corresponding values without phonon transport, i.e. setting $\hat{T}_{j,j+1} = 0$ in Hamiltonian (2). (c) Variance of generalized position operator minus vacuum variance, i.e. $\langle \Delta \hat{Q}^2 \rangle - 1$, with $\hat{Q}_j = e^{i\theta} \hat{a}_j^\dagger + e^{-i\theta} \hat{a}_j$ for site j in center of cluster of size $m = 9$, with $\kappa = \Omega$, and at time $\Omega t = 20$. For positive couplings, $\kappa > 0$, the system exhibits squeezed position states and for negative couplings, $\kappa < 0$, the system exhibits squeezed momentum states.

The phonon dispersion (plotted in Fig. 2a) is given by

$$\tilde{\omega}(k) = \sqrt{\omega^2 + 8\omega\kappa(1 - \cos k)}. \quad (6)$$

From this we can readily see that the phonons become unstable at the critical coupling strength $\kappa_c \equiv -\frac{\omega}{16}$. Since we use $\omega = 8\Omega$ for all simulations, this corresponds to $\kappa_c = -\frac{1}{2}\Omega$. At κ_c we find a mode softening for $k = \pm\pi$. For $\kappa > \kappa_c$ the ground state of the phonon Hamiltonian is the vacuum state in all \hat{d}_q , corresponding to a correlated squeezed vacuum of the local oscillators \hat{a}_j .

Since in any realistic experiment, the ground state of the total Hamiltonian cannot be prepared, we in the following consider a system prepared in a finite spin domain of length m and all atoms to be prepared in the ground state of the local oscillators \hat{a}_j . As shown in Fig. 3b due to the phonon transport terms, local observables quickly approach a stationary value in the center of a large spin chain.

The long-time expectation values of the local phonon operators within the spin domain, i.e. $\langle \hat{a}^\dagger \hat{a} \rangle$ and $\langle \hat{a}^2 \rangle$, can be calculated as follows: As the phonon Hamiltonian is diagonal in the \hat{d} basis, $\langle \hat{d}^\dagger \hat{d} \rangle$ is constant, and $\langle \hat{d}^2 \rangle_t =$

$\langle \hat{d}^2 \rangle_0 e^{-2i\tilde{\omega}t}$. Therefore, the time averaged values of $\langle \hat{a}^\dagger \hat{a} \rangle$ and $\langle \hat{a}^2 \rangle$ can be obtained by expressing these operators in the \hat{d} basis and neglecting $\langle \hat{d}^2 \rangle$ terms. We receive the time averaged operator values (for details see Supplementary Material) as

$$\langle \hat{a}^\dagger \hat{a} \rangle = +\frac{\kappa}{\omega} + \frac{1}{8} \left(\sqrt{\frac{\omega}{\omega + 16\kappa}} - 1 \right) \quad (7a)$$

$$\langle \hat{a}^2 \rangle = -\frac{\kappa}{\omega} + \frac{1}{8} \left(\sqrt{\frac{\omega}{\omega + 16\kappa}} - 1 \right). \quad (7b)$$

In Fig. 2b we have plotted these values as dashed lines along with the time evolution of local phonon correlations inside the domain including (dark lines) and excluding (faint lines) transport, obtained by TEBD simulations. We see a very good agreement. Without transport terms, i.e. $\hat{T}_{j,j+1} = 0$, the local phonon operators oscillate, whereas, in the presence of phonon transport these quantities thermalize despite the pure unitary evolution of \hat{H} , following the eigenstate thermalization hypothesis (ETH) [30, 31].

Finally, we want to quantify the degree of squeezing present in local oscillators, as a result of dipolar interactions. To this extent, we can regard the variance of a generalized position operator $\langle \Delta \hat{Q}^2 \rangle$, defined as [32] $\hat{Q} = e^{i\theta} \hat{a}_j^\dagger + e^{-i\theta} \hat{a}_j$, where the angle θ allows us to sample (q, p) phase space. Under this convention, the vacuum value is $\langle \Delta \hat{Q}^2 \rangle_{\text{vac}} = 1$. In Fig. 2d, $\langle \Delta \hat{Q}^2 \rangle - 1$ is plotted over the coupling κ and the angle θ . In the figure, negative values correspond to states which are more strongly localized than vacuum fluctuations, i.e. squeezed states.

For positive couplings, i.e. $\kappa > 0$, we find squeezed position states, i.e. the variance is minimal for $\theta = 0$. This results from atoms being subject to the tweezer trapping potential and an additional trapping potential emerging from the Rydberg-Rydberg interaction. For negative couplings, i.e. $\kappa < 0$, the Rydberg-Rydberg interaction potential is inverted and the system converges toward a mode softening at criticality at $k = \pm\pi$. Consequently, momentum states become squeezed.

Correlated Phonon Behavior - Having discussed the local behavior of phonons we now turn to their correlations. To this extent, we can regard the displacement correlation $C_{ij} \equiv \langle \hat{x}_i \hat{x}_{i+j} \rangle$. For positive values of C_{ij} , phonons i and j displace from equilibrium in the same direction, whereas for negative values of C_{ij} they displace in opposite directions. Within spin domains we find strong phonon-phonon correlations, which become long-range near κ_c . Moreover, we find the oscillatory behavior of phonons in the domain to change qualitatively from in-phase correlations ($\kappa > 0$) to out-of-phase correlations ($\kappa < 0$) (see Fig. 3a).

Using $\hat{x}_i = \hat{a}_i^\dagger + \hat{a}_i$, we can express C_{ij} in terms of \hat{d} -basis phonons. Neglecting the oscillating terms \hat{d}^2 , this

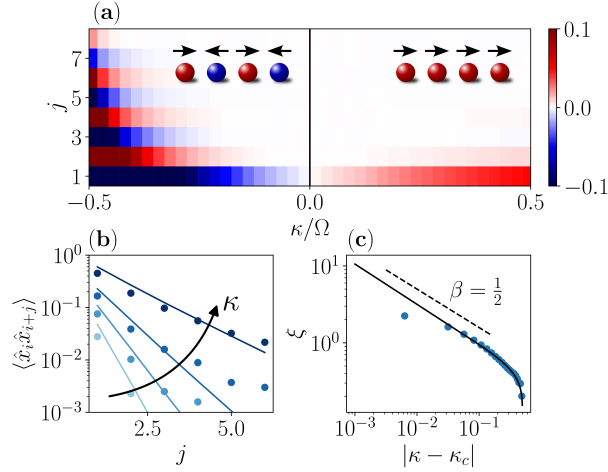


FIG. 3. *Phonon Correlations.* (a) Time-averaged displacement correlation $C_{ij} \equiv \langle \hat{x}_i \hat{x}_{i+j} \rangle$ from TEBD simulations for $i = -3$ and an initial spin domain size $r_0 = 9$ ($i = 0$ is the domain center). A positive product (red) signifies phonons oscillating in phase and a negative product (blue) corresponds to out of phase oscillations. (b) Spatial correlation of i, j for $\kappa/\Omega = [-0.44, -0.34, -0.24, -0.14]$ and for $i = -3$ from numerics (dots), as well as analytically calculated correlation C_{ij} from eq. (8) (solid lines). (c) Correlation length ξ taken from exponential fit of decay of C_{ij} with distance between (i, j) from numerics (dots) and analytics (solid black line). The correlation length extracted from numerics saturates due to the finite size of the spin domain. Approaching κ_c , ξ diverges yielding the mean field exponent $\beta = \frac{1}{2}$.

yields

$$C_{ij} = \frac{1}{2\pi} \int_0^{2\pi} dk \quad (8)$$

$$e^{ik(i-j)} (u+v)^2 + 2v^2 (u+v)^2 \cos(k(i-j)),$$

where u and v are k dependent (see text above). The solution to this integral yields an exponential decay of C_{ij} with the distance between (i, j) for $|\kappa - \kappa_c| > 10^{-4}$ (solid lines in Fig. 3b). From this we can extract a correlation length ξ using $C_{ij} \sim e^{-\frac{|i-j|}{\xi}}$. This correlation length diverges near the critical point κ_c and scales as

$$\xi \sim |\kappa - \kappa_c|^{-\beta}, \quad (9)$$

yielding the mean field critical exponent $\beta = \frac{1}{2}$ (cf. Fig. 3c).

Dynamics of spin domains – Finally, we want to investigate the dynamics of spin domains. As stated above, spin domains can either grow or shrink at rate Ω , but can never coalesce or split. Given an initial spin domain of size, say $m_0 = 5$, the domain can either grow or shrink by flipping a spin on the left or right. Therefore, the domain state, characterized by its size and denoted as $|5\rangle$, is resonantly coupled to the states $|6_L\rangle$, $|6_R\rangle$, $|4_L\rangle$, and $|4_R\rangle$ at

rate Ω . Here, the number refers to the size of the domain, and L (left) and R (right) refer to the position of the flipped spin relative to the domain center. The Hamiltonian conserves parity. Therefore, the initial state $|5\rangle$ only couples to the symmetric states $|6S\rangle \equiv \frac{1}{\sqrt{2}}(|6_L\rangle + |6_R\rangle)$ and $|4S\rangle \equiv \frac{1}{\sqrt{2}}(|4_L\rangle + |4_R\rangle)$. The states $|6S\rangle$ and $|4S\rangle$ in turn couple resonantly with the states $|7S\rangle$ and $|3S\rangle$ respectively. Therefore, the dynamics of the spin domain reduce to a ladder, with individual states being characterized only by their size. Utilizing this, we can describe the spin domain of size m as a particle at position m in a lattice [25] and the Hamiltonian reduces to

$$\hat{H} = \sum_{m=1}^{\infty} \Omega(|m\rangle \langle m+1| + \text{h.c.})$$

$$+ \left[m\Delta + (m-1)V_{\text{NN}}^{(0)} + \hat{h}_p(m) \right] |m\rangle \langle m|. \quad (10)$$

This Hamiltonian describes the tight-binding model [33] of a particle at position m in a semi-infinite lattice, i.e. $m \in [1, \infty)$, with hopping amplitude Ω . Furthermore, there is a site dependent energy given by \hat{h}_p (cf. eq. (5)) under the facilitation constraint, i.e. $\Delta + V_{\text{NN}}^{(0)} = 0$. For sufficiently large cluster sizes, where the continuum approximation (5) is valid, only the vacuum term in the phonon Hamiltonian $\hat{h}_p(m)$ depends on the cluster size m , and $\hat{d}^\dagger(k)\hat{d}(k)$ which is a constant of motion, can be treated as a number C . Thus the Hamiltonian reduces to

$$\hat{H} = \sum_{m=1}^{\infty} \Omega(|m\rangle \langle m+1| + \text{h.c.}) + \epsilon_0(m) |m\rangle \langle m|, \quad (11)$$

where $\epsilon_0(m) = C + m\Delta + (m-1) \left[V_{\text{NN}}^{(0)} + \frac{\langle \tilde{\omega}(k) \rangle_k - \omega}{2} \right]$, and $\langle \tilde{\omega} \rangle_k = \frac{1}{2\pi} \int_0^{2\pi} dk \tilde{\omega}(k)$ (this integral is explicitly evaluated in the Supplementary Material). Importantly the on-site energy $\epsilon_0(m)$ is *linear* in m , which corresponds to a potential gradient. Such a system is known to show Bloch oscillations [34]. The Bloch period is given by $T = 2\pi/|\partial_m \epsilon_0|$. Under the facilitation constraint, $\Delta + V_{\text{NN}}^{(0)} = 0$, T only depends on the difference in phonon ground state energy between the \hat{a} and \hat{d} basis, and is given by

$$T = \frac{4\pi}{|\langle \tilde{\omega}(k) \rangle_k - \omega|}. \quad (12)$$

In Fig. 4 we have shown the cluster dynamics starting from an initial cluster of size 9, obtained from TEBD simulations of the microscopic Hamiltonian (2), for different values of the spin-phonon coupling strength κ . Both, density plots (a)-(c) and the autocorrelation function (d) clearly show Bloch-like oscillations with a period that agrees perfectly with eq.(12) (see red dashed lines in Fig. 4).

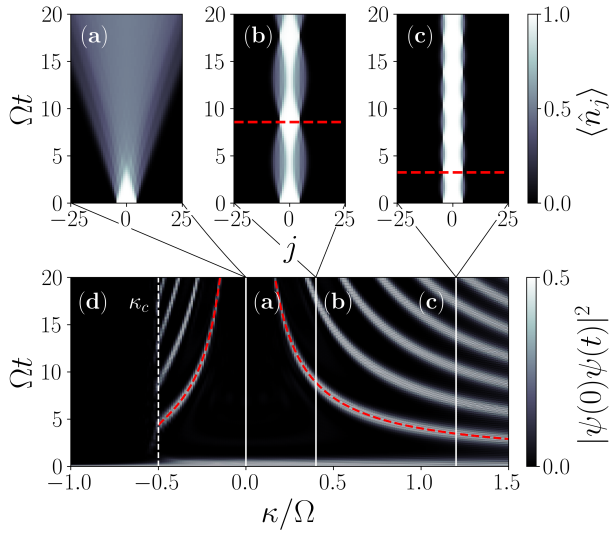


FIG. 4. *Spin Dynamics.* Population of Rydberg state $|\uparrow\rangle$ over time under the facilitation constraint with: (a) no spin-phonon coupling $\kappa = 0$ showing ballistic expansion, and with coupling showing Bloch oscillations in time for (b) $\kappa = 0.4\Omega$ and (c) $\kappa = 1.2\Omega$. Autocorrelation function in time (d) showing periodic behavior, which diverges without coupling at $\kappa = 0$ and when the phonons become unstable at $\kappa = \kappa_c$ (see main text). The red dashed line in all figures corresponds to the Bloch period given by eq. (12). The initial domain size is $r_0 = 9$.

Summary – In summary, we have looked at the dynamics of a chain of Rydberg atoms trapped in tweezer arrays under the facilitation constraint. By tailoring the interaction potential to a Lennard-Jones-type potential, spin-phonon coupling due to Rydberg-Rydberg interactions not only stabilize the chain from mechanical forces, but also lead to the emergence of strong correlations and non-classical motional states in the system. Moreover, as a result of spin-phonon interactions causing emergent Bloch oscillations, the original spin domain becomes localized for spin-phonon coupling strengths on the order of the Rabi frequency.

ACKNOWLEDGMENTS

The authors thank M. Magoni for fruitful discussions. Financial support from the DFG through SFB TR 185, Project No. 277625399, is gratefully acknowledged. The authors also thank the Allianz für Hochleistungsrechnen (AHRP) for giving us access to the “Elwetritsch” HPC Cluster.

- [1] A. Browaeys and T. Lahaye, *Nature Physics* **16**, 132 (2020).
- [2] T. F. Gallagher, *Rydberg Atoms* (Cambridge University Press, 1994).
- [3] D. Barredo, S. De Léséleuc, V. Lienhard, T. Lahaye, and A. Browaeys, *Science* **354**, 1021 (2016).
- [4] M. Endres, H. Bernien, A. Keesling, H. Levine, E. R. Anschuetz, A. Krajenbrink, C. Senko, V. Vuletic, M. Greiner, and M. D. Lukin, *Science* **354**, 1024 (2016).
- [5] D. Barredo, V. Lienhard, S. De Léséleuc, T. Lahaye, and A. Browaeys, *Nature* **561**, 79 (2018).
- [6] H. Weimer, M. Müller, I. Lesanovsky, P. Zoller, and H. P. Büchler, *Nature Physics* **6**, 382 (2010).
- [7] H. Weimer, R. Löw, T. Pfau, and H. P. Büchler, *Phys. Rev. Lett.* **101**, 250601 (2008).
- [8] H. Labuhn, D. Barredo, S. Ravets, S. De Léséleuc, T. Macrì, T. Lahaye, and A. Browaeys, *Nature* **534**, 667 (2016).
- [9] P. Schauß, J. Zeiher, T. Fukuhara, S. Hild, M. Cheneau, T. Macrì, T. Pohl, I. Bloch, and C. Groß, *Science* **347**, 1455 (2015).
- [10] V. Lienhard, S. de Léséleuc, D. Barredo, T. Lahaye, A. Browaeys, M. Schuler, L.-P. Henry, and A. M. Läuchli, *Physical Review X* **8**, 021070 (2018).
- [11] E. Guardado-Sánchez, P. T. Brown, D. Mitra, T. Devakul, D. A. Huse, P. Schauß, and W. S. Bakr, *Physical Review X* **8**, 021069 (2018).
- [12] D. Barredo, H. Labuhn, S. Ravets, T. Lahaye, A. Browaeys, and C. S. Adams, *Physical Review Letters* **114**, 113002 (2015).
- [13] S. De Léséleuc, V. Lienhard, P. Scholl, D. Barredo, S. Weber, N. Lang, H. P. Büchler, T. Lahaye, and A. Browaeys, *Science* **365**, 775 (2019).
- [14] J. Schachenmayer, I. Lesanovsky, A. Micheli, and A. Daley, *New Journal of Physics* **12**, 103044 (2010).
- [15] H. Bernien, S. Schwartz, A. Keesling, H. Levine, A. Omran, H. Pichler, S. Choi, A. S. Zibrov, M. Endres, M. Greiner, et al., *Nature* **551**, 579 (2017).
- [16] R. Samajdar, S. Choi, H. Pichler, M. D. Lukin, and S. Sachdev, *Physical Review A* **98**, 023614 (2018).
- [17] G. Semeghini, H. Levine, A. Keesling, S. Ebadi, T. T. Wang, D. Bluvstein, R. Verresen, H. Pichler, M. Kalinowski, R. Samajdar, A. Omran, S. Sachdev, A. Vishwanath, M. Greiner, V. Vuletić, and M. D. Lukin, *Science* **374**, 1242 (2021).
- [18] S. Ohler, M. Kiefer-Emmanouilidis, and M. Fleischhauer, *Physical Review Research* **5**, 013157 (2023).
- [19] C. Ates, T. Pohl, T. Pattard, and J. M. Rost, *Physical Review Letters* **98**, 023002 (2007).
- [20] T. Wintermantel, M. Buchhold, S. Shevate, M. Morgado, Y. Wang, G. Lochead, S. Diehl, and S. Whitlock, *Nature Communications* **12**, 103 (2021).
- [21] D. Brady and M. Fleischhauer, *Physical Review A* **108**, 052812 (2023).
- [22] S. Helmrich, A. Arias, G. Lochead, T. Wintermantel, M. Buchhold, S. Diehl, and S. Whitlock, *Nature* **577**, 481 (2020).
- [23] D. Brady, J. Bender, P. Mischke, S. Ohler, T. Niederprüm, H. Ott, and M. Fleischhauer, *Physical Review Research* **6**, 013052 (2024).

- [24] S. Ohler, D. Brady, P. Mischke, J. Bender, H. Ott, T. Niederprüm, W. Ripken, J. S. Otterbach, and M. Fleischhauer, arXiv preprint [10.48550/arXiv.2502.14757](https://arxiv.org/abs/10.48550/arXiv.2502.14757) (2025).
- [25] M. Magoni, P. P. Mazza, and I. Lesanovsky, *Physical Review Letters* **126**, 103002 (2021).
- [26] M. Magoni, C. Nill, and I. Lesanovsky, *Physical Review Letters* **132**, 133401 (2024).
- [27] W. Li, C. Ates, and I. Lesanovsky, *Physical Review Letters* **110**, 213005 (2013).
- [28] S. Hollerith, J. Zeiher, J. Rui, A. Rubio-Abadal, V. Walther, T. Pohl, D. M. Stamper-Kurn, I. Bloch, and C. Gross, *Science* **364**, 664 (2019).
- [29] G. Vidal, *Physical Review Letters* **91**, 147902 (2003).
- [30] J. M. Deutsch, *Physical Review A* **43**, 2046 (1991).
- [31] M. Srednicki, *Physical Review E* **50**, 888 (1994).
- [32] L. Mandel and E. Wolf, *Optical Coherence and Quantum Optics* (Cambridge University Press, 1995).
- [33] J. C. Slater and G. F. Koster, *Physical Review* **94**, 1498 (1954).
- [34] F. Bloch, *Zeitschrift für Physik* **52**, 555 (1929).

SUPPLEMENTAL MATERIAL
COHERENT SPIN-PHONON COUPLING IN A LATTICE USING RYDBERG FACILITATION

Diagonalization of Phonon Hamiltonian

In the following we diagonalize the phonon Hamiltonian under the Born-Oppenheimer approximation for a fixed domain length m . This is given by

$$\hat{h}_p = \sum_{l=1}^{m-1} \omega \left(\hat{a}_l^\dagger \hat{a}_l + \frac{1}{2} \right) + \kappa \left(\hat{S}_l + \hat{S}_{l+1} - 2\hat{T}_{l,l+1} \right), \quad (13)$$

with *local* squeezing terms $\hat{S}_l = \hat{a}_l^{\dagger 2} + \hat{a}_l^2 + 2\hat{a}_l^\dagger \hat{a}_l + 1$ and *non-local* pair creation/annihilation and transport terms $\hat{T}_{l,l+1} = \hat{a}_{l+1}^\dagger \hat{a}_l^\dagger + \hat{a}_{l+1}^\dagger \hat{a}_l + \text{h.c.}$. First, we perform a Fourier transform of the phonon operators with

$$\hat{a}_l = \frac{1}{\sqrt{m-1}} \sum_{q=1}^{m-1} e^{iqja} \hat{A}_q, \quad (14)$$

with the integer $q = 1, 2, \dots, m-1$ and $a = \frac{2\pi}{m-1}$. Inserting eq. (14) into Hamiltonian (13), we receive

$$\hat{h}_p = \sum_{q=1}^{m-1} \frac{\omega + 4\kappa}{2} + (\omega + 2\gamma_q) \hat{A}_q^\dagger \hat{A}_q + \gamma_q \left(\hat{A}_q^\dagger \hat{A}_{-q}^\dagger + \hat{A}_q \hat{A}_{-q} \right), \quad (15)$$

with $\gamma_q \equiv 2\kappa(1 - \cos(aq))$. This corresponds to a squeezing Hamiltonian, with the strength of squeezing given by $\gamma_k \propto \kappa$ and vanishing for $\kappa = 0$. With the Bogoliubov transformation

$$\hat{A}_q^\dagger = u\hat{d}_q^\dagger + v\hat{d}_{-q}, \quad (16)$$

with $u = \cosh \theta$, $v = \sinh \theta$, and $u^2 - v^2 = 1$, we can eliminate the squeezing terms. Inserting eq. (16) into the Fourier transformed Hamiltonian (15), we receive

$$\begin{aligned} \hat{h}_p = \sum_{q=1}^{m-1} \frac{\omega + 4\kappa}{2} &+ \left((\omega + 2\gamma_q)uv + \gamma_q(u^2 + v^2) \right) (\hat{d}_q^\dagger \hat{d}_{-q}^\dagger + \hat{d}_q \hat{d}_{-q}) \\ &+ \left((\omega + 2\gamma_q)(u^2 + v^2) + 4\gamma_q uv \right) \left(\hat{d}_q^\dagger \hat{d}_q + \frac{1}{2} \right) - \frac{\omega + 2\gamma_q}{2}. \end{aligned} \quad (17)$$

Where the following term vanishes, if the domain size is large enough, i.e.

$$\sum_{q=1}^{m-1} \frac{\omega + 4\kappa}{2} - \frac{\omega + 2\gamma_q}{2} = -2\kappa \sum_{q=1}^{m-1} \cos(aq) \approx 0. \quad (18)$$

The squeezing terms $\hat{d}_q^\dagger \hat{d}_{-q}^\dagger$ and $\hat{d}_q \hat{d}_{-q}$ in eq. (17) are eliminated for the critical angle

$$\theta_c = \frac{1}{2} \operatorname{artanh} \left(- \frac{4\kappa(1 - \cos aq)}{\omega + 4\kappa(1 - \cos aq)} \right). \quad (19)$$

Inserting θ_c into eq. (17), following some arithmetic we receive the Hamiltonian

$$\hat{h}_p(m) = \sum_k \tilde{\omega}_k \left(\hat{d}_k^\dagger \hat{d}_k + \frac{1}{2} \right), \quad (20)$$

where we have introduced the normalized lattice momentum $k = \frac{2\pi}{m-1}q$ with $q = 1, 2, \dots, m-1$, and the oscillator frequency

$$\tilde{\omega}_k = (\omega + 2\gamma_q) \cosh 2\theta_c + 2\gamma_q \sinh 2\theta_c \quad (21)$$

$$\begin{aligned} &= \frac{\omega + 2\gamma_q}{\sqrt{1 - \left(\frac{2\gamma_q}{\omega + 2\gamma_q} \right)^2}} + \frac{-\frac{4\gamma_q^2}{\omega + 2\gamma_q}}{\sqrt{1 - \left(\frac{2\gamma_q}{\omega + 2\gamma_q} \right)^2}} \end{aligned} \quad (22)$$

$$= \sqrt{\omega^2 + 8\omega\kappa(1 - \cos(k))}. \quad (23)$$

Hamiltonian (20) is now diagonal in the \hat{d} basis. Assuming a sufficiently large domain, we can perform an integral approximation of the sum in eq. (20). With this, the ladder operators \hat{d}_k are now treated as field operators $\hat{d}(k)$ for the continuous variable k . Assuming $m \gg 1$ and using the continuum mapping

$$\hat{d}_k \longrightarrow \hat{d}(k) \sqrt{\frac{2\pi}{m-1}}, \quad \sum_k \longrightarrow \frac{m-1}{2\pi} \int_0^{2\pi} dk, \quad (24)$$

such that $\sum_k \hat{d}_k^\dagger \hat{d}_k = \int dk \hat{d}^\dagger(k) \hat{d}(k)$ we receive the Hamiltonian

$$\hat{h}_p(m) = \int_0^{2\pi} dk \tilde{\omega}(k) \left(\hat{d}^\dagger(k) \hat{d}(k) + \frac{m-1}{4\pi} \right), \quad (25)$$

with $\tilde{\omega}(k) = \sqrt{\omega^2 + 8\omega\kappa(1 - \cos k)}$. In particular, with the exception of the factor $(m-1)$ in the vacuum term, \hat{h}_p is completely independent of the domain size, position, center of mass, or any real space index j .

Squeezed Phonon Ground State Energy

From eq. (25) we can get the ground state energy of \hat{h}_p for $\hat{d}^\dagger(k) \hat{d}(k) = 0$. The solution of the integral is given by

$$\langle \tilde{\omega}(k) \rangle_k \equiv \frac{1}{2\pi} \int_0^{2\pi} dk \tilde{\omega}(k) \quad (26)$$

$$= \frac{1}{2\pi} \int_0^{2\pi} dk \sqrt{\omega^2 + 8\omega\kappa(1 - \cos k)} \quad (27)$$

$$= \frac{1}{2\pi} \left[2\omega \text{EllipticE} \left(-\frac{16\kappa}{\omega} \right) + 2\sqrt{\omega^2 + 16\omega\kappa} \text{EllipticE} \left(\frac{16\omega\kappa}{\omega^2 + 16\omega\kappa} \right) \right], \quad (28)$$

where $\text{EllipticE}(\cdot)$ denotes the complete elliptic integral of the second kind. Therefore, we find the ground state energy of the phonon Hamiltonian to be $(m-1) \frac{\langle \tilde{\omega} \rangle_k}{2}$, i.e. it is proportional to the domain size m and parametrically dependent on κ and ω .

Calculation of Phonon Observables

In this section we want to calculate the phonon observables $\langle \hat{a}^\dagger \hat{a} \rangle$, $\langle \hat{a}^2 \rangle$, and $C_{ij} \equiv \langle \hat{x}_i \hat{x}_{i+j} \rangle$. All of these can be obtained by expressing them in the \hat{d} -basis and neglecting fluctuations, i.e. $\langle \hat{d}^2 \rangle \approx 0$. Since $n_d \equiv \langle \hat{d}^\dagger \hat{d} \rangle$ is constant, we can write $n_d(t) = n_d(0)$. For the initial condition that \hat{a} -phonons are in the Fock $|0\rangle$ state, all contributions $\langle \hat{a}_j^\dagger \hat{a}_j \rangle$ and $\langle \hat{a}_j^2 \rangle$ vanish at $t = 0$, and the population of \hat{d} phonons is given by

$$n_d(t) = n_d(0) = v^2. \quad (29)$$

Expressing the above mentioned observables in \hat{d} -phonons, with $a = \frac{2\pi}{m-1}$, and neglecting fluctuations, we receive in the homogeneous limit

$$\langle \hat{a}_j^\dagger \hat{a}_j \rangle = \frac{1}{m-1} \sum_q (u^2 + v^2) v^2 + v^2 \equiv \frac{1}{m-1} \sum_q 2u^2 v^2 \quad (30a)$$

$$\langle \hat{a}_j^2 \rangle = \frac{1}{m-1} \sum_q (u^2 + v^2) u v \quad (30b)$$

$$C_{ij} = \frac{1}{m-1} \sum_q e^{iqa(i-j)} (u + v)^2 + 2(u^2 + v^2) v^2 \cos(qa(i-j)), \quad (30c)$$

where we used $u^2 - v^2 = 1$. Assuming a sufficiently large cluster, $m \gg 1$, we can perform an integral approximation. Inserting $u = \cosh \theta_c$ and $v = \sinh \theta_c$, with θ_c given by eq. (19), using trigonometric relations we receive the integrals

$$\langle \hat{a}_j^\dagger \hat{a}_j \rangle = \frac{1}{\pi} \int_0^{2\pi} dk \frac{4\kappa^2(1-\cos k)^2}{\omega^2 + 8\omega\kappa(1-\cos k)} \quad (31a)$$

$$\langle \hat{a}_j^2 \rangle = \frac{1}{2\pi} \int_0^{2\pi} dk \frac{-2\omega\kappa(1-\cos k) - 8\kappa^2(1-\cos k)^2}{\omega^2 + 8\omega\kappa(1-\cos k)} \quad (31b)$$

$$C_{ij} = \frac{1}{2\pi} \int_0^{2\pi} dk e^{ik(i-j)} (u+v)^2 + 2(u^2+v^2)v^2 \cos(k(i-j)). \quad (31c)$$

The first two integrals can be analytically solved, yielding

$$\langle \hat{a}^\dagger \hat{a} \rangle = +\frac{\kappa}{\omega} + \frac{1}{8} \left(\sqrt{\frac{\omega}{\omega + 16\kappa}} - 1 \right) \quad (32a)$$

$$\langle \hat{a}^2 \rangle = -\frac{\kappa}{\omega} + \frac{1}{8} \left(\sqrt{\frac{\omega}{\omega + 16\kappa}} - 1 \right). \quad (32b)$$

7. Dephasing in Rydberg Facilitation Due to State-Dependent Dipole Forces

T. Schlegel*, E. Konstantinidou*, M. Fleischhauer, and D. Brady
[arXiv:2505.09314 \(2025\)](https://arxiv.org/abs/2505.09314)

In our final study, we want to find an analytic description of the dephasing rate of the Rydberg state. High dephasing rates are a well-known feature of Rydberg systems [18–20], however, a quantitative understanding has largely been missing. In this study, we analyze one source of dephasing, namely the dipolar repulsion between Rydberg atoms and derive an analytic expression for the dephasing rate. In the regime where the detuning is only slightly larger than the Rabi frequency, we are able to extract a dephasing rate from our simulations and find this to fit very well with our analytic expression.

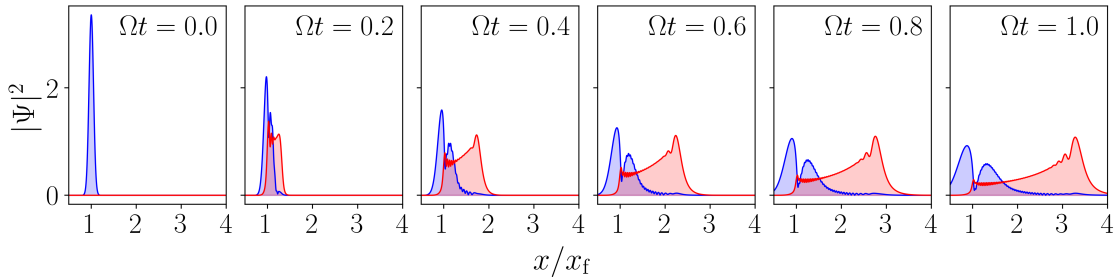


Figure 7.1.: Dynamics of ground (blue) and Rydberg state (red) wave packets in the dipole potential of an external Rydberg atom (located at $x = 0$). At $x/x_f = 1$ the atom is *facilitated*, i.e. the Rydberg state can be excited resonantly. Over time, the ground state diffuses in place, while the Rydberg state is first excited and then subsequently repelled away.

We consider an atom, laser-driven between an internal ground state with wavefunction Ψ_G and a high-lying Rydberg state with wavefunction Ψ_R . The atom is initially in its ground state and inside a tweezer trap with width σ which is turned off at time $t = 0$. We consider the atom to be in the dipole potential of an external Rydberg atom at the facilitation distance x_f . Since typically $x_f \gg \sigma$, for short time evolutions we can consider the problem to be one-dimensional, i.e. with the radial distance x to the external Rydberg atom.

In the dipole potential of the external Rydberg atom a force acts on the Rydberg state of the atom, repelling it, while the ground state of the atom diffuses in place. When looking at the density matrix ρ of the atom, we can identify the overlap of the ground and Rydberg state wavefunctions as the coherence of the atom, i.e.

$$\rho_{RG} = \int_{-\infty}^{\infty} dx \Psi_R^*(x, t) \Psi_G(x, t). \quad (7.1)$$

From the Maxwell-Bloch equations of a two-level atom in the presence of dephasing (with rate γ_{\perp}), we expect the coherence to decay exponentially. In our simulations and for facilitation conditions, where the laser detuning Δ is much larger than the Rabi frequency Ω , we find this coherence to decay incredibly fast. However, for $\Delta \gtrsim \Omega$, we find the coherence to decay exponentially on a longer time-scale than Ω , allowing us to extract a dephasing rate by fitting this decay with an exponent function.

In our analytic approach, we model the atom in first quantization. Starting from a Gaussian wave packet $\Psi_G(x, t = 0)$ in the potential $U(x)$ of the external Rydberg atom, we time evolve the system with respect to the time-dependent Schrödinger equation

$$i \frac{d}{dt} \begin{pmatrix} \Psi_R(x, t) \\ \Psi_G(x, t) \end{pmatrix} = \left[-\frac{1}{2m} \begin{pmatrix} \partial_x^2 & 0 \\ 0 & \partial_x^2 \end{pmatrix} + \begin{pmatrix} U(x) & \Omega \\ \Omega & 0 \end{pmatrix} \right] \begin{pmatrix} \Psi_R(x, t) \\ \Psi_G(x, t) \end{pmatrix}. \quad (7.2)$$

Assuming only small displacements from the facilitation distance, i.e. $x \approx x_f$, allows us to use perturbation theory in $U(x)$, where $U(x_f) = 0$. Using this, we can analytically solve the differential equation (7.2) and we receive a very good agreement between our analytical values of the dephasing rate γ_{\perp} and those extracted from numerical simulations of the wave packet dynamics.

Author Contributions

Contribution	Primary Role	Supportive Role
Analytic derivation of γ_{\perp}	T.S., D.B.	M.F.
Numeric simulations	E.K.	D.B.

*These authors contributed equally. The project was conceived by M.F. and supervised by M.F. and D.B.

Copyright

This work is licensed under the [Creative Commons Attribution 4.0 International license \(CC BY 4.0\)](#).

Dephasing in Rydberg Facilitation Due to State-Dependent Dipole Forces

Tom Schlegel*, Evangelia Konstantinidou*, Michael Fleischhauer, and Daniel Brady¹

¹Department of Physics and Research Center OPTIMAS,
RPTU Kaiserslautern, D-67663 Kaiserslautern, Germany

(Dated: May 15, 2025)

Rydberg atoms allow for the experimental study of open many-body systems and nonequilibrium phenomena. High dephasing rates are a generic feature of these systems, and therefore they can often be described by rate equations, i.e. in the classical limit. In this work, we analyze one potential origin of the decoherence in Rydberg atoms: dipole-force induced dephasing. As the wave function of the Rydberg (spin-up) state is repelled in the presence of another nearby Rydberg atom, while the ground (spin-down) state diffuses in place, the Franck-Condon overlap between the two spin components quickly decays causing a decoherence of the spin transition. With an analytic approach we obtain a simple expression for the dephasing rate of the Rydberg state depending on atomic and laser parameters, which agrees with numerical findings.

I. INTRODUCTION

Many-body systems of Rydberg atoms have proven to be an incredibly useful and versatile platform to study interacting spin systems, both in the quantum and classical regime, due to their strong interactions and long lifetimes [1]. Through recent advances in experimental control of neutral atoms, e.g. with tweezer arrays [2–4], Rydberg systems offer a powerful approach to investigate many-body lattice models [5, 6]. This includes simulations of the quantum spin Ising model [7–11], topological transport properties [12, 13], and nonequilibrium phase transitions [14–17] to name a few.

Laser driven Rydberg gases often feature strong dephasing. While this is a well known feature of these systems [18–20], a comprehensive understanding along with a quantitative description is largely missing. In the present paper, we identify one mechanism responsible for such a dephasing, which is of particular relevance for Rydberg facilitation. When regarded in the anti-blockade (facilitation) regime, excitations of Rydberg atoms can only occur in the presence of an already excited Rydberg atom [21]. In tweezer arrays, this allows for the study of many-body dynamics under localization [22] and kinetic constraints [23, 24]. When regarding the dynamics in a gas, strong dephasing rates emerge. Consequently, the dynamics become effectively classical and very large systems can be described to great accuracy by diagonal density matrix elements, leading to classical rate equations [25–28]. The incoherent regime is especially well suited for the study of open systems and nonequilibrium phase transitions [14, 17, 29]. In particular, in this regime experiments can be compared to large-scale numerical simulations.

In studies of lattice spin models with Rydberg atoms, ground-state atoms are initially trapped in an optical lattice or in tweezer potentials, which are subsequently switched off during the interaction. Therefore, we consider the case of an initially localized ground state atom here. In the regime of Rydberg facilitation differential dipole forces acting on the excited and ground states

cause a rapid dephasing of the transition, which we will analyze in the following.

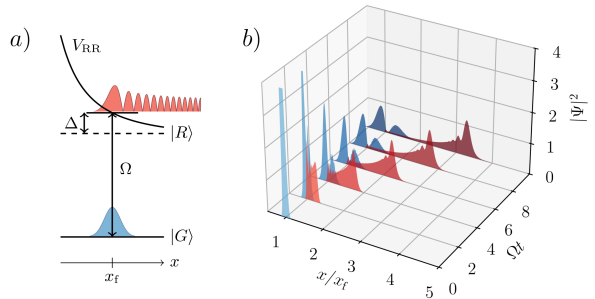


FIG. 1: (a) Internal atomic structure of an atom in an external Rydberg potential V_{RR} . The initially spatially localized ground state $|G\rangle$ is laser-coupled with a high-lying Rydberg state $|R\rangle$ with Rabi frequency Ω and detuning from resonance Δ . The Rydberg potential repels the excited part of the atom. (b) Spatially and temporally resolved dynamics of the ground (blue) and Rydberg state (red) wave packets for $\Delta/\Omega = 30$ and $\xi/\Omega = 0.01 \cdot 10^{-3}$.

In the facilitation regime, the laser coupling between the internal ground $|G\rangle$ and Rydberg $|R\rangle$ states of the atom, with Rabi frequency Ω , is off-resonant, with detuning from resonance $\Delta \gg \Omega$ (cf. Fig. 1a). In the absence of further couplings, the large detuning strongly suppresses the excitation of the Rydberg state. However, in the presence of another Rydberg atom, the energy of the excited state is shifted and becomes resonant at the interatomic distance x_f , i.e. $V_{RR}(x_f) - \Delta = 0$. As a result of the repulsive van-der-Waals potential, a strong dipole force acts on the excited state. Consequently, there is a fast decay of the Franck-Condon overlap between the ground and Rydberg state wavefunctions of the atom (cf. Fig. 1b). As we quantitatively analyze in the following, this leads to an effective dephasing of the internal-state dynamics. The motion-induced dephasing will in general not follow a simple exponential law and

the dephasing rate will be time dependent. However, for the excitation dynamics only short times after excitation are relevant and we will focus on this regime.

II. SYSTEM

To investigate the short-time dephasing dynamics, we consider a two-level atom coupled by a laser between its ground and a high-lying Rydberg state. The coupling laser has the Rabi frequency Ω and detuning from resonance Δ . Additionally, we consider the atom to be in the dipolar potential of an external Rydberg atom, located at position $\mathbf{x} = 0$. This dipolar potential typically takes the form $V_{RR} = \frac{c_\nu}{|\mathbf{x}|^\nu}$, where ν is an integer and c_ν is the potential coefficient [1]. If both atoms are coupled to the same Rydberg state, e.g. $|nS\rangle$, then the interaction potential is of a van-der-Waals (vdW) type [6] and $\nu = 6$. In order to account for the interplay between dipole forces acting on the spatial degree of freedom of the atom in the Rydberg state, we treat the atom in second quantization with two Schrödinger fields $\Psi_G(x)$ and $\Psi_R(x)$ describing the ground and Rydberg states, respectively. Since the vdW potential only depends on the euclidean distance between the atoms, we can restrict the problem to one spatial dimension, i.e. the radial distance x . For the relevant time scales, diffusion in the orthogonal directions is negligible.

The total potential $U_\nu(x)$ acting on the Rydberg state is the sum of the dipole potential V_{RR} and the detuning Δ , i.e.

$$U_\nu(x) = \frac{c_\nu}{x^\nu} - \Delta. \quad (1)$$

At the *facilitation distance* $x_f \equiv \sqrt[6]{\frac{c_\nu}{\Delta}}$ the interaction potential cancels the detuning and a resonant excitation of the state $|R\rangle$ becomes possible, i.e. $U_\nu(x_f) = 0$ (cf. Fig. 1a).

In the following, we consider an initial state $|\psi_0\rangle$ of the atom as a wave packet in the ground state with width σ and initial position at the facilitation distance, i.e. $x(t=0) = x_f$.

$$\Psi_R(x, t=0) = \langle 0 | \hat{\Psi}_R(x) | \psi_0 \rangle = 0. \quad (2a)$$

$$\Psi_G(x, t=0) = \langle 0 | \hat{\Psi}_G(x) | \psi_0 \rangle = \frac{1}{(\pi\sigma^2)^{\frac{1}{4}}} e^{-\frac{(x-x_f)^2}{2\sigma^2}} \quad (2b)$$

Under the time-dependent Schrödinger equation, the equations of motion for the ground and Rydberg state wave packets are given as

$$i\partial_t \begin{pmatrix} \Psi_R \\ \Psi_G \end{pmatrix} = \begin{pmatrix} -\frac{\partial_x^2}{2m} + U_\nu(x) & \Omega \\ \Omega & -\frac{\partial_x^2}{2m} \end{pmatrix} \begin{pmatrix} \Psi_R \\ \Psi_G \end{pmatrix}, \quad (3)$$

where we set $\hbar = 1$.

III. ANALYTICAL APPROACH

In the following, we derive an analytic expression for the short-time evolution of the coherence $\rho_{RG}(t)$ from which we extract a dephasing rate γ_\perp . To this extent, we linearize the potential $U_\nu(x)$ at the facilitation distance x_f and define $y \equiv (x - x_f)/x_f$. Applying this to the time-dependent Schrödinger equation (3), we obtain

$$i\partial_t \begin{pmatrix} \Psi_R \\ \Psi_G \end{pmatrix} = \begin{pmatrix} -\xi\partial_y^2 - \nu\Delta y & \Omega \\ \Omega & -\xi\partial_y^2 \end{pmatrix} \begin{pmatrix} \Psi_R \\ \Psi_G \end{pmatrix}, \quad (4)$$

where we defined $\xi \equiv 1/2mx_f^2$. This allows us to treat the system in a perturbative approach with the linearized potential $-\nu\Delta y$ as the perturbation under the assumptions $\sigma \ll x_f$ and $|y| \ll |\frac{\Omega}{\nu\Delta}|$. The latter constraint also restricts this approach to be valid only for short times as a result of diffusion and dipolar repulsion. In addition, this implies an upper limit to the ratio Δ/Ω .

The unperturbed system, i.e. $-\nu\Delta y = 0$, can be solved exactly in k -space. It obeys Rabi-oscillations between the ground and Rydberg states, as expected, with the solution given by

$$\tilde{\Psi}_{R/G}^{(0)}(k, t) = \tilde{\Psi}_G(k, 0) e^{-i\xi k^2 t} \begin{cases} -i \sin \Omega t \\ \cos \Omega t \end{cases}, \quad (5)$$

where $\tilde{\Psi}_{R/G}^{(0)}(k, t)$ correspond to the unperturbed solutions. In first order perturbation theory, the time-dependent Schrödinger equation in k -space reads

$$i\partial_t \begin{pmatrix} \tilde{\Psi}_R^{(1)} \\ \tilde{\Psi}_G^{(1)} \end{pmatrix} = \begin{pmatrix} \xi k^2 & \Omega \\ \Omega & \xi k^2 \end{pmatrix} \begin{pmatrix} \tilde{\Psi}_R^{(1)} \\ \tilde{\Psi}_G^{(1)} \end{pmatrix} + i\nu\Delta k \left(\frac{\sigma^2}{x_f^2} + i2\xi t \right) \begin{pmatrix} \tilde{\Psi}_R^{(0)} \\ 0 \end{pmatrix}. \quad (6)$$

We can solve eq. (6) exactly using variation of constants and receive

$$\begin{aligned} \tilde{\Psi}_R^{(1)}(k, t) = & \tilde{\Psi}_G(k, 0) e^{-i\xi k^2 t} \left[-i \sin \Omega t + \frac{\nu\Delta k}{2\Omega} \right. \\ & \left. \cdot \left(\frac{\xi}{\Omega} \sin \Omega t - \xi t \cos \Omega t - i\Omega \left(\frac{\sigma^2}{x_f^2} t + i\xi t^2 \right) \sin \Omega t \right) \right] \end{aligned} \quad (7a)$$

$$\begin{aligned} \tilde{\Psi}_G^{(1)}(k, t) = & \tilde{\Psi}_G(k, 0) e^{-i\xi k^2 t} \left[\cos \Omega t - \frac{\nu\Delta k}{2\Omega} \right. \\ & \left. \cdot \left(\frac{\sigma^2}{x_f^2} \sin \Omega t + i\xi t \sin \Omega t - \Omega \left(\frac{\sigma^2}{x_f^2} t + i\xi t^2 \right) \cos \Omega t \right) \right]. \end{aligned} \quad (7b)$$

Inserting the inverse Fourier transform $\Psi_{R/G}(y, t) = \frac{1}{\sqrt{2\pi}} \int dk \tilde{\Psi}_{R/G}(k, t) e^{iky}$, the coherence then reads

$$\rho_{RG}(t) = x_f \int dk \tilde{\Psi}_R^*(k, t) \tilde{\Psi}_G(k, t). \quad (8)$$

This finally yields an analytical expression for the coher-

ence $\rho_{\text{RG}}(t)$ and up to first order in t it is

$$\begin{aligned} \text{Re}[\rho_{\text{RG}}] &= -\frac{\nu^2 \Delta^2}{8\Omega} \left(\frac{\xi}{\Omega^2} \sin^2 \Omega t - \frac{2\xi}{\Omega} t \sin \Omega t \cos \Omega t \right) \\ &\quad + \mathcal{O}(t^2) \end{aligned} \quad (9a)$$

$$\begin{aligned} \text{Im}[\rho_{\text{RG}}] &= \sin \Omega t \cos \Omega t - \frac{\nu^2 \Delta^2}{8\Omega} \left(\frac{\sigma^2}{x_f^2} + \frac{\xi^2 x_f^2}{\Omega^2 \sigma^2} \right) t \sin^2 \Omega t \\ &\quad + \mathcal{O}(t^2). \end{aligned} \quad (9b)$$

From eq. (9a), we recognize that $\text{Re}[\rho_{\text{RG}}](t_n) = -\frac{\nu^2 \Delta^2}{16m x_f^2 \Omega^3} (\frac{1}{2} - \Omega t_n)$, where $\Omega t_n = \frac{\pi}{4} + n\pi$ and n being an integer. Here, the real part of ρ_{RG} only yields a negligible contribution compared to the imaginary part at short times t_n (cf. Fig. 3). This allows us to approximate $|\rho_{\text{RG}}|(t_n) \approx |\text{Im}[\rho_{\text{RG}}]|(t_n)$, since $\text{Re}[\rho_{\text{RG}}]^2 \ll \text{Im}[\rho_{\text{RG}}]^2$. Consequently, we extract the dephasing rate simply from the imaginary part. Evaluating eq. (9b) at the times t_n yields

$$|\rho_{\text{RG}}|(t_n) \approx \frac{1}{2} (1 - \gamma_{\perp} t_n) + \mathcal{O}(t_n^2) \quad (10)$$

with the dephasing rate

$$\frac{\gamma_{\perp}}{\Omega} = \frac{\nu^2}{8} \left(\frac{\Delta}{\Omega} \right)^2 \left(\frac{\sigma}{x_f} \right)^2 \left[1 + \left(\frac{x_f}{\sigma} \right)^4 \left(\frac{\xi}{\Omega} \right)^2 \right]. \quad (11)$$

Eq. (11) is the main result of our work. For Rydberg facilitation $|\Delta| \gg \Omega$, so the first term is large. Note, however, that we assumed $\sigma \ll x_f$, and thus the second factor compensates the first. The impact of the atom mass is described by ξ as its reciprocal value, i.e. $x_f^4 \xi^2 = 1/(2m)^2$. When $m \rightarrow \infty$ the second term in the bracket vanishes. Note, however, that for a given trapping (tweezer) potential also $\sigma \rightarrow 0$ as $m \rightarrow \infty$.

IV. NUMERICAL BENCHMARK

In order to benchmark our analytic results on the effect of the differential dipole forces on the coherences between the internal states of the atom, we performed numerical simulations. To this extent, we solve eq. (3) numerically for a time interval $[0, t]$, discretize time in steps δt , and use a split-step Fourier algorithm [30] to compute the unitary time evolution. The time evolution operator $e^{-i\hat{H}\delta t}$ for the time step δt is split according to a second-order Trotter-Suzuki decomposition [31] as $e^{-i(\hat{T}+\hat{V})\delta t} = e^{-i\hat{T}\frac{\delta t}{2}} e^{-i\hat{V}\delta t} e^{-i\hat{T}\frac{\delta t}{2}} + \mathcal{O}(\delta t^3)$, where

$$\hat{T} = \frac{\hat{p}^2}{2m} \cdot \mathbb{1} \quad \hat{V} = \begin{pmatrix} U_{\nu}(x) & \Omega \\ \Omega & 0 \end{pmatrix}. \quad (12)$$

Here, \hat{T} corresponds to the kinetic and \hat{V} to the potential components of the coupled partial differential equations (PDEs). In the simulation, the kinetic time evolutions are calculated in k -space by using a Fast-Fourier-Transformation (FFT) of the wave function. The potential term is evaluated in real space, following another

FFT. However, since \hat{V} is not diagonal, we express the time evolution operator $e^{-i\hat{V}\delta t}$ in terms of Pauli matrices using $e^{ia\hat{n}\cdot\hat{\sigma}} = \mathbb{1} \cos a + i\hat{n}\cdot\hat{\sigma} \sin a$, for a real valued a and with $|\hat{n}| = 1$. Applying this onto the time evolution operator of the potential term, i.e. $e^{-i\hat{V}\delta t}$, we receive the real space evolution in a time step as

$$\begin{aligned} \Psi_{\text{R}}(t + \delta t) &= e^{-i\varphi} \left(\cos(\omega\delta t) - i \sin(\omega\delta t) \frac{U_{\nu}(x)}{2\omega} \right) \Psi_{\text{R}}(t) \\ &\quad - ie^{-i\varphi} \sin(\omega\delta t) \frac{\Omega}{\omega} \Psi_{\text{G}}(t) \end{aligned} \quad (13a)$$

$$\begin{aligned} \Psi_{\text{G}}(t + \delta t) &= e^{-i\varphi} \left(\cos(\omega\delta t) + i \sin(\omega\delta t) \frac{U_{\nu}(x)}{2\omega} \right) \Psi_{\text{G}}(t) \\ &\quad - ie^{-i\varphi} \sin(\omega\delta t) \frac{\Omega}{\omega} \Psi_{\text{R}}(t), \end{aligned} \quad (13b)$$

with $\varphi = \frac{U_{\nu}(x)}{2} \delta t$ and $\omega = \sqrt{\frac{1}{4} U_{\nu}^2(x) + \Omega^2}$.

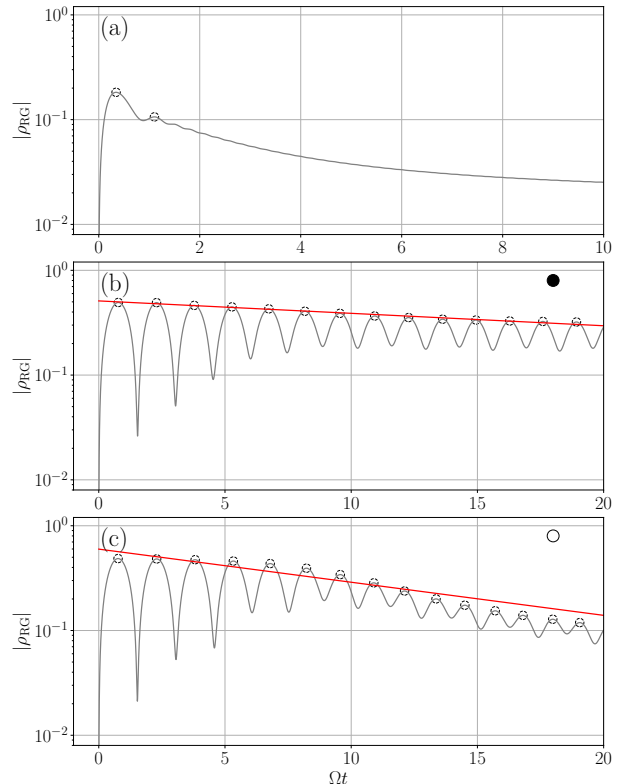


FIG. 2: Absolute value of ρ_{RG} (grey) over time from numerical simulations. The maxima (black circles) are fitted with an exponential decay function (red), yielding the dephasing rate. Here, the parameters are (a) $\Delta/\Omega = 28.57$, $\xi/\Omega = 0.07 \cdot 10^{-3}$ (b) $\Delta/\Omega = 1.32$, $\xi/\Omega = 1.25 \cdot 10^{-3}$ and (c) $\Delta/\Omega = 2.14$, $\xi/\Omega = 0.03 \cdot 10^{-3}$. In (c) the decay does not perfectly follow an exponential form, consequently values of γ_{\perp} extracted from such fits are marked as hollow points in later plots when compared to analytic predictions (cf. Fig. 4).

The algorithm generates the wavefunctions $\Psi_R(x, t)$ and $\Psi_G(x, t)$, where we discretize space in the interval $x/x_f \in [0.1, 10.5]$ using $N = 2^{17} \sim 10^5$ grid points. Finally, we calculate the coherence with

$$\rho_{RG}(t) = \int dx \Psi_R^*(x, t) \Psi_G(x, t). \quad (14)$$

We find the absolute value of the coherence $|\rho_{RG}|$ to oscillate and decay in amplitude over time, before reaching a steady state. In particular, during this time, we find the maxima of $|\rho_{RG}|$ to decay exponentially to a reasonable degree of accuracy. We fit this decay with an exponential function of the form $e^{-\gamma_{\perp} t}$, where γ_{\perp} is then identified as the dephasing rate.

For typical facilitation parameters, i.e. where $\Delta/\Omega \gg 1$, we find this decay to be on the order of, or faster than Rabi oscillations, making a rigorous fitting of the maxima difficult (cf. Fig. 2a). For this reason, we investigate the regime where $\Delta/\Omega \gtrsim 1$. Finally, for all simulations we use $\sigma/x_f = 0.05$, which corresponds to typical experimental ratios between tweezer trap spacings and trap widths. In Fig. 2b-c we give two examples of such a simulation, showing Rabi-oscillations damped by an effective dephasing. Note that spontaneous emission was assumed to be negligible on the time scales shown.

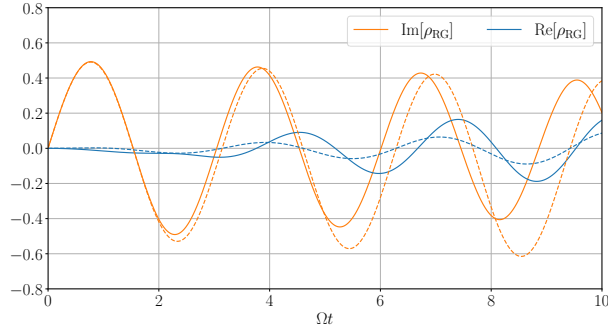


FIG. 3: Time resolved imaginary value (orange), and real value (blue) of the coherence ρ_{RG} from numerics (solid) and from analytics in first order perturbation theory (cf. eq. (9)) (dashed), using $\Delta/\Omega = 1.32$ and $\xi/\Omega = 1.25 \cdot 10^{-3}$.

In Fig. 3 we compare the analytic short-time approximations to the full numerics. We recognize good agreement between analytics and numerics and see that at the peak values of $\text{Im}[\rho_{RG}](t)$ the real part $\text{Re}[\rho_{RG}](t)$ is indeed small.

We now compare the analytic predictions for the short-time dephasing rate, eq. (11), with numerical simulations. This is shown in Fig. 4, where we plotted γ_{\perp}/Ω as function of Δ/Ω for different ξ/Ω . One recognizes very good agreement.

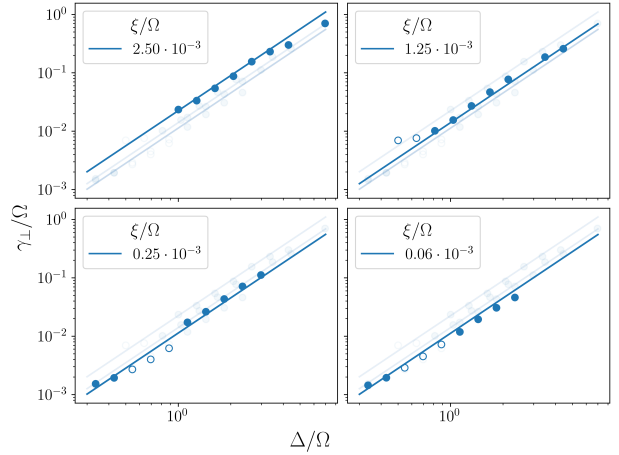


FIG. 4: Dephasing rate from exponential fit of numeric simulations. Hollow dots correspond to simulations where $\rho_{RG}(t)$ does not perfectly follow an exponential function in time (cf. Fig. 2c). The lines correspond to eq. (11).

V. SUMMARY

In the present paper we discussed the effects of the dipole force acting on the Rydberg-state wavefunction on the dynamics of a single atom, laser coupled between an initially spatially localized ground state and a high-lying Rydberg state under conditions of Rydberg facilitation, i.e. in the presence of an already excited Rydberg atom at the facilitation distance. In the dipole potential of an already excited Rydberg atom, the atom under consideration experiences a decay of coherences due to dipole forces acting solely on the Rydberg state.

We model this in second quantization, by explicitly taking into account the motional degrees of freedom of the atomic ground and Rydberg states, coupled by a laser. Initially, the atom is assumed in the ground state with a well-localized spatial wavefunction, typical for lattice experiments with Rydberg atoms. As a result of dipole forces, the Rydberg state wave function is repelled from the external Rydberg atom, and the overlap between ground and Rydberg state wavefunctions decays. Using a perturbative solution of the coupled equations, we derived an analytic expression for the (short time) dephasing rate γ_{\perp} , which we have benchmarked with numerical simulations for values of Δ/Ω up to $\sim \mathcal{O}(1)$.

Authors contribution

*These authors contributed equally. T.S. performed the analytic calculations and E.K. performed the numeric simulations. D.B. supervised the project with support by M.F. M.F. conceived the project. All authors were involved in the discussion of results and writing of the manuscript.

Acknowledgments

Financial support from the DFG through SFB TR 185, Project No. 277625399, is gratefully acknowledged. The authors also thank the Allianz für Hochleistungsrechnen (AHRP) for giving us access to the “Elwetritsch” HPC Cluster.

[1] T. F. Gallagher, [Rydberg Atoms](#) (Cambridge University Press, 1994).

[2] D. Barredo, S. De Léséleuc, V. Lienhard, T. Lahaye, and A. Browaeys, [Science](#) **354**, 1021 (2016).

[3] M. Endres, H. Bernien, A. Keesling, H. Levine, E. R. Anschuetz, A. Krajenbrink, C. Senko, V. Vuletic, M. Greiner, and M. D. Lukin, [Science](#) **354**, 1024 (2016).

[4] D. Barredo, V. Lienhard, S. De Leseleuc, T. Lahaye, and A. Browaeys, [Nature](#) **561**, 79 (2018).

[5] H. Weimer, M. Müller, I. Lesanovsky, P. Zoller, and H. P. Büchler, [Nature Physics](#) **6**, 382 (2010).

[6] N. Šibalić and C. S. Adams, [Rydberg Physics](#), 2399-2891 (IOP Publishing, 2018).

[7] H. Labuhn, D. Barredo, S. Ravets, S. De Léséleuc, T. Macrì, T. Lahaye, and A. Browaeys, [Nature](#) **534**, 667 (2016).

[8] H. Bernien, S. Schwartz, A. Keesling, H. Levine, A. Omran, H. Pichler, S. Choi, A. S. Zibrov, M. Endres, M. Greiner, et al., [Nature](#) **551**, 579 (2017).

[9] P. Schauß, J. Zeiher, T. Fukuhara, S. Hild, M. Cheneau, T. Macrì, T. Pohl, I. Bloch, and C. Groß, [Science](#) **347**, 1455 (2015).

[10] V. Lienhard, S. de Léséleuc, D. Barredo, T. Lahaye, A. Browaeys, M. Schuler, L.-P. Henry, and A. M. Läuchli, [Physical Review X](#) **8**, 021070 (2018).

[11] E. Guardado-Sánchez, P. T. Brown, D. Mitra, T. Devakul, D. A. Huse, P. Schauß, and W. S. Bakr, [Physical Review X](#) **8**, 021069 (2018).

[12] D. Barredo, H. Labuhn, S. Ravets, T. Lahaye, A. Browaeys, and C. S. Adams, [Physical Review Letters](#) **114**, 113002 (2015).

[13] S. De Léséleuc, V. Lienhard, P. Scholl, D. Barredo, S. Weber, N. Lang, H. P. Büchler, T. Lahaye, and A. Browaeys, [Science](#) **365**, 775 (2019).

[14] S. Helmrich, A. Arias, G. Lochead, T. Wintermantel, M. Buchhold, S. Diehl, and S. Whitlock, [Nature](#) **577**, 481 (2020).

[15] T. Wintermantel, M. Buchhold, S. Shevate, M. Morgado, Y. Wang, G. Lochead, S. Diehl, and S. Whitlock, [Nature Communications](#) **12**, 103 (2021).

[16] D. Brady, J. Bender, P. Mischke, S. Ohler, T. Niederprüm, H. Ott, and M. Fleischhauer, [Physical Review Research](#) **6**, 013052 (2024).

[17] S. Ohler, D. Brady, P. Mischke, J. Bender, H. Ott, T. Niederprüm, W. Ripken, J. S. Otterbach, and M. Fleischhauer, arXiv preprint [10.48550/arXiv.2502.14757](#) (2025).

[18] T. Johnson, E. Urban, T. Henage, L. Isenhower, D. Yavuz, T. Walker, and M. Saffman, [Physical Review Letters](#) **100**, 113003 (2008).

[19] U. Raitzsch, R. Heidemann, H. Weimer, B. Butscher, P. Kollmann, R. Löw, H. P. Büchler, and T. Pfau, [New Journal of Physics](#) **11**, 055014 (2009).

[20] W. Li, C. Ates, and I. Lesanovsky, [Physical Review Letters](#) **110**, 213005 (2013).

[21] C. Ates, T. Pohl, T. Pattard, and J. M. Rost, [Physical Review Letters](#) **98**, 023002 (2007).

[22] M. Marcuzzi, J. Minář, D. Barredo, S. De Léséleuc, H. Labuhn, T. Lahaye, A. Browaeys, E. Levi, and I. Lesanovsky, [Physical Review Letters](#) **118**, 063606 (2017).

[23] M. Magoni, P. P. Mazza, and I. Lesanovsky, [Physical Review Letters](#) **126**, 103002 (2021).

[24] M. Magoni, C. Nill, and I. Lesanovsky, [Physical Review Letters](#) **132**, 133401 (2024).

[25] C. Ates, T. Pohl, T. Pattard, and J. Rost, [Journal of Physics B: Atomic, Molecular and Optical Physics](#) **39**, L233 (2006).

[26] I. Lesanovsky and J. P. Garrahan, [Physical review letters](#) **111**, 215305 (2013).

[27] M. Marcuzzi, J. Schick, B. Olmos, and I. Lesanovsky, [Journal of Physics A: Mathematical and Theoretical](#) **47**, 482001 (2014).

[28] E. Levi, R. Gutiérrez, and I. Lesanovsky, [Journal of Physics B: Atomic, Molecular and Optical Physics](#) **49**, 184003 (2016).

[29] D. Brady, S. Ohler, J. Otterbach, and M. Fleischhauer, [Physical Review Letters](#) **133**, 173401 (2024).

[30] R. H. Hardin, [Siam Rev.](#) , 423 (1973).

[31] N. Hatano and M. Suzuki, Finding exponential product formulas of higher orders, in [Quantum Annealing and Other Optimization Methods](#), edited by A. Das and B. K. Chakrabarti (Springer Berlin Heidelberg, Berlin, Heidelberg, 2005) pp. 37–68.

8. Summary and Outlook

In the first part of this thesis, we used large scale numeric Monte Carlo simulations to analyze a three-dimensional gas of Rydberg atoms in the high dephasing regime. We found that at low temperatures, the dynamics are constrained to an underlying *Erdős–Rényi* (ER) network, which, depending on the density of the gas, is either percolating or non-percolating. Furthermore, in the non-percolating regime, we have proven the existence of a heterogeneous Griffiths phase and have shown this to arise from the underlying network structure and not from different velocity classes of Rydberg atoms as was postulated in Ref. [16].

Furthermore, we improve on the mean field Langevin equations presented in Ref. [12], by adding the effects of Rydberg blockade and the underlying network structure. For low temperatures, we find that even in the percolating regime, the network structure needs to be taken into account in the mean field equations. We have found the modified mean field equations to agree much better with our Monte Carlo simulations.

Building on this, we investigated the universality class of the absorbing-state phase transition, characteristic for Rydberg facilitation, and have found this to fall into *directed percolation* (DP) universality in the low temperature, percolating gas and mean field universality in the high temperature gas. For the low temperature, non-percolating gas we found no universal collapse of data reflecting the extended Griffiths which replaces the absorbing-state phase transition. For intermediate temperatures and a percolating gas, we have found universal behavior at each gas temperature, albeit with a *continuously varying* critical exponent. This behavior emerges from rare, long-range spreading processes called Lévy flights. Here, a few, very fast Rydberg atoms are able to facilitate (infect) atoms at very large distances. This behavior gives rise to the *anomalous directed percolation* (ADP) universality class, which is characterized by critical exponents that depend on the characteristic length scale of the Lévy flights [10].

In the experiment of Ref. [12], a significant deviation from the expected DP critical exponent was measured and it was postulated that *self-organized criticality* (SOC) might be modifying the universal behavior. However, we were able to replicate the value of this exponent, showing that this deviation stems from Lévy flights. Furthermore, by numerically determining DP critical exponents in the *frozen* gas and in the presence of SOC, we have shown that SOC does *not* modify universal behavior in Rydberg facilitation. Finally, we underlined this by calculating and measuring *avalanche* exponents at criticality. Since a mapping of the DP critical exponents to the avalanche exponents exists [10], we were able to extract the full set of DP critical exponents from avalanches.

Our work has allowed for a deeper understanding of universality in the Rydberg facilitation gas. In particular, the temperature dependent, *tunable* universality class we discovered allows for the study of DP and ADP universality in controlled, experimental environments. Furthermore, we have shown that facilitation is constrained to a *static* network at temperature $T = 0$, and that this network becomes *dynamic* at finite temperature, with links *changing* between nodes on the time-scale of excitation spreading. Future experiments could thus allow for a deeper understanding of nonequilibrium universality and spreading processes on dynamic networks.

One open question which remains, is how the universality class is affected in the quan-

tum regime. One major result from equilibrium statistical mechanics is the equivalence in the universal behavior of the d -dimensional quantum Ising model to the $d+1$ -dimensional classical Ising model near criticality [82]. However, as the observation of universal behavior typically requires large numbers of atoms in an ensemble, fully quantum simulations remain out of reach. However, some semi-classical approaches, most notably the truncated Wigner approximation for spins [126] might allow for the exploration of this regime after all.

Following this, we switched gears from the gas of Rydberg atoms to a 1-dimensional tweezer array of Rydberg atoms. Here, facilitation dynamics simplify to the growing and shrinking of spin (Rydberg $\equiv |\uparrow\rangle$, ground $\equiv |\downarrow\rangle$) domains [25]. Dipole interactions between Rydberg atoms lead to a coupling of spin states with motional (phonon) states within the respective tweezer traps [26]. In Ref. [26], the dipole potential was expanded up to linear order and the resulting spin-phonon interaction led to a slower-than-ballistic growth of spin domains. However, up to linear order, all spin-phonon interaction terms within a given domain completely cancel out and there is no phonon transport. For this reason, we have regarded this system up to quadratic order with a harmonic dipole interaction potential between Rydberg atoms. We have found this simple system to house a number of non-trivial effects, such as strong phonon correlations, non-classical positional states of the Rydberg atoms in their tweezer traps (squeezed states), or the emergence of Bloch oscillations in the spin domain size over time. By analytically decoupling spin and phonon degrees of freedom, we have derived an analytic understanding of the effects at play within the tweezer array.

While a in leading order purely harmonic potential can be realized in Rydberg atoms using a Lennard-Jones style dipole potential [27], the question arises as to how the system behaves under a dipole expansion with both linear and quadratic terms. Here, the linear terms act as phonon source on the edges of the domain, while the quadratic terms allow for phonon transport through the domain. It is unclear how this interplay affects the properties of the system, e.g. if non-ergodic behavior in the form of Bloch oscillations can persist in the presence of phonon sources. If this were to be the case, it would have a profound impact on Rydberg facilitation experiments in tweezer arrays, as these effects would be a generic feature of these systems.

In our final study, we shifted gears yet again to the dynamics of single, laser-driven atom in the dipole potential of an external Rydberg atom. Here, we derived an analytic expression for the dephasing rate a Rydberg atom experiences as a result of dipole forces. We have shown this to agree very well with numeric simulations for laser detunings Δ , which are larger, but on the order of the Rabi frequency Ω . This paves the way for a better understanding of dephasing rates in Rydberg systems and an experimental verification of this would be highly useful.

Appendix

A. Simulating a Gas of Rydberg Atoms using the Monte Carlo Method

In this Appendix, the Monte Carlo algorithm used for the numeric simulations of the Rydberg facilitation gas in [P1, P2, P3, P4, P7] will be explained. First, the general *fixed time-step Monte Carlo* (**ftsMC**) algorithm for simulating the time dynamics of a many-body system according to a set of classical rate equations will be detailed. Following this, the **ftsMC** algorithm will be applied to the many-body gas of Rydberg atoms in the high dephasing regime.

The Monte Carlo Method

The Monte Carlo method is based on using the average of many, random trajectories to accurately describe a system. Originally created by Nicholas Metropolis and Stanisław Ulam in Los Alamos in 1949 [127], they named the method *Monte Carlo* after the Monte Carlo casino in Monaco, inspired by the gambling habits of Ulam's uncle. Today, the Monte Carlo method refers to an entire family of methods which utilize averaging random trajectories to solve problems, e.g. Monte Carlo integration for solving integrals.

Many problems in classical and quantum physics can be - to various degree of approximation - reduced to a master equation of the form [128]

$$\frac{d}{dt}P(s_k, t) = \sum_j \Gamma(s_j \rightarrow s_k)P(s_j, t) - \sum_j \Gamma(s_k \rightarrow s_j)P(s_k, t), \quad (\text{A.1})$$

where $P(s_k, t)$ is the probability of finding the system in state s_k at time t and $\Gamma(s_l \rightarrow s_k)$ is the rate at which the system changes from state s_l to s_k . The solution of eq. (A.1) describes the time evolution of the probability of finding the system in a given state. This equation describes a continuous-time Markov process [128] and the Monte Carlo method provides a numerical solution to it [129].

For dynamical simulations, multiple different Monte Carlo algorithms exist [130]. For the application to a many-body system of interacting particles two candidates emerge: *kinetic Monte Carlo* (**KMC**) and **ftsMC**. In a **KMC** algorithm, the time between transitions is a *random variable* and is determined by a Poissonian distribution [129] as

$$\delta t = -\frac{\log u}{\sum_j \Gamma_j}, \quad (\text{A.2})$$

where $u \in (0, 1]$ is a uniformly distributed random number and Γ_j are the transition rates in the system. At each time step exactly one transition occurs, i.e. the algorithm is *rejection free*. On the other hand, in an **ftsMC** algorithm, the length of time steps are constant and any number of transitions can occur in a given time step. Here, δt is chosen in such a way, that more than one transition occurring in a given time step becomes unlikely.

Typically one would use the **KMC** algorithm as the **ftsMC** algorithm is merely an approximation of the **KMC** algorithm, becoming more accurate as $\delta t \rightarrow 0$ [130, 131]. However, the waiting time in a **KMC** algorithm requires *constant* transition rates Γ_j during the waiting time δt . If the transition rates change within the time interval δt

between transitions, one has to resort to the [ftsMC](#) algorithm. In a gas of Rydberg atoms with motion, i.e. a gas temperature $T > 0$, transition rates will change in during the time interval δt , since interactions are distance dependent. Moreover, specifically Rydberg facilitation, the transition rates can be very sensitive to the distance between atoms (cf. Fig. B.1). For this reason, we utilize the [ftsMC](#) algorithm for all our Monte Carlo simulations.

The Fixed Time Step Monte Carlo Algorithm

The [ftsMC](#) algorithm uses a fixed time step δt with a *stochastic* number of transitions per time step. Strictly speaking, the [ftsMC](#) algorithm is only valid if no more than one transition occurs in a given time step. Therefore, a fixed time step δt is chosen such that $\sum_j \Gamma_j \delta t \ll 1$, making it unlikely that more than one transition occurs in δt . However, since the number of transitions per time step is stochastic, more than one transition per time step can always occur. Therefore, it is advisable to benchmark the simulation results for different δt , to see at which δt the results begin to converge.

For a given system in the state s_k , and with n transition rates $\Gamma(s_k \rightarrow s_l)$, the [ftsMC](#) algorithm goes as follows:

1. Initialize simulation: $t = 0$, $s_k = s_0$
2. Calculate transition rates: $\Gamma_l \equiv \Gamma(s_k \rightarrow s_l) \forall l$
3. Calculate the probability that a transition will occur: $p_{\text{trans}} = 1 - e^{-\sum_l \Gamma_l \delta t}$
4. Generate a random number $u_1 \in [0, 1)$
5. If $u_1 < p_{\text{trans}}$ a transition occurs (5a. – 5c.):
 - 5a. Generate a random number $u_2 \in [0, 1)$
 - 5b. Find the smallest j such that $u_2 < \frac{\sum_{l=1}^j \Gamma_l}{\sum_{l=1}^n \Gamma_l}$
 - 5c. Execute transition $s_k \rightarrow s_j$
6. Advance time $t + \delta t$
7. Repeat from step 2. until t_{final} is reached.

Application to a Gas of Optically Driven Atoms

We will now apply the [ftsMC](#) algorithm to a gas of N interacting Rydberg atoms in the high dephasing regime. The algorithm is schematically displayed as a flowchart in Fig. A.1. In the following, steps I.-V. from the flowchart will be detailed.

I. Initialize system – The simulation starts at time $t = 0$ and we initialize the internal (ground / Rydberg) and external (position / velocity) states for each of the N atoms. The internal states are saved in a vector \mathbf{s} of length N with entries $s_i \in \mathbb{N}$ corresponding to the internal state of the atom, i.e. the ground state $0 \hat{=} |G\rangle$, the Rydberg state $1 \hat{=} |R\rangle$, and a removed/ionized atom $2 \hat{=} |0\rangle$.

For the external states, the positions are randomly sampled within a 3-dimensional box of size L , i.e. each component of \mathbf{x}_i is a random number between 0 and L . The velocities are then sampled from a Maxwell-Boltzmann distribution, i.e. each component

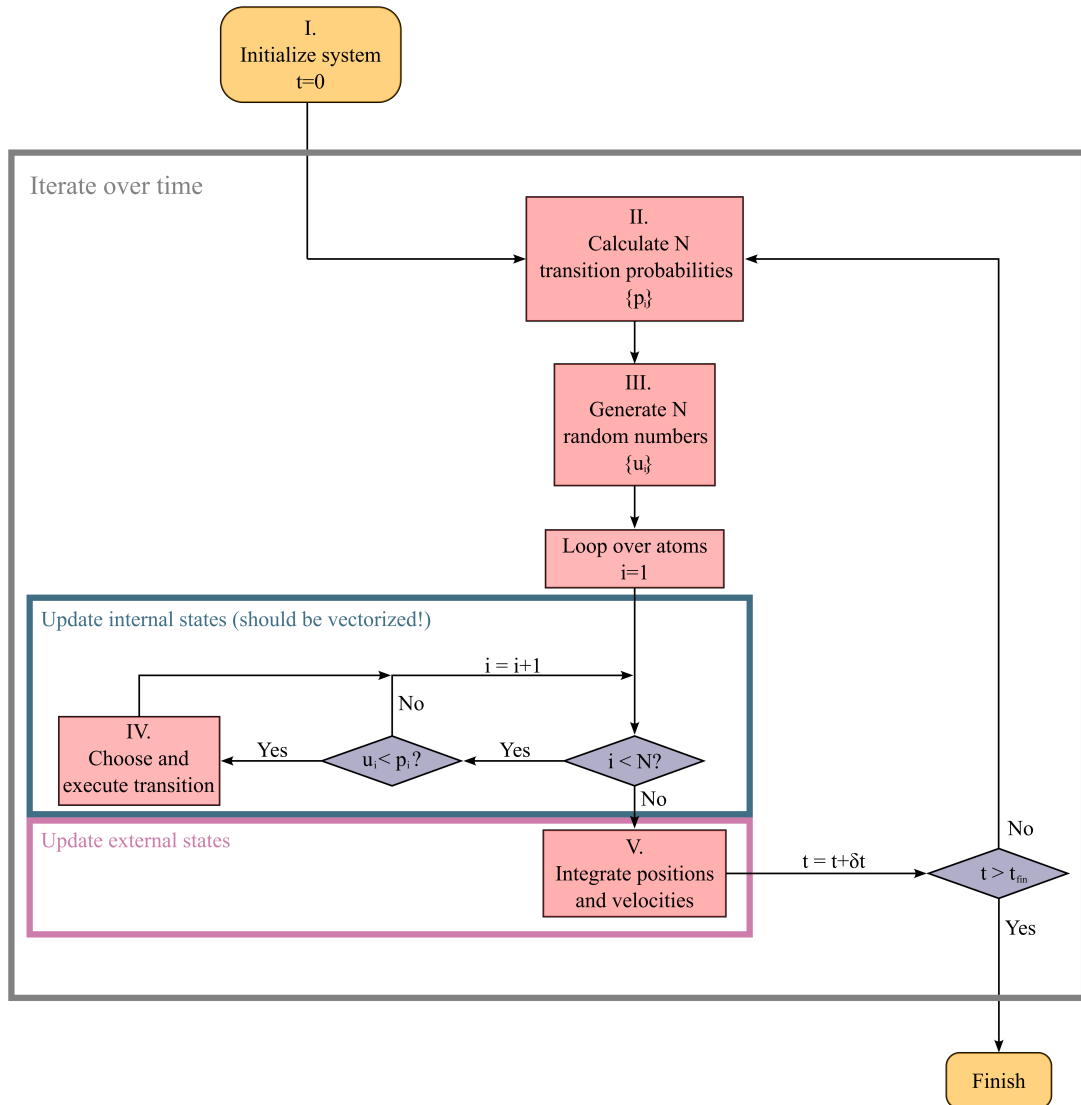


Figure A.1.: Flowchart of the `ftsMC` algorithm used to simulate the gas of Rydberg atoms. For details on each of the steps see parts I.-V. in the main text. The updating of internal states (blue box) can and should be vectorized as opposed to looping over each atom.

of \mathbf{v}_i is sampled from a Gaussian distribution with mean 0 and standard deviation $\sigma = \sqrt{\frac{2k_B T}{m}} \equiv \hat{v}$, corresponding to the most likely velocity.

II. Calculate transition probabilities – Due to interactions between Rydberg atoms, transition probabilities depend on the internal states of other atoms. In the classical, rate equation limit, the dynamics of the internal ground, Rydberg, and ionized states of a given atom with index i , are given by

$$\frac{d}{dt}P_R^{(i)} = -(\gamma_{\text{stim}} + \gamma_{\text{spont}})P_R^{(i)} + \gamma_{\text{stim}}P_G^{(i)}, \quad (\text{A.3a})$$

$$\frac{d}{dt}P_G^{(i)} = +(\gamma_{\text{stim}} + (1-b)\gamma_{\text{spont}})P_R^{(i)} - \gamma_{\text{stim}}P_G^{(i)}, \quad (\text{A.3b})$$

$$\frac{d}{dt}P_0^{(i)} = +b\gamma_{\text{spont}}P_R^{(i)}, \quad (\text{A.3c})$$

where γ_{spont} corresponds to the spontaneous decay rate, and $b \in [0, 1]$ is the *branching factor*, which determines which portion of spontaneously decaying Rydberg atoms decay into the $|0\rangle$ state and can no longer reach $|G\rangle$ or $|R\rangle$ states. The stimulated (de-)excitation rate γ_{stim} is given by¹

$$\gamma_{\text{stim}} = \frac{2\Omega^2\gamma_{\perp}}{\gamma_{\perp}^2 + (\Delta + \sum_{j < i} V_{ij}\Pi_j)^2}, \quad (\text{A.4})$$

with the Rabi frequency Ω , the laser detuning Δ , the dephasing rate of the Rydberg state γ_{\perp} , the Rydberg-Rydberg interaction potential V_{ij} (cf. Sec. 1.2), and the projector

$$\Pi_j = \begin{cases} 1, & j \text{ in Rydberg state,} \\ 0, & \text{else.} \end{cases} \quad (\text{A.5})$$

Note that the stimulated (de-)excitation rate of atom i depends on the states and distances of other atoms. In the van-der-Waals regime, regarded in all publications [P1-P7], the interaction potential takes the form $V_{ij} = \frac{c_6}{|\mathbf{r}_i - \mathbf{r}_j|^6}$. For very small distances between atoms i and j , V_{ij} can take extreme values making the simulation unstable. For this reason, the maximum of V_{ij} must be truncated. In our Monte Carlo simulations we truncate the potential with

$$V_{ij} = \begin{cases} \frac{c_6}{|\mathbf{r}_i - \mathbf{r}_j|^6}, & |\mathbf{r}_i - \mathbf{r}_j| > 10^{-2}, \\ c_6 \cdot 10^{12}, & \text{else,} \end{cases} \quad (\text{A.6})$$

with the potential being in units of the decay rate γ and all distance being in units of the facilitation distance r_f .

For the `ftsMC` algorithm, the probability that a transition occurs depends on the rate at which the system *leaves* its current state. This rate is given by the decay rate of

¹The stimulated rate, and furthermore even the rate equations, can simply be derived from the Lindblad master equation. A derivation can be found in the Supplementary Materials of Ref. [12], albeit with slightly different factors in the Hamiltonian.

the given state in eqs. (A.3). For example, if atom i is in the Rydberg state, then from eq. (A.3a) the rate at which it leaves this state is given by

$$\Gamma_i = \gamma_{\text{stim}} + \gamma_{\text{spont}}. \quad (\text{A.7})$$

From the Poissonian distribution, the transition probability, i.e. the probability that a transition occurs within the time interval δt , is given by

$$p_i = 1 - e^{-\Gamma_i \delta t}. \quad (\text{A.8})$$

III. Generate N random numbers – In a typical KMC algorithm one would choose one random number which determines if the transition occurs. Here, any number of transitions can occur in a given time step, and therefore, we need to generate N random numbers u_i , uniformly distributed in the interval $u_i \in [0, 1]$.

It is advisable to use a random number generator and set a seed for each trajectory. In Python, using NumPy, one could use the command: `numpy.random.default_rng(seed)`. If a seed is not used and trajectories are run in parallel, it can occur that separate trajectories utilize the same random numbers leading to numeric errors in the data.

IV. Choose and execute transition – Once it is determined that atom i will leave its current state, i.e. $u_i < p_i$, the transition it performs needs to be chosen. Similar to the KMC algorithm, this is done by comparing the individual rates. Again, using the example of atom i being in the Rydberg state, two channels emerge, i.e. it can decay to $|G\rangle$ or $|0\rangle$, and the respective decay probabilities are given by

$$p_{R \rightarrow G} = \frac{\gamma_{\text{stim}} + (1-b)\gamma_{\text{spont}}}{\gamma_{\text{stim}} + (1-b)\gamma_{\text{spont}} + b\gamma_{\text{spont}}} \equiv \frac{\gamma_{\text{stim}} + (1-b)\gamma_{\text{spont}}}{\gamma_{\text{stim}} + \gamma_{\text{spont}}}, \quad (\text{A.9})$$

$$p_{R \rightarrow 0} = \frac{b\gamma_{\text{spont}}}{\gamma_{\text{stim}} + (1-b)\gamma_{\text{spont}} + b\gamma_{\text{spont}}} \equiv \frac{b\gamma_{\text{spont}}}{\gamma_{\text{stim}} + \gamma_{\text{spont}}}. \quad (\text{A.10})$$

V. Integrate positions and velocities – After updating the internal states of all atoms, the positions and velocities need to be updated as well. These are integrated from their equations of motion using a Verlet "leapfrog" integrator [132]. Due to the symplectic nature of this integrator, it is often more accurate than simple second-order integrators [128]. The leapfrog integrator scheme is given by

$$\mathbf{r}_i(t + \delta t) = \mathbf{r}_i(t) + \mathbf{v}_i(t)\delta t + \frac{1}{2}\mathbf{a}_i(t)(\delta t)^2, \quad (\text{A.11a})$$

$$\mathbf{v}_i(t + \delta t) = \mathbf{v}_i(t) + \frac{1}{2}[\mathbf{a}_i(t) + \mathbf{a}_i(t + \delta t)]\delta t, \quad (\text{A.11b})$$

where $\mathbf{a}_i(t + \delta t)$ is the acceleration calculated using the positions $\mathbf{r}_i(t + \delta t)$.

B. Derivation of the Facilitation Width

In this Appendix, we derive the width of the facilitation shell δr_f in the high dephasing limit where facilitation dynamics are accurately described by classical rate equations [21–24]. This width determines the density at which the percolation transition occurs in the Rydberg facilitation gas, i.e. $n_{\text{perc}} = \frac{1}{V_s} \approx \frac{1}{4\pi\delta r_f r_f^2}$, where V_s is the volume of the facilitation shell. For a system of N atoms coupled between a ground $|G\rangle$ and Rydberg state $|R\rangle$ with Rabi frequency Ω and detuning from resonance Δ , the system Hamiltonian is given by

$$\hat{H} = \sum_{i=1}^N \Omega \hat{\sigma}_i^x - \Delta \hat{n}_i + \sum_{j \neq i} \Delta \frac{r_f^6}{r_{ij}^6} \hat{n}_j \hat{n}_i, \quad (\text{B.12})$$

with the interatomic distance r_{ij} and the projection operator onto the Rydberg state \hat{n}_i . Furthermore, we consider spontaneous decay from the Rydberg state to the ground state with rate γ and dephasing of the Rydberg state with rate γ_\perp . Using this, we can define a Lindblad master equation for the density matrix $\hat{\rho}$ as

$$\frac{d}{dt} \hat{\rho} = i[\hat{\rho}, \hat{H}] + \sum_l \hat{L}_l \hat{\rho} \hat{L}_l^\dagger - \frac{1}{2} \{ \hat{L}_l^\dagger \hat{L}_l, \hat{\rho} \}, \quad (\text{B.13})$$

with the jump operators $\hat{L}_1 = \sqrt{\gamma} |G\rangle \langle R|$ and $\hat{L}_2 = \sqrt{\gamma_\perp} |R\rangle \langle R|$. The equation of motion of the projection operator \hat{n}_i is given by

$$\frac{d}{dt} \langle \hat{n}_i \rangle = \text{Tr} \left\{ \hat{n}_i \frac{d}{dt} \hat{\rho} \right\}. \quad (\text{B.14})$$

After adiabatic elimination of coherences (cf. [12] for an explicit formulation) we receive the facilitated transition rate Γ_{ij} between the ground and Rydberg states of atom j as [P1] (cf. [12]²)

$$\Gamma_j = 2\Omega^2 \frac{\gamma_\perp}{\gamma_\perp^2 + \Delta^2 \left(1 - \sum_{i \neq j} \frac{r_f^6}{r_{ij}^6} \hat{n}_i \right)^2}. \quad (\text{B.15})$$

If we consider atom j to be in the presence of exactly one Rydberg atom, then the sum only has one non-zero value. In the Rydberg gas, this is a good approximation since the interaction potential decays as r^{-6} and the density of Rydberg atoms is relatively low due to Rydberg blockade. In this case, we can write the facilitation rate depending on the distance r of atom j to a Rydberg atom as

$$\Gamma(r) = 2\Omega^2 \frac{\gamma_\perp}{\gamma_\perp^2 + \Delta^2 \left(1 - \frac{r_f^6}{r^6} \right)^2}. \quad (\text{B.16})$$

²Note the Hamiltonian in this reference is slightly different.

Assuming small displacements from r_f , we can Taylor expand the term corresponding to the interaction potential, giving us

$$\left(1 - \frac{r_f^6}{r^6}\right) = 0 + 6 \frac{r - r_f}{r_f} + \dots \quad (\text{B.17})$$

Inserting this into eq. (B.16) and truncating after the first order we receive

$$\Gamma(r) = 2\Omega^2 \frac{\gamma_\perp}{\gamma_\perp^2 + \left(\frac{6\Delta}{r_f}(r - r_f)\right)^2} \quad (\text{B.18})$$

$$= \frac{2\Omega^2 r_f}{6\Delta} \frac{\frac{\gamma_\perp}{6\Delta} r_f}{\left(\frac{\gamma_\perp}{6\Delta} r_f\right)^2 + (r - r_f)^2}. \quad (\text{B.19})$$

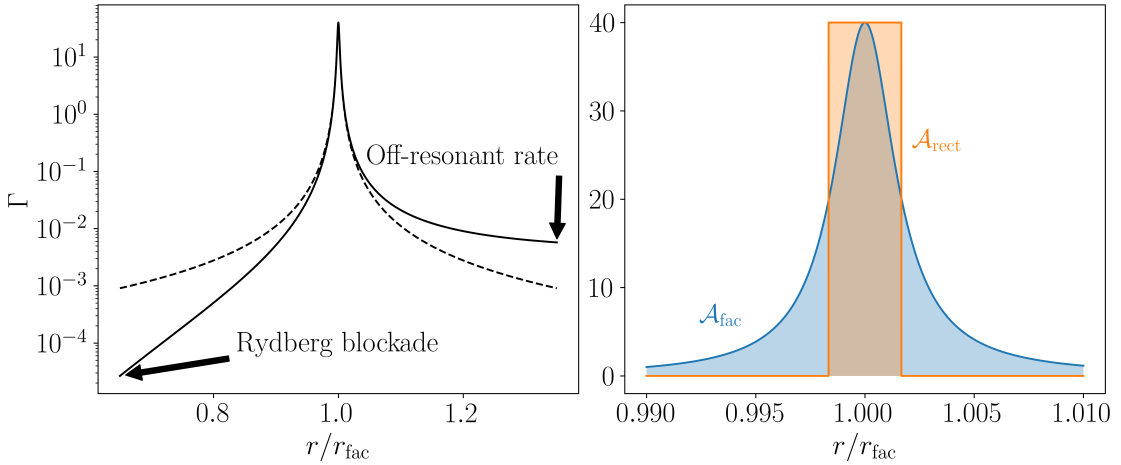


Figure B.1.: *Facilitation rate depending on distance to Rydberg atom.* (Left) Comparison of distance dependent facilitation rate $\Gamma(r)$ (solid) with a Lorentzian $L(r)$ (dashed). Rydberg blockade and off-resonant excitation rates cause $\Gamma(r)$ to deviate from $L(r)$. (Right) Two curves with equal pulse area, i.e. $\mathcal{A}_{\text{fac}} = \mathcal{A}_{\text{rec}}$. The blue curve is the distance dependent facilitation rate $\Gamma(r)$ and the orange curve is a rect function with width δr_f and height $\max\{\Gamma\}$.

In the first order expansion of the interaction potential, we see that $\Gamma(r)$ corresponds exactly to a Lorentzian function $L(x)$, with width ν and center x_0 , i.e. [133]

$$L(x) = \frac{1}{\pi} \frac{\frac{1}{2}\nu}{(x - x_0)^2 + \left(\frac{1}{2}\nu\right)^2}. \quad (\text{B.20})$$

The higher order terms of the interaction potential expansion represent deviations in the facilitation rate from a pure Lorentzian due to the off-resonant excitation rate and Rydberg blockade (see Fig. B.1 (left)). Comparing eq. (B.18) and eq. (B.20), we can identify $\delta r_f \equiv \nu$, and write down the width of the facilitation shell in the high dephasing limit and in first order approximation of the interaction potential as

$$\delta r_f^{\text{FWHM}} = \frac{\gamma_\perp}{3\Delta} r_f. \quad (\text{B.21})$$

We receive a slightly different width if we do not regard the FWHM of the Lorentzian, but instead search for a rectangle function with the same maximum and the same *pulse area* as the Lorentzian (see Fig. B.1 (right)). The logic behind this is that we are interested in total number of excitations which a Rydberg atom can facilitate. At very large distances the Lorentzian still gives a non-zero, albeit very small, contribution to the facilitation rate, meaning here excitations can still occur. These are neglected when only regarding the FWHM.

To this extent, we define the following rectangular function as

$$\text{rect}(r) = \begin{cases} \frac{2\Omega^2}{\gamma_\perp}, & |r - r_f| < \delta r_f^{\text{Pulse}}/2, \\ 0, & \text{else,} \end{cases} \quad (\text{B.22})$$

with the width $\delta r_f^{\text{Pulse}}$. We determine this width by comparing the pulse areas of the two functions. The pulse area is received by integrating eq. (B.18), i.e.

$$\mathcal{A}_{\text{fac}} = \frac{\Omega^2 r_f}{3\Delta} \int_0^\infty dr \frac{\frac{\gamma_\perp}{6\Delta} r_f}{\left(\frac{\gamma_\perp}{6\Delta} r_f\right)^2 + (r - r_f)^2} \quad (\text{B.23})$$

$$= \frac{\Omega^2 r_f}{3\Delta} \cdot \pi \quad (\text{B.24})$$

$$\approx \frac{\Omega^2}{\Delta} r_f. \quad (\text{B.25})$$

Equating this pulse area \mathcal{A}_{fac} with the pulse area of the rect function, given by $\mathcal{A}_{\text{rect}} = \frac{2\Omega^2}{\gamma_\perp} \delta r_f^{\text{Pulse}}$, we receive the width of the facilitation shell for equal pulse areas as

$$\delta r_f^{\text{Pulse}} \approx \frac{\gamma_\perp}{2\Delta} r_f. \quad (\text{B.26})$$

Bibliography

- [1] T. F. Gallagher, *Rydberg atoms* (Cambridge University Press, 1994).
- [2] M. Saffman, T. G. Walker, and K. Mølmer, “Quantum information with rydberg atoms”, *Reviews of Modern Physics* **82**, 2313–2363 (2010).
- [3] C. Ates, T. Pohl, T. Pattard, and J. M. Rost, “Antiblockade in rydberg excitation of an ultracold lattice gas”, *Physical Review Letters* **98**, 023002 (2007).
- [4] C. Pérez-Espigares, M. Marcuzzi, R. Gutiérrez, and I. Lesanovsky, “Epidemic dynamics in open quantum spin systems”, *Physical Review Letters* **119**, 140401 (2017).
- [5] M. Marcuzzi, M. Buchhold, S. Diehl, and I. Lesanovsky, “Absorbing state phase transition with competing quantum and classical fluctuations”, *Physical Review Letters* **116**, 245701 (2016).
- [6] M. Marcuzzi, E. Levi, W. Li, J. P. Garrahan, B. Olmos, and I. Lesanovsky, “Non-equilibrium universality in the dynamics of dissipative cold atomic gases”, *New Journal of Physics* **17**, 072003 (2015).
- [7] R. Gutiérrez et al., “Experimental signatures of an absorbing-state phase transition in an open driven many-body quantum system”, *Physical Review A* **96**, 041602 (2017).
- [8] H.-K. Janssen, “On the nonequilibrium phase transition in reaction-diffusion systems with an absorbing stationary state”, *Zeitschrift für Physik B Condensed Matter* **42**, 151–154 (1981).
- [9] P. Grassberger, “On phase transitions in schlögl’s second model”, *Zeitschrift für Physik B Condensed Matter* **47**, 365–374 (1982).
- [10] M. Henkel, H. Hinrichsen, and S. Lübeck, *Non-equilibrium phase transitions* (Springer, 2008).
- [11] K. A. Takeuchi, M. Kuroda, H. Chaté, and M. Sano, “Directed percolation criticality in turbulent liquid crystals”, *Physical Review Letters* **99**, 234503 (2007).
- [12] S. Helmrich, A. Arias, G. Lochead, T. Wintermantel, M. Buchhold, S. Diehl, and S. Whitlock, “Signatures of self-organized criticality in an ultracold atomic gas”, *Nature* **577**, 481–486 (2020).
- [13] D.-S. Ding, H. Busche, B.-S. Shi, G.-C. Guo, and C. S. Adams, “Phase diagram and self-organizing dynamics in a thermal ensemble of strongly interacting rydberg atoms”, *Physical Review X* **10**, 021023 (2020).
- [14] P. Bak, C. Tang, and K. Wiesenfeld, “Self-organized criticality: an explanation of the 1/f noise”, *Physical Review Letters* **59**, 381 (1987).
- [15] N. W. Watkins, G. Pruessner, S. C. Chapman, N. B. Crosby, and H. J. Jensen, “25 years of self-organized criticality: concepts and controversies”, *Space Science Reviews* **198**, 3–44 (2016).
- [16] T. Wintermantel et al., “Epidemic growth and griffiths effects on an emergent network of excited atoms”, *Nature Communications* **12**, 103 (2021).

- [17] M. A. Munoz, R. Juhász, C. Castellano, and G. Ódor, “Griffiths phases on complex networks”, *Physical Review Letters* **105**, 128701 (2010).
- [18] T. A. Johnson, E. Urban, T. Henage, L. Isenhower, D. D. Yavuz, T. G. Walker, and M. Saffman, “Rabi oscillations between ground and rydberg states with dipole-dipole atomic interactions”, *Physical Review Letters* **100**, 113003 (2008).
- [19] U. Raitzsch et al., “Investigation of dephasing rates in an interacting rydberg gas”, *New Journal of Physics* **11**, 055014 (2009).
- [20] W. Li, C. Ates, and I. Lesanovsky, “Nonadiabatic motional effects and dissipative blockade for rydberg atoms excited from optical lattices or microtraps”, *Physical Review Letters* **110**, 213005 (2013).
- [21] C. Ates, T. Pohl, T. Pattard, and J. Rost, “Strong interaction effects on the atom counting statistics of ultracold rydberg gases”, *Journal of Physics B: Atomic, Molecular and Optical Physics* **39**, L233 (2006).
- [22] I. Lesanovsky and J. P. Garrahan, “Kinetic constraints, hierarchical relaxation, and onset of glassiness in strongly interacting and dissipative rydberg gases”, *Physical Review Letters* **111**, 215305 (2013).
- [23] M. Marcuzzi, J. Schick, B. Olmos, and I. Lesanovsky, “Effective dynamics of strongly dissipative rydberg gases”, *Journal of Physics A: Mathematical and Theoretical* **47**, 482001 (2014).
- [24] E. Levi, R. Gutiérrez, and I. Lesanovsky, “Quantum non-equilibrium dynamics of rydberg gases in the presence of dephasing noise of different strengths”, *Journal of Physics B: Atomic, Molecular and Optical Physics* **49**, 184003 (2016).
- [25] M. Magoni, P. P. Mazza, and I. Lesanovsky, “Emergent bloch oscillations in a kinetically constrained rydberg spin lattice”, *Physical Review Letters* **126**, 103002 (2021).
- [26] M. Magoni, C. Nill, and I. Lesanovsky, “Coherent spin-phonon scattering in facilitated rydberg lattices”, *Physical Review Letters* **132**, 133401 (2024).
- [27] S. Hollerith et al., “Quantum gas microscopy of rydberg macrodimers”, *Science* **364**, 664–667 (2019).
- [28] M. D. Lukin, M. Fleischhauer, R. Cote, L. Duan, D. Jaksch, J. I. Cirac, and P. Zoller, “Dipole blockade and quantum information processing in mesoscopic atomic ensembles”, *Physical Review Letters* **87**, 037901 (2001).
- [29] E. Urban, T. A. Johnson, T. Henage, L. Isenhower, D. Yavuz, T. Walker, and M. Saffman, “Observation of rydberg blockade between two atoms”, *Nature Physics* **5**, 110–114 (2009).
- [30] M. Weidemüller, “There can be only one”, *Nature Physics* **5**, 91–92 (2009).
- [31] D. Barredo, S. De Léséleuc, V. Lienhard, T. Lahaye, and A. Browaeys, “An atom-by-atom assembler of defect-free arbitrary two-dimensional atomic arrays”, *Science* **354**, 1021–1023 (2016).
- [32] M. Endres et al., “Atom-by-atom assembly of defect-free one-dimensional cold atom arrays”, *Science* **354**, 1024–1027 (2016).

- [33] D. Barredo, V. Lienhard, S. De Leseleuc, T. Lahaye, and A. Browaeys, “Synthetic three-dimensional atomic structures assembled atom by atom”, *Nature* **561**, 79–82 (2018).
- [34] H. Weimer, M. Müller, I. Lesanovsky, P. Zoller, and H. P. Büchler, “A rydberg quantum simulator”, *Nature Physics* **6**, 382–388 (2010).
- [35] D. Barredo, H. Labuhn, S. Ravets, T. Lahaye, A. Browaeys, and C. S. Adams, “Coherent excitation transfer in a spin chain of three rydberg atoms”, *Physical Review Letters* **114**, 113002 (2015).
- [36] S. De Léséleuc et al., “Observation of a symmetry-protected topological phase of interacting bosons with rydberg atoms”, *Science* **365**, 775–780 (2019).
- [37] P. Schauß et al., “Crystallization in ising quantum magnets”, *Science* **347**, 1455–1458 (2015).
- [38] H. Labuhn, D. Barredo, S. Ravets, S. De Léséleuc, T. Macri, T. Lahaye, and A. Browaeys, “Tunable two-dimensional arrays of single rydberg atoms for realizing quantum ising models”, *Nature* **534**, 667–670 (2016).
- [39] H. Bernien et al., “Probing many-body dynamics on a 51-atom quantum simulator”, *Nature* **551**, 579–584 (2017).
- [40] V. Lienhard et al., “Observing the space-and time-dependent growth of correlations in dynamically tuned synthetic ising models with antiferromagnetic interactions”, *Physical Review X* **8**, 021070 (2018).
- [41] E. Guardado-Sánchez, P. T. Brown, D. Mitra, T. Devakul, D. A. Huse, P. Schauß, and W. S. Bakr, “Probing the quench dynamics of antiferromagnetic correlations in a 2d quantum ising spin system”, *Physical Review X* **8**, 021069 (2018).
- [42] G. Semeghini et al., “Probing topological spin liquids on a programmable quantum simulator”, *Science* **374**, 1242–1247 (2021).
- [43] S. Ohler, M. Kiefer-Emmanouilidis, and M. Fleischhauer, “Quantum spin liquids of rydberg excitations in a honeycomb lattice induced by density-dependent peierls phases”, *Physical Review Research* **5**, 013157 (2023).
- [44] J. Schachenmayer, I. Lesanovsky, A. Micheli, and A. Daley, “Dynamical crystal creation with polar molecules or rydberg atoms in optical lattices”, *New Journal of Physics* **12**, 103044 (2010).
- [45] R. Samajdar, S. Choi, H. Pichler, M. D. Lukin, and S. Sachdev, “Numerical study of the chiral $z=3$ quantum phase transition in one spatial dimension”, *Physical Review A* **98**, 023614 (2018).
- [46] J. R. Rydberg, “Xxxiv. on the structure of the line-spectra of the chemical elements”, *The London, Edinburgh, and Dublin philosophical magazine and journal of science* **29**, 331–337 (1890).
- [47] W. Pauli Jr., “Über das wasserstoffspektrum vom standpunkt der neuen quantenmechanik”, *Zeitschrift für Physik A Hadrons and nuclei* **36**, 336–363 (1926).
- [48] N. Šibalic and C. S. Adams, “Rydberg physics”, in (IOP Publishing, 2018), pp. 2399–2891.

- [49] C. S. Adams, J. D. Pritchard, and J. P. Shaffer, “Rydberg atom quantum technologies”, *Journal of Physics B: Atomic, Molecular and Optical Physics* **53**, 012002 (2019).
- [50] B. Höglund and P. Mezger, “Hydrogen emission line $n110 \rightarrow n109$: detection at 5009 megahertz in galactic h ii regions”, *Science* **150**, 339–348 (1965).
- [51] R. Löw, H. Weimer, J. Nipper, J. B. Balewski, B. Butscher, H. P. Büchler, and T. Pfau, “An experimental and theoretical guide to strongly interacting rydberg gases”, *Journal of Physics B: Atomic, Molecular and Optical Physics* **45**, 113001 (2012).
- [52] A. Browaeys, D. Barredo, and T. Lahaye, “Experimental investigations of dipole–dipole interactions between a few rydberg atoms”, *Journal of Physics B: Atomic, Molecular and Optical Physics* **49**, 152001 (2016).
- [53] T. G. Walker and M. Saffman, “Consequences of zeeman degeneracy for the van der waals blockade between rydberg atoms”, *Physical Review A* **77**, 032723 (2008).
- [54] T. Förster, “Zwischenmolekulare energiewanderung und fluoreszenz”, *Annalen der Physik* **437**, 55–75 (1948).
- [55] F. Engel et al., “Observation of rydberg blockade induced by a single ion”, *Physical Review Letters* **121**, 193401 (2018).
- [56] D. Jaksch, J. I. Cirac, P. Zoller, S. L. Rolston, R. Côté, and M. D. Lukin, “Fast quantum gates for neutral atoms”, *Physical Review Letters* **85**, 2208 (2000).
- [57] L. Isenhower et al., “Demonstration of a neutral atom controlled-not quantum gate”, *Physical Review Letters* **104**, 010503 (2010).
- [58] J. Zeiher, P. Schauß, S. Hild, T. Macri, I. Bloch, and C. Gross, “Microscopic characterization of scalable coherent rydberg superatoms”, *Physical Review X* **5**, 031015 (2015).
- [59] S. M. Burroughs and S. F. Tebbens, “Power-law scaling and probabilistic forecasting of tsunami runup heights”, *Pure and Applied Geophysics* **162**, 331–342 (2005).
- [60] B. Gutenberg and C. F. Richter, “Frequency of earthquakes in california”, *Bulletin of the Seismological Society of America* **34**, 185–188 (1944).
- [61] A. Sornette and D. Sornette, “Self-organized criticality and earthquakes”, *Europhysics Letters* **9**, 197 (1989).
- [62] B. D. Malamud, G. Morein, and D. L. Turcotte, “Forest fires: an example of self-organized critical behavior”, *Science* **281**, 1840–1842 (1998).
- [63] J. B. Elsner, T. H. Jagger, H. M. Widen, and D. R. Chavas, “Daily tornado frequency distributions in the united states”, *Environmental Research Letters* **9**, 024018 (2014).
- [64] L. de Arcangelis, C. Godano, E. Lippiello, and M. Nicodemi, “Universality in solar flare and earthquake occurrence”, *Physical Review Letters* **96**, 051102 (2006).
- [65] J. Hesse and T. Gross, “Self-organized criticality as a fundamental property of neural systems”, *Frontiers in Systems Neuroscience* **8**, 166 (2014).

- [66] C. J. Rhodes and R. M. Anderson, “Power-laws governing epidemics in isolated populations”, *Nature* **381**, 600–602 (1996).
- [67] H. Hinrichsen, “Non-equilibrium phase transitions”, *Physica A: Statistical Mechanics and its Applications* **369**, 1–28 (2006).
- [68] S. Sachdev, “Quantum phase transitions”, *Physics World* **12**, 33 (1999).
- [69] E. Ising, “Beitrag zur theorie des ferromagnetismus”, *Zeitschrift für Physik* **31**, 253–258 (1925).
- [70] C. Kittel and P. McEuen, *Introduction to solid state physics* (John Wiley & Sons, 2018).
- [71] K. G. Wilson, “Renormalization group and critical phenomena. i. renormalization group and the kadanoff scaling picture”, *Physical review B* **4**, 3174 (1971).
- [72] K. G. Wilson, “Renormalization group and critical phenomena. ii. phase-space cell analysis of critical behavior”, *Physical Review B* **4**, 3184 (1971).
- [73] G. S. Rushbrooke, “On the thermodynamics of the critical region for the ising problem”, *The Journal of Chemical Physics* **39**, 842–843 (1963).
- [74] B. Widom, “Equation of state in the neighborhood of the critical point”, *The Journal of Chemical Physics* **43**, 3898–3905 (1965).
- [75] J. W. Essam and M. E. Fisher, “Padé approximant studies of the lattice gas and ising ferromagnet below the critical point”, *The Journal of Chemical Physics* **38**, 802–812 (1963).
- [76] B. D. Josephson, “Relation between the superfluid density and order parameter for superfluid he near t_c ”, *Physics Letters* **21**, 608–609 (1966).
- [77] A. O’Hagan, *Kendall’s advanced theory of statistic 2b* (John Wiley & Sons, 2010).
- [78] M. A. Munoz, G. Grinstein, R. Dickman, and R. Livi, “Critical behavior of systems with many absorbing states”, *Physical Review Letters* **76**, 451 (1996).
- [79] M. A. Munoz, G. Grinstein, and R. Dickman, “Phase structure of systems with infinite numbers of absorbing states”, *Journal of Statistical Physics* **91**, 541–569 (1998).
- [80] K. A. Takeuchi, M. Kuroda, H. Chaté, and M. Sano, “Experimental realization of directed percolation criticality in turbulent liquid crystals”, *Physical Review E* **80**, 051116 (2009).
- [81] J. A. Bonachela and M. A. Munoz, “Self-organization without conservation: true or just apparent scale-invariance?”, *Journal of Statistical Mechanics* **2009**, P09009 (2009).
- [82] M. Vojta, “Quantum phase transitions”, *Reports on Progress in Physics* **66**, 2069 (2003).
- [83] H. J. Jensen, *Self-organized criticality: emergent complex behavior in physical and biological systems*, Vol. 10 (Cambridge University Press, 1998).
- [84] D. Sornette, *Critical phenomena in natural sciences: chaos, fractals, selforganization and disorder: concepts and tools* (Springer Science & Business Media, 2006).
- [85] B. Drossel and F. Schwabl, “Self-organized critical forest-fire model”, *Physical Review Letters* **69**, 1629 (1992).

- [86] R. Pastor-Satorras, C. Castellano, P. Van Mieghem, and A. Vespignani, “Epidemic processes in complex networks”, *Reviews of Modern Physics* **87**, 925–979 (2015).
- [87] W. O. Kermack and A. G. McKendrick, “A contribution to the mathematical theory of epidemics”, *Proceedings of the Royal Society of London. Series A* **115**, 700–721 (1927).
- [88] R. M. Anderson and R. M. May, *Infectious diseases of humans: dynamics and control* (Oxford University Press, 1991).
- [89] N. T. J. Bailey, “The mathematical theory of epidemics”, *Journal of the Royal Statistical Society. Series C* **8**, 60–61 (1959).
- [90] M. J. Keeling and K. T. D. Eames, “Networks and epidemic models”, *Journal of the Royal Society Interface* **2**, 295–307 (2005).
- [91] C. Viboud, L. Simonsen, and G. Chowell, “A generalized-growth model to characterize the early ascending phase of infectious disease outbreaks”, *Epidemics* **15**, 27–37 (2016).
- [92] A.-L. Barabási, “Network science”, *Philosophical Transactions of the Royal Society A: Mathematical, Physical and Engineering Sciences* **371**, 20120375 (2013).
- [93] P. Erdos and A. Rényi, “On the evolution of random graphs”, *Publications of the Mathematical Institute of the Hungarian Academy of Sciences* **5**, 17–60 (1960).
- [94] R. Pastor-Satorras and A. Vespignani, “Epidemic dynamics in finite size scale-free networks”, *Physical Review E* **65**, 035108 (2002).
- [95] M. E. J. Newman, “Spread of epidemic disease on networks”, *Physical Review E* **66**, 016128 (2002).
- [96] H. Andersson and B. Djehiche, “A threshold limit theorem for the stochastic logistic epidemic”, *Journal of Applied Probability* **35**, 662–670 (1998).
- [97] D. F. Walls, “Squeezed states of light”, *Nature* **306**, 141–146 (1983).
- [98] L. Mandel and E. Wolf, *Optical coherence and quantum optics* (Cambridge University Press, 1995).
- [99] R. J. Glauber, “Coherent and incoherent states of the radiation field”, *Physical Review* **131**, 2766–2788 (1963).
- [100] E. C. G. Sudarshan, “Equivalence of semiclassical and quantum mechanical descriptions of statistical light beams”, *Physical Review Letters* **10**, 277–279 (1963).
- [101] K. Husimi, “Some formal properties of the density matrix”, *Proceedings of the Physico-Mathematical Society of Japan. 3rd Series* **22**, 264–314 (1940).
- [102] E. Wigner, “On the quantum correction for thermodynamic equilibrium”, *Physical Review* **40**, 749–759 (1932).
- [103] M. O. Scully and M. S. Zubairy, *Quantum optics* (Cambridge University Press, 1997).
- [104] V. Weisskopf, “Probleme der neueren quantentheorie des elektrons”, *Naturwissenschaften* **23**, 631–637 (1935).
- [105] T. A. Welton, “Some observable effects of the quantum-mechanical fluctuations of the electromagnetic field”, *Physical Review* **74**, 1157 (1948).

- [106] W. E. Lamb Jr and R. C. Retherford, “Fine structure of the hydrogen atom by a microwave method”, *Physical Review* **72**, 241 (1947).
- [107] H. B. G. Casimir and D. Polder, “The influence of retardation on the london-van der waals forces”, *Physical Review* **73**, 360–372 (1948).
- [108] D. Leibfried, R. Blatt, C. Monroe, and D. Wineland, “Quantum dynamics of single trapped ions”, *Reviews of Modern Physics* **75**, 281–324 (2003).
- [109] R. J. Glauber, “Some notes on multiple-boson processes”, *Physical Review* **84**, 395–400 (1951).
- [110] R. P. Feynman, “An operator calculus having applications in quantum electrodynamics”, *Physical Review* **84**, 108–128 (1951).
- [111] R. Slusher, L. W. Hollberg, B. Yurke, J. C. Mertz, and J. F. Valley, “Observation of squeezed states generated by four-wave mixing in an optical cavity”, *Physical Review Letters* **55**, 2409 (1985).
- [112] L.-A. Wu, H. J. Kimble, J. L. Hall, and H. Wu, “Generation of squeezed states by parametric down conversion”, *Physical Review Letters* **57**, 2520 (1986).
- [113] C. M. Caves, “Quantum-mechanical noise in an interferometer”, *Physical Review D* **23**, 1693–1708 (1981).
- [114] B. P. Abbott et al. (LIGO Scientific Collaboration and Virgo Collaboration), “Observation of gravitational waves from a binary black hole merger”, *Physical Review Letters* **116**, 061102 (2016).
- [115] M. Tse et al., “Quantum-enhanced advanced ligo detectors in the era of gravitational-wave astronomy”, *Physical Review Letters* **123**, 231107 (2019).
- [116] H. Grote, K. Danzmann, K. L. Dooley, R. Schnabel, J. Slutsky, and H. Vahlbruch, “First long-term application of squeezed states of light in a gravitational-wave observatory”, *Physical Review Letters* **110**, 181101 (2013).
- [117] M. Kitagawa and M. Ueda, “Squeezed spin states”, *Physical Review A* **47**, 5138 (1993).
- [118] J. Ma, X. Wang, C.-P. Sun, and F. Nori, “Quantum spin squeezing”, *Physics Reports* **509**, 89–165 (2011).
- [119] O. Gühne and G. Tóth, “Entanglement detection”, *Physics Reports* **474**, 1–75 (2009).
- [120] O. Hosten, N. J. Engelsen, R. Krishnakumar, and M. A. Kasevich, “Measurement noise 100 times lower than the quantum-projection limit using entangled atoms”, *Nature* **529**, 505–508 (2016).
- [121] A. V. Chechkin, R. Metzler, J. Klafter, and V. Y. Gonchar, “Introduction to the theory of lévy flights”, *Anomalous Transport: Foundations and Applications*, 129–162 (2008).
- [122] G. Vidal, “Efficient classical simulation of slightly entangled quantum computations”, *Physical Review Letters* **91**, 147902 (2003).
- [123] F. Bloch, “Über die quantenmechanik der elektronen in kristallgittern”, *Zeitschrift für Physik* **52**, 555–600 (1929).

- [124] G. H. Wannier, “Wave functions and effective hamiltonian for bloch electrons in an electric field”, *Physical Review* **117**, 432 (1960).
- [125] J. C. Slater and G. F. Koster, “Simplified lcao method for the periodic potential problem”, *Physical Review* **94**, 1498 (1954).
- [126] J. Hartmann, D. Breu, T. Schlegel, and M. Fleischhauer, “Truncated wigner approximation for unitary and open many-body spin systems”, To be published (2025).
- [127] N. Metropolis and S. Ulam, “The monte carlo method”, *Journal of the American Statistical Association* **44**, 335–341 (1949).
- [128] A. Chotia, M. Viteau, T. Vogt, D. Comparat, and P. Pillet, “Kinetic monte carlo modeling of dipole blockade in rydberg excitation experiment”, *New Journal of Physics* **10**, 045031 (2008).
- [129] K. A. Fichthorn and W. H. Weinberg, “Theoretical foundations of dynamical monte carlo simulations”, *The Journal of Chemical Physics* **95**, 1090–1096 (1991).
- [130] A. Jansen, “An introduction to monte carlo simulations of surface reactions”, arXiv preprint cond-mat/0303028, <https://doi.org/10.48550/arXiv.cond-mat/0303028> (2003).
- [131] V. R. Barlett, J. Bigeón, M. Hoyuelos, and H. Martín, “Differences between fixed time step and kinetic monte carlo methods for biased diffusion”, *Journal of Computational Physics* **228**, 5740–5748 (2009).
- [132] M. Tuckerman, B. J. Berne, and G. J. Martyna, “Reversible multiple time scale molecular dynamics”, *The Journal of Chemical Physics* **97**, 1990–2001 (1992).
- [133] E. W. Weisstein, *Lorentzian function*, <https://mathworld.wolfram.com/LorentzianFunction.html>, From MathWorld—A Wolfram Web Resource. Accessed: 2025-03-19.

Curriculum Vitae

Daniel Steven Brady

 brady@rptu.de

Pirmasenser Straße 50, 67655 Kaiserslautern

Geboren: 12.09.1995 in Langen (Hessen)

Nationalität: Deutsch, U.S. Amerikanisch



Berufserfahrung

Aug 2025 –

Wissenschaftlicher Mitarbeiter (Post-Doc)

RPTU Kaiserslautern-Landau

Simulation und Analyse komplexer Vielteilchensysteme.

Sep 2021 – Jun 2025

Wissenschaftlicher Mitarbeiter (Promotion)

Technische Universität Kaiserslautern / RPTU Kaiserslautern-Landau

Simulation und Analyse komplexer Vielteilchensysteme im Rahmen der Promotion.

Präsentationen auf nationalen und internationalen Konferenzen.

Sep 2020 – Apr 2021

Hilfswissenschaftler (HiWi)

Technische Universität Kaiserslautern

Simulationen zur Untersuchung von Festkörperbandstrukturen im Rahmen des Projekts *Influence of Structural Dynamics on Ultrafast Magnetization Dynamics*. Analyse des Einflusses struktureller Dynamik auf ultrakurze Magnetisierungsprozesse in metallischen Ferromagneten.

Sep 2018 – Apr 2020

Studentische Hilfskraft (HiWi)

Technische Universität Kaiserslautern

Betreuung des physikalischen Anfängerpraktikums in den Monaten *September 2018, März 2019, September 2019* und *März 2020*.

Zuständig für die Betreuung der Studierenden bei den Experimenten, Korrektur der Laborhefte sowie Durchführung der Testate.

Jul 2017 – Mrz 2018

Hilfswissenschaftler (HiWi)

Technische Universität Kaiserslautern

Experimentelle Analyse der Auswirkung von Oberflächenstrukturen auf die Struktur von Wassertropfen.

Ausbildung

Sep 2021 – Jun 2025

Promotion in theoretischer Physik

Technische Universität Kaiserslautern / RPTU Kaiserslautern-Landau

Titel der Dissertation: *Nonequilibrium Dynamics with Rydberg Facilitation: From Epidemic Spreading to Motional Squeezing*
mit Auszeichnung

Feb 2019 – Aug 2021

Studium M.Sc. Physik

Technische Universität Kaiserslautern

Thema der Masterarbeit: *geteilte experimentelle und theoretische Untersuchung von selbst-organisierter Kritikalität in einem Rydberg-Gas*

Note: 1,3

Sep 2015 – Feb 2019

Studium B.Sc. Physik

Technische Universität Kaiserslautern

Note: 2,0

Ausbildung (continued)

Sep 2013 – Mai 2015  **Qualifikationsphase der gymnasialen Oberstufe**
Gymnasium am Mosbacher Berg, Wiesbaden
Note: 2,4

Sep 2009 – Jun 2013  **High School Grades 9-12**
General H. H. Arnold High School, Wiesbaden
GPA: 3.125

Veröffentlichungen

Fachzeitschriften

- 1 D. M. Fieguth, T. Schlachter, D. S. Brady, J. R. Anglin. "Hamiltonian Active Particles in an Environment". *Physical Review E* **106**, 044201 (2022).
- 2 S. Ohler, D. Brady, W. Lötzsch, M. Fleischhauer, and J. S. Otterbach. "Towards Learning Self-Organized Criticality of Rydberg Atoms using Graph Neural Networks". *ICML 2nd AI4Science Workshop, Baltimore, MD* (2022).
- 3 D. Brady and M. Fleischhauer. "Mean-field approach to Rydberg facilitation in a gas of atoms at high and low temperatures". *Physical Review A* **108**, 052812 (2023).
- 4 D. Brady, J. Bender, P. Mischke, S. Ohler, T. Niederprüm, H. Ott, and M. Fleischhauer. "Griffiths Phase in a Facilitated Rydberg Gas at Low Temperatures". *Physical Review Research* **6**, 013052 (2024).
- 5 D. Brady, S. Ohler, J. Otterbach, and M. Fleischhauer. "Anomalous Directed Percolation on a Dynamic Network Using Rydberg Facilitation". *Physical Review Letters* **133**, 173401 (2024).
- 6 S. Ohler, D. Brady, P. Mischke, J. Bender, H. Ott, T. Niederprüm, W. Ripken, J. S. Otterbach, and M. Fleischhauer. "Nonequilibrium Universality of Rydberg-Excitation Spreading on a Dynamic Network". arXiv:2502.14757 (2025). (*Physical Review Research* in review).
- 7 D. Brady and M. Fleischhauer. "Non-Classical Spin-Phonon Correlations Induced by Rydberg Facilitation in a Lattice". arXiv:2504.19679 (2025). (*Physical Review Letters* submitted).
- 8 T. Schlegel*, E. Konstantinidou*, M. Fleischhauer, and D. Brady. "Dephasing in Rydberg Facilitation Due to State-Dependent Dipole Forces". arXiv:2505.09314 (2025). (*Physical Review A* submitted).

Vorträge

- 1 *Epidemic Dynamics in a Facilitated Rydberg Gas*
Contributed talk, *GiRyd Annual Meeting*, Tübingen, 2023.
- 2 *Heterogeneous Effects in a Facilitated Rydberg Gas*
Contributed talk, *DPG SAMOP Spring Meeting*, Hannover, 2023.
- 3 *Self-Organized Criticality and Griffiths Effects in Facilitated Rydberg Gases*
Contributed talk, *APS DAMOP Annual Meeting*, Spokane WA, 2023.
- 4 *Nonequilibrium Phase Transitions in Rydberg Gases*
Contributed talk, *APS DAMOP Annual Meeting*, Fort Worth TX, 2024.
- 5 *Anomalous Directed Percolation and Self-Organized Criticality in Rydberg Gases*
Invited talk, *FUUD24*, Dresden, 2024.

6 *Interplay Between Coherent Facilitation and Phonons*

Contributed talk, APS DAMOP Annual Meeting, Portland OR, 2025.

Skills

Sprachen	Englisch und Deutsch als Muttersprache
Programmiersprachen	Python, Julia, Mathematica, etwas Matlab und PyTorch
weitere Software	LaTeX, Inkscape, Git

Acknowledgments

Of course, this is not all of my own merit. Without the help and support of countless people, I don't know how far I would have gotten down this road. First and foremost, I want to thank Michael for the unbelievable support he has given me both in physics and beyond, while supervising. Thanks in great part to you, I can look back on my PhD years with genuine appreciation. I also want to thank Herwig Ott and Matthew Eiles for agreeing to be part of my defense committee, meaning they actually had to read this thesis. Especially, I also want to thank Herwig for the great experiment/theory cooperation we have had.

Next, I want to thank the group. I especially want to thank Simon for the amazing cooperation we had on many of the projects within this thesis and Julius for his help in setting up and bug fixing my TEBD algorithm. This probably saved me a month of time and a lot of headaches. Also I want to thank Eva and Tom for their dedication and perseverance when working on our project. And of course I want to thank all group members, both current and former, for the many fun and pleasant memories. Thanks to: Akash, Andrei, Benno, Carsten, Chris, Dennis, Enrico, Eric, Hoang, Hugo, Jens, Lukas, Max, and Razmik.

Finally, I want to thank my friends and my family. Your support throughout these years – whether through conversation, humor, or simply being there – have been invaluable. Especially, I want to thank Linda for her enduring support, and I want to thank my parents and my sister for their love and support throughout my entire studies and beyond.

Fachbereich Physik

Rheinland-Pfälzische Technische
Universität Kaiserslautern Landau

Postfach 3049
67653 Kaiserslautern, Germany

www.physik.rptu.de/

R **TU** Rheinland-Pfälzische
Technische Universität
P Kaiserslautern
Landau